Spectroscopic Study of $CaMnO_3$ / $CaRuO_3$ Superlattices and $YTiO_3$ Single Crystals

Von der Fakultät Mathematik und Physik der Universität Stuttgart
zur Erlangung der Würde eines Doktors der Naturwissenschaften (Dr. rer. nat.)
genehmigte Abhandlung

vorgelegt von

Petar Yordanov
aus Sofia, Bulgarien

Hauptberichter: Prof. Dr. Bernhard Keimer
Mitberichter: Prof. Dr. Gert Denninger
Vorsitzender: Prof. Dr. Alejandro Muramatsu

Tag der mündlichen Prüfung: 3 Dezember 2009

Max-Planck-Institut für Festkörperforschung
Stuttgart 2009

Contents

Chapter 1

Introduction

1.1 Transition Metal Oxides (TMO) and TMO-based Superlattices

Transition metal oxides (TMO) of Perovskite type with general formula (ABO_3) and their layered variations (Fig. 1.1.1), are among the most fascinating classes of materials studied in solid state physics. An exceptional variety of ground states is revealed in their phase diagrams upon chemical doping. The Mott insulating state, unconventional superconductivity, non-Fermi liquid metallic states, orbital liquid states in systems with orbital degeneracy, various ordering phenomena of charge, spin and orbitals, spin-dependent transport effects, are all part of the rich physics of transition metal oxides [1.1][1.2][1.3][1.4][1.5][1.6]. Many of these phenomena are still not fully understood and their theoretical description together with the experimental search for new properties is currently at the forefront of solid state physics. Indeed, TMOs represent a special category in which electrons are *strongly correlated.* These correlations imply a many-body quantum mechanical problem in which the *full set* of electron's degrees of freedom: *charge*, *spin,* and *orbital* (Fig.1.1.2) is involved. In some cases coupling to the *lattice* may also be of importance. Another factor of fundamental significance is the dimensionality of the transition metal-oxide bond network. The *quasi-two dimensional* (*2D*) layered crystal structure of some of the member compounds in the Ruddlesden-Popper phases (Fig.1.1.1) determines the spatial anisotropy to the electrons motion. This additional structural factor, apart from the magnetic and Coulomb interaction, is known to play a decisive role, for instance, in the phenomenon of unconventional superconductivity. Indeed, this phenomenon has so far only been discovered in 2D

layered systems like: $La_{2-x}Ba_xCuO_4$, $YBa_2Cu_3O_{6+x}$, Sr_2RuO_4, $Na_xCoO_2{\times}yH_2O$, and only recently in $LaFeAs(O_{1-x}F_x)$ [1.3][1.7][1.8][1.9][1.10].

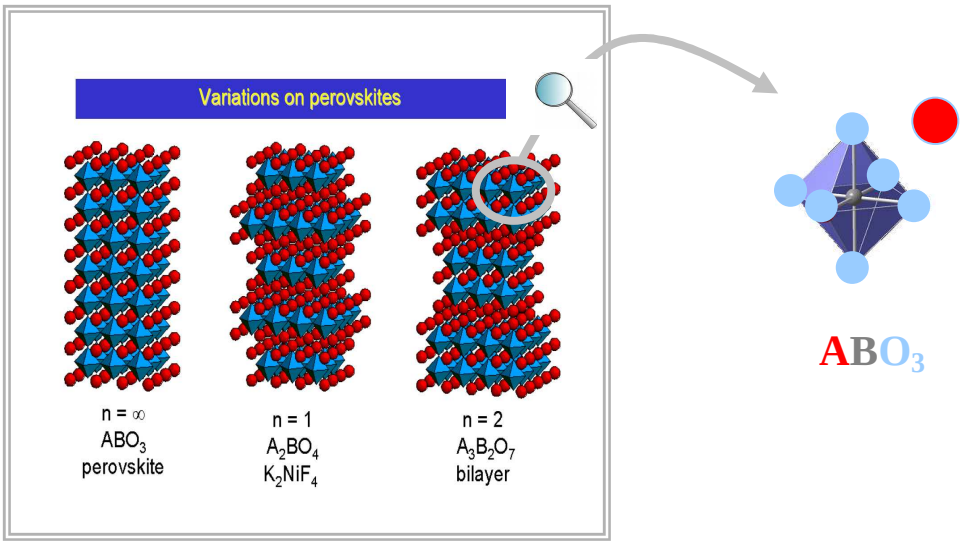

Figure 1.1.1 Perovskite crystal structure; A-rare-earth or alkaline-earth metal, B-transition metal, O-oxygen. Together with the layered modifications, the Perovskite structure form the Ruddlesden-Popper phases [1.11].

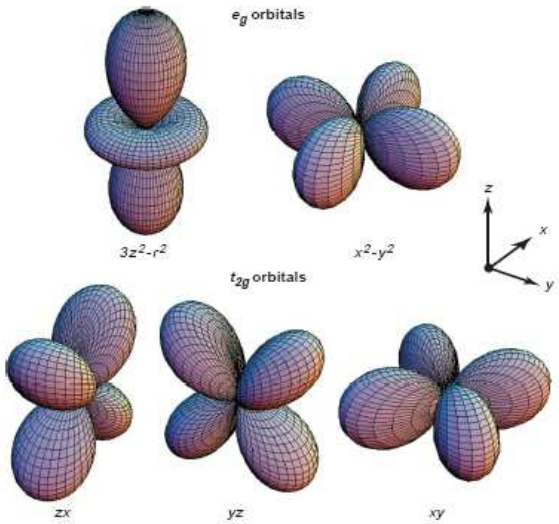

Figure 1.1.2 3*d*-orbitals. In a cubic crystal field, the *3d*-levels are split to triply degenerate t_{2g} (lower in energy) and doubly degenerate e_g manifolds [1.4]. Further splitting can be induced by additional symmetry lowering, like the Jahn-Teller distortion or strong spin-orbit coupling.

Thus, the coupling between the different degrees of freedom in the electron system and the spatial dimensionality on the other hand, will define the state in which the system eventually collapses. Not surprisingly, the numerous ground states found in the phase diagrams of these compounds lie close in energy and often just a fine tuning of a selected degree of freedom, by external fields, pressure etc., is sufficient to turn the system from one state into another. These are part of the reasons transition metal oxides are of great fundamental and practical importance. Their intriguing properties hold the promise for the design of multifunctional devices and challenge theoreticians to develop new, more general models, adequately describing the collective behaviour of the electronic system.

The concept of artificial *superlattices (SL)* made from TMO compounds is a relatively new, promising and quickly developing field in solid state research. It offers a different approach of studying and *engineering properties* of materials embedded in specially selected surroundings. By precise synthesis of thin films and SLs, the 2D-properties and related phenomena that arise at the interface when two materials are brought in contact can be widely explored. Furthermore, conditions for electron charge transfer across the interfaces can be ensured that is not normally achievable in bulk by means of conventional chemical doping. The resulting new electronic states in the vicinity of the junction may then locally modify the orbital and / or the magnetic properties. Some recent examples are: $YBa_2Cu_3O_7$ / $La_{2/3}Ca_{1/3}MnO_3$, a SL system that combines two antagonistic order parameters such as superconductivity and ferromagnetism in which an interesting interface orbital reconstruction was recently observed [1.12][1.13], Mott insulator / band insulator in $LaTiO_3$ / $SrTiO_3$ heterostructures [1.14][1.15], antiferromagnetic insulator / paramagnetic metal in $CaMnO_3$ / $CaRuO_3$ [1.16], and the $SrTiO_3$ / $LaAlO_3$ SLs, comprising two band insulators with a polar boundary due to $LaAlO_3$. This particular system attracted strong interest and initiated many related projects after the discovery of high-mobility 2D-electron gas at the interfaces [1.17]. Even though rapidly expanding, the research on TMO superlattices is currently far from the perfection level semiconductor researchers have reached in preparing low-dimensional structures. Some of the reasons originate in the complexity of the TMOs, which are in the simplest case ternary compounds, and often, two different materials require very different growth conditions. These circumstances may impose certain

limitations on the crystal growth process and make difficult the precise control of stoichiometry and / or the interface roughness, hence limitations on the choice of materials for a SL structure etc. [1.18]. The perspectives however, do not seem less exciting. As the deposition methods and the knowledge in TMO research advance, it is not difficult to imagine a situation where a perfect *artificial superlattice unit cell* is prepared out of two or more different materials that will constitute a *new "3D" entity*, or in other words *new material*, with properties owing to local and long range effects that aren't just a simple combination of features inherent to the precursors. Referring again to the layered systems with large complex unit cells (Fig.1.1.3), this seems an achievable goal.

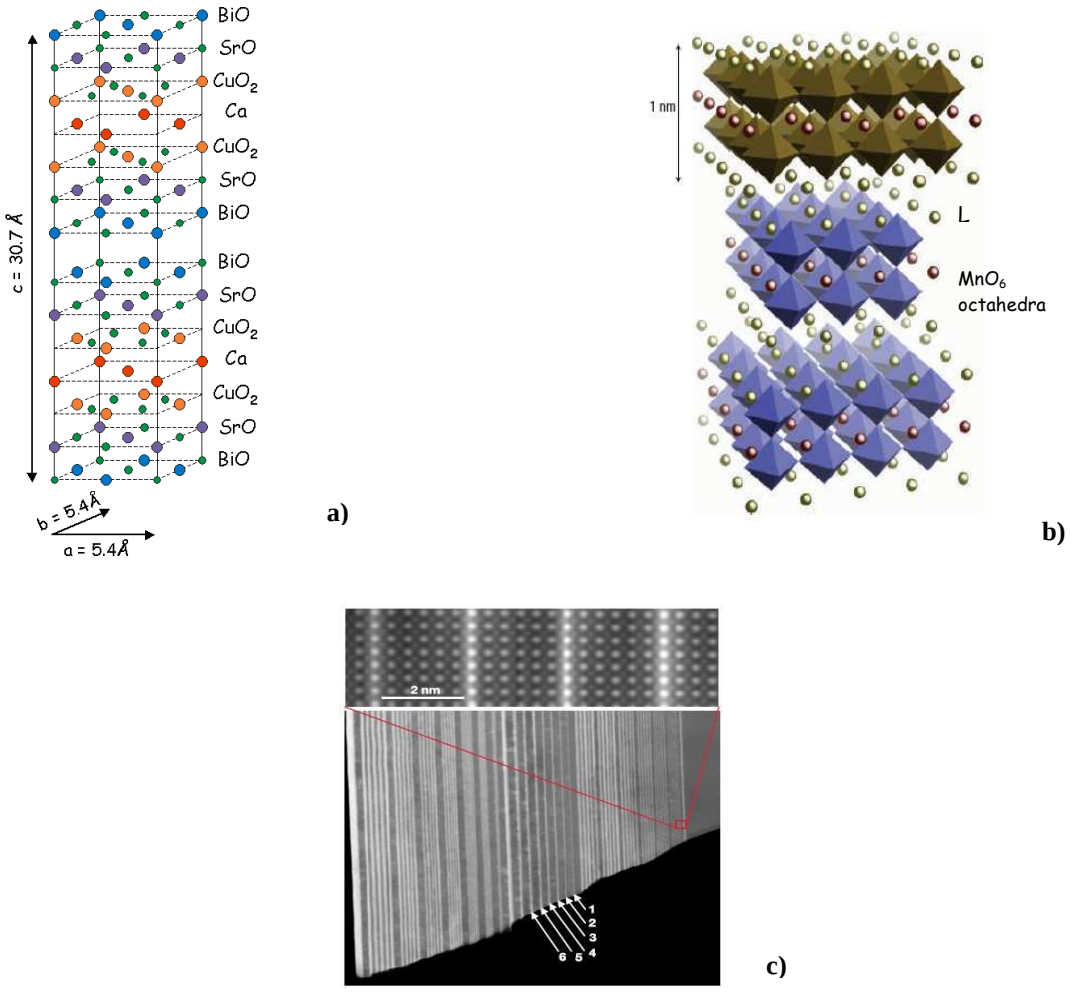

Figure 1.1.3 a) High-Temperature Superconductor $Bi_2Sr_2Ca_1Cu_2O_x$ [1.19] **b)** Structure of the naturally bilayered metallic manganite $La_{1.2}Sr_{0.8}Mn_2O_7$ [1.20] **c)** Superlattice made of $LaTiO_3$ layers (bright) spaced by $SrTiO_3$ layers (dark grey). The numbers in the image indicate the number of $LaTiO_3$ unit cells in each layer [1.14].

1.2 Solid State Spectroscopy

Spectroscopy is originally the study of light-matter interaction as a function of the wavelength λ, and historically, the visible light. The word "spectrum" was introduced by Newton in 17th century naming the coloured figure obtained by scattering sunlight through a prism. This is by far not the first experimental approach to light phenomena. Some sources even date back to 300 BC, when Euclid discussed the focus of a spherical mirror [1.21]. Nowadays, spectroscopy is a key experimental research method and tool in all natural sciences, medicine, engineering, in aeronautics, for military purposes, quality and security control and it is not restricted to the use of electromagnetic radiation. Many spectroscopy techniques make use of particles or acoustic waves and allow application of external stimuli such as magnetic field, pressure etc. A modern definition of spectroscopy would be - energy analysis of an object's response exposed to a perturbation.

In a solid material each *elementary excitation* has its characteristic space / time (r,t) or wavevector (momentum $p = \hbar q$) / frequency (q,ω) dispersion domain that requires specific spectroscopy technique in order to be studied [1.22][1.23]. When the external "probe" perturbation is small and couples to the elementary excitations, we assume linear reactions. The linear response theory then links the *response functions* to the relevant excitations through the fluctuation-dissipation theorem. These response functions are properties of the solid state system itself and are assumed independent of the driving force. Their theoretical derivation is based on very general principles which make them practically universal in a sense that they consider, in principle, all possible excitations and hold for all momentum / energy ($q, E = \hbar\omega$) ranges. They are formulated in time and space (r,t), but since the response is momentum / frequency (q,ω) dependent and more convenient to mathematically operate, a conversion in the Fourier space is often preferred. The general form of a response function is given by:

$$\langle A(\omega)\rangle = \Phi_{AB}(\omega)B(\omega) = \chi_{AB}(\omega)B(\omega) \qquad (1.2.1)$$

$$\chi_{AB}(\omega) = \frac{\langle A(\omega)\rangle}{B(\omega)} = \int_0^\infty dt\Phi_{AB}(t)e^{i\omega t}$$

where $\langle A(\omega)\rangle$ is the change in the observable A induced by the perturbation $B(\omega)$, and $\Phi_{AB}(\omega)$ is defined as "response" of the system to the perturbation. $\chi_{AB}(\omega)$ is called generalized susceptibility, and it is a complex function:

$$\chi(\omega) = \chi_r(\omega) + i\chi_i(\omega) \tag{1.2.2}$$

$$\chi(-\omega) = \chi^*(\omega)$$

$$\chi_r(-\omega) = \chi_r(\omega) \qquad \chi_i(-\omega) = -\chi_i(\omega)$$

with real and imaginary parts that are even and odd with respect to the frequency.

The response functions are analytical complex functions, tensors in the general case, and there exists a fundamental causality principle that implies a connection between the real and imaginary part. This is expressed by the Kramers-Kronig integral relations:

$$\chi_r(\omega) = \frac{2}{\pi} P\int_0^\infty \frac{\omega'\chi_i(\omega')}{\omega'^2 - \omega^2} d\omega' \qquad \chi_i(\omega) = -\frac{2\omega}{\pi} P\int_0^\infty \frac{\chi_r(\omega')}{\omega'^2 - \omega^2} d\omega' \tag{1.2.3}$$

where P, stands for the principle part of the integral.

Very useful in the spectral analysis of solids are the sum rules. They are derived in quantum mechanics on general grounds but specific sum rules can be defined for a particular problem. Sum rules exist for all spectral excitations in solids. An example is:

$$\chi(q,\omega) = \frac{Ne^2}{\varepsilon_0 m}\sum_j \frac{f_j}{\omega_{oj}^2 - \omega^2 - i\gamma_j\omega}$$

$$\sum_j f_j = 1 \tag{1.2.4}$$

Equation (1.2.4) is the so called *f*-sum rule (or Thomas-Reiche-Kuhn sum rule). Here, f_j is oscillator strength which measures the probability of a transition at frequency ω_o. γ is scattering rate, e - the elementary charge, N – the charge, per unit volume, with band mass m, and ε_0 is the dielectric constant (permittivity) of free space.

The spectroscopic methods available nowadays are numerous. Each of them is utilized to resolve in an optimal way a specific physical problem. The choice of technique depends on the type of excitation (for instance, of charge or of magnetic origin) to be analyzed, its energy and momentum domain, anisotropy considerations (polarization dependence), and resolution requirements. For the analysis of the charge dynamics in solids, the response to electromagnetic radiation is considered. Few response functions are commonly used,

these are: the *dielectric function* $\hat{\varepsilon}(\omega) = \varepsilon_1(\omega) + i\varepsilon_2(\omega)$, the *optical conductivity* $\hat{\sigma}(\omega) = \sigma_1(\omega) + i\sigma_2(\omega)$, and the *complex refractive index* $\hat{N}(\omega) = n(\omega) + ik(\omega)$. All of them describe the material properties and are often called *material parameters* and *optical constants*, respectively. The broad range from microwaves up to the deep ultraviolet (UV) is covered by the *optical spectroscopy*. In this range the photon momentum is much smaller than the typical electron momentum in solids, hence the optical spectroscopy measures practically at ($q=0$) limit. The first step in the quantitative analysis of the electromagnetic response of a solid is the determination of optical constants out of the experimental observables. These observables include: *reflectance*, *transmission* and the so-called *ellipsometric angles*. The real and imaginary part of the complex dielectric function $\varepsilon(\omega)$, or the complex conductivity $\sigma(\omega)$, can then be inferred by one of the following: (1) measuring both - reflectivity $R(\omega)$ and transmission $T(\omega)$, or by Kramers-Kronig analysis or modeling of $R(\omega)$ or $T(\omega)$, (2) by measuring ellipsometric angles, $\psi(\omega)$ and $\Delta(\omega)$, which are subsequently used to determine the dielectric function through analytical expressions.

One of the most powerful attributes of optical spectroscopy is its ability to probe very wide range of photon energies. Figure 1.2.1 displays a diagram of some of the physical phenomena in solid matter, in particular, correlated electron systems, observed by means of optical spectroscopy along with their characteristic energies [1.24].

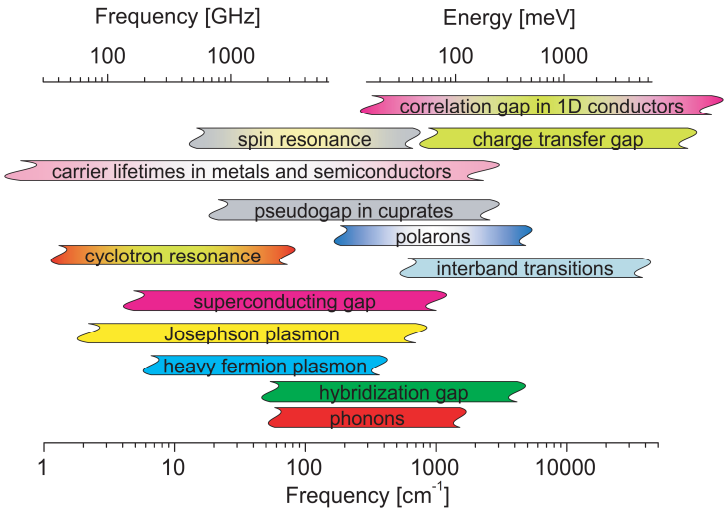

Figure 1.2.1 Selected physical phenomena in solid matter observed by optical spectroscopy [1.24].

When it comes to the magnetic response of solids, neutron scattering is indispensable. Neutrons do not couple directly to the charge and interact with the electron magnetic moment via dipole-dipole interaction. The inelastic neutron scattering provide direct access to the imaginary part of the magnetic susceptibility $\chi''_M(q,\omega)$ i.e., the magnetic excitation spectrum [1.25]. Concerning low-dimensional TMO systems, polarized neutron reflectivity measurements (elastic scattering), has been successfully applied to determine the magnetic structure in superlattices [1.12].

The resonant x-ray spectroscopy methods with synchrotron radiation, including scattering (elastic / inelastic) and x-ray absorption, are increasingly becoming primary experimental research tool in condensed matter physics. Due to the intrinsic properties of synchrotron radiation: energy tunability, very high brilliance and degree of polarization, the x-ray techniques allow high-resolution, element specific probes of charge, spin and orbital states in complex materials such as transition-metal oxides and their superlattices. The inelastic x-ray scattering can even provide access to low-energy charge, orbital, magnetic and lattice excitations [1.26][1.27][1.28].

1.3 Scope of the Thesis

The first two sections of **Chapter 1** give a general overview of the research topics and experimental methods discussed in the thesis. Further on, in **Chapter 2**, some of the most important characteristics and mechanisms underlying the physics of transition metal oxides are presented. As the experimental part of the thesis includes studies on manganites and titanates, these two classes of compounds are exemplified in the exposition of Chapter 2. Several recent works in the emerging research field of transition metal oxide interfaces and superlattices are also discussed along with a brief introduction in x-ray spectroscopic methods with synchrotron radiation. **Chapter 3** introduces the principles of optical spectroscopy and the simplest models for dielectric function, i.e., Lorentz oscillator and Drude dielectric function. The following **Chapter 4** introduces two of the experimental techniques in optical spectroscopy, reflectance and spectroscopic ellipsometry. Further on, we describe the design of a new home-built apparatus for near-normal reflectance with high magnetic fields. Several critical technical details and

findings during the assembling process are also discussed. **Chapter 5** represents a comprehensive experimental spectroscopic study of a prototypical superlattice system made from an antiferromagnetic insulator $CaMnO_3$ and a paramagnetic metal $CaRuO_3$. The resulting interface ferromagnetic state was closely investigated by means of optical spectroscopy as well as by soft x-ray scattering and absorption methods. This study led us to the conclusion that magnetic bound states, i.e. magnetic polarons, have to be considered in the description of this SL system. **Chapter 6** describes a polarized far infrared reflectance study with high magnetic field on the ferromagnetic Mott insulator $YTiO_3$, single crystals. All 25 infrared-active phonon modes were observed. The temperature and magnetic-field dependence of the phonon modes revealed a weak spin-phonon coupling in $YTiO_3$ and largely extended temperature range (up to $T_M \sim 80$ - 100K), for the field-induced effects on the oscillator parameters. This later observation, uncovered short-range magnetic order state which remains even at temperatures as high as three times the temperature of the actual ferromagnetic transition of $T_c \sim 30$K. While a quantitative theoretical description of these data is thus far not available, they point to a complex interplay between spin, orbital, and lattice degrees of freedom due to the near-degeneracy of the Ti t_{2g} orbitals in $YTiO_3$.

Chapter 2

Transition Metal Oxides

The discovery of High-Temperature Superconductivity (HTSC) in the cuprates and the paramagnetic insulating (PI) to ferromagnetic metallic (FM) state transition in the mixed-valence manganites, along with its magnetic field-induced counterpart - the Colossal Magnetoresistance (CMR) Effect, have sparked great interest in the physics of transition metal oxides (TMO). Particularly interesting are the systems with orbital degeneracy. It is nowadays well recognized that the orbital degree of freedom plays an essential role, specifying the spatial electron density distribution. Depending on the orbitals nature, the electronic properties can be largely modified in a directional and/or time scale manner with all the respective consequences, for example, on the magnetic and transport properties. Several classes of compounds have become emblematic to the field of "orbital physics". Among the most well-studied and frequently exemplified are: $LaMnO_3$, a ($t_{2g}^3 e_g^1$) electron system and parent compound to $La_{1-x}Ca_xMnO_3$, exhibiting the CMR effect at particular doping level. The other pair is representative of triply degenerate ($t_{2g}^1 e_g^0$) systems, $LaTiO_3$ and $YTiO_3$. In contrast to $LaMnO_3$, subject to a large Jahn-Teller effect (see § 2.1.2 below), the $3d^1$ electron in these titanates reside in t_{2g} orbitals the lobes of which are directed away from the nearest-neighbour oxygen ligands (see Fig. 2.1). As a consequence the lattice coupling is much weaker, compared to systems with e_g orbital degeneracy, and the structure does not suffer significant Jahn-Teller distortions. Hence, titanates attract attention as model systems for various theoretical studies where "pure" orbital and spin-orbital models can be examined. The titanate compounds, $LaTiO_3$ and $YTiO_3$, are among the possible candidates in which quantum orbital fluctuations generate an "orbital-liquid state" [2.1][2.2][2.3][2.4].

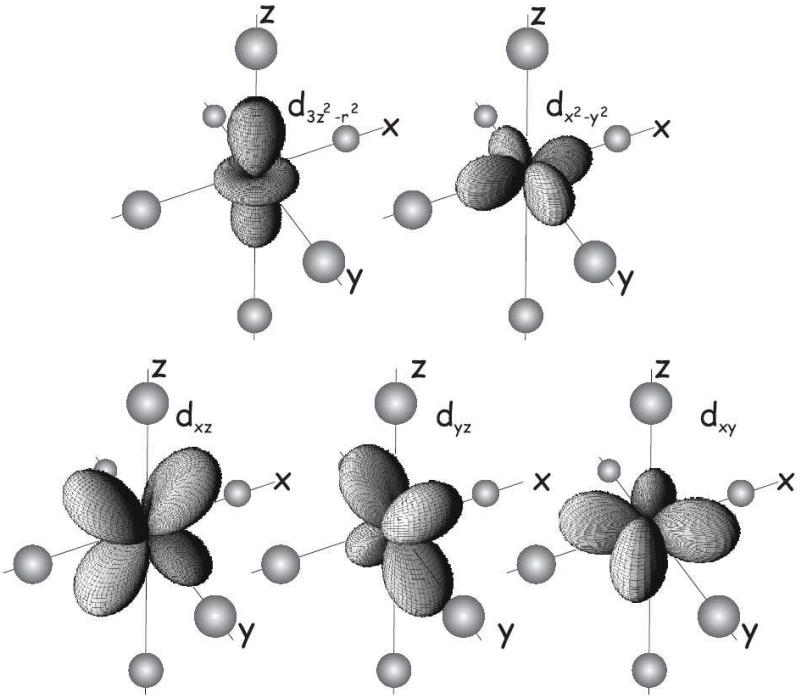

Figure 2.1 3*d*-orbitals and oxygen ligands (the small spheres), from [2.5].

In the following chapter we give an introduction to two important families of compounds: the manganites, exemplified by $LaMnO_3$, the mixed valence $La_{1-x}Ca_xMnO_3$ and $CaMnO_3$, and the titanates $LaTiO_3$ and $YTiO_3$, which both fall into the class of systems with orbital degeneracy. Central models and concepts, some of them valid in principle for all TMOs with perovskite structure, as well as experimental data from the literature are presented in order to outline the current understanding of the physics of these interesting compounds. The amount of scientific work devoted to these compounds is simply too numerous to be reviewed here, see for example [2.1][2.2][2.6].

2.1 Manganites

Perovskite manganites with general formula $Re_{1-x}A_xMnO_3$ (Re - trivalent rare earth and A - divalent alkali cations) (Fig. 2.1.1) have been in the focus of solid state research ever since the discovery of their intriguing properties by Jonker and Van Santen in the 50's [2.7]. Manganites attract attention not only because of their potential for technological applications, mainly due to the famous colossal magnetoresistance effect (see for example [2.8]), but also because these compounds reveal a remarkable wealth of ground states upon chemical doping and numerous important physical effects, including long range ordering phenomena in all possible channels - charge, spin, orbital and lattice.

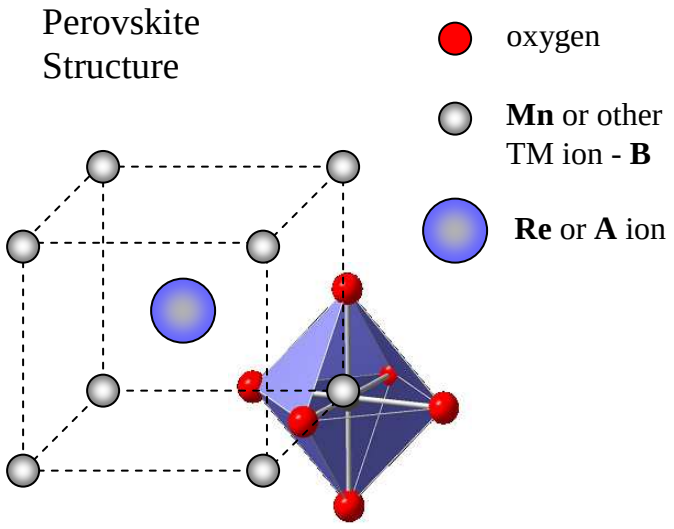

Figure 2.1.1 Ideal cubic perovskite crystal structure. The Mn ion (or other transition metal ion - B) is surrounded by six oxygen O ions forming a MnO_6 octahedron.

2.1.1 Crystal Structure

Transition metal oxides exist in a large variety of crystal structures. Most of them are derived from variations and distortions of the ideal perovskite structure, with general

formula ABO_3, where A is in general a rare earth or alkali, B is the transition metal ion and O is oxygen (Fig. 2.1.1). Ideally, the ionic radii r_A , r_B and r_O satisfy the condition:

$$r_A + r_O = \sqrt{2}(r_B + r_O)$$

In reality, the perovskite-based structures show lattice distortions as modifications from the perfect cubic structure. One possible origin of the lattice distortions is the deformation of the MnO_6 octahedra arising from the Jahn–Teller effect inherent for example, to the high-spin (S = 2) Mn^{3+} ion in $LaMnO_3$ (with doubly degenerate e_g orbitals) (see Fig. 2.1.2.1 in the next section). Another lattice deformation comes from the connecting pattern of the MnO_6 octahedra in the perovskite structure, forming a rhombohedral or orthorhombic structure, the so-called $GdFeO_3$-type lattice. In these perovskites, the MnO_6 octahedra show alternating buckling as shown in (Fig. 2.1.1.1).

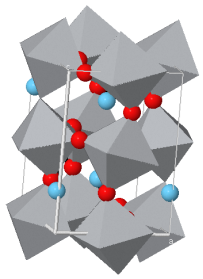

Figure 2.1.1.1 Perovskite crystal structure with $GdFeO_3$ - type lattice distortion, the so-called "buckling" of the MnO_6 octahedra.

Such a lattice distortion of the cubic perovskite structure is governed by the so-called tolerance factor *f*, defined as:

$$f = (r_B + r_O)/\sqrt{2}(r_A + r_O)$$

The tolerance factor *f* measures the lattice matching of the sequential AO and BO_2 planes. When *f* is close to 1, the cubic structure is realized. As r_A or equivalently *f* decreases, the lattice structure transforms to the rhombohedral ($0.96 < f < 1$), and then to the orthorhombic (the $GdFeO_3$ - type) structure for (f < 0.96), in which the B–O–B bond angle is bent and deviates from 180°. In general, the bond angle distortions decrease the electron bandwidth *W* (being proportional to the hopping *t*), since the effective *d*-electron transfer interaction between the neighboring B-sites is governed by the super-transfer process via O 2*p* states (see § 2.1.3). An important consequence for materials with antiferromagnetic spin ordering and $GdFeO_3$-type lattice distortion is that the Dzyaloshinsky–Moriya interaction causes a canting of the spins towards the *c*-axis and hence produces a weak ferromagnetic moment below the Neel temperature - T_N.

Some ionic radii for the respective elements in perovskite-like structures of manganites are listed in the table 2.1.1.1.

Ca^{2+}	Sr^{2+}	Ba^{2+}	Mn^{3+}	Mn^{4+}	O^{2-}			
1.34	1.44	1.61	0.645	0.53	1.40			
La^{3+}	Pr^{3+}	Nd^{3+}	Sm^{3+}	Eu^{3+}	Gd^{3+}	Tb^{3+}	Ho^{3+}	Y^{3+}
1.36	1.29	1.27	1.24	1.23	1.21	1.20	1.18	1.18

Table 2.1.1.1 Ionic radii (in Angstroms) of elements often incorporated in the perovskite structure of manganites [2.6].

Compounds with chemical formula of the type $A_{n+1}B_nO_{3n+1}$ possess two-dimensional layered structure known as the layered perovskite structure. For n = 1, this formula gives the so-called K_2NiF_4-structure, which is composed of layers of octahedra that are corner-sharing only in two dimensions, with larger ions of the metal-A, separating two successive octahedra layers (Fig. 2.1.1.2), [2.10][2.11].

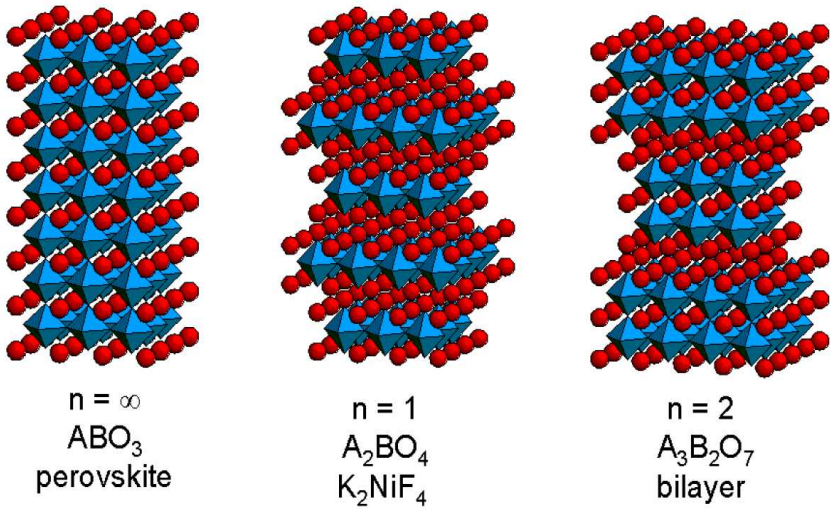

Figure 2.1.1.2 Variations on perovskites. Together with the layered modifications the perovskites form the so-called Ruddlesden-Popper phases, from [2.9].

2.1.2 Crystal Field Splitting and the Jahn-Teller Effect

The electrons in the *d*-shell of a transition metal ion have orbital angular momentum quantum number $l = 2$, and magnetic quantum number m_l, with $-2 \leq m_l \leq 2$. The resulting five quantum states of the *d*-electrons are degenerate, that is, they have the same energy when the ion is in a spherical potential. In a perfect octahedral coordination, the crystal field (often denoted $10Dq$) of the surrounding oxygen splits the $3d$-orbitals into a threefold degenerate t_{2g} (lower in energy), and a twofold degenerate e_g manifolds (Fig. 2.1.2.1). Further, there may be an additional splitting due to lattice distortions (Jahn-Teller effect), or other symmetry lowering of some kind. In e_g electron systems like the Mn^{3+} manganese compounds, the electronic configuration is $t_{2g}^3 e_g^1$ (high-spin state $S=2$, and $10Dq < J_H$ - Hunds coupling energy) hence the e_g electron occupies an orbital, the lobes of which are directed towards the nearest-neighbor oxygen ligands establishing a strong lattice coupling. The Jahn–Teller coupling lifts the degeneracy of the e_g orbital by causing a large deformation of the MnO_6 octahedra. The most frequently observed deformation of the cubic perovskite lattice is an elongation of the *z*-axis (apical) oxygen position coupled with the occupied $3dz^2–r^2$ orbital (shown on Fig. 2.1.2.1). Another possible deformation is an elongation of *x* and *y* axes (in-plane) oxygen positions coupled with the occupied $x^2–y^2$ orbital. When the e_g band filling is close to 1 (or otherwise to some commensurate value), the individual Jahn–Teller distortions are cooperatively induced leading to symmetry lowering of the lattice or even to a new superstructure. Thus, the peculiar orbital ordering in the manganites is always associated with the cooperative Jahn–Teller distortion.

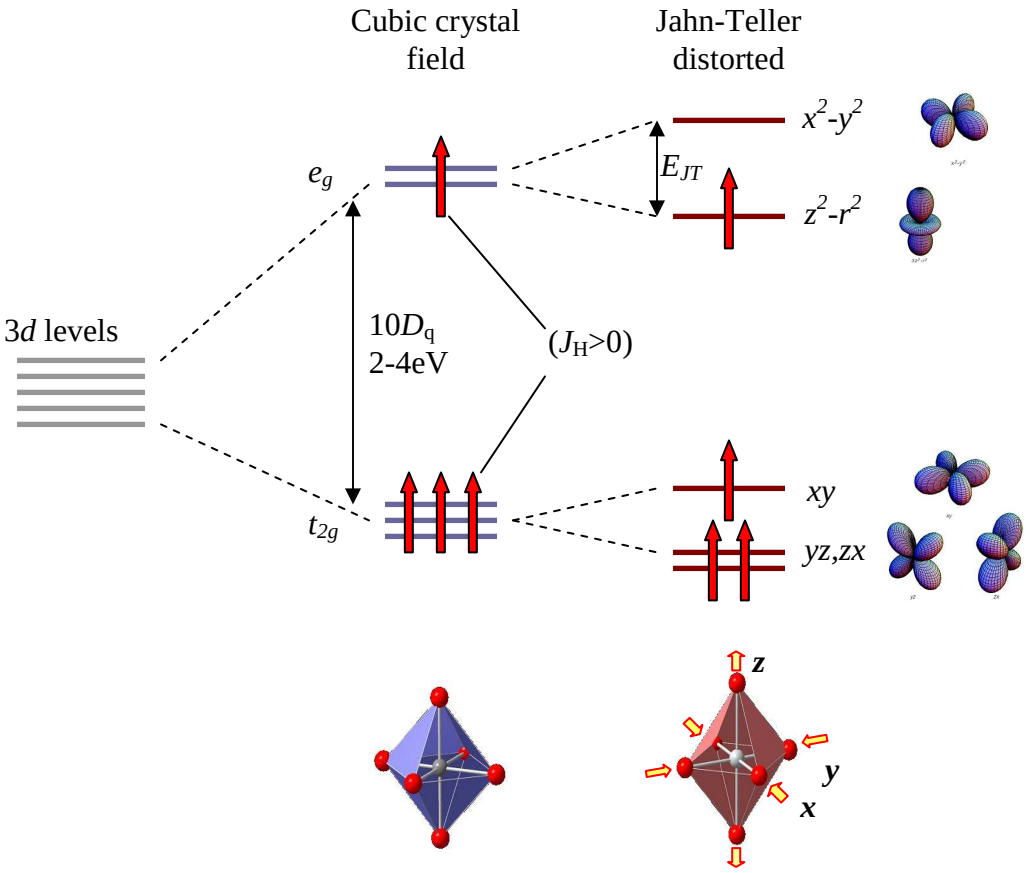

Figure 2.1.2.1 Crystal-field splitting (10*Dq*) of the five-fold degenerate atomic 3*d*-levels into lower t_{2g} (triply degenerate) and higher e_g (doubly degenerate) levels. The Jahn–Teller distortion of the MnO_6 octahedron further lifts the degeneracy. The system depicted here is in its high-spin state (S=2) because 10*D*q < J_H . This is the case in $LaMnO_3$.

Another effect of the crystal field is the quenching of the orbital moment. This is usually the case in 3*d*-transition metal oxides in which the crystal field is much stronger than the spin-orbit interaction. If strong, the hybridization of the *d*-orbitals of the transition metal ion with the oxygen *p*-orbitals may also contribute to the crystal field splitting (covalency contribution). It leads to splitting of *p*- and *d*-levels. The e_g orbitals have larger overlap compared to t_{2g} (Fig. 2.1), and hence stronger hybridization, forming σ- bonds.

2.1.3 Exchange Interactions

The Coulomb repulsion between the electrons is ultimately responsible for most of physics of transition metal oxides, including the long-range spin order. This situation manifests itself most clearly in the Mott-Hubbard insulating antiferromagnetic state. Amongst the first studied Mott insulators is CoO. This compound has an odd number of valence electrons per unit cell (Co: $3d^7 4s^2$ and O: $2s^2 2p^4$), for which the single electron band theory predicts metallic properties. Instead, its ground state is antiferromagnetic and insulating. In systems with interacting electrons the energy U of the on-site Coulomb interaction is the most important term in the Hamiltonian. If this energy is sufficiently high, that is, if the on-site Coulomb repulsion of the electrons is sufficiently strong, the hopping of electrons from site to site is suppressed and the material is insulating although the highest occupied bands are not completely full.

Superexchange

Despite the localization of the electrons in Mott insulators, the kinetic energy term that describes the band motion of the electrons is still present and plays a very important role, for example, in the antiparallel nearest-neighbor spin interactions that lead to the antiferromagnetic properties of the Mott state. The simplest model that can provide an understanding of their magnetic properties is the Hubbard model, introduced in 1963, as an approach to a theory of correlation effects in the *d*-bands of transition metals [2.12]. The model introduces a many-body Hamiltonian (the Hubbard Hamiltonian) for the description of *d*-electrons of a transition metal taking into account the two main opposing properties of these electrons: on one hand, the tendency for delocalization via electron hopping into itinerant states leading to metallic behavior, and on the other, their tendency to localize on particular sites due to the electron-electron interactions between them. The Hamiltonian reads:

$$H = -t \sum_{\langle ij \rangle \sigma} (c_{i\sigma}^{\dagger} c_{j\sigma} + h.c.) + U \sum_{i} n_{i\uparrow} n_{i\downarrow} \qquad (2.1.1)$$

where t is the hopping integral of electrons between nearest neighbor sites i and j; $c_{i\sigma}^{\dagger}c_{j\sigma}$ are the creation and annihilation operators, respectively, for an electron in the Wannier state $\phi(r-R_i)$ at lattice site i with spin σ, $n_{i\sigma}=c_{i\sigma}^{\dagger}c_{j\sigma}$ is the corresponding occupation number operator, and U is the energy of the on-site Coulomb interaction between the electrons sharing the same orbital. It is assumed that there is only one Wannier state for each site (single-orbital Hubbard model).

The zero-temperature behavior of the Hubbard model is governed by two parameters: the relative interaction strength U/t, and the electron density $n = N/L$, where N is the total number of electrons and L, the number of lattice sites (or unit cells, for non-Bravais lattices). Instead of U/t, the ratio U/W is often used as a measure of the strength of the electron-electron interactions in a material (W denote the bandwidth). For the single-orbital Hubbard model, the electron density takes values: $0 \leq n \leq 2$. For $n = 1$, one has the half filling case, where the number of electrons is equal to the number of sites. It is in this case, that above a particular critical value of U, the electrons are completely localized at the ion sites and the material is a Mott insulator. Away from half-filling ($n \neq 1$), the electrons always maintain a propagating motion, even for infinitely strong Hubbard interactions ($U \rightarrow \infty$).

For more quantitative estimate one can start from Mott insulating state and take t as a perturbation. The second order processes in t are shown on (Fig. 2.1.3.1), [2.13].

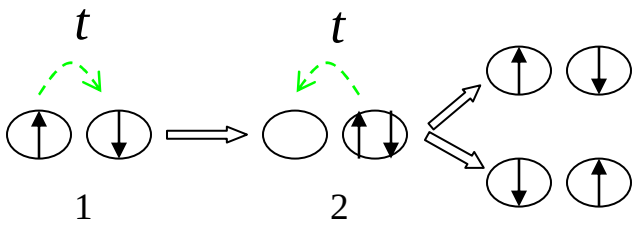

Figure 2.1.3.1 Superexchange interaction. 1-ground state, 2-intermediate state.

The intermediate state (2) has energy larger by U than the ground state (1). The intermediate state with parallel spins configuration is not allowed because of the Pauli exclusion principle. There are two possible final states depending on which electron goes to which ion. The energy due to this second order process corresponds to:

$$H' = -\sum_{\langle i,j \rangle} \sum_{\sigma,\sigma'} \frac{2t^2}{U} c^{\dagger}_{i\sigma'} c_{j\sigma'} c^{\dagger}_{j\sigma} c_{i\sigma} \tag{2.1.2}$$

Taking the sum over the spin and rewriting the electron operators in terms of spin operators, the expression (2.1.2) becomes:

$$H' = \sum_{\langle i,j \rangle} \frac{4t^2}{U} \left(S_i \cdot S_j - \frac{1}{4} n_i n_j \right) \tag{2.1.3}$$

In the half filling case, $n_i = n_j = 1$ (the Heisenberg model), the energy goes to zero for parallel spin configuration ($S_i \cdot S_j = 1/4$). This directly reflects the fact that electron cannot hop on a neighbouring site if both spins are parallel. Equation (2.1.3) is the antiferromagnetic interaction between the spins caused by the motion of the electrons (also called kinetic exchange interaction). As this interaction is mediated by the oxygen in the transition metal oxides, the exchange is called superexchange interaction and in many cases the 2*p* oxygen orbitals must be taken into account explicitly. The excitation energy of an electron from oxygen to the transition metal ion is called charge transfer energy Δ. Materials are classified as being charge-transfer ($\Delta < U$) or Mott-Hubbard ($U < \Delta$) insulators (Fig. 2.1.3.2).

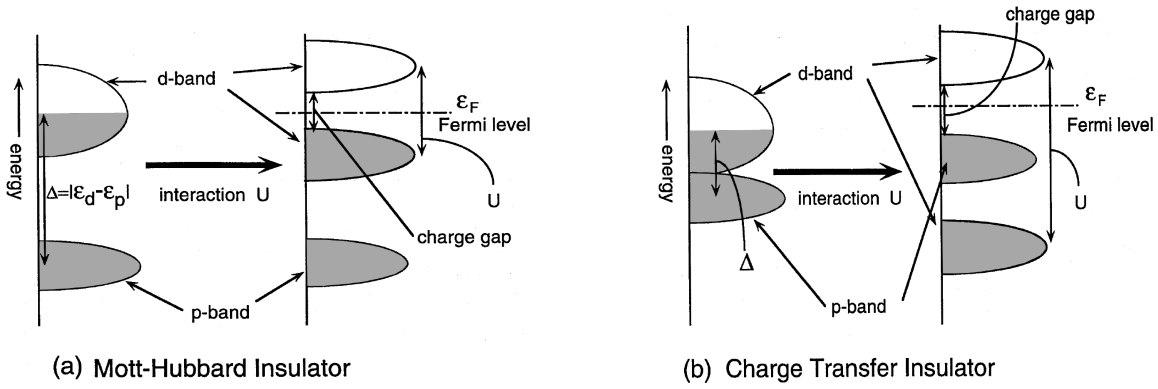

Figure 2.1.3.2 Energy diagrams of **a)** Mott-Hubbard insulator **b)** Charge transfer insulator, from [2.14].

Orbital Degeneracy

In the non-degenerate single-orbital Hubbard model the superexchange interaction of the *d*-electrons is always antiferromagnetic. However, in systems with orbital degrees of freedom, that is, with orbital degeneracy in the *d*-shell, the physics of transition metal oxides is much more complicated and can show a number of interesting phenomena. In such a system the sign of the superexchange interaction (ferro- or antiferromagnetic), as well as its strength, depend on the orbital occupation, which determines the degree of the overlap of the participating states.

Let us consider two systems, $CaMnO_3$ and $LaMnO_3$, in Mn^{4+} and Mn^{3+} valence state, respectively. As discussed above, the cubic crystal field splits the 3*d*-states into a triply degenerate t_{2g} and a doubly degenerate e_g states and the spins of the electrons align due to Hund's coupling (Fig. 2.1.3.3).

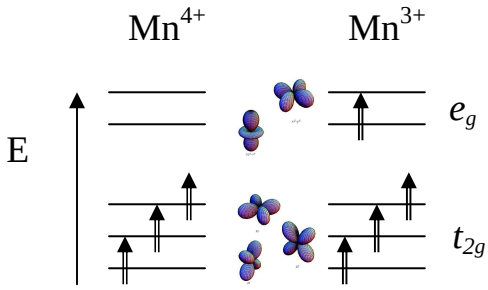

Figure 2.1.3.3 Electronic states in $CaMnO_3$ – a t_{2g} system (left) and $LaMnO_3$ -an e_g system (right).

Now, because the t_{2g} orbitals are orthogonal to the oxygen $2p_\sigma$ orbitals, the electrons exhibit a weak superexchange interaction with neighboring Mn ions via oxygen $2p_\pi$ orbitals. $CaMnO_3$ is an antiferromagnetic insulator with T_N=125K. The magnetism in this system can be described with the Hamiltonian:

$$H_{t_{2g}} = J_{t_{2g}} \sum_{\langle ij \rangle} S_i \cdot S_j \qquad (2.1.4)$$

with $J_{t_{2g}} \sim 1.5meV$ and $S = 3/2$, where the sum runs over the nearest neighbor sites. On the other hand, the e_g orbitals of the Mn^{3+} ion are differently oriented and have a large overlap with the oxygen $2p_\sigma$ orbitals resulting in a strong superexchange interaction. In this case the degeneracy of the e_g orbitals has a dramatic effect.

The Hamiltonian for the 3*d*-electrons in e_g orbitals is:

$$H_{e_g} = -\sum_{\langle ij \rangle}\sum_{\gamma\gamma'}\sum_{\sigma} t_{ij}^{\gamma\gamma'}\left(d_{i\gamma\sigma}^{\dagger} d_{j\gamma'\sigma} + h.c.\right) + U\sum_{i}\sum_{\gamma} n_{i\gamma\uparrow} n_{i\gamma\downarrow} + U'\sum_{i} n_{ia} n_{ib} + J_H \sum_{i}\sum_{\sigma\sigma'} d_{ia\sigma}^{\dagger} d_{ib\sigma'}^{\dagger} d_{ia\sigma'} d_{ib\sigma} \qquad (2.1.5)$$

where the orbitals are considered as mixtures of e_g orbitals of Mn^{3+} with the $2p_\sigma$ levels of the oxygen ions. $d_{i\gamma\sigma}^{\dagger}(d_{i\gamma\sigma})$ are the creation and annihilation operators for an electron with spin σ in orbital γ at site i. $t_{ij}^{\gamma\gamma'}$ is the hopping integral between γ at site i and γ' at site j. The Coulomb U and U' correspond to interactions within and between orbitals on a given site, and the Hund's coupling for the e_g orbitals is J_H. Realistic values are $U \sim 7eV$, $U' \sim 5eV$ and $J_H \sim 2eV$ with the relationship $U = U' + 2J_H$. *a* and *b* denote two different e_g orbitals, and $n_{i\gamma\uparrow} = d_{i\gamma\uparrow}^{\dagger} d_{i\gamma\uparrow}$, $n_{ia} = n_{ia\uparrow} + n_{ia\downarrow}$.

The superexchange is a second order process in the hopping integral and it depends on the nature of the respective orbitals. In this case, it is between the $3d_\gamma$ orbital of a Mn ion and a $2p_\sigma$ orbital of an O ion. The hopping integral $t_{ij}^{\gamma\gamma'}$, in *x*,*y* or *z* direction, can be estimated by integrating the angular part of the wavefunctions along the corresponding axis [2.13].

The results for $\gamma = d(3z^2 - r^2)$ and $\gamma' = d(x^2 - y^2)$ orbitals in *z* and *x* directions are summarized in figure 2.1.3.4. Along *z*, the only hopping allowed, $t_{ij}^{\gamma\gamma} = t_o$, is between $(3z^2 - r^2)$ orbitals the lobes of which are uniaxial with the $2p_\sigma$ orbital. In all other cases the hopping is hindered because of the $(x^2 - y^2)$ orbital: $t_{ij}^{\gamma'\gamma'} = t_{ij}^{\gamma\gamma'} = t_{ij}^{\gamma'\gamma} = 0$. Along *x*-axis (similar for *y*), there is a common component in the wavefunctions in all configurations hence the hopping integral assumes always a finite value: $t_{ij}^{\gamma\gamma} = -t_o/4$, $t_{ij}^{\gamma\gamma'} = t_{ij}^{\gamma'\gamma} = \pm\sqrt{3}t_o/4$ and $t_{ij}^{\gamma'\gamma'} = -3t_o/4$.

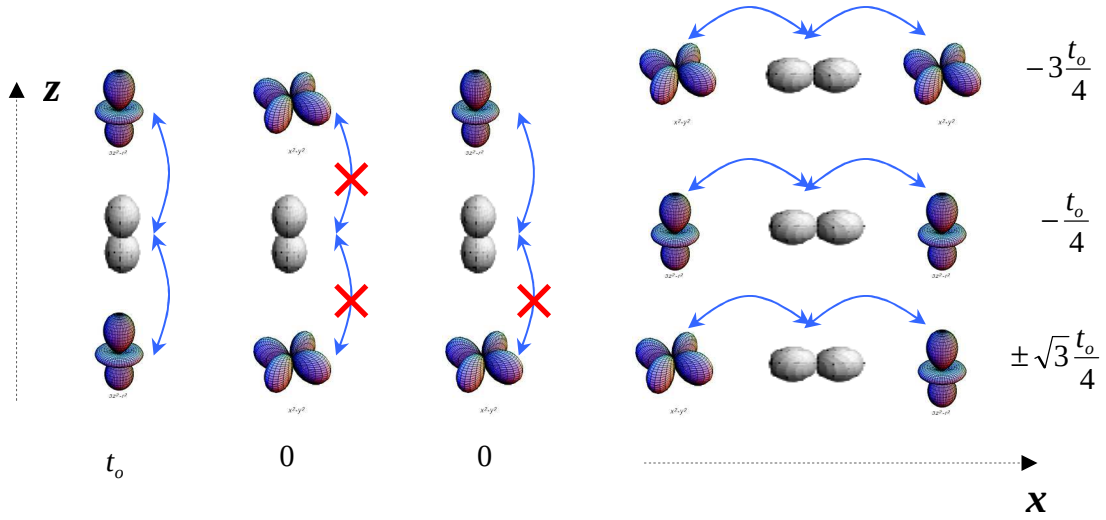

Figure 2.1.3.4 Hopping integral between e_g orbitals, $\gamma = d(3z^2 - r^2)$ and $\gamma' = d(x^2 - y^2)$, via O $2p_\sigma$ orbital in ***z*** direction (left) and ***x*** direction (right).

Now, depending on the orbitals involved in the superexchange interaction, several processes are possible. Some of them are represented on (Fig. 2.1.3.5). In process (a), the orbital degeneracy does not affect the interaction, so that the interaction is antiferromagnetic as in the non-degenerate Hubbard model (Fig. 2.1.3.1) and has the value $J = \xi 2t_o^2 / U$, where ξ is a constant reflecting the orbital's nature. In process (b), two degenerate orbitals are involved into the intermediate state with energy $U' + J_H$. However, this process is essentially the same as process (a) and results as well in an antiferromagnetic interaction with energy $J = \xi 2t_o^2 / (U + J_H)$. In contrast, process (c) is quite different. Since the Hund's coupling affects the intermediate state, a ferromagnetic interaction with energy $J = \xi 2t_o^2 / (U' - J_H)$ occurs. Among all processes, the process (c) is the most effective since the intermediate state is lowest in energy.

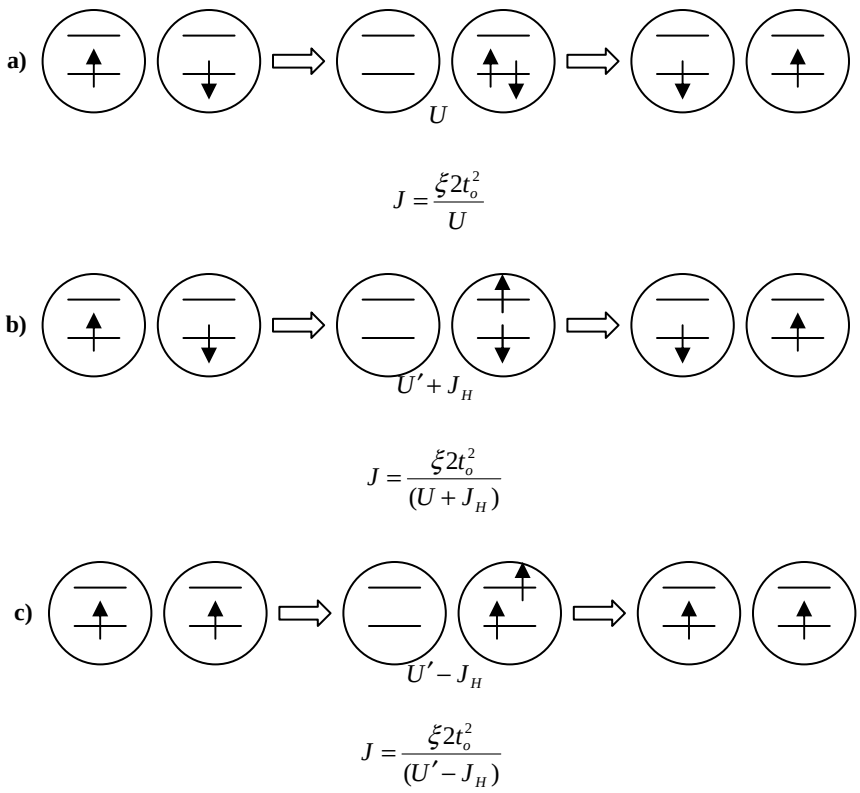

Figure 4.1.3.5 Superexchange processes between e_g orbitals. Spins are denoted by the arrows, from [2.13].

This means that when orbital degeneracy is present, the intra-atomic interactions of the electrons lead to intersite ferromagnetic exchange, instead of antiferromagnetic like in the single-electron Hubbard model. At the same time it becomes obvious that for the establishment of ferromagnetic exchange coupling it is necessary that the electrons at neighboring sites occupy different orbitals. This means that in general the ferromagnetism which results from the intra-atomic exchange interactions favors an antiferro-orbital pattern of orbital order. The sign of superexchange in transition metal systems depends however also on the angle of the chemical bond between the transition metal ions and the oxygen ions. The exact way the magnetic superexchange determines the orbital configuration and vice versa is summarized in the Goodenough-Kanamori-Anderson (GKA) rules [2.15], (see Fig. 2.1.3.6).

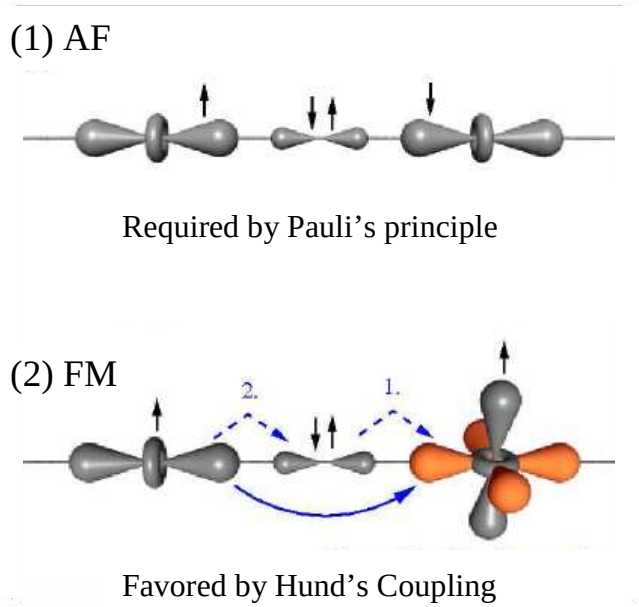

Figure 2.1.3.6 GKA rules. **(1) upper:** The so-called, 180°-exchange between half-filled orbitals. It is strong and favours AF spin order **(2) lower:** 90°-exchange between half-filled orbitals is FM and relatively weak. This figure also illustrates the exchange due to overlap between occupied and empty orbitals, which is again, FM and weak. Figures from [2.16].

The compound $LaMnO_3$, is very often used to represent the physics in e_g systems with orbital degeneracy. It shows alternating $d(3x^2-r^2)/\ d(3y^2-r^2)$ orbital ordering (OO) in the *xy* plane, the C-type, below T_{oo}=780K, accompanied by a Jahn–Teller type lattice distortion of the MnO_6 octahedra. The orbital order introduces an anisotropy in the electron transfer interaction, which in turn determines the type of superexchange interaction (ferro- or antiferro-), depending on the direction, hence the complex spin/orbit configuration. At T_N=140K, the spins in $LaMnO_3$ align ferromagnetically in the *xy* plane but since there is no ferromagnetic superexchange along the *z*-axis, the planes are antiferromagnetically coupled forming the A-type spin ordering (Fig. 2.1.3.7). A spectroscopic ellipsometry study of the spectrum weight redistribution supported by a parameter-free superexchange model calculations, unambiguously ascribed $LaMnO_3$ as a Mott insulator [2.17]. This compound attracted interest also as a system in which orbital waves (orbitons) were experimentally observed [2.18]. An interesting and open question in $LaMnO_3$, and in general to the manganites, is whether the orbitally ordered state is induced by electron-lattice or by electron-electron interactions. In the theoretical study of

Yin *et al*. [2.19], the authors estimated a value for electron-electron interaction strength of U_{eff}~1.7eV, and hence conclude that this is the interaction primarily responsible for the orbital ordering. For the electron-lattice interaction they find a much smaller value insufficient to stabilize an ordered state.

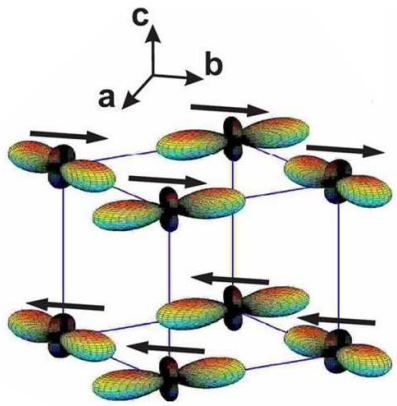

Figure 2.1.3.7 Spin and orbital ordering in $LaMnO_3$.

Double-Exchange Interaction

Many transition metal oxide compounds are in a mixed-valence state and exhibit metallic properties. Central phenomena in the study of magnetoresistive manganites is the paramagnetic insulating (PI) to ferromagnetic metallic (FM) transition along with its magnetic field induced counterpart, the colossal magnetoresistance (CMR) effect. The connection between the metallic state and the ferromagnetism in these compounds is crucial in understanding their properties. Shortly after the discovery of metallic ferromagnetic state in $La_{1-x}Ca_x(Mn^{+3}_{1-x}, Mn^{+4}_x)O_3$ by Jonker and van Santen [2.7], Zener [2.20][2.21], Anderson and Hasegawa [2.22], and de Gennes [2.23], theoretically examined the relation between metallicity and ferromagnetism. In $La_{1-x}Ca_x(Mn^{+3}_{1-x}, Mn^{+4}_x)O_3$, there are three 3*d* electrons in t_{2g} state of a Mn^{4+} ion, three 3*d* electrons in the same state and one in the e_g state for the Mn^{3+} ion (see Fig. 2.1.3.3). The spins of these electrons are aligned parallel to each other because of the Hund's coupling. Now, if Mn^{3+}/Mn^{4+} ions are neighbors, the e_g electron from Mn^{3+} can hop on an empty e_g state at the Mn^{4+} site, thus exchanging valence and a resonance process Mn^{3+}-Mn^{4+} ←→

Mn^{4+}-Mn^{3+} occurs. This is possible only if the spins on both sites are parallel. If they are antiparallel, the hopping is inhibited by the Hund's coupling (Fig. 2.1.3.8). This means that the ferromagnetism and the metallic state occur cooperatively. The mechanism was named "double-exchange" by Zener. The Hamiltonian describing this interaction is:

$$H = -\sum_{\langle ij \rangle}\sum_{\sigma} t_{ij}\left(c_{i\sigma}^{\dagger}c_{j\sigma} + h.c.\right) + U\sum_{i} n_{i\uparrow}n_{i\downarrow} - \frac{1}{2}J_H\sum_{i}\sum_{\sigma\sigma'} S_i \cdot c_{i\sigma}^{\dagger}\sigma_{\sigma\sigma'}c_{i\sigma'} + J\sum_{\langle ij \rangle} S_i \cdot S_j \quad (2.1.6)$$

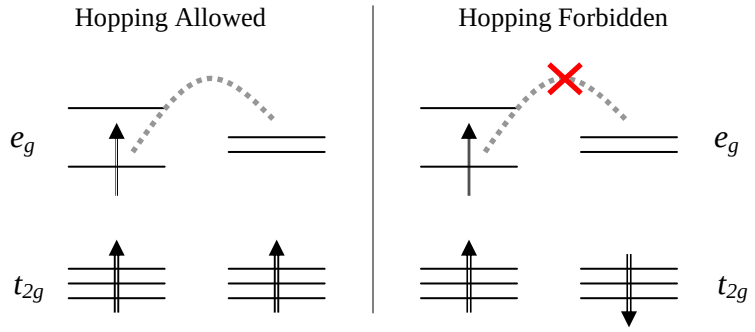

Figure 2.1.3.8 Schematic of the Double-Exchange (DE) mechanism.

In this (DE) Hamiltonian, the e_g degeneracy and the electron-lattice interactions are neglected. The spin, S=3/2, of the three electrons localized in the t_{2g} states is treated classically. $c_{i\sigma}^{\dagger}c_{i\sigma}$ denote the creation/annihilation operators of an e_g electron with spin σ at site i, $n_{i\sigma} = c_{i\sigma}^{\dagger}c_{i\sigma}$, S_i is the spin operator of the t_{2g} electrons and σ are the Pauli spin matrices. t_{ij} is the hopping integral of the e_g electron between sites, U is the Coulomb interaction between e_g electrons and J_H is the Hund's coupling between e_g and t_{2g} spins. The superexchange interaction between neighboring t_{2g} spins (J>0), is estimated to be J~20K from the Neel temperature $T_N = 6JS(S+1)/3k_B$ of $CaMnO_3$. For manganites, usual values are U~5-8eV and J_H~1-2eV. Therefore, the limit of large U and J_H is taken and the spin of the e_g electron is always parallel to the t_{2g} spin at each site [2.13].

In the treatment of (2.1.6), the electron operators are usually expressed in polar coordinates (θ_i, ϕ_i). Skipping the mathematical details, the Hamiltonian can be rewritten as:

$$H = -\sum_{\langle ij \rangle} t_{ij}^{eff} \left(c_i^{\dagger} c_j + h.c. \right) + J \sum_{\langle ij \rangle} S_i \cdot S_j \tag{2.1.7}$$

where $c_i^{\dagger} c_j$ represent a spinless fermion and the spin information is now included in (θ_i and ϕ_i) - the polar and azimuth angles of the spin on a site *i*. The hopping:

$$t_{ij}^{eff} = t\left[\cos\frac{\theta_i}{2}\cos\frac{\theta_j}{2} + e^{i(-\phi_i+\phi_j)} \sin\frac{\theta_i}{2}\sin\frac{\theta_j}{2} \right] \tag{2.1.8}$$

now contains a phase part which is related to a contribution to the Berry phase in the process of hopping, thus anomalous Hall effect could in principle be anticipated in the manganites.

Neglecting the phase factor t_{ij}^{eff} reduces to:

$$t_{ij}^{eff} = t\cos\frac{\theta_{ij}}{2} \tag{2.1.9}$$

where θ_{ij} is the angle between spins at sites *i* and *j* (Fig. 2.1.3.9).

Thus, in antiferromagnetic spin configuration $\theta_{ij} = \pi$, and $t_{ij}^{eff} = 0$. When spins are aligned ferromagnetically $\theta_{ij} = 0$, $t_{ij}^{eff} = t$ and the electrons can move freely, that is, the ferromagnetic metallic state is stabilized by maximizing the kinetic energy of the conduction electrons.

The electron hopping with matrix element t^{eff}, in a cubic lattice, will form a band:

$$E_k = -2t^{eff}\cos k \tag{2.1.10}$$

A small number of doped electrons would occupy states at the bottom of this band near $E_{\min} = -6t^{eff}$. Hence, whereas the initial state is antiferromagnetic and insulating, the doped system, electrons in $CaMnO_3$ or holes in $LaMnO_3$, will gain energy by increasing t^{eff}. Following the two-sublattice model by de Gennes [2.23], the total energy per site, as a function of θ, and for a small concentration of doped carriers (x<<1), is:

$$E(\theta) = JS^2\cos\theta - 6tx\cos\frac{\theta}{2} \tag{2.1.11}$$

The minimization $(\partial E(\theta)/\partial\theta = 0)$ of this energy gives for the angle:

$$\cos\frac{\theta}{2} = \frac{3}{2}\frac{t}{JS^2}x \tag{2.1.12}$$

i.e. with the doping (increase of x), the original antiferromagnetic structure becomes canted and there will be both - antiferromagnetic and ferromagnetic components in the magnetic order. With further increase of x, the canting angle θ will decrease and for some critical value:

$$x > x_c = \frac{2JS^2}{3t} \tag{2.1.13}$$

the magnetic order will become purely ferromagnetic [2.24].

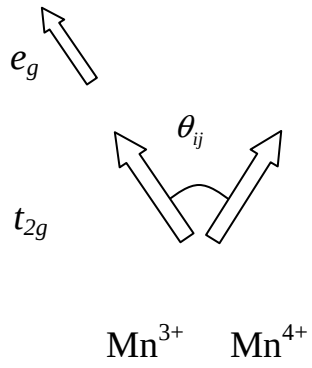

Figure 2.1.3.9 Sketch of a pair of spins at neighbouring sites with some canting angle, θ_{ij}.

2.1.4 Phase Diagram of $La_{1-x}Ca_xMnO_3$

The physics of manganites is, however, much more complex (Fig. 2.1.4.1). As pointed out by Millis *et al* [2.25], there are certainly other important factors than in the above simple DE scenario which are necessary to interpret important features observed experimentally. These are, for example, electron–lattice interaction (predominantly of the Jahn–Teller type), ferromagnetic/antiferromagnetic superexchange interaction between the local spins, intersite exchange interaction between the e_g orbitals (orbital ordering tendency), intra- and intersite Coulomb repulsion interactions among the e_g electrons. These interactions/instabilities occasionally compete with the ferromagnetic DE interaction producing complex electronic phases as well as gigantic responses of the system to external stimuli, such as the CMR effect.

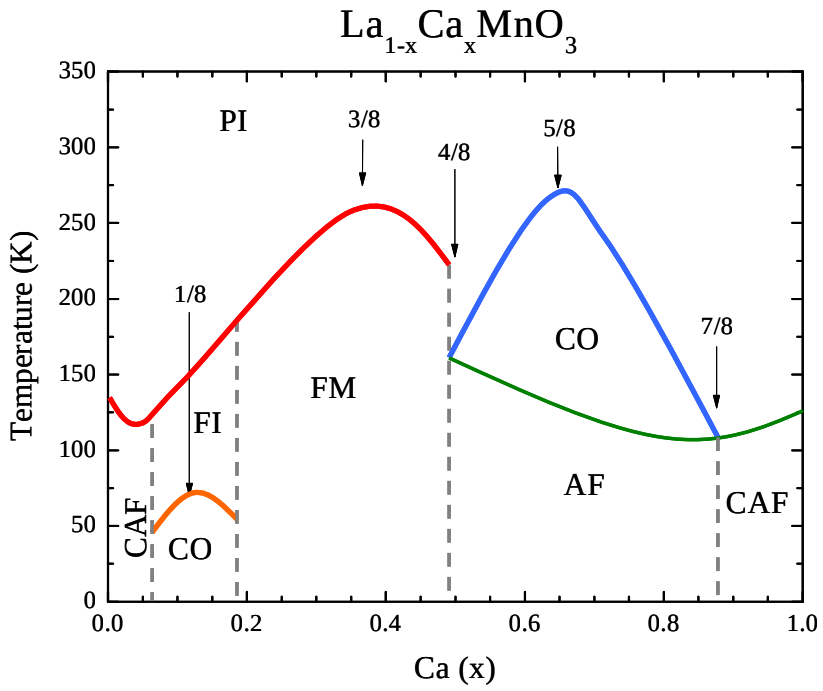

Figure 2.1.4.1 Phase diagram of the mixed-valence manganite system: $La_{1-x}Ca_xMnO_3$. PI – paramagnetic insulating state, FM- ferromagnetic metallic, FI – ferromagnetic insulating, AF – antiferromagnetic, CAF – canted antiferromagnetic, CO – charge/orbital ordered state [2.26].

In this section, the important points and features characterizing the different ground states in the phase diagram of mixed valence La_{1-x} Ca_x MnO_3 (Fig. 2.1.4.1) are briefly summarized.

$LaMnO_3$

As it was already discussed in the above, the compound is a Mott insulator due to strong electron-electron interaction between the Mn 3*d* electrons. The electronic configuration is $t_{2g}^3 e_g^1$ (high-spin state, S=2). The staggered orbital order accompanied by a strong Jahn-Teller distortion introduces an anisotropy in the sign and the magnitude of the exchange interaction, ferro ($J_{ab} > 0$) in-plane, and antiferro ($J_c < 0$) out-of-plane with $|J_{ab}|/|J_c| = 1.4$, and is responsible for the peculiar A-type spin configuration below T_N.

CAF state (low doping regime)

When small amounts of holes are introduced (doping with Ca), the canted antiferromagnetic state (CAF) occurs. The average ferromagnetic spin component increases along the *c*-axis. However, detailed neutron scattering experiment revealed that the magnetic state is inhomogeneous and consists of small (~16Å) anisotropic magnetic clusters. The doping dependence of the spin-wave spectra in the CAF region is a subject to various theoretical models but generally associated with an activation of a double-exchange mechanism on distances involving two or several lattice spacings [2.27].

The CAF/FI transition

It occurs at x=0.125 and the transition line corresponds precisely to the cancelling of the AF coupling along *c*-axis, J_c, with only one spin-wave branch as expected from one spin lattice in the ferromagnetic state. The resistivity retains an insulating behaviour, however, first signs of "metallicity" (quasi-metallic state) appear as decrease in resistivity below T_c. At lower temperature another transition occurs, characterized by an increase in resistivity, as well as structural and magnetic anomalies. This second transition cannot be explained by the DE interaction and indicates the appearance of different interactions. Based on the observation of a weak superlattice Bragg peak in $La_{1-x}Sr_xMnO_3$, this

transition has been associated with a charge ordering and the origin attributed to a new type of orbital or lattice polaron order [2.27].

FM state

When enough holes are created in the e_g states (Mn^{4+} species in the Mn^{3+} matrix), the metallic phase occurs. The spins polarize nearly perfectly to facilitate the hopping process, such that the system gains kinetic energy. In the FM state, there is no experimental evidence of charge or orbital ordering. The suggested orbital picture involves $3d_{z^2-r^2}$<->$3d_{x^2-y^2}$ orbital fluctuations [2.14]. When the temperature is raised to near or above the ferromagnetic transition temperature T_c, the configuration of the spins is dynamically disordered and accordingly, the effective hopping interaction is also subject to disorder and is reduced on average. This leads to enhancement of the resistivity near and above T_c. Therefore, a large magnetoresistance effect can be expected around T_c, since the local spins are relatively easily aligned by an external field and hence the randomness of the e_g hopping interaction is reduced (Fig. 2.1.4.2). This is the simple explanation of the magnetoresistance effect observed around T_c, in terms of the double-exchange (DE) model.

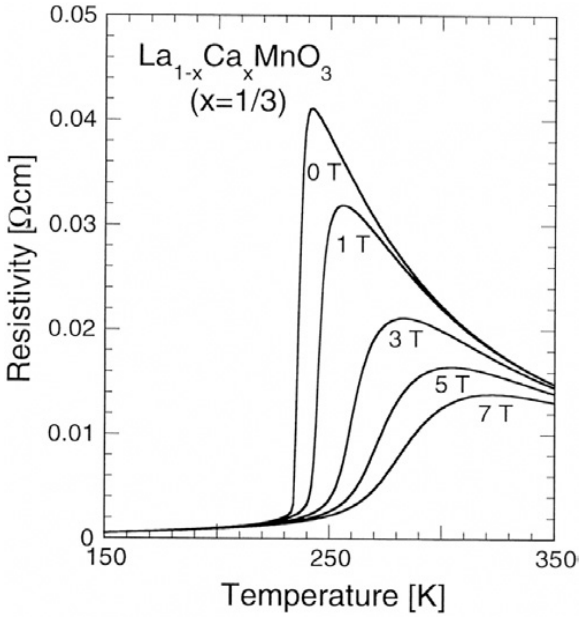

Figure 2.1.4.2 Temperature/magnetic field dependence of resistivity for La_{1-x} Ca_x MnO_3 at x=1/3 doping. The PI->FM transition occurs at T~250K. The strong suppression of the resistivity upon application of magnetic field is the CMR effect [2.10].

CO/AF domain

In the range $0.5 \le x \le 0.9$, the system is not very well studied except at a few particular doping points, x=1/2 and x=2/3, where two distinctive phases have been revealed. At half doping (x=1/2), the material undergoes at first a PI->FM transition at T_c~230K. Upon further cooling, it enters an antiferromagnetic (AF) insulating state, T_N~160K. This antiferromagnetic phase is characterized by a charge and spin ordering structure of type-CE, where real-space order of Mn^{3+}/Mn^{4+} takes place forming a superstructure (Fig. 2.1.4.3). A pattern of orbital order may exist independently from the charge order.

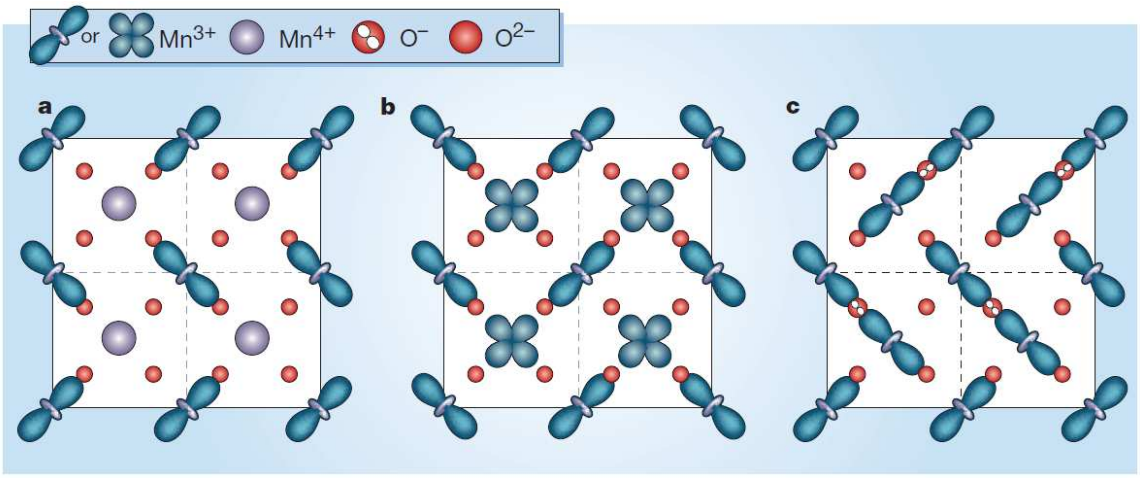

Figure 2.1.4.3 Different charge/orbital ordering patterns proposed for the x=1/2 doping state in $La_{1-x}Ca_xMnO_3$, from [2.28].

For x=2/3, below T_{co}~260K, the system transforms to a charge ordered orthorhombic phase with a tripled unit cell ($a_{co}=3a$, $b_{co}=b$, $c_{co}=c$). In addition, the system displays a noncollinear antiferromagnetic structure with tripled a–axis and doubled c-axis lattice parameters accompanied by a d_z^2 - orbital ordering and Jahn-Teller distorted $Mn^{3+}O_6$ octahedra in the ac-plane. This state was associated with the formation of a stripe-like structure of the Mn ions in [2.29], and Wigner-crystal like arrangement in [2.30]. Using elastic neutron diffraction and magnetization experiments, Pissas and Kallias [2.31], have proposed a detailed phase diagram for $La_{1-x}Ca_xMnO_3$ in the doping range $0.5 \le x \le 0.9$. They identify four distinctive stable phases at (x=1/2,2/3,4/5,1), denoted by the solid lines in figure 2.1.4.4, and a meta-stable one (x=3/4), denoted by a dashed line.

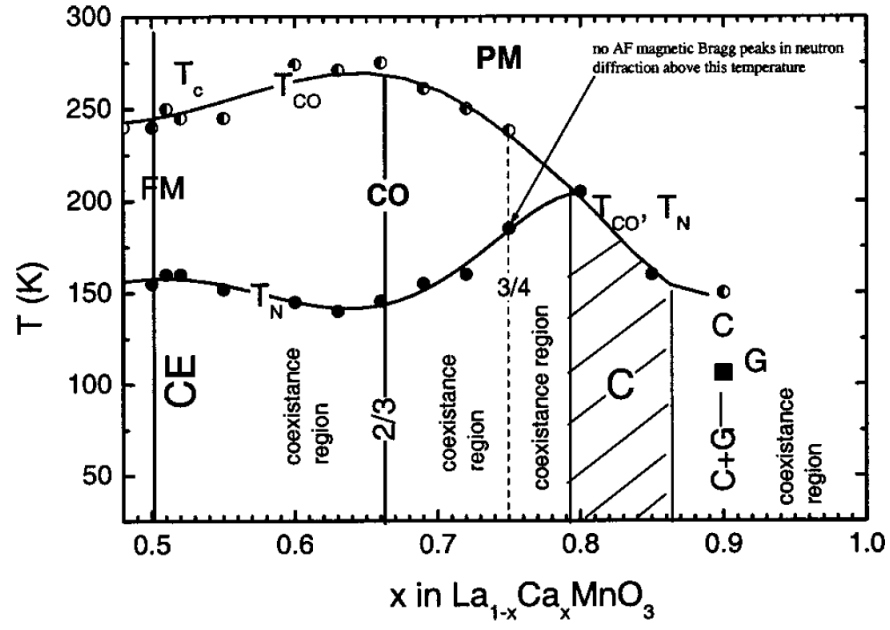

Figure 2.1.4.4 Phase diagram of La_{1-x} Ca_x MnO_3 compound in the high Ca-doping range x=0.5-0.9, according to [2.31].

CAF and $CaMnO_3$

Finally, the doping range, x>0.85-1, is characterized by the coexistence of C- and G-type magnetic structures. The latter is adopted by $CaMnO_3$. In this compound, Mn is in the 4+ valence state with electronic configuration $t_{2g}^3 e_g^0$ and therefore possesses no orbital degree of freedom, hence the isotropic G-type magnetic lattice. The three 3*d* electrons are localized in the t_{2g} orbitals in the high-spin state S=3/2. Compared to $LaMnO_3$, the research work on $CaMnO_3$ is much less abundant. A more detailed discussion of the properties of this compound is given in the next Chapter 5, in connection to the spectroscopic study of the superlattice system $CaMnO_3$ / $CaRuO_3$.

For completeness, a generic phase diagram - bandwidth W versus hole concentration x, for several rare-earth ions in $Re_{1-x}A_xMnO_3$, with different ionic radii, is given in figure 2.1.4.5.

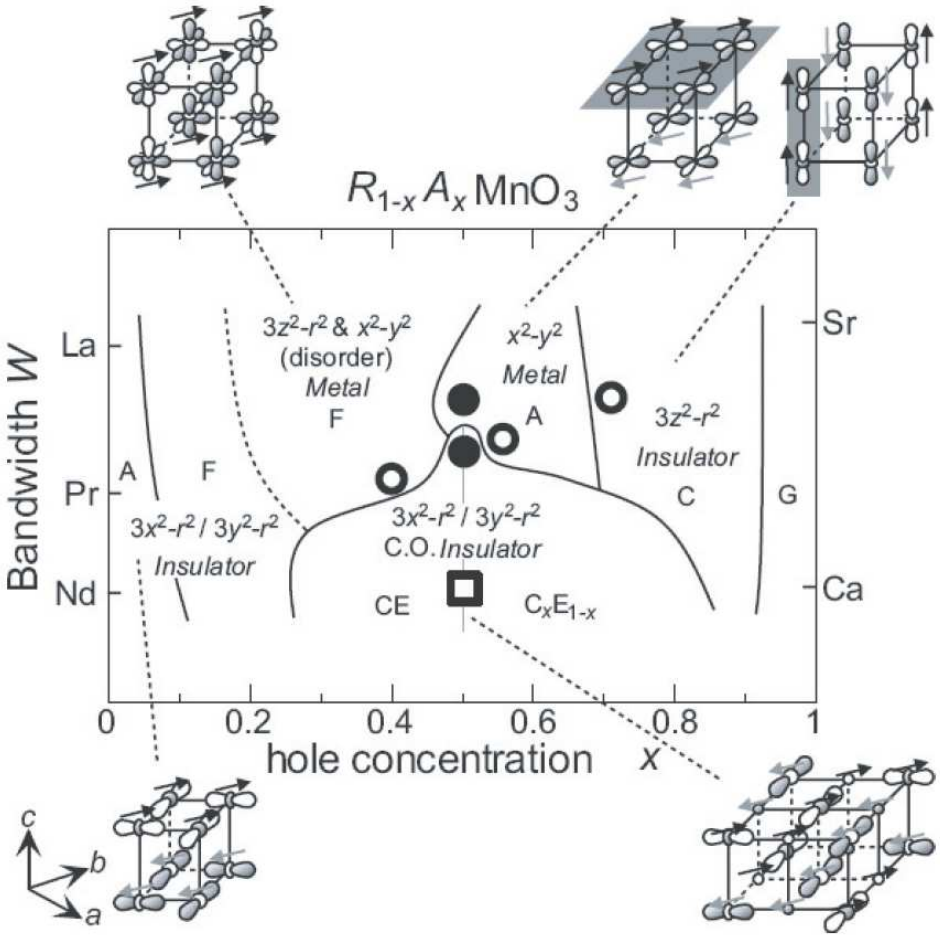

Figure 2.1.4.5 Phase diagram (bandwidth *W* versus hole concentration *x*) for the ground state of $Re_{1-x}A_xMnO_3$ [2.10].

The research on the manganites continues to be a subject of a large amount of experimental and theoretical work. Even though great progress has been made in the recent years [2.6][2.32], much remains unclear and requires development of additional models even for the well-studied parts of the phase diagram. Some of the notorious ideas include electron-phonon coupling [2.33], phase separation and its importance to the CMR effect [2.34][2.35], magnetic polarons [2.36], orbital polarons [2.37], structural correlations on nanoscopic and mesoscopic scales [2.38], and so on.

2.2 Titanates

The physical properties of compounds with t_{2g} orbital degeneracy can be very different and in some sense more interesting, when compared to those with e_g orbital degeneracy. The lobes of t_{2g} orbitals point away from the nearest oxygen 2*p* orbitals and the crystal structure is less prone to distortions. Indeed, titanates ($RTiO_3$, R = rare earth), in electronic configuration $t_{2g}^1 e_g^0$, do not undergo significant Jahn-Teller distortions, despite their degeneracy, but experience only rotations of the TiO_6 octahedra, the $GdFeO_3$ - type distortion. This type of distortion can be controlled by the variation of the ionic size of the R-cation upon chemical substitution. Hence, the titanate compounds retain a structure relatively close to ideally cubic in which the large threefold degeneracy may be preserved and enhance quantum mechanical orbital effects such as orbital fluctuations [2.3]. Therefore, titanates, so as the vanadates (t_{2g}^2 systems), attract attention as model systems to various degenerate orbital theories in a cubic symmetry in which the direct link between orbitals and magnetism can be studied [2.4][2.13].

The crystal structure of $RTiO_3$ is a distorted perovskite with orthorhombic cell of P_{bnm} space group. The structural, magnetic and orbital properties, have been systematically studied by changing the ionic radius r_R of the R-ion in the sequence La-Y. The smaller is the radius r_R, the larger is the rotation of the TiO_6 octahedron. This distortion bends the Ti-O-Ti bond. In $LaTiO_3$ the value is: 157^o and in $YTiO_3$: 140^o (in the *ab* plane) and 144^o (along c-axis). The large bond angle implies a small overlap of the transition metal 3*d*, and the oxygen 2*p* wavefunctions, which leads to small electron transfer between nearest neighbor Ti sites. In this way, the ratio of the bandwidth *W* to the Coulomb interaction *U* can be controlled. With this control, these Mott insulators exhibit a peculiar antiferromagnetic (AFM) to ferromagnetic (FM) phase transition reflecting the rich orbital physics in the titanates. Nearly the same phase change is found in the solid solution $La_{1-x}Y_xTiO_3$ (Fig. 2.2.1) [2.39].

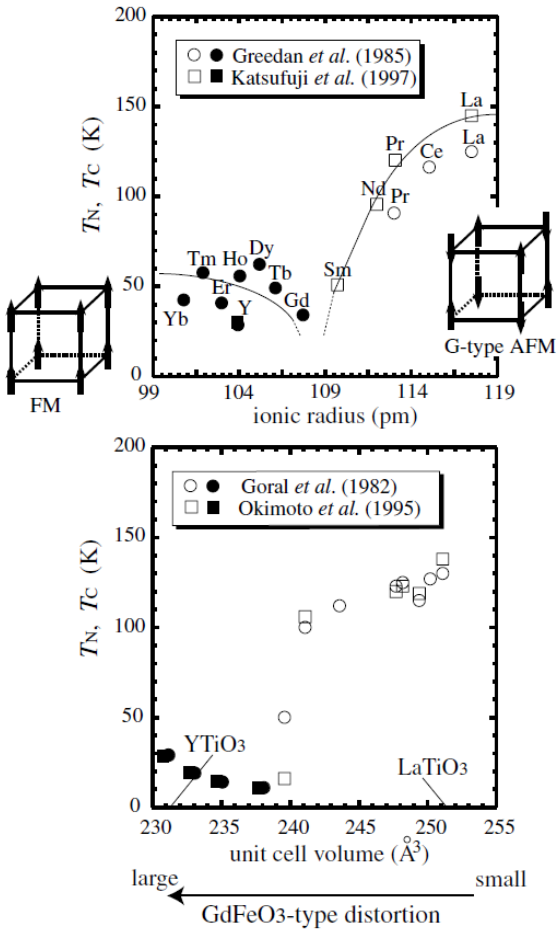

Figure 2.2.1 Magnetic phase diagrams of $RTiO_3$ (upper) and $La_{1-x}Y_xTiO_3$ (lower figure) as a function of the ionic radius of the R-ion and the unit cell volume, respectively. The open symbols denote T_N and the closed, T_c. From [2.39].

The end members, $YTiO_3$ and $LaTiO_3$, are both Mott-Hubbard insulators with optical gaps of (~1eV) and (~0.2eV), respectively [2.40][2.41]. The spins in $YTiO_3$ order ferromagnetically at T_c=30K and the saturated FM moment is about 80% of what is expected from the spin-only value of S=1/2. With increasing r_R, T_c monotonically decreases and the system eventually exhibits G-type antiferromagnetic order with T_N=145K, in $LaTiO_3$.

One of the first studies that stimulated the strong experimental and theoretical interest in the research of titanates was an inelastic neutron scattering on $LaTiO_3$, by Keimer *et al.* [2.3]. As the magnetic moment observed in the nearly cubic $LaTiO_3$ is greatly reduced, $\mu \sim 0.45\mu_B$, one would expect a picture of an unquenched orbital angular

momentum opposite to the spin due to the spin-orbit interaction. Surprisingly, the spin wave spectra (Fig. 2.2.2) revealed nearly no anisotropy in the exchange interaction, which is inconsistent with the existence of an appreciable unquenched orbital moment. X-ray scattering experiments also failed to detect any orbital ordering in the $LaTiO_3$ compound.

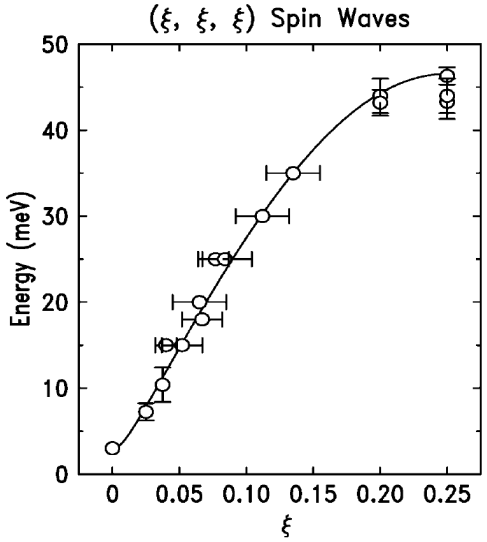

Figure 2.2.2 Spin-wave dispersion in (1,1,1) direction in the reciprocal space for $LaTiO_3$. The line is an isotropic spin-1/2 Heisenberg model fit to the experimental data. (J=15.5meV and a fairly small spin gap of Δ~0.3meV).

The results were interpreted as unusual many-body state with AFM long-range order but strong orbital fluctuations (Fig. 2.2.3), - an obvious departure from the Goodenough-Kanamori rules that would imply a static orbital pattern.

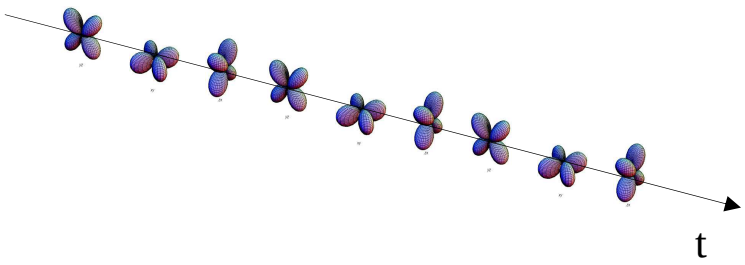

Figure 2.2.3 A sketch of orbital fluctuating state. The electron reside some time ***t*** on each of the triply degenerate t_{2g} orbital states.

The idea was further developed theoretically and led to the concept of "orbital liquid state" as a coherent, orbitally disordered ground state that explained the experimental findings [2.4]. Several Raman scattering experiments with visible and synchrotron soft x-ray photons (Resonant Inelastic X-ray Scattering) have also identified high energy spectral features, in both $LaTiO_3$ and $YTiO_3$, that could be ascribed as to orbital excitations (orbitons) [2.42][2.43]. These are part of the issues that have recently stimulated many experiments and competitive theoretical model calculations [2.44] in the perovskite titanates with orbital degeneracy and in particular, for $LaTiO_3$ and $YTiO_3$. The physical properties of $YTiO_3$ will be discussed in more details in Chapter 6, where a spectroscopic study on this compound will be presented.

Finally, it is important to point the difference between the t_{2g} and e_g systems in the hopping integral. As already discussed, the electron hopping between the nearest neighbor transition metal ions in the perovskite structure occurs through the oxygen 2*p* orbitals. In a perfect crystal lattice, the $3d_{xy}$ orbital couples with $2p_x$ ($2p_y$) along the *x*(*y*) direction and decouples with $2p_z$. For example, for a bond along the *x* -direction, an electron hops between the d_{xz} orbitals and the d_{xy} orbitals, which are called "active", but not between the d_{yz} "inactive orbitals" (Fig. 2.2.4). Explicitly, the transfer integral between sites i orbital γ and j with γ' is given by:

$$t_{ij}^{\gamma\gamma'} = t\delta_{\gamma\gamma'}(\delta_{\gamma a l} + \delta_{\gamma b l}) \qquad (2.2.1)$$

where l denotes the direction of the bond connecting i and j. a_l, b_l and c_l correspond to the two active and the single inactive orbitals for the respective direction $l = x, y, z$. The hopping integral t is a second order process involving the hopping between t_{2g} and $O2p$ orbitals, i.e. to a "π" bond, denoted by $t_{pd\pi}$ which is about two times smaller than for the "σ" bond $t_{pd\sigma}$. In principle, there is a finite hopping integral $t_{dd\delta}$ between the nearest neighbor inactive orbitals through direct overlap with the t_{2g} orbitals, which is usually neglected due to its small magnitude compared to t.

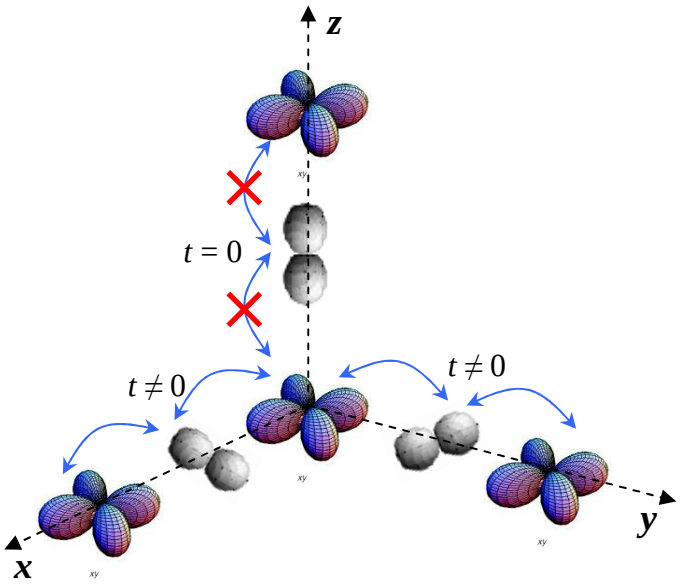

Figure 2.2.4 Hopping between t_{2g} orbitals in different directions. "active orbitals" along *x* and *y*, and "inactive orbitals" along *z*.

A rigorous treatment with generalized Hubbard Hamiltonian and comprehensive discussion of systems with t_{2g} degeneracy can be found in [2.13].

2.3 TMO Interfaces and Superlattices: Recent Advances and Spectroscopic Methods

The concept of a superlattice structure comprised of at least two different materials (Fig. 2.3.1) is not a new one. It dates back to the 70's, a time when the semiconductor materials were experiencing a great boost [2.45]. The development of semiconductor superlattices, and in general, low-dimensional structures like the quantum wells, wires and dots, in which purely quantum mechanical effects dominate, led to many important discoveries with a great impact in electronics and optoelectronics technology. Discoveries such as the Integer (IQHE), and the Fractional Quantum-Hall Effect (FQHE), even addressed questions to the very nature of the electrons as particles obeying fermion statistics when confined in reduced dimensions and subjected to large magnetic fields [2.46][2.47]. The possibility that the collective excitations in matter in two dimensions (2D) can satisfy an arbitrary statistics between fermionic and bosonic, including them, is a subject of intense research nowadays [2.48][2.49].

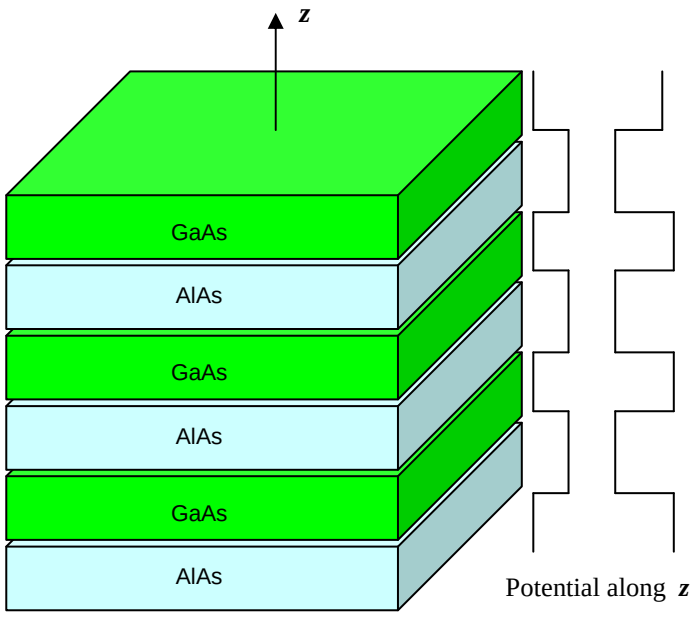

Figure 2.3.1 A superlattice structure made of two alternating semiconductor materials, GaAs and AlAs.

The above is just one of many examples for intriguing phenomena emerging in low-dimensional structures even though, in this case, from conventional semiconductors - a class of materials with properties based predominantly on the charge degree of freedom. In contrast to that, the layered modifications of the perovskite transition metal oxides (TMO) naturally form 2D structures with large unit cells (see Fig. 1.1.3). Their structural complexity and specific electronic properties, carrying full set degrees of freedom, make them unique and showing an exceptional variety of unconventional ground states. The refinement of the thin film deposition technologies on the other hand, opens up great chances for the engineering of artificial complex unit cells and thereby "constructing" physical properties using TMO materials. Therefore, identifying mechanisms that modify the electronic properties or eventually lead to new physical effects, when materials are brought in contact, is of major importance to the development of the field.
In order to outline the current progress in the physics of TMO superlattices we first give a review of few selected systems along with a basic introduction to resonant soft x-ray spectroscopy techniques with synchrotron radiation, as being powerful, element-specific structural (electronic/orbital and magnetic) probe. Some examples for elastic neutron scattering and optical spectroscopy applied to multilayer structures are also included.

2.3.1 X-ray Spectroscopy with Synchrotron Radiation

The intrinsic characteristics of synchrotron radiation: high brilliance, broad-range energy tunability, high degree of polarization, small angular divergence and coherence, made possible the development of x-ray techniques such as x-ray absorption spectroscopy (XAS), x-ray magnetic circular dichroism (XMCD), x-ray resonant elastic scattering (XRS), and recently, resonant inelastic x-ray scattering (RIXS). This arsenal of x-ray spectroscopy techniques is currently experiencing a serious boost due to their great potential in solid state physics, and in particular, applied to TMO and their superlattices. With the footnote that a comprehensive description is out of the scope of this thesis, here we only give a basic introduction of the techniques necessary for the discussion of some of the results in the following chapters.

First of all, the energy range that is particularly suitable for investigation of transition-metal oxides and rare-earth materials, their superlattices, or other long period electronic superstructures (charge, magnetic and orbital order), matches the soft x-ray wavelengths, i.e. the range of 200-2000 eV. Resonant excitations taking place in this region are for instance: the oxygen 1*s* -> 2*p* (K-edge), the 3*d* transition metals 2*p* -> 3*d* ($L_{2,3}$ edge) and the rare-earth 3*d* -> 4*f* ($M_{4,5}$ edge) transition. The 4*d* transition metals have their 2*p* -> 4*d* edge at higher energies 2000-3500 eV [2.50]. Because every element has its characteristic core-level binding energies, all x-ray core level spectroscopies are element specific. These transitions are also dipole allowed, very effective, and therefore do have high enough intensities to make the spectra sensitive to the charge, spin and orbital state of the ions. The resonant excitations are also extremely useful for "resonant enhancement" on performing angular scans in diffraction experiments.

X-ray absorption is a core-level excitation through a transition from a core state to an unoccupied state by absorbing photons (Fig. 2.3.1.1).

The probability for electronic transition that eventually gives the absorption cross section is given by the Fermi golden rule:

$$\sigma_{abs} \sim \left|\left\langle f\left|\hat{P}\right|i\right\rangle\right|^2 \delta\left(E_f - E_i - \hbar\omega\right) \qquad (2.3.1)$$

where $\hat{P}$, is the dipole operator that couples the initial $|i\rangle$ and final $|f\rangle$ states.

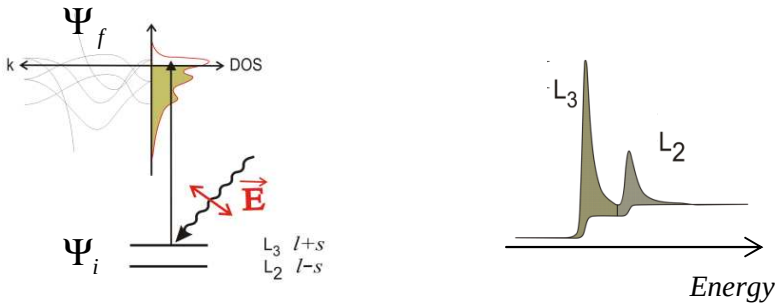

Figure 2.3.1.1 left: Excitation from core state to an unoccupied state **right:** Typical absorption spectra. The L-edge is split to L_3 and L_2 due to strong spin-orbit coupling in the *p*-shell, from [2.51].

The final state, as shown in figure 2.3.1.1, consists of core-hole and an additional valence electron. This core-hole created by the incident photon will strongly interact with the

valence electrons through the Coulomb interaction. Therefore, the process cannot be described in a simple one-electron picture. In the case of transition metal oxides, which are narrow band systems, the x-ray absorption is of strongly excitonic character since these strong Coulomb interactions are larger than the one electron bandwidth of the valence electrons. In case of 2*p* -> 3*d* excitation process, symmetry considerations for the initial and the final states (the matrix element in equation 2.3.1) yield the following dipole selection rules for excitations to be allowed:

$$\begin{aligned} \Delta l &= \pm 1 \\ \Delta j &= 0, \pm 1 \\ \Delta m_l &= 0, \pm 1 \\ \Delta m_s &= 0 \\ \Delta L &= 0, \pm 1 \\ \Delta S &= 0 \\ \Delta J &= 0, \pm 1 \end{aligned}$$

were small characters denote one-electron quantum numbers and capitals, the corresponding atomic quantum numbers. Cluster and full multiplet calculations are required for accurate calculation of absorption spectra [2.52].

XAS is indispensible probe in determination of valence state (Fig. 2.3.1.2), as well as for the symmetry of the orbital state. The latter is done by polarization dependence study - x-ray linear dichroism (XLD) (Fig. 2.3.1.3). In x-ray linear dichroism study, linearly polarized light, parallel and perpendicular to the plane of incidence (commonly denoted by π and σ) is used to examine the orbital symmetry of the unoccupied state. The XLD spectrum is the difference in the absorption spectra for the two polarizations.

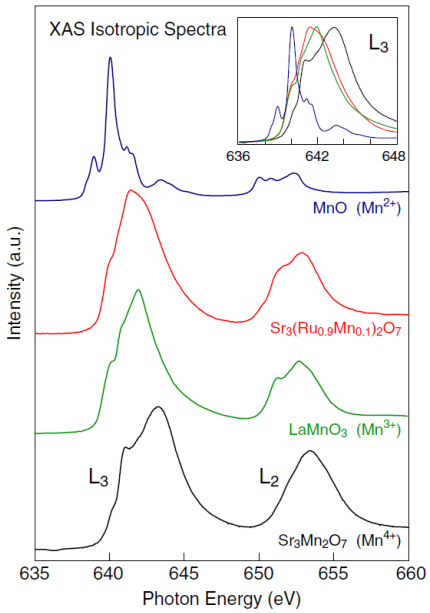

Figure 2.3.1.2 Change of valence state can be inferred by controlling the XAS spectra. The curves represent Mn $L_{2,3}$ edge in various Mn valence states [2.53].

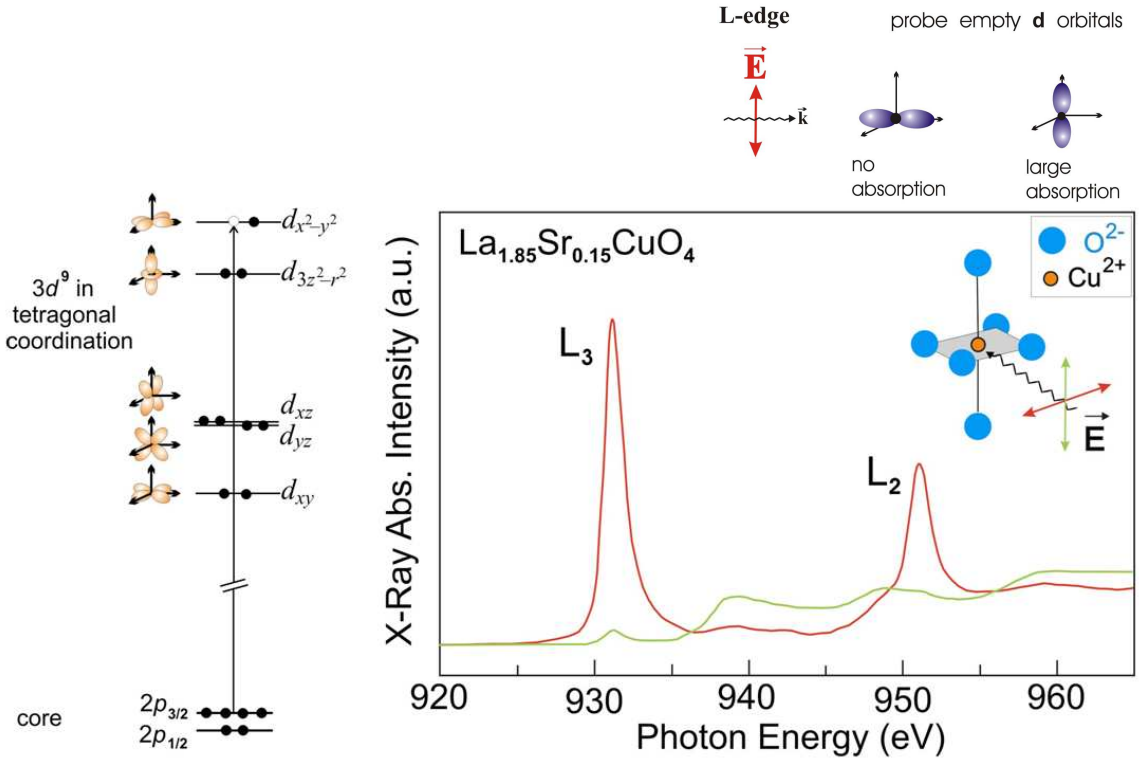

Figure 2.3.1.3 X-ray linear dichroism (XLD) spectrum. The example is $La_{1-x}Sr_xCuO_4$ with partially occupied $d3x^2$-y^2 orbital giving a large absorption when the polarization is chosen such that the electric vector is in the *xy* plane [2.54].

The x-ray magnetic circular dichroism (XMCD) on the other hand, allows a direct and independent deduction of the spin and orbital magnetic moments, m_{spin} and m_{orb}, again, in an element specific way by utilizing the absorption of circularly polarized x-rays (Fig. 2.3.1.4) [2.55]. In contrast to the XLD spectra, here circularly polarized light, left and right, is used to trigger the core-valence (2*p*->3*d*) excitation of the atom. The interaction of the spin or angular momentum of electrons with the angular momentum of circularly polarized photons is what makes the method possible. If there is a nonzero spin (imbalance in the spin up and spin down moments) and/or orbital moment in the valence band, the absorption of right circularly polarized light is different from that of left circularly polarized at the resonance absorption edges.

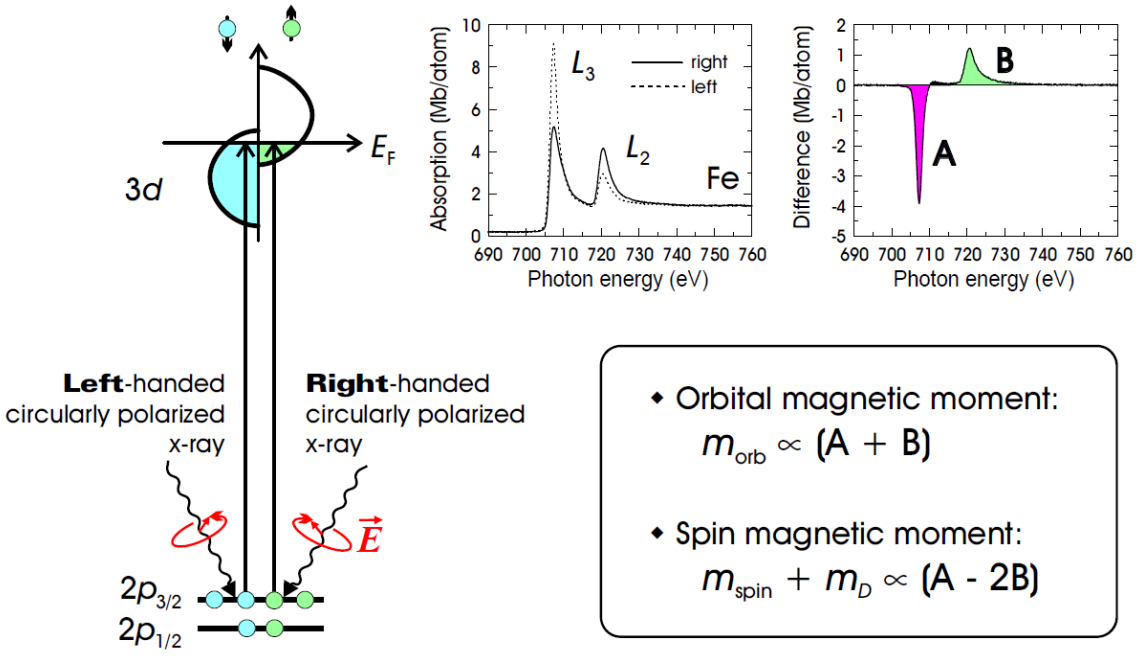

Figure 2.3.1.4 Principle of XMCD technique. From [2.55].

The integrated areas of the difference in the two absorption spectra, A and B on figure 2.3.1.4, are then directly related to the spin and orbital magnetic moments.

XAS spectra detection, as in all other x-ray spectroscopy techniques discussed here, is most commonly done in two regimes - fluorescence yield (FY) and total electron yield

(TEY). In the FY mode, (Fig. 2.3.1.5), one detects the electromagnetic radiation resulting from the radiative decay of the electrons from the occupied density of states (DOS) to refill the core hole created by the X-ray absorption process [2.5]. The number of photons is proportional to the number of core holes created by the absorption process. It is also important to note that this detection method is quite bulk sensitive, since at these low photon energies there are almost no photon scattering processes. The probing depth in FY mode is ~2000 Å. The drawback of this technique is that the mean free path of the fluorescent photons can be comparable to that of the incoming photons, hence self-absorption effects can take place, with the result that the fluorescent yield will no longer be proportional to the absorption coefficient.

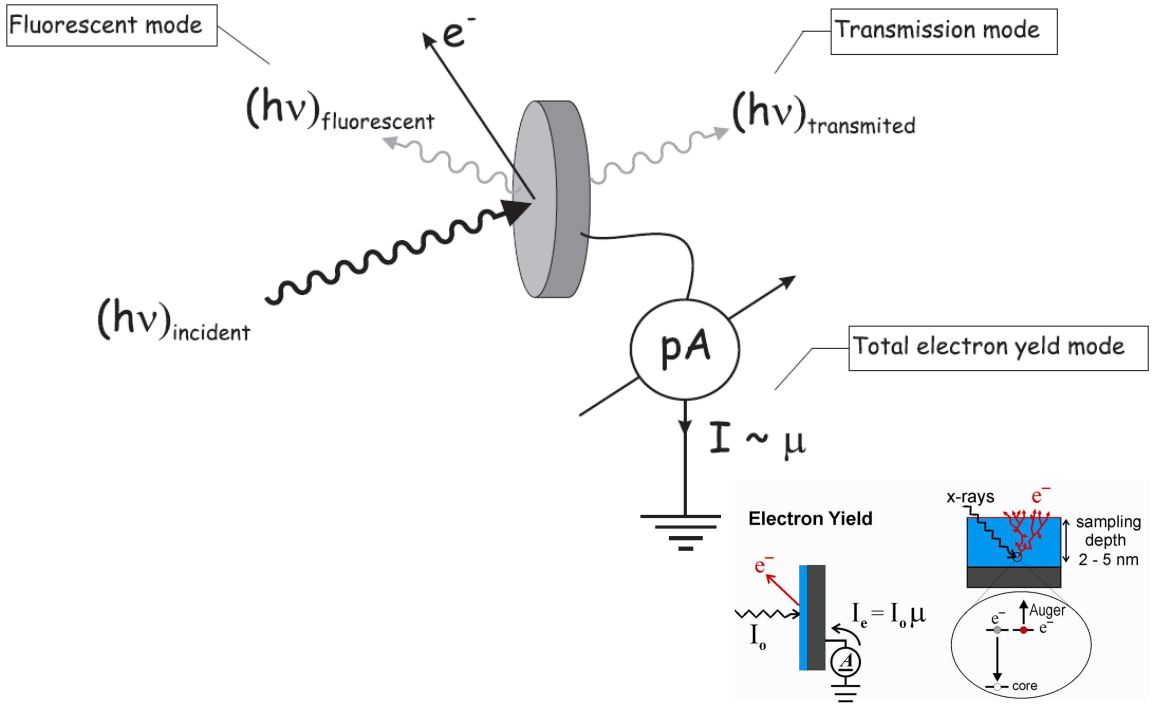

Figure 2.3.1.5 XAS spectra detection modes. Fluorescence Yield (FY) and Total Electron Yield (TEY). One can also measure the transmitted photons to obtain the absorption, but this mode put severe limitations to the samples. From [2.5].

In TEY mode the electrical current (proportional to the absorption coefficient), supplied from the ground in order to neutralize the "charged" sample, is measured. The unfilled core hole left behind by the x-ray absorption process is filled by an electron which decays from the occupied DOS. In this case the process is not radiative but an Auger process.

The energy gained from this decay is transferred to another electron, which can escape from the material. The TEY mode probing depth is much less than that of FY mode and varies in the range of approximately 20 to 50Å.

The resonant x-ray (magnetic) scattering XRS (XRMS) combines the well-known x-ray diffraction experiment (Fig. 2.3.1.6) with the advantages of synchrotron radiation, which makes it an extremely powerful method for spectroscopic and structural studies.

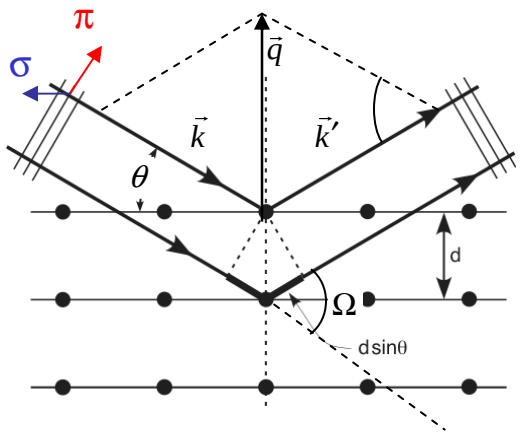

momentum transfer

$$\hbar\vec{q} = \hbar\vec{k}' - \hbar\vec{k}$$

$$2d\sin\theta = n\lambda$$

$$q = \frac{4\pi}{\lambda}\sin\theta$$

elastic scattering

$$|\vec{k}| = |\vec{k}'|$$

Figure 2.3.1.6 Sketch of a diffraction setup. The wavevector of the incoming $\vec{k}$ and the out-coming $\vec{k}'$ waves span the scattering plane. The angle $\Omega = 2\theta$ is called scattering angle. The momentum transfer in the scattering process is given by the scattering vector $\vec{q}$ and d is distance between crystal planes. π is the polarization in the plane and σ perpendicular to the plane of incidence. On the right hand side the Bragg law and analogously the Laue condition for elastic scattering are shown.

The atomic form factor that describes the response of atoms to the electromagnetic x-ray field is generally expressed as:

$$\hat{f}(\vec{q},\omega) = f^0(\vec{q}) + \hat{f}'(\omega) + i\hat{f}''(\omega) \qquad (2.3.2)$$

where $f^0(q)$ is isotropic non-resonant term, and $\hat{f}'(\omega)$, $\hat{f}''(\omega)$ give the resonance contribution, also called dispersion or anomalous corrections (3x3) tensors. Their symmetry is given by the local symmetry at the scattering atom. The nonresonant and the resonant contributions in equation 2.3.2 can be derived by solving the equation of motion for bound electrons in an alternating electromagnetic field. The resulting cross section of the whole elastic scattering process is:

$$\sigma_{scatter} \sim \left| \left\langle f \left| H_{\text{int}}(A^2) \right| i \right\rangle + \sum_n \frac{\left\langle f \left| H_{\text{int}}^{\dagger}(A) \right| n \right\rangle \left\langle n \left| H_{\text{int}}(A) \right| i \right\rangle}{E_i - E_n + \hbar\omega + i\Gamma/2} \right|^2 \qquad (2.3.3)$$

where H_{int} is the interaction between the electrons and the electromagnetic wave, linear and quadratic respectively, in the vector potential *A*. The first term represents the non-resonant contribution ($f^0(q)$, in equation 2.3.2), and is determined by the Fourier transform (FT) of the charge and spin contributions that can be further split to a charge $f_c^0(q)$, and a magnetic $f_m^0(q)$, part. The second term, involving an excitation from initial $|i\rangle$ to an intermediate state $|n\rangle$, quantifies the resonant contribution (Fig. 2.3.1.7).

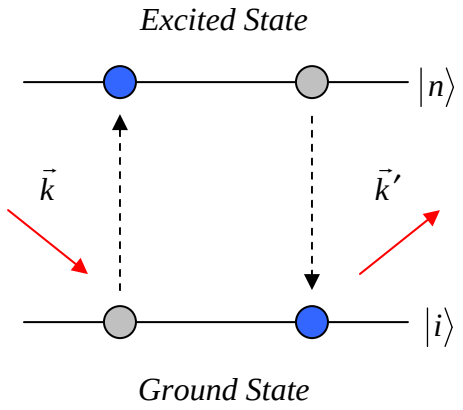

Figure 2.3.1.7 Resonant x-ray scattering process

This contribution becomes very large for photons with energies equal to the resonance energies $E_i - E_n$. Therefore, the potential of resonant scattering results from the high sensitivity to the intermediate state $|n\rangle$. While in the non-resonant process, the change of valence state of an atom usually causes only a very small difference in the scattered amplitude, the resonant scattered signal is sensitive even to small changes of the degree of occupancy of the intermediate state. Hence, the resonant scattering process is a very efficient probe of charge and orbital ordering phenomena. This resonance enhancement of the signal ensures also the magnetic sensitivity (XRMS). The absorption probabilities of left and right circularly polarized photons are different due to the dipole selection rules applied to the occupied states (Fig. 2.3.1.8). This leads to an asymmetry in the absorption of photons of different helicities, depending on the direction of the local magnetization, known as the x-ray magnetic circular dichroism in absorption regime (XMCD).

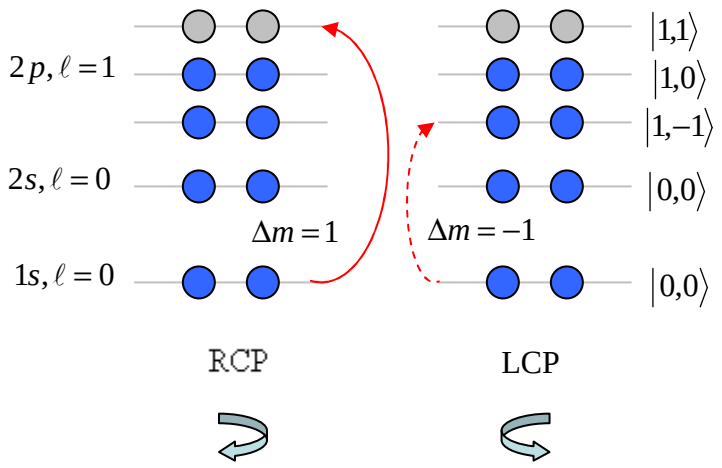

Figure 2.3.1.8 Energy level diagram of an atom with 8 electrons. The dipole selection rule $\Delta m = +1$ for right circularly polarized (RCP) and $\Delta m = -1$ for left circularly polarized (LCP) photons causes an asymmetry in the absorption probability since the $\Delta m = -1$ transition is not possible due to the fully occupied $|1,-1\rangle$ state. From [2.56].

Since the absorption coefficient is related to the imaginary part of the atomic scattering strength by the optical theorem and both, real and imaginary parts of the dispersion correction are related, this asymmetry also manifests in the atomic scattering strength, which consequently depends on the local direction of the magnetization.

$$\sigma_{scatter}(E) \sim \left[\left| \hat{f}'(E) \right|^2 + \left| \hat{f}''(E) \right|^2 \right] \tag{2.3.4}$$

$$\sigma_{abs}(E) \sim \frac{f''(E)}{E}$$

Therefore the absorption is complementary to the diffraction experiments.

The direct dipole excitation into the states responsible for the magnetism results in a much larger magnetic scattering strength. The resonant scattering amplitude for such a dipole excitation is [2.56][2.57]:

$$f_{res} = \left(\varepsilon_f^* \cdot \varepsilon_i\right) F^0 + i\left(\varepsilon_f^* \times \varepsilon_i\right) m F^1 + \left(\varepsilon_f^* \cdot m\right)\left(\varepsilon_i \cdot m\right) F^2 \tag{2.3.5}$$

Here, ε_i and ε_f denote the polarization vectors of the incident and scattered light and F^i are resonance oscillator strengths. The first term describes resonant charge scattering, the latter two depend on the unit vector *m*, pointing along the local magnetization direction. The term linear in *m* corresponds to the circular dichroism while the latter, of second order in *m*, describes linear dichroic effects. Since the signal is here sensitive to both, charge and magnetic structure with a certain periodicity, XRS (XRMS) is therefore especially efficient for characterization of long period electronic, orbital and magnetic superstructures in bulk specimens and multilayer systems. One can perform scans where either the momentum transfer or the photon energy is kept constant (Fig. 2.3.1.9). Similarly, in XRMS one does the experiment in a magnetic field and makes use of circularly polarized photons to obtain the magnetic structure in terms of the asymmetry ratio and dichroic difference [2.58][2.59][2.60].

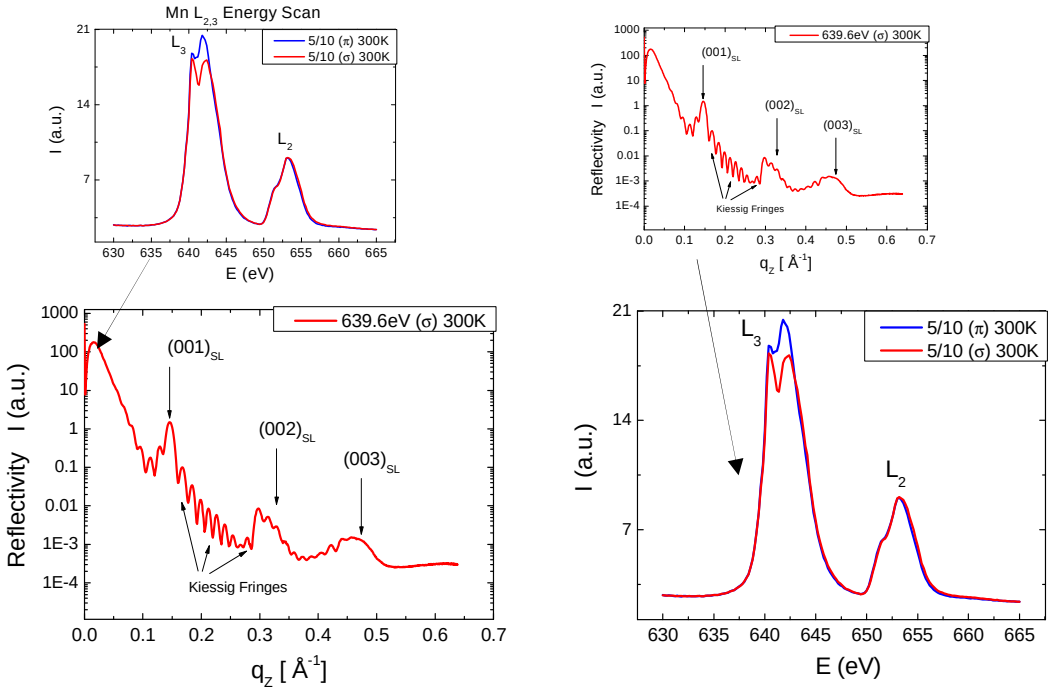

Figure 2.3.1.9 left: Typical angular scan of a superlattice sample taken at Mn $L_{2,3}$ resonance edge. First three SL Bragg reflections are clearly visible. The Kiessig fringes in between them give the number of repetitions of the SL unit cell in the sample. This curve is essentially a Fourier transform image of the electronic density in the sample **right:** Mn $L_{2,3}$ edge at fixed *q*, for two different polarizations.

2.3.2 Interface between High-Temperature Superconductor $YBa_2Cu_3O_7$ and Ferromagnetic Metal $La_{2/3}Ca_{1/3}MnO_3$

Recently, the synthesis of artificial superlattices (SL) of the optimally doped high-temperature superconductor (SC) $YBa_2Cu_3O_7$ and the ferromagnetic metallic (FM) $La_{2/3}Ca_{1/3}MnO_3$, (YBCO/LCMO), offered an elegant route to the experimental study of the interplay between superconductivity and magnetism on a microscopic level. Routine *dc*-transport and magnetization measurements of these superlattices have established that there is a strong interaction between SC and FM order parameters since both critical temperatures, T_c=92K and T_{mag}=250K, were considerably suppressed even for superlattices with relatively thick layers, d >10 nm. These observations implied that the proximity coupling effects may involve unexpectedly large length scales. Equally interesting were also reports for a considerable suppression of the normal state electronic conductivity. This is also a puzzling finding since both materials, at their optimal doping levels, possess good metallic properties. The latter was also confirmed by means of spectroscopic ellipsometry in the FIR region by T. Holden *et al*. [2.61], (Fig. 2.3.2.1).

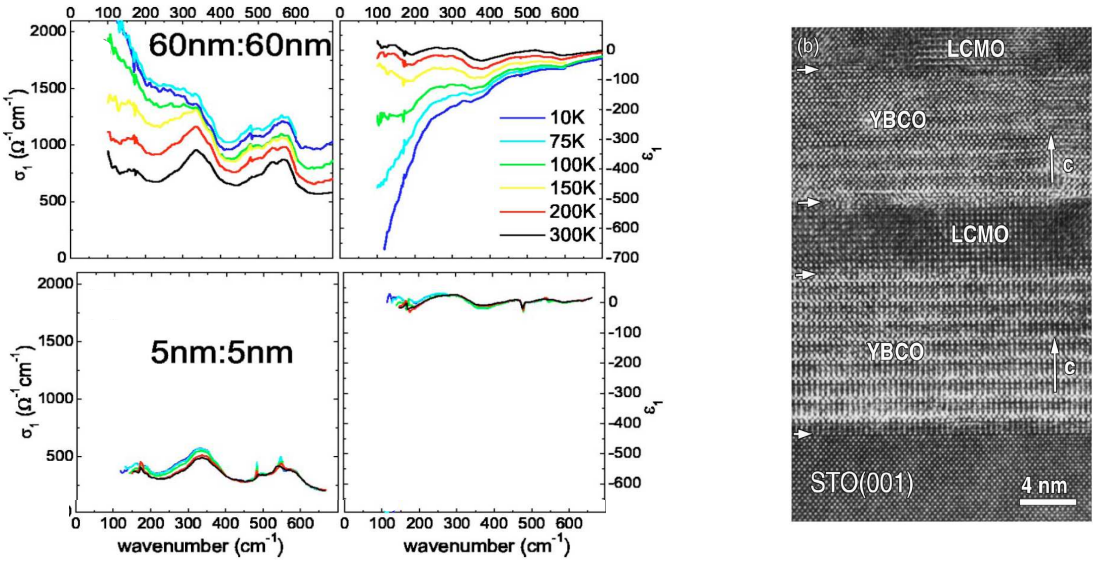

Figure 2.3.2.1 left: Temperature dependence of the in-plane conductivity σ_1, and the real part of the dielectric function ε_1, for SLs YBCO/LCMO with equal thickness of both layer materials: 60nm/60nm (upper panel) and 5nm/5nm (lower pannel) **right:** High-resolution TEM image of YBCO/LCMO SL structure.

In order to unambiguously prove the intrinsic origin of this metal-insulator transition in YBCO/LCMO superlattices several control experiments were carried out. Poor SL quality, including significant chemical mixtures across the layer boundaries was excluded by x-ray, high-resolution TEM image and ion-mass spectrometry. Furthermore, an additional set of superlattices of YBCO/LNO ($LaNiO_3$) were prepared, but found to remain metallic for all thicknesses. Thus, the observed significant free-charge carriers suppression was explained as a consequence of a massive charge transfer between adjacent layers, namely, holes from YBCO towards LCMO, as well as a charge localization due to magnetic correlations induced by long-range proximity effects involving distances of ~ 20nm. The detailed microscopic picture of the electron/orbital and magnetic state at the YBCO/LCMO interface was further inferred by elastic neutron scattering, soft x-ray absorption spectroscopy, XMCD and XAS – (FY / TEY) modes comparison strategy on specially prepared samples, and led to conclusive results. The instrumental combination described, can serve as a general experimental scheme in the study of interfacial properties in superlattices [2.62][2.63]. Figure 2.3.2.2, shows unpolarized neutron reflectivity curves taken under specular conditions, momentum transfer perpendicular to the SL planes, on a YBCO/LCMO superlattice sample with equal thickness for both materials, i.e. 1:1 ratio. At high temperatures, where only nuclear scattering contributes, the first Bragg reflection is clearly visible, while the second one is absent, as expected, due to the 1:1 configuration in the superlattice. The development of a second order Bragg reflection below the magnetization temperature $T < T_{mag}$ ~165K, is indicative of a substantial difference between the spatial profiles of the nuclear and magnetic potentials. The best model fit of the experimental data selected sizable magnetic polarization within the YBCO layer that couples antiferromagnetically (AF) to the LCMO layer (antiphase magnetic proximity effect) as the most likely scenario.

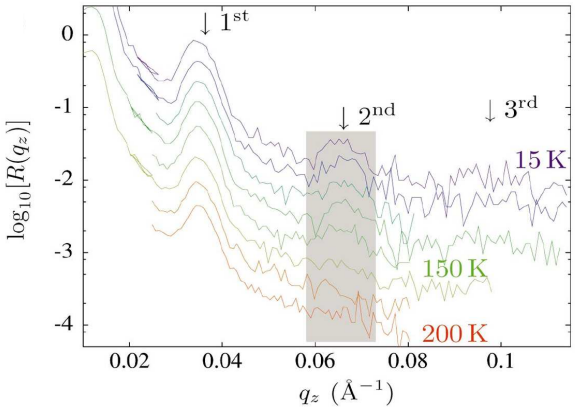

Figure 2.3.2.2 Temperature dependence of specular neutron reflectivity on YBCO/LCMO (1:1) superlattice (with equal thickness for both layer materials). Structurally forbidden second order Bragg peak (shaded area) develops below the magnetic transition temperature T_{mag}~165K [2.62].

The interface magnetic profile was determined quantitatively by XMCD and confirmed the suggested antiferromagnetic coupling across the interface. The mutual orientation of Mn and Cu magnetic moments can be deduced from the relative sign of the XMCD signal at L_3 resonance for the same helicity of the light. As seen on figure 2.3.2.3, Cu dichroism is small compared to that of Mn and has the opposite sign, which indicates an antiparallel orientation of the corresponding magnetic moments. Furthermore, the induced net magnetic moment at the Cu site was estimated to be $\mu_s = 0.2\mu_B$ / Cu.

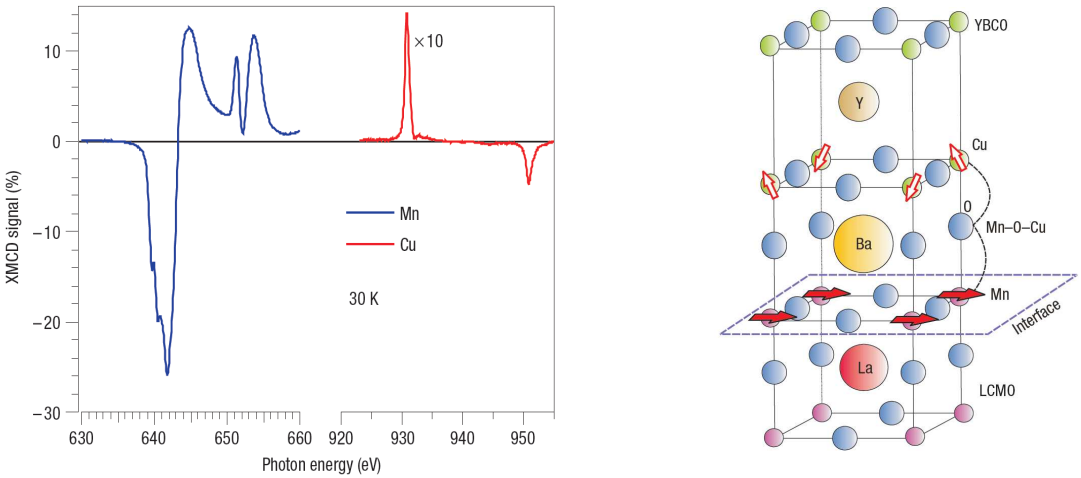

Figure 2.3.2.3 left: XMCD signals obtained from core level absorption spectra for Mn (blue) and Cu (red). The data is taken at temperature T=30K. **right:** A model of an interface in YBCO/LCMO superlattice. The arrows represent the relative orientation of the net magnetic moments as deduced from XMCD [2.63].

The remaining question concerning the exchange interaction is the origin of the AF coupling. The only active orbital in YBCO is the partially occupied d_{x2-y2}, and the conducting e_g electron in metallic ferromagnetic LCMO is believed to be in a fluctuating d_{x2-y2} <-> d_{z2-r2} orbital state. The question is relevant since the alternating occupation of different orbitals on neighboring lattice sites favors ferromagnetism, whereas the uniform occupation of orbitals on all lattice sites tends to generate antiferromagnetism.

In order to elucidate the orbital state right at the interface, J.Chakhalian *et al*. [2.64] measured linear dichroism (XLD) spectra on specially prepared samples, such that the difference in the probing depth for fluorescence yield (FY) and total electron yield (TEY) modes make possible the spectroscopic distinction between the interface and the "bulk" part of the samples (Fig. 2.3.2.4).

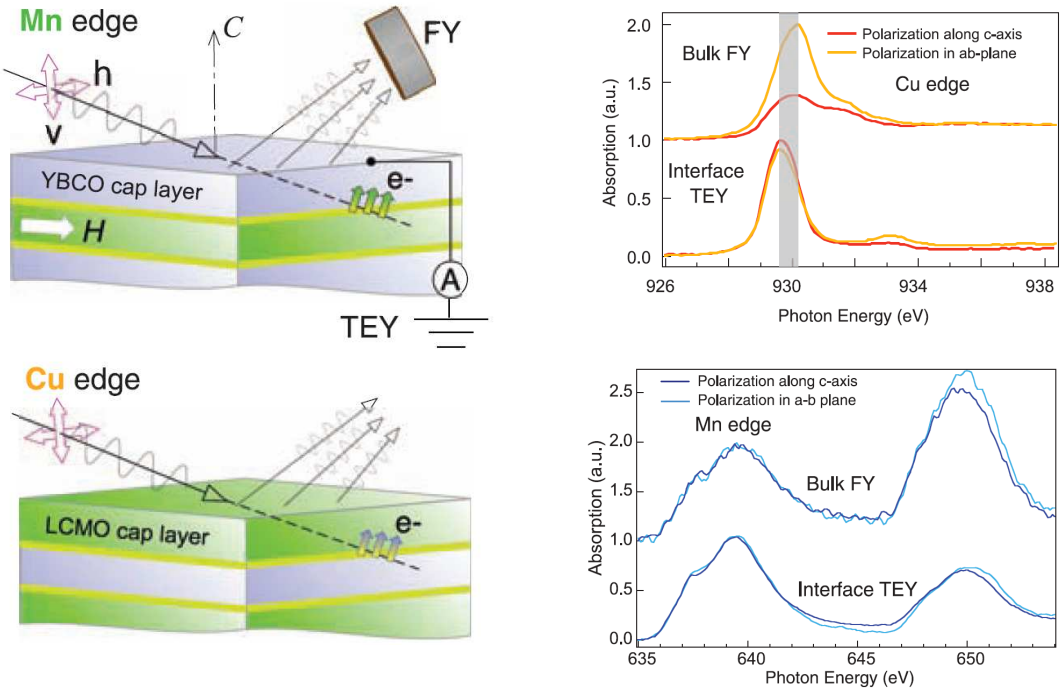

Figure 2.3.2.4 left: Schematic of the experimental setup used to obtain the XAS and XLD data in TEY and FY modes. Data sensitive to interfacial Cu (Mn) atoms are taken in TEY mode on samples with LCMO (YBCO) capping layer. **right:** Normalized x-ray absorption spectra for both modes, FY (bulk sensitive) / TEY (interface sensitive), and polarizations along *c*-axis and in *ab*-plane. Cu L_3 edge (upper panel) and Mn $L_{2,3}$ absorption edge (lower panel), from [2.64].

The first sign for modification of the electronic structure of the CuO_2 layer adjacent to the interface (TEY mode) is the shift (~0.4eV) of the Cu L_3 edge towards lower energy. The shift of the peak is evidence of a change in valence state of Cu ions near the interface. Comparison to XAS spectra of reference materials containing Cu^{1+} and Cu^{2+} ions yield a rough estimate of 0.2*e*/Cu charge transfer across the interface, such that the hole density in YBCO is reduced at the interface. The second striking observation is that the strength of the absorption signals in TEY (interface sensitive) mode for polarization perpendicular and parallel to the layers are almost equal, in stark contrast to the FY (bulk sensitive) mode where the pronounced polarization dependence is in full agreement to the partially occupied d_{x2-y2} orbital, characteristic for bulk YBCO. This is a clear signature of orbital reconstruction at the interface. The nearly isotropic cross section implies that the hole content of the Cu d_{z2-r2} orbital is similar to that of the d_{x2-y2} orbital. The spectra at Mn $L_{2,3}$ edge show no dependence of photon polarization, an observation consistent with orbitally disordered state in metallic LCMO with equal occupation of Mn d_{x2-y2} <-> d_{x2-y2} orbitals. Based on the experimental findings and supported by cluster calculations, a model for the interfacial orbital state was obtained explaining the unusual magnetic behavior. The Cu d_{z2-r2} orbital points directly towards the interface and hybridizes effectively with the Mn d_{z2-r2} orbital via the apical oxygen ion O(2), (Fig. 2.3.2.5), generating a covalent chemical bond bridging the interface and hence naturally explaining the antiferromagnetic coupling.

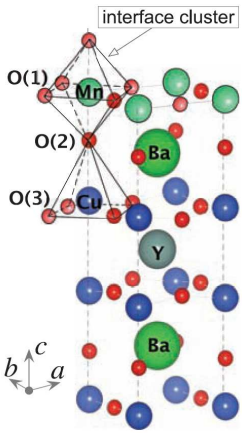

Figure 2.3.2.5 Atomic positions near the YBCO/LCMO interface. $MnCuO_{10}$ interface cluster is used in the theoretical calculations [2.64].

The observed interfacial orbital reconstruction in YBCO/LCMO superlattices is a nice example of the realization of an orbital state not achievable in bulk samples.

2.3.3 Polar / Non-polar Interface

The interface between polar and non-polar materials suggests an interesting mechanism for electronic reconstruction. Even interfaces between formally neutral planes can have interface dipoles resulting from band offsets, for example in semiconductor heterostructures. However, electrostatic potential at the boundaries ("polarity discontinuities") can be a dominant factor in determining the electronic state when two materials are brought in contact. Considerable interest was generated after the experimental findings of unusual metallic state with very high carrier mobility at the interface between two wide-band gap insulators $LaAlO_3$ and $SrTiO_3$ [2.65]. In the (001) direction, the perovskite structure ABO_3 can be considered as an alternating stack of AO and BO_2 layers. Whereas $Sr^{2+}O^{2-}/Ti^{4+}O_2^{2-}$ is a sequence of charge neutral sheets, $La^{3+}O^{2-}/Al^{3+}O_2^{2-}$ alternates between $\pm e$ charged sheets in the ionic limit. The heterointerface $LaAlO_3$ / $SrTiO_3$, therefore, presents an extra $\pm e/2$ charge per two-dimensional unit cell depending on the interface termination structure (Fig. 2.3.3.1).

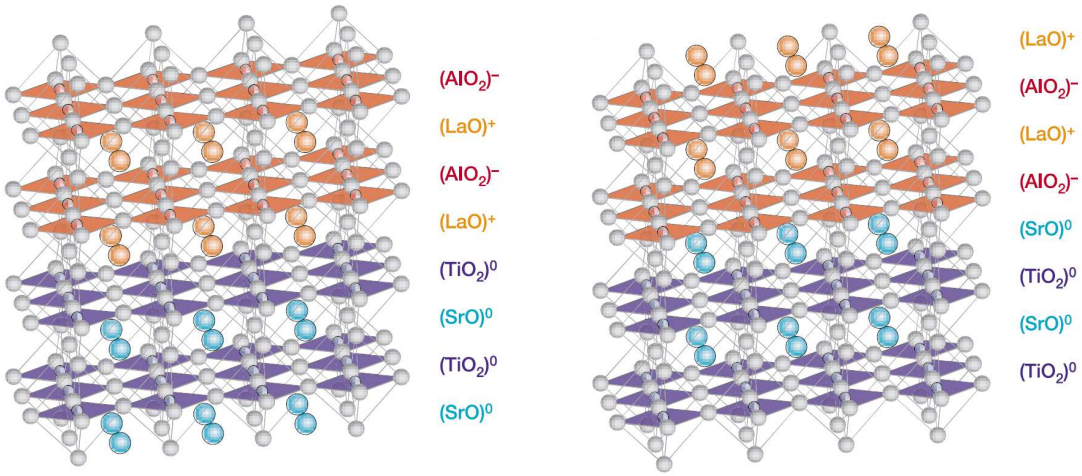

Figure 2.3.3.1 Schematic of $LaAlO_3$ / $SrTiO_3$ interface **left:** $(LaO)^+$ / $(TiO_2)^0$ **right:** $(AlO_2)^-$ / $(SrO)^0$. The interface structure is controlled by direct deposition of $LaAlO_3$ on TiO_2-terminated $SrTiO_3$ (001) or after a monolayer of SrO is deposited on the TiO_2 surface. From [2.65].

Furthermore, transport measurements revealed that the electron-doped interface is conducting with extremely high carrier mobility exceeding 10000 $cm^2V^{-1}s^{-1}$, while the hole-doped interface is found to be insulating. The observed interface asymmetry and the underlying mechanism are of great experimental interest since it can be implemented in

the design of superlattices with specific interfacial properties. Nakagawa *et al*. [2.66], proposed a model in which the electronic reconstruction at the (001) $LaAlO_3$ / $SrTiO_3$ interface arises as a consequence of electrostatic potential increase that is a function of thickness of the polar material. This electrostatic potential eventually diverges with respect to the termination line, i.e. the polar/non-polar interface, which in turn triggers charge redistribution across the interface in order to resolve the "polar catastrophe". Whenever this charge can be provided from ion with variable valence state, the resulting interface does not suffer significant atomic rearrangements or roughness. In the opposite limit, the relaxation process is at the expense of introduction of oxygen vacancies. Namely, the AlO_2/LaO/TiO interfaces are compensated by mixed-valence Ti sites that place extra electrons in the $SrTiO_3$ conduction band. In contrast to this electronic interface reconstruction, the AlO_2/SrO/TiO_2 interface is compensated by oxygen vacancies – an atomic interface reconstruction.

The results on $LaAlO_3$ / $SrTiO_3$ interface system stimulated a large amount of research work and a concomitant debate about the role of oxygen vacancies in the origin of this unusual metallic state, see for example [2.67]. Metallic conductivity has also been observed in the $LaTi^{3+}O_3$ / $SrTi^{4+}O_3$ system. Ohtomo *et al*. [2.68] showed that these two materials can be grown in superlattices of superior quality (Fig. 2.3.3.2). Similarly, a charge modulation was found to involve charge transfer from $LaTiO_3$ towards $SrTiO_3$. The resulting electronic state near the interfaces is the mixed-valence $Ti^{3.5+}$, deduced from electron energy-loss spectroscopy measurement (EELS).

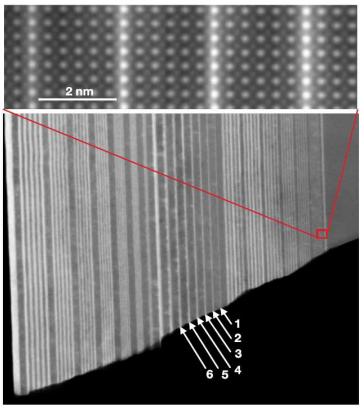

Figure 2.3.3.2 High-resolution STEM image of $LaTiO_3$ / $SrTiO_3$ superlattice. Digits denote the number of $LaTiO_3$ unit cells in each layer. From [2.68].

As $LaTiO_3$ is a Mott insulator, this superlattice system addresses yet another aspect of fundamental interest, that is, what kind of electronic phases can appear at interfaces between a strongly correlated insulator and a band insulator. Theoretical studies indeed find significant electronic reconstructions and intriguing ground states, including a metallic state, consistent with the experimental results on the $LaTiO_3$ / $SrTiO_3$ superlattice system [2.69].

Critical in the characterization of metallic states is the electrodynamic response. A spectroscopic ellipsometry study recently provided quantitative information about the electrodynamic properties of itinerant electrons in $LaTiO_3$ / $SrTiO_3$ superlattices [2.70]. The IR ellipsometry spectra showed that all $LaTiO_3$ / $SrTiO_3$ superlattices exhibit a Drude-like metallic response regardless of the SL periodicity and the individual layer thicknesses (Fig. 2.3.3.3). The data yielded also nearly constant sheet carrier concentration per interface of about ~$3x10^{14}cm^{-2}$ with a small scattering rate of ~ $120cm^{-1}$, sizable mean free path ~ 25 unit cells at T=10K and fairly high mobility of ~35 $cm^2V^{-1}s^{-1}$ according to the relation $\mu = e\tau / m^*$ with $m^* = 1.8m_e$, extracted from ellipsometric data in the framework of the extended Drude- model.

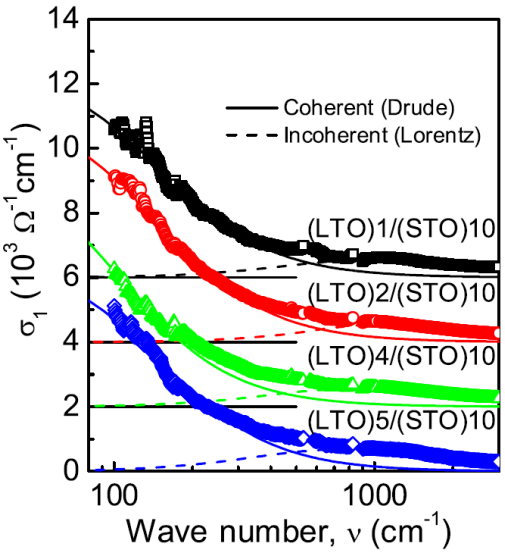

Figure 2.3.3.3 Optical conductivity spectra of SL samples with various $LaTiO_3$ thickness (unit cells) at 10K, containing coherent (Drude) and incoherent (Lorentz) contributions [2.70].

2.3.4 Selecting Orbital State by Strain

In Ref. [2.71], the $LaMnO_3/SrMnO_3$, (LMO/SMO or La/Sr are sometimes used for simplicity), superlattices have been investigated in order to elucidate the interface electronic phases created by adjoining two antiferromagnetic insulators with electronic configuration $t_{2g}^3 e_g^1$ and $t_{2g}^3 e_g^0$, respectively. Due to the apparent similarity in the electronic configuration realized in the hole doping procedure in mixed-valence $La_{1-x}Sr_xMnO_3$ and $La_{1-x}Ca_xMnO_3$ systems, one would expect a double-exchange promoted metallic-like state near the interfaces and activation of a magnetoresistive effect. However, the magnitude of the resulting electronic reconstruction will also depend on the orbital state across the interface. It is well known that anisotropic strain can favor energetically a certain orbital state. In thin films and superlattices samples the strain effects can be controlled by a careful selection of the substrate material for coherent epitaxy. In their work Yamada *et al*. studied two sets of samples: [La6, Sr4] and [La3, Sr2], where the digits denote the number of unit cells comprising the superlattice unit cell. In order to investigate the evolution of the electronic properties as a function of strain, three different substrates were chosen; $SrTiO_3$ (STO)(a_{sub}=3.905Å), $La_{0.3}Sr_{0.7}Al_{0.65}Ta_{0.35}O_3$ (LSAT) (a_{sub}=3.870Å) and $LaAlO_3$ (LAO) (a_{sub}=3.792Å), so as their lattice constant gradually decrease in the sequence, going from tensile through lattice-matched to compressive type strain.

Based on detailed *dc*-resistivity, optical and magnetization measurements for the epitaxially and coherently strained LMO/SMO superlattices, and the respective solid solution LSMO control samples, the authors propose a model for the orbital structures at the LMO/SMO interfaces, figure 2.3.4.1.

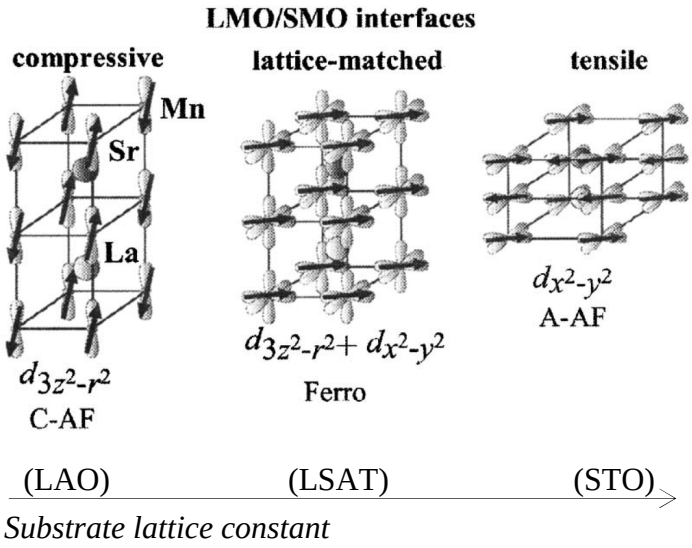

Figure 2.3.4.1 Different spin and orbital structures realized at the LMO/SMO interface and stabilized by the epitaxial strain: LAO-compressive, LSAT-lattice matched and STO-tensile [2.71].

The tensile strain (stretching *x,y*) by STO stabilizes the $d(x^2-y^2)$ orbital state resulting in a layered A-type antiferromagnetic and conducting interface. The lattice matching, in the case of LSAT substrate leads to a ferromagnetic interface with a disordered orbital state. When compressive strain is induced by LAO, the $d(z^2-r^2)$ orbital state is favored (see also Fig. 2.3.4.2), C-type antiferromagnetism occurs giving rise to an insulating state.

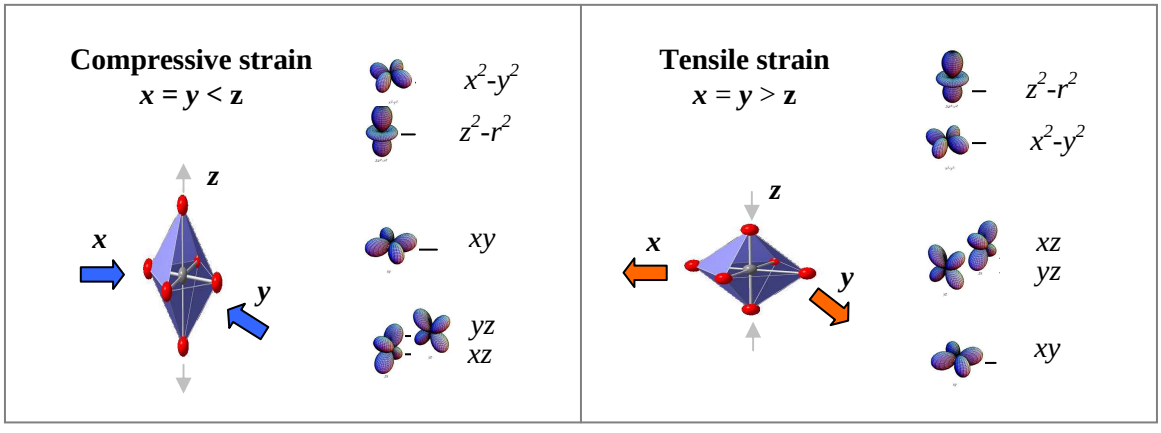

Figure 2.3.4.2 left: Compressive strain favors $d(z^2-r^2)$ orbital state, and **right:** Tensile strain favors the $d(x^2-y^2)$ orbital state.

Whilst in the case of a STO substrate, the superlattice LMO/SMO system is conducting, it is hard to conclude from simple transport measurements whether this metallic state occurs right at the interfaces. Recently, Smadici *et al*. [2.72], provided that evidence by carrying out a resonant soft x-ray scattering experiment on LMO/SMO on STO superlattices, with carefully selected periodicity, (LMO)2n/(SMO)n, i.e.(2:1), with n = 4 and 5. The key experimental result in this work is the observation of a structurally forbidden (L=3) superlattice Bragg reflection (Fig. 2.3.4.3), when photons are tuned close to the Fermi energy $E_{F,}$ obtained from XAS data. In off-resonance conditions, including hard x-rays, the peak is suppressed in accordance with symmetry considerations. Evidently, while preserved by the atomic lattice, the symmetry is broken electronically near the Fermi energy.

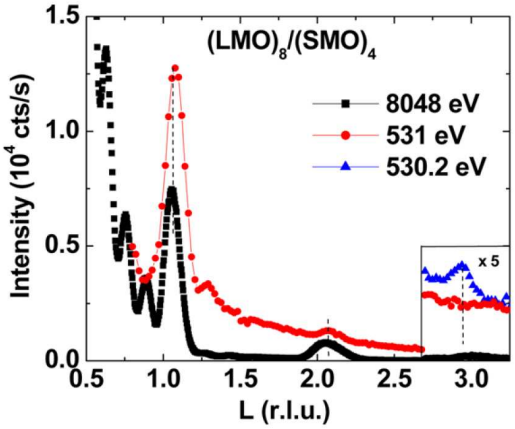

Figure 2.3.4.3 Specular x-ray scattering from n=4 superlattice with non-resonant hard x-rays (black), non-resonant soft x-rays (red) and soft x-rays tuned close to the Fermi energy (blue) [2.72].

The main conclusion is that the resonance observed at 530 eV corresponds to the presence of a quasiparticle peak at E_F, as predicted for the Mott-band insulator interface [2.73], and demonstrating the potential of the x-ray resonant scattering technique.

Chapter 3

Basic Principles of Optical Spectroscopy

3.1 Dielectric Function, Optical Conductivity and Refractive Index

The interaction of electromagnetic radiation with matter is fully described by the Maxwell equations. The response of the material to electromagnetic field can be taken into account by relating the displacement field with the electric field: $D(r,t) = \varepsilon E(r,t)$ or alternatively, using the current density and the electric field, $J(r,t) = \sigma E(r,t)$ (the Ohm's law), and the magnetic induction with the magnetic field strength $B(r,t) = \mu H(r,t)$. The material parameters: ε, μ and σ, are the dielectric function (also called permittivity), magnetic permeability and conductivity respectively. In free space there is no charge $\rho(r,t) = 0$ and currents $J(r,t) = 0$ and $D(r,t) = \varepsilon_0 E(r,t)$, $B(r,t) = \mu_0 H(r,t)$, where $\varepsilon_0 = 8.8542 \times 10^{-12} AsV^{-1}m^{-1}$ is the permittivity, and $\mu_0 = 1.2566 \times 10^{-6} VsA^{-1}m^{-1}$ the permeability of free space. A possible solution to the wave equation for the electric field, analogously for the magnetic induction, is a harmonic wave $E(r,t) = E_0 e^{i(q.r-\omega t)}$, with a wavevector $|q| = \omega / c$ and $c = 2.99792458 \times 10^8 ms^{-1}$ [3.1][3.2][3.3]. Thus, in free space, the wave travels undisturbed with no attenuation at all (Fig. 3.1.1).

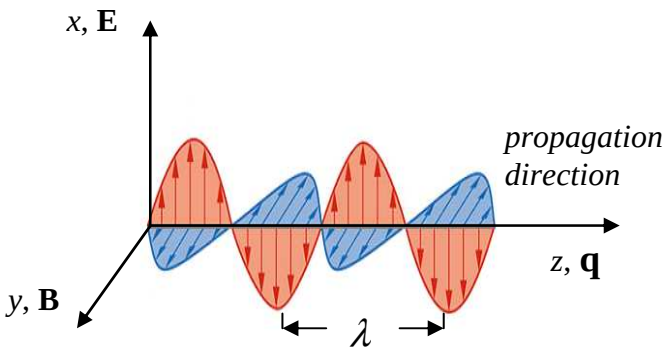

Figure 3.1.1 Linearly polarized electromagnetic wave in free space with wavelength $\lambda = 2\pi/|q|$.

When matter is present, the electromagnetic wave will, in general, induce or redistribute electric and magnetic dipole moments as well as currents. Hence, the electric and magnetic fields no longer have the uniform distribution as in vacuum, but will acquire a non-trivial one instead, reflecting the space / time dispersion of the material parameters. In order to determine the resulting fields and currents in the matter we need to account for all contributors that may modify them. Table 3.1.1 below, represents such a summary:

Electric Field	$E = \begin{cases} E_{ext} = \varepsilon_1 E \\ + \\ E_{ind} = -4\pi P \end{cases}$
Current Density	$J = \left.\begin{cases} J_{pol} = \dfrac{\partial P}{\partial t} \\ + \\ J_{mag} = c\nabla \times M \\ + \\ J_{cond} = \sigma_1 E \\ + \\ J_{ext} \end{cases}\right\} = J_{ind}$
Charge Density	$\rho = \begin{cases} \rho_{pol} \\ + \\ \rho_{ext} \end{cases}$

Table 3.1.1 All possible contributions to the electric quantities J, ρ and E (induced and external to the system). ρ_{ext} is the charge added from outside, E_{ext} is the electric field and J_{ext} , the corresponding current density. $\rho_{pol} = -\nabla \cdot P$, where P is the polarization, is the charge density due to spatially varying polarization, and J_{pol} the resulting current called displacement current or bound current density J_{bound}. To J_{bound} contributes also J_{mag} caused by the spatially dependent magnetization: $\nabla \times M$. J_{cond} is the motion of electrons in presence of electric field. ε_1, σ_1 are the dielectric constant and the conductivity of the material [3.1][3.2].

In the range of wavelengths larger than the characteristic lattice spacing in the material, we can assume some mean value for the resulting fields and neglect ρ_{pol} in case of homogeneous polarization. Assuming no external currents ($J_{ext}=0$) either, the total current density J_{total} will be:

$$J_{total} = J_{cond} + J_{bound} \tag{3.1.1}$$

The displacement field D and the magnetic field strength H, in presence of matter are:

$$D = \varepsilon_1 E = (1 + 4\pi\chi_e)E = E + 4\pi P \tag{3.1.2}$$

$$B = \mu_1 H = (1 + 4\pi\chi_m)H = H + 4\pi M$$

where ε_1 and μ_1 are now, the dielectric constant and the permeability of the material. $P = \chi_e E$ is the electric dipole moment density, $M = \chi_m H$ - the magnetic moment density and χ_e, χ_m - the dielectric and the magnetic susceptibility respectively. For non-magnetic media: $\chi_e >> \chi_m$, being the reason for the widely used assumption $\mu_1 = 1$. As already mentioned in (§1.2), the material parameters are complex functions, which takes into account possible time delay of medium reaction with respect to the perturbation. They are tensors in the general case, and are related by simple analytical connections (see also table 3.1.2 below):

$$\hat{\varepsilon} = \varepsilon_1 + i\varepsilon_2 \tag{3.1.3}$$

$$\hat{\sigma} = \sigma_1 + i\sigma_2$$

$$\hat{\varepsilon} = 1 + \frac{4\pi i}{\omega}\hat{\sigma}$$

$$\hat{\varepsilon} = \varepsilon_1 + i\frac{4\pi\sigma_1}{\omega} = \varepsilon_1 + i\varepsilon_2$$

The change in magnitude and the phase shift is now included in the expressions for the resulting fields and currents: $D = \hat{\varepsilon}E$, $J_{tot} = \hat{\sigma}E$. In case of non-zero losses in the system ($\sigma_1 \neq 0$) and assuming no net charge ($\rho_{ext} = 0$) is present, the wavevector is also complex and it is given by:

$$q = \frac{\omega}{c}\left[\varepsilon_1\mu_1 + i\frac{4\pi\sigma_1\mu_1}{\omega}\right]^{1/2} n_q, \qquad \text{with } n_q = \frac{q}{|q|} \tag{3.1.4}$$

describing the wavelength change and the attenuation of a wave propagating in the medium.

The complex refractive index is another material response function that describes the propagation and the energy dissipation of electromagnetic wave:

$$\hat{N} = n + ik = \left[\varepsilon_1 \mu_1 + i \frac{4\pi \mu_1 \sigma_1}{\omega} \right]^{1/2} = \left[\hat{\varepsilon} \mu_1 \right]^{1/2} \tag{3.1.5}$$

with real part *n*, called refractive index and imaginary *k* - extinction coefficient. These are related to the material parameters through the following expressions:

$$n^2 = \frac{\mu_1}{2} \left\{ \left[\varepsilon_1^2 + \left(\frac{4\pi\sigma_1}{\omega} \right)^2 \right]^{1/2} + \varepsilon_1 \right\} \tag{3.1.6}$$

$$k^2 = \frac{\mu_1}{2} \left\{ \left[\varepsilon_1^2 + \left(\frac{4\pi\sigma_1}{\omega} \right)^2 \right]^{1/2} - \varepsilon_1 \right\}$$

$$n^2 - k^2 = \varepsilon_1 \mu_1$$

$$2nk = \frac{4\pi \mu_1 \sigma_1}{\omega}$$

The complex wavevector can also be expressed using the complex refractive index:

$$\hat{q} = \frac{\omega}{c} \hat{N} = \frac{n\omega}{c} + i \frac{k\omega}{c} \tag{3.1.7}$$

Substituting the wavevector into the wave equation,

$$E(r,t) = E_0 \exp\{i(q \cdot r - \omega t)\}$$

and decomposing to real and imaginary parts yields:

$$E(r,t) = E_0 \exp\left\{ i\omega \left(\frac{n}{c} n_q \cdot r - t \right) \right\} \exp\left\{ -\frac{\omega k}{c} n_q \cdot r \right\} \tag{3.1.8}$$

Now it can be seen that the real part of the complex wavevector *q*, expresses a traveling wave while the imaginary part takes into account the attenuation. The first exponent describes the light velocity reduction with respect to its value in vacuum c/*n*, while the second gives the wave damping (Fig. 3.1.2).

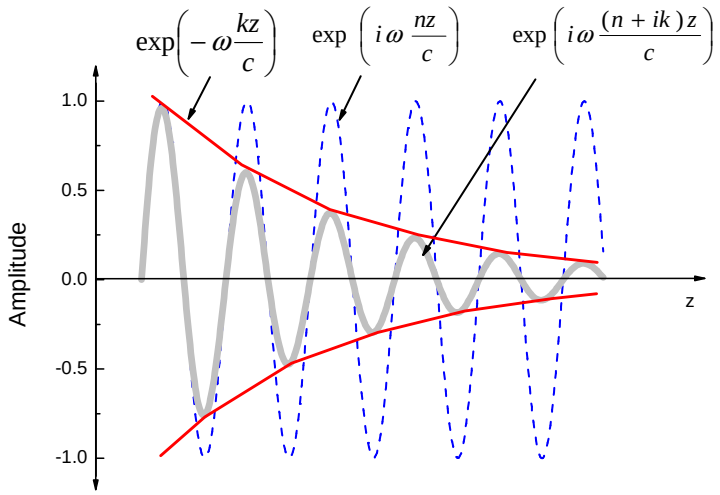

Figure 3.1.2 Sketch of a damped wave, from [3.1].

The characteristic length for the electromagnetic wave attenuation over which the field amplitude decreases by a factor of *1/e* , *e=2.718*, defines the skin depth (or penetration depth):

$$\delta_0 = \frac{1}{\mathrm{Im}\{\hat{q}\}} = \frac{c}{\omega k} \tag{3.1.9}$$

As this quantity depends on the imaginary part of the complex wavevector, it is also a measure of the wave phase shift caused by the material.

Complementary to the penetration depth, the absorption coefficient (in units of inverse length) is defined to describe the attenuation of the light intensity on propagating in medium with extinction coefficient *k*:

$$\alpha = 2\,\mathrm{Im}\{\hat{q}\} = \frac{2\omega}{c}k = \frac{4\pi}{\lambda}k = \frac{4\pi\sigma_1\mu_1}{nc} = \frac{\omega\varepsilon_2\mu_1}{nc} \tag{3.1.10}$$

$\sigma_1 = \omega\varepsilon_2/4\pi$	$\varepsilon_1 = 1 - 4\pi\sigma_2/\omega$	$n = \left\{\frac{\mu_1}{2}\left[\varepsilon_1^2+\varepsilon_2^2\right]^{1/2} + \frac{\varepsilon_1\mu_1}{2}\right\}^{1/2}$
$\sigma_2 = (1-\varepsilon_1)\omega/4\pi$	$\varepsilon_2 = 4\pi\sigma_1/\omega$	$k = \left\{\frac{\mu_1}{2}\left[\varepsilon_1^2+\varepsilon_2^2\right]^{1/2} - \frac{\varepsilon_1\mu_1}{2}\right\}^{1/2}$
$\sigma_1 = nk\omega/2\pi\mu_1$	$\varepsilon_1 = (n^2-k^2)/\mu_1$	$n = \left\{\frac{\mu_1}{2}\left[\left(1-\frac{4\pi\sigma_2}{\omega}\right)^2+\left(\frac{4\pi\sigma_1}{\omega}\right)^2\right]^{1/2} + \frac{\mu_1}{2} - \frac{2\pi\mu_1\sigma_2}{\omega}\right\}^{1/2}$
$\sigma_2 = \left(1-\frac{n^2-k^2}{\mu_1}\right)\frac{\omega}{4\pi}$	$\varepsilon_2 = 2nk/\mu_1$	$k = \left\{\frac{\mu_1}{2}\left[\left(1-\frac{4\pi\sigma_2}{\omega}\right)^2+\left(\frac{4\pi\sigma_1}{\omega}\right)^2\right]^{1/2} - \frac{\mu_1}{2} - \frac{2\pi\mu_1\sigma_2}{\omega}\right\}^{1/2}$

Table 3.1.2 Connections between the material parameters and the optical constants.

3.2 Properties of the Material Parameters

In (§1.2), the generalized susceptibility was briefly discussed along with some of its properties. These properties are very general and apply to all functions that have been recognized as response functions to an applied periodic perturbation. Here we briefly give the properties of the material parameters $\hat{\varepsilon}$ and $\hat{\sigma}$:

1) In principle, all fields characterizing the electromagnetic wave can be split into longitudinal and transverse components with respect to the wavevector *q*. For the electric field *E*, it can be shown that:

$$\nabla \cdot (\hat{\varepsilon} E) = \nabla \cdot \hat{\varepsilon} E^{L} = 4\pi \rho_{ext} \tag{3.2.1}$$

$$\nabla \times E = \nabla \times E^{T} = -\frac{1}{c}\frac{\partial B}{\partial t}$$

i.e., the longitudinal component corresponds to the rearrangement of the charge, while the transverse component is related to the induced electrical currents. With such a decomposition, and assuming isotropic material, the dielectric function has the form:

$$\varepsilon^{L} \equiv \varepsilon_1 + i\frac{4\pi\sigma_1}{\omega} \tag{3.2.2}$$

$$\frac{\omega^2}{c^2}(\varepsilon^{T} - \varepsilon^{L}) \equiv q^2\left(1 - \frac{1}{\mu_1}\right)$$

In the long wavelength limit ($q \to 0$), $\varepsilon^{T} \equiv \varepsilon^{L}$, i.e. the media does not distinguish between fields parallel or perpendicular to *q*.

2) Since $\hat{\varepsilon}(\omega) = \hat{\varepsilon}^{*}(-\omega)$, the real part is an even function: $\varepsilon_1(-\omega) = \varepsilon_1(\omega)$ and the imaginary part: $\varepsilon_2(-\omega) = -\varepsilon_2(\omega)$, an odd function of the frequency. The same holds for the complex conductivity: $\hat{\sigma}(\omega) = \hat{\sigma}^{*}(-\omega)$.

3) The optical parameters of an electromagnetic wave; its amplitude and phase, always undergo changes upon interaction with matter and therefore constitute complex response functions. General considerations, involving causality principle, connect their real and imaginary parts through the Kramers-Kronig relations:

$$\varepsilon_1(\omega)-1=\frac{2}{\pi}\mathrm{P}\int_0^\infty\frac{\omega'\varepsilon_2(\omega')}{\omega'^2-\omega^2}d\omega' \qquad \varepsilon_2(\omega)=-\frac{2}{\pi\omega}\mathrm{P}\int_0^\infty\frac{\omega'^2[\varepsilon_1(\omega')-1]}{\omega'^2-\omega^2}d\omega'$$

$$\sigma_1(\omega)=\frac{2}{\pi}\mathrm{P}\int_0^\infty\frac{\omega'\sigma_2(\omega')}{\omega'^2-\omega^2}d\omega' \qquad \sigma_2(\omega)=-\frac{2\omega}{\pi}\mathrm{P}\int_0^\infty\frac{\sigma_1(\omega')}{\omega'^2-\omega^2}d\omega' \qquad (3.2.3)$$

$$\sigma_{dc}(\omega)=\sigma_1(0)=\frac{1}{2\pi^2}\int_0^\infty(1-\varepsilon_1(\omega'))d\omega'$$

4) A fundamentally important sum rule is the so-called *f*-sum rule or oscillator-strength sum rule. It involves the real part of the optical conductivity and is the most frequently used one:

$$\int_0^\infty\sigma_1(\omega)d\omega=\frac{\pi ne^2}{2m}\equiv\frac{\omega_p^2}{8} \qquad (3.2.4)$$

where $\omega_p=\left(\frac{4\pi ne^2}{m}\right)^{1/2}$ is the plasma frequency, *n* - the total electron density, and *m* – the electron band mass. For cases where various types of electronic excitations are well separated in frequency, a partial sum rule can be used for the determination of the integrated oscillator strength (also called spectral weight - $SW(\omega)$):

$$N_{eff}(\omega)=\frac{2m}{\pi ne^2}\int_0^{\omega_c}\sigma_1(\omega)d\omega \qquad (3.2.5)$$

N_{eff} is the effective number of electrons per formula unit. Applied to the low frequency region, dominated by free electrons, this sum rule is a way to estimate the conduction electron's plasma frequency. An important property of the integrated area under $\sigma_1(\omega)$ is that it is independent of factors such as temperature and phase transitions, and contains information about the interactions in the system. Valuable physical information can be obtained by analyzing the spectral weight redistribution as a function of temperature or other external parameters. For example, if σ_{dc} increases with decreasing temperature then $\sigma_1(\omega)$ must decrease at higher frequencies so as to conserve the spectral weight [3.4].

An important issue when sum rules are applied is the proper choice of integration limit, i.e. the cutoff frequency ω_c. As it was already mentioned, sum rules exist for all spectral excitations, and it can be shown that:

$$\int_0^\infty\sigma_1(\omega)d\omega=\frac{\pi}{2}\sum_j\frac{(Q_j)^2}{M_j} \qquad (3.2.6)$$

where Q is charge and M is mass, holds for any kind of excitation in a solid when charge is involved.

5) $\sigma_1(\omega) \geq 0$ (3.2.7)

6) $\lim_{\omega \to 0} \sigma_1(\omega) = \sigma_{dc}$ (3.2.8)

3.3 Reflection and Transmission

Since the information about solid materials is very often obtained from reflectivity $R(\theta,\omega)$ and transmission $T(\theta,\omega)$ experiments, the propagation of electromagnetic waves across planar interfaces between materials with different optical properties has to be taken into account. This is done by considering continuous transitions of the tangential components of the electric - E and the magnetic - H fields (boundary conditions to the Maxwell equations), and the conservation of energy. The result relates the amplitudes of the incident electromagnetic wave with the transmitted and the reflected waves at the interface between two media ($\hat{N} \neq \hat{N}'$). At average angle of incidence θ, these relations are given by the Fresnel equations for the complex reflection $\hat{r}$, and transmission $\hat{t}$ (amplitude) coefficients. For perpendicular *s*-, and parallel *p*-, polarizations and semi-infinite media (i.e. no size effects are assumed, see also Fig 3.3.1), they read:

$$\hat{r}_s = \frac{E_{0r,s}}{E_{0i,s}} = \frac{\hat{N}\cos\theta - \hat{N}'\cos\theta'}{\hat{N}\cos\theta + \hat{N}'\cos\theta'} = \frac{\sin(\theta' - \theta)}{\sin(\theta + \theta')} \tag{3.3.1}$$

$$\hat{r}_p = \frac{E_{0r,p}}{E_{0i,p}} = \frac{\hat{N}'\cos\theta - \hat{N}\cos\theta'}{\hat{N}'\cos\theta + \hat{N}\cos\theta'} = \frac{\tan(\theta - \theta')}{\tan(\theta + \theta')}$$

$$\hat{t}_s = \frac{E_{0t,s}}{E_{0i,s}} = \frac{2\hat{N}\cos\theta}{\hat{N}\cos\theta + \hat{N}'\cos\theta'} = \frac{2\sin\theta'\cos\theta}{\sin(\theta + \theta')}$$

$$\hat{t}_p = \frac{E_{0t,p}}{E_{0i,p}} = \frac{2\hat{N}\cos\theta}{\hat{N}\cos\theta' + \hat{N}'\cos\theta} = \frac{2\sin\theta'\cos\theta}{\sin(\theta + \theta')\cos(\theta - \theta')}$$

In the general case, all quantities are of course complex: $\hat{N}$, $\hat{N}'$, $\hat{r} = r(\theta,\omega)e^{i\phi_r(\theta,\omega)}$, $\hat{t} = t(\theta,\omega)e^{i\phi_t(\theta,\omega)}$. The generalized Snell's law: $\hat{N}\sin\hat{\theta} = \hat{N}'\sin\hat{\theta}'$ requires complex quantities for the incidence/refraction angles too.

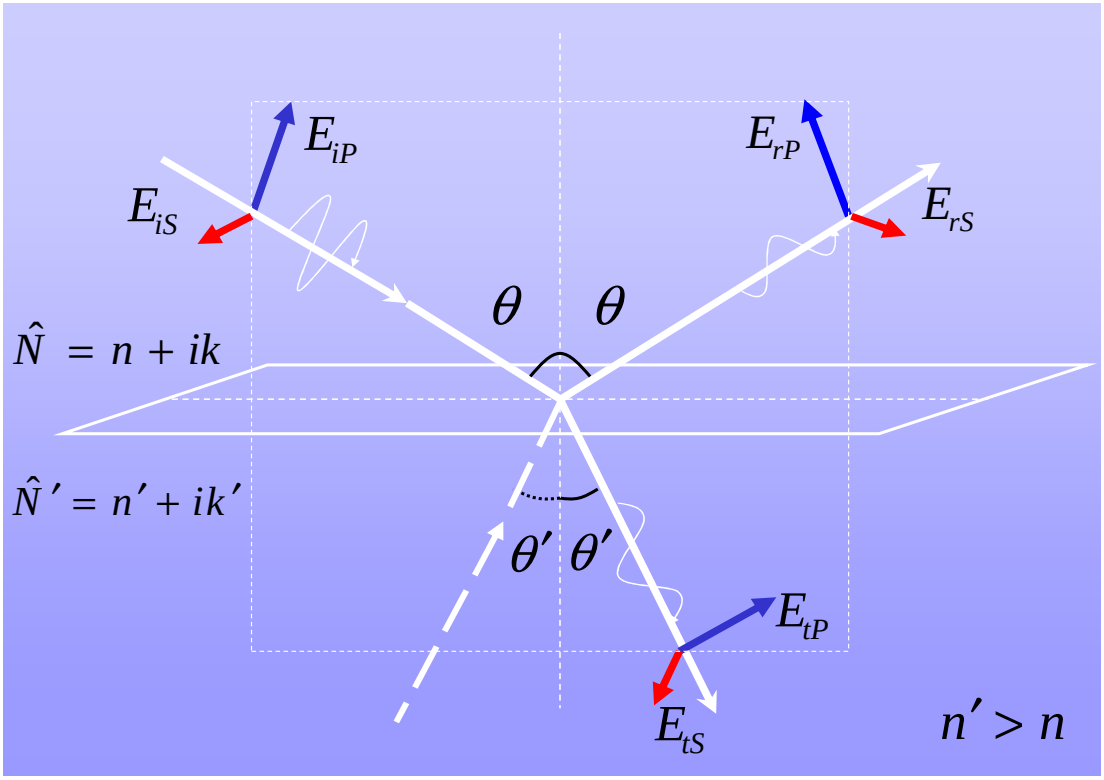

Figure 3.3.1 Plane of incidence. θ and θ' are angles of incidence (reflection) and refraction. The two media are characterized by complex refractive indices, $\hat{N}$ and $\hat{N}'$. The electric vectors of the incoming, the reflected and the transmitted (refracted) beams are E_i E_r and E_t , respectively. *S* (red) and *P* (blue) denote the different polarizations, perpendicular and coplanar with the plane of incidence.

The reflectivity *R*, is the squared absolute value (norm) of the complex field $\hat{r} = re^{i\phi_r}$:

$$R = |\hat{r}|^2 = \hat{r}\hat{r}^* \tag{3.3.2}$$

hence:

$$\hat{r} = \sqrt{R}e^{i\phi_r}$$

and for the transmission *T* :

$$T = \sqrt{\varepsilon_1}|\hat{t}|^2 = 1 - R \tag{3.3.3}$$

As R and T are defined as ratios of intensities on detecting, if not specially measured, the phase information ϕ is lost.

Figure 3.3.2 represents the angular dependence of R, for s and p polarizations: R_s and R_p.

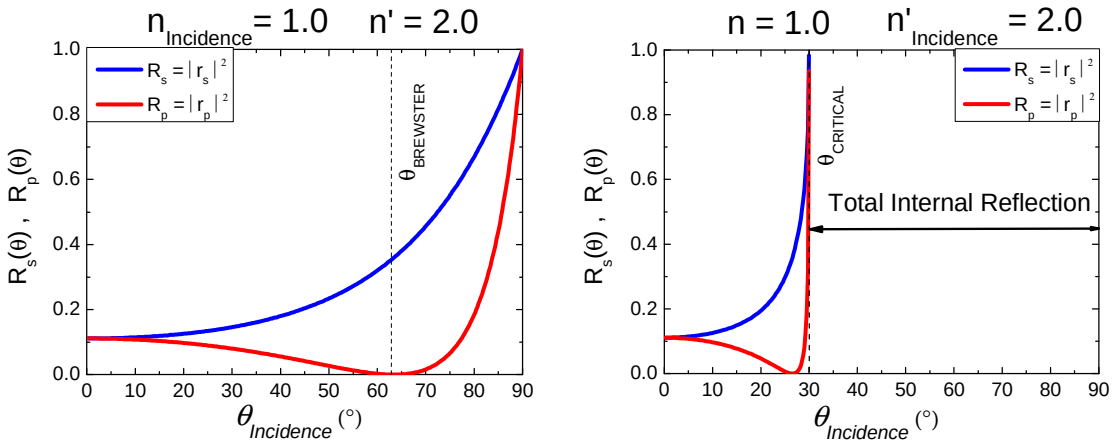

Figure 3.3.2 Angular dependence for R_s and R_p. For all $\theta, R_s \geq R_p$ and $R_p = 0$ at the Brewster angle: $\theta_B = \arctan(n'/n)$. At near-normal incidence angles: $\theta \to 0$, $R_s = R_p = R$.
left: $n_{Incidence} < n'$ **right:** $n'_{Incidence} > n$, and for angles equal, or bigger than the critical: $\theta_C = \arcsin(n'/n)$, $R_s = R_p = 1$.

Under normal incidence ($\theta \to 0$) conditions (often realized in experiments), the distinction between both polarizations (s and p) becomes irrelevant and the Fresnel expressions are reduced to:

$$\hat{r} = \frac{\hat{N} - \hat{N}'}{\hat{N} + \hat{N}'} \qquad \hat{t} = \frac{2\hat{N}}{\hat{N} + \hat{N}'} \tag{3.3.4}$$

with corresponding phase changes upon reflection / transmission:

$$\phi_r = \arctan\left(\frac{2(kn' - k'n)}{n^2 + k^2 - n'^2 - k'^2}\right) \qquad \phi_t = \arctan\left(\frac{n'k - nk'}{nn' - n^2 + kk' + k^2}\right) \tag{3.3.5}$$

Assuming now $\hat{N} = 1$ (air), and giving $\hat{N}'$ the notation $\hat{N}$, for the reflectivity and the transmission we obtain:

$$R = |\hat{r}|^2 = \left|\frac{1-\hat{N}}{1+\hat{N}}\right|^2 = \frac{(1-n)^2 + k^2}{(1+n)^2 + k^2} \qquad T = \frac{4n}{(1+n)^2 + k^2} \tag{3.3.6}$$

$$\phi_r = \arctan\left(\frac{-2k}{1-n^2-k^2}\right) \qquad \phi_t = \arctan\left(\frac{-k}{n+1}\right)$$

The amplitude $|\hat{r}| = \sqrt{R}$, of the complex field reflectivity (reflectance) $\hat{r} = \sqrt{R}e^{i\phi_r}$, and its phase ϕ_r, are Kramers-Kronig related via:

$$\phi_r(\omega) = \frac{\omega}{\pi}\int_0^\infty \frac{\ln\sqrt{R(\omega')} - \ln\sqrt{R(\omega)}}{\omega^2 - \omega'^2} d\omega' \tag{3.3.7}$$

which requires wide experimentally available $R(\omega)$, as well as extrapolations beyond the measured frequency interval. At high frequencies, power laws are commonly used: $R \approx \omega^{-p}$ with $0 \le p \le 4$. For the low frequency range: $R = const.$ if the material is an insulator, and the Hagen-Rubens relation $R = 1 - A\sqrt{\omega}$, in case of a metal.

Having obtained both parameters; $R(\omega)$ and $\phi_r(\omega)$, the conversion to $\hat{\varepsilon}(\omega)$ or $\hat{\sigma}(\omega)$ is trivial:

$$n = \frac{1-R}{1+R-2\sqrt{R}\cos\phi_r} \qquad k = \frac{2\sqrt{R}\sin\phi_r}{1+R-2\sqrt{R}\cos\phi_r} \tag{3.3.8}$$

$$\varepsilon_1 = n^2 - k^2 \qquad \varepsilon_2 = 2nk$$

$$\sigma_1 = \frac{\omega\varepsilon_2}{4\pi} \qquad \sigma_2 = \frac{\omega(1-\varepsilon_1)}{4\pi}$$

Another strategy, where no Kramers-Kronig procedure is necessary, is the modeling of $R(\omega)$ in terms of $\hat{\varepsilon}(\omega) = \varepsilon_1(\omega) + i\varepsilon_2(\omega)$ by introducing a set of Lorentzians, or other appropriate model dielectric function.

3.4 Ellipsometric parameters

From the Fresnel equations (3.3.1), it follows that upon reflection / transmission, the change of the electromagnetic wave parameters may differ significantly depending on the polarization state. In the very general case, the light is elliptically polarized, and the polarization ellipse can be fully defined by introducing two parameters (in case of reflection), (see Fig. 3.4.1):

$$\tan\Psi = \frac{|\hat{r}_p|}{|\hat{r}_s|} \qquad \Delta = \phi_p - \phi_s \tag{3.4.1}$$

i.e. the ratio and the difference of the wave parameters, amplitude and phase, for *s* and *p* polarization respectively. They are also called ellipsometry angles and constitute a complex quantity:

$$\hat{\rho} = \frac{\hat{r}_p}{\hat{r}_s} = \tan\Psi e^{i\Delta} \tag{3.4.2}$$

This expression is known as fundamental ellipsometry equation.

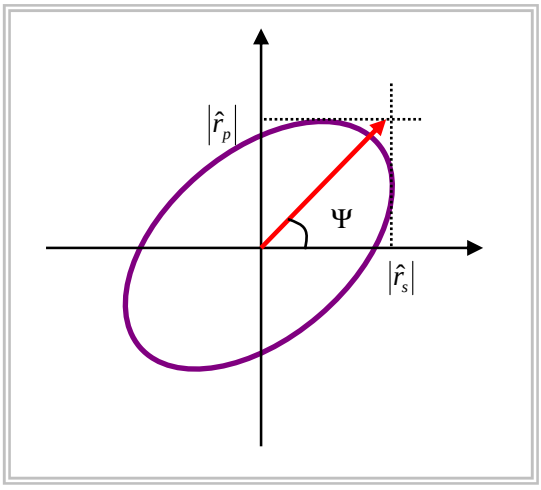

Figure 3.4.1 Polarization ellipse.

The reflectivity and the transmission can now be expressed as:

$$R = R_p \cos^2\Psi + R_s \sin^2\Psi \tag{3.4.3}$$

$$T = T_p \cos^2\Psi + T_s \sin^2\Psi$$

for which the energy conservation is also fulfilled:

$$R + T = 1 \tag{3.4.5}$$

3.5 Lorentz Oscillator and the Drude Model

The Lorentz Oscillator is a simple phenomenological and very useful dielectric function model for the response of a bound charge to an external harmonic electric field $E(t) = E_0 e^{-i\omega t}$. This model captures the main features of the electrodynamics of semiconductors and insulators such as phonon modes and interband transitions. Considering a damped harmonic oscillator with mass *m*, charge *e*, eigenfrequency ω_o and scattering rate $\gamma = 1/\tau$. The equation of motion reads:

$$m\ddot{r} + m\gamma\dot{r} + m\omega_o r = -eE_0 e^{-i\omega t} \tag{3.5.1}$$

with a harmonic solution $\hat{r} = r_0 e^{-i\omega t}$. Inserting back into the equation of motion we obtain:

$$\hat{r} = \frac{-eE_0 e^{-i\omega t}/m}{(\omega_o^2 - \omega^2) - i\omega\gamma} \tag{3.5.2}$$

The macroscopic polarizability for *n* oscillators with dipole moment $\hat{p} = -e\hat{r}$ per unit volume is $P = n\langle \hat{p} \rangle = \hat{\chi}_e E$, and since the dielectric constant is related to the electric susceptibility through $\hat{\varepsilon} = 1 + 4\pi\hat{\chi}_e$, we derive for the dielectric function:

$$\hat{\varepsilon}(\omega) = 1 + \frac{4\pi ne^2}{m}\frac{1}{(\omega_o^2 - \omega^2) - i\omega\gamma} = 1 + \frac{\omega_p^2}{(\omega_o^2 - \omega^2) - i\omega\gamma} \tag{3.5.3}$$

with real and imaginary parts:

$$\varepsilon_1(\omega) = 1 + \frac{\omega_p^2(\omega_0^2 - \omega^2)}{(\omega_0^2 - \omega^2)^2 + \omega^2\gamma^2} \qquad \varepsilon_2(\omega) = \frac{\omega_p^2\omega\gamma}{(\omega_0^2 - \omega^2)^2 + \omega^2\gamma^2}$$

Note that in the general case, the optical dielectric constant $\varepsilon(\omega \to \infty) = \varepsilon_\infty$, adds to the dielectric function too. Here, $\omega_p = (4\pi ne^2/m)^{1/2}$ is again, the plasma frequency that describes the oscillator strength. The expression (3.5.3) is also called Kramers-Heisenberg dielectric function. For the complex conductivity we have:

$$\hat{\sigma}(\omega) = \frac{\omega_p^2}{4\pi i}\frac{\omega}{(\omega_o^2 - \omega^2) + \omega\gamma} \tag{3.5.4}$$

$$\sigma_1(\omega) = \frac{\omega_p^2}{4\pi} + \frac{\omega^2\gamma}{(\omega_0^2 - \omega^2)^2 + \omega^2\gamma^2} \qquad \sigma_2(\omega) = -\frac{\omega_p^2}{4\pi}\frac{\omega(\omega_0^2 - \omega^2)}{(\omega_0^2 - \omega^2)^2 + \omega^2\gamma^2}$$

Figures 3.5.1 below visualise several optical quantities calculated according to the Lorentz oscillator model.

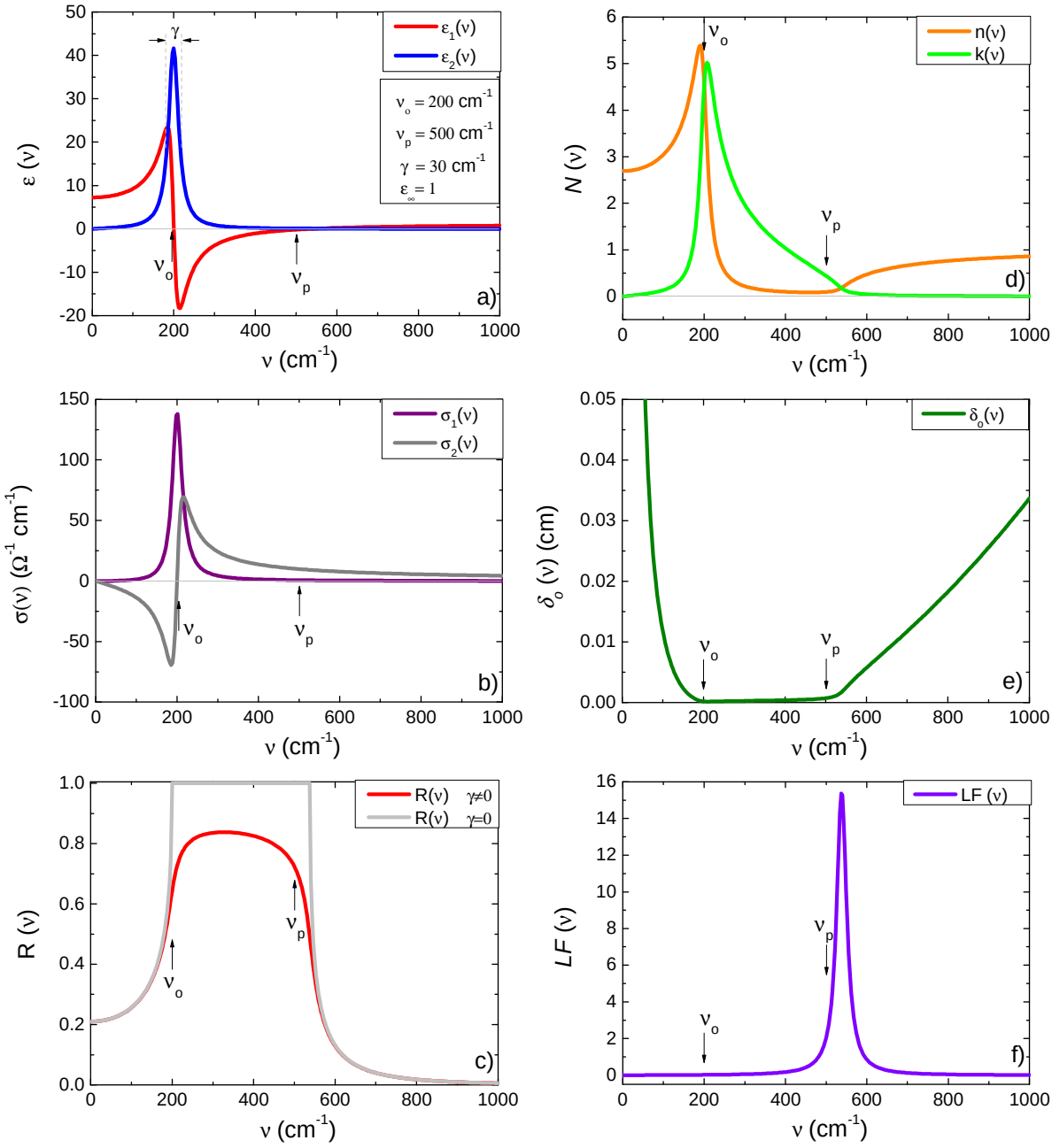

Figure 3.5.1 Spectral dependence (in $\nu=\omega/2\pi c$ units) for several optical quantities calculated by Lorentz oscillator model: **a)** real and imaginary part of the dielectric function $\varepsilon_1(\nu)$ and $\varepsilon_2(\nu)$ (the inset shows the input parameters) **b)** optical conductivity $\sigma_1(\nu)$ and $\sigma_2(\nu)$ **c)** reflectivity $R(\nu)$ **d)** refractive index and extinction coefficient $n(\nu)$ and $k(\nu)$ **e)** penetration depth $\delta_o(\nu)$ **f)** loss function $-\mathrm{Im}(1/\varepsilon(\nu))$.

Using the relations presented above, the implications of ε_1 and ε_2 on the optical constants and the reflectivity in the different spectral regions can be evaluated (see also figures 3.5.1):

Region 1 - Transparent, $\omega < (\omega_o - \gamma)$ (low frequency region)

This region is characterized by high transparency, little or no absorption, and small reflectivity. We can assume $k \to 0$ and: $\varepsilon_2(\omega) = 2nk = 0$, $\sigma_1(\omega) = 0$, $\varepsilon_1(\omega) = n^2 - k^2 > 1$ and $R(\omega) = (1 - n/1 + n)^2 = \left(1 - \sqrt{\varepsilon_1}/1 + \sqrt{\varepsilon_1}\right)^2$. The real part, $\varepsilon_1 = n^2$, tends to a constant value at $\varepsilon_1(\omega \to 0) = 1 + \omega_p^2 / \omega_o^2$.

Region 2 – Absorption, $(\omega_o - \gamma/2) < \omega < (\omega_o + \gamma/2)$

The light is strongly absorbed at frequencies around the oscillator eigenfrequency ω_o with maximum in $\sigma_1(\omega)$ and $\varepsilon_2(\omega)$. The width of this absorption range is determined by the scattering rate γ. The real part ε_1, crosses zero at ω_o with negative slope and becomes positive again at ω_p. In the frequency interval between the two extrema of the dielectric function, $\omega_{extr} = \omega_o \pm \gamma/2$, the dispersion is negative and it is called "region of anomalous dispersion". All optical quantities exhibit strong changes in this region except the loss function $LF = -\mathrm{Im}(1/\hat{\varepsilon})$.

Region 3 – Reflection, $\omega_o + \gamma < \omega < \omega_p$

This region is characterized by high and nearly constant reflectivity. The electromagnetic wave has enough energy and the excited charge behaves as if it was free. In the idealized case of $\gamma = 0$, the light is fully reflected (see figure 3.5.1 (c)). This is also seen from the penetration depth $\delta_o(\omega)$, which is greatly reduced in this particular region. The conductivity decreases as: $\sigma_1(\omega) \propto (\omega/\gamma)^{-2}$ and $\sigma_2(\omega) \propto (\omega/\gamma)^{-1}$. The dielectric function can be approximated: $\varepsilon_1(\omega) \approx 1 - \omega_p^2/\omega^2$ and $\varepsilon_2(\omega) \approx \omega_p^2 \gamma/\omega^3$. The extinction coefficient is larger than the refractive index, $k(\omega) > n(\omega)$.

Region 4 – Transparent, $\omega_p < \omega$

The onset of this region is defined by $\varepsilon_1(\omega) = 0$, i.e., at ω_p. $k(\omega)$ assumes small values again and the reflectivity is determined again mainly by $n(\omega)$. The optical dielectric

constant $\varepsilon_1(\omega \to \infty) = \varepsilon_\infty$, approaches unity from below and the reflectivity drops to zero above ω_p, subsequently, the material becomes transparent. The imaginary part of the loss function, $-\mathrm{Im}(1/\hat{\varepsilon})$, is sensitive to ω_p and has its maximum there.

The dielectric function for free carriers, the Drude dielectric function, is immediately obtained from equation (3.5.3), in the ($\omega_o \to 0$) limit:

$$\hat{\varepsilon}_D(\omega) = 1 - \frac{\omega_p^2}{\omega^2 - i\omega\gamma} \tag{3.5.5}$$

$$\varepsilon_1(\omega) = 1 - \frac{\omega_p^2}{\omega^2 + \gamma^2} \qquad \varepsilon_2(\omega) = \frac{\gamma}{\omega}\frac{\omega_p^2}{\omega^2 + \gamma^2}$$

And the optical conductivity is:

$$\hat{\sigma}(\omega) = \frac{\sigma_{dc}}{(1 - i\omega/\gamma)}, \quad \text{with} \quad \sigma_{dc} = \frac{ne^2}{m\gamma} = \frac{1}{4\pi}\frac{\omega_p^2}{\gamma} \tag{3.5.6}$$

$$\sigma_1(\omega) = \frac{\omega_p^2}{4\pi\gamma}\frac{1}{1 + \omega^2/\gamma^2} \qquad \sigma_2(\omega) = \frac{\omega_p^2}{4\pi\gamma}\frac{\omega/\gamma}{1 + \omega^2/\gamma^2}$$

In the case of free carriers response, three spectral regions can be distinguished:

1) Hagen-Rubens Regime (low frequency region), $\omega << \gamma$

In this region the optical properties are dictated by the *dc*-conductivity $\sigma_1(\omega) \approx \sigma_{dc}$, that is frequency independent and $\sigma_1(\omega) >> \sigma_2(\omega)$, while the imaginary part increases linearly with the frequency $\sigma_2(\omega) \approx \sigma_{dc}\omega/\gamma = \omega_p^2\omega/4\pi\gamma^2$. The real part of the dielectric function is large and negative, and can be simplified to a constant value $\varepsilon_1(\omega) = \varepsilon_1(0) \approx 1 - \omega_p^2/\gamma^2$, and for the imaginary part $\varepsilon_2(\omega) \approx 1 - \omega_p^2/\omega\gamma$. The analysis of the complex refractive index yields equal real and imaginary parts:

$$\hat{N} = n + ik \approx (i\varepsilon_2)^{1/2} \approx (\varepsilon_2/2)^{1/2}(1+i)$$

$$n(\omega) = k(\omega) = \left[\frac{\varepsilon_2(\omega)}{2}\right]^{1/2} = \left[\frac{2\pi\sigma_{dc}}{\omega}\right]^{1/2} >> 1$$

The reflectivity is given by the Hagen-Rubens relation:

$$R(\omega) \approx \frac{k(\omega)-1}{k(\omega)+1} \approx 1-\frac{2}{k(\omega)}+\frac{2}{(k(\omega))^2} \approx 1-\left(\frac{2\omega}{\pi\sigma_{dc}}\right)^{1/2} = 1-\left(\frac{8\omega\gamma}{\omega_p^2}\right)^{1/2}$$

The skin depth is determined by the *dc*-conductivity:

$$\delta_0 = \left(\frac{c^2}{2\pi\omega\sigma_{dc}}\right)^{1/2}$$

2) Relaxation Regime, $\gamma << \omega << \omega_p$

For frequencies between the scattering rate and the plasma frequency, the optical constants can be approximated as:

$$\sigma_1(\omega) \approx \frac{\sigma_{dc}}{(\omega/\gamma)^2} \qquad \sigma_2(\omega) \approx \frac{\sigma_{dc}}{(\omega/\gamma)}$$

$$\varepsilon_1(\omega) \approx 1-\omega_p^2/\omega^2 \qquad \varepsilon_2(\omega) \approx \omega_p^2\gamma/\omega^3$$

$$n(\omega) \approx \omega_p\gamma/2\omega^2 \qquad k(\omega) \approx \omega_p/\omega$$

$$1-R(\omega) \approx \frac{2\gamma}{\omega_p} = \frac{1}{(\pi\sigma_{dc}/\gamma)^{1/2}}$$

In the limit ($\gamma = 1/\tau = v_F/l \to 0$), the dielectric function is real and negative $\hat{\varepsilon} = \mathrm{Re}\,\hat{\varepsilon} \le 0$, and:

$$\varepsilon(\omega) = \varepsilon_\infty - \frac{\omega_p^2}{\omega^2}, \quad \text{with}\, \varepsilon_1(\omega \to \infty) = \varepsilon_\infty \tag{3.5.7}$$

The zeroes of this function (3.5.7), correspond to longitudinal plasma oscillation with frequency $\omega_{pl} = \omega_p/\sqrt{\varepsilon_\infty}$, or the screened plasma frequency. The refractive index has an imaginary part only $\hat{N} = \mathrm{Im}\,\hat{N} \approx ik$, and the reflectivity $R \to 1$, (see figures 3.5.1 & 2):

$$R = \frac{(1-n)^2+k^2}{(1+n)^2+k^2} \approx 1-\frac{2}{\omega_p/\gamma} \to 1$$

and again, the energy loss function peaks up at the plasma frequency.

3) Transparent Regime, $\omega >> \omega_p$

At the plasma frequency the reflectivity drops significantly, assumes minimal value, and the metal enters the transparent regime. The optical conductivity decrease monotonically with increasing frequency as: $\sigma_1(\omega) \propto \omega^{-2}$ and $\sigma_2(\omega) \propto \omega^{-1}$.

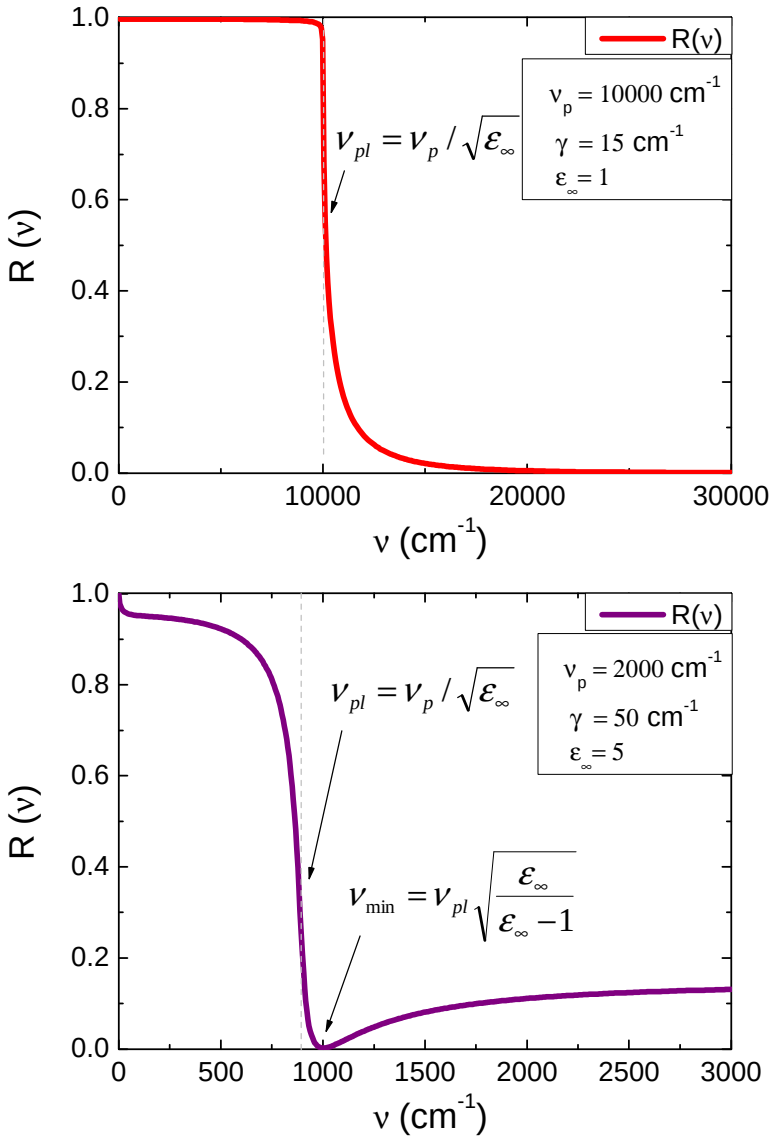

Figure 3.5.2 Calculated plasma reflection spectra with parameters typical for: a good metal (upper panel), and for semiconductors (lower panel). In good metals $\varepsilon_\infty \approx 1$ and $\omega_{pl} \approx \omega_p$, while in semiconductors $\varepsilon_\infty > 1$ and $\omega_{pl} < \omega_p$.

On modeling experimental data with Drude-Lorentz model one uses a sum of a Drude mode and an arbitrary number *j*, of different Lorentz oscillators (see [3.5]):

$$\hat{\varepsilon}(\omega) = \varepsilon_\infty - \frac{\omega_p^2}{\omega(\omega + i\gamma)} + \sum_j \frac{\omega_{pj}^2}{(\omega_{oj}^2 - \omega^2) - i\omega\gamma_j} \qquad (3.5.8)$$

with high-frequency contribution ε_∞. A useful relation in practical units is:

$$\sigma_{dc}\left[\Omega^{-1}cm^{-1}\right]=\frac{\omega_p^2\left[cm^{-1}\right]/\gamma\left[cm^{-1}\right]}{60} \tag{3.5.9}$$

Strictly speaking, the conditions at which the Drude formula (3.5.5), is valid are limited to low temperatures and frequencies. The scattering processes are quasielastic, with electrons having both initial and final state energies very close to the Fermi energy. At higher frequencies, low lying states of the system can be excited and inelastic scattering becomes possible. Thus, the constant, frequency independent scattering rate, will no longer represent correctly the physical situation. An example is the electron-phonon interaction where electrons can loose energy on creating phonons.

In this situation, frequency dependent scattering $\gamma(\omega)=1/\tau(\omega)$ is considered, with imaginary part interpreted as the electron band mass $m^*(\omega)/m$ modification, such that the casualty principle is satisfied (extended Drude formalism) [3.4]. Physically, the coupling of the excitation to the electrons changes both the real and the imaginary parts of the electron self energy and therefore, its mass and lifetime. Both quantities, $1/\tau(\omega)$ and $m^*(\omega)/m$, can be obtained from the complex optical conductivity as [3.6]:

$$1/\tau(\omega)=\frac{\omega_p^2}{4\pi}\mathrm{Re}\left[\frac{1}{\hat{\sigma}(\omega)}\right]=\frac{\omega_p^2}{4\pi}\frac{\sigma_1(\omega)}{\sigma_1^2(\omega)+\sigma_2^2(\omega)} \tag{3.5.9}$$

$$m^*(\omega)/m=\frac{\omega_p^2}{4\pi}\mathrm{Im}\left[\frac{1}{\hat{\sigma}(\omega)}\right]\frac{1}{\omega}=\frac{\omega_p^2}{4\pi}\frac{\sigma_2(\omega)}{\sigma_1^2(\omega)+\sigma_2^2(\omega)}\frac{1}{\omega} \tag{3.5.10}$$

Although originally introduced for systems with strong electron-phonon interaction in the limit (*T->0*), the extended Drude approach is believed to be valid in describing Fermi liquid coupling to bosonic excitations of any kind even at finite temperatures. It is widely applied for the analysis of elemental metals, transition metal compounds, high-T_c superconductors, and heavy-fermion systems, in which the effective mass enhancement is particularly strong.

3.6 Layered Systems

Various methods exist for calculation of the reflection *r* and the transmission *t* coefficients in the case of layered systems (Fig. 3.6.1), [3.7][3.8]. Assuming normal incidence ($\theta = 0$) conditions, the matrix approach is particularly straightforward. In this method each layer is characterized by a 2×2 matrix:

$$M_j = \begin{bmatrix} \cos\left(\frac{2\pi}{\lambda}\hat{N}_j d_j\right) & \frac{i}{\hat{N}_j}\sin\left(\frac{2\pi}{\lambda}\hat{N}_j d_j\right) \\ i\hat{N}_j \sin\left(\frac{2\pi}{\lambda}\hat{N}_j d_j\right) & \cos\left(\frac{2\pi}{\lambda}\hat{N}_j d_j\right) \end{bmatrix} \tag{3.6.1}$$

with $\hat{N}_j$ and d_j being the complex refractive index and thickness of layer *j*, respectively, and λ - the wavelength. The total multilayered system is given by the matrix product of all characteristic matrices:

$$M = \begin{bmatrix} a_{11} & a_{12} \\ a_{21} & a_{22} \end{bmatrix} = M_1 M_2 ... M_{m-1} \tag{3.6.2}$$

The reflection and transmission coefficients *r* and *t*, are then calculated from:

$$\begin{pmatrix} 1+r \\ \hat{N}_0(1-r) \end{pmatrix} = M \begin{pmatrix} t \\ \hat{N}_m t \end{pmatrix} \tag{3.6.3}$$

where different refractive indices $\hat{N}_0$ and $\hat{N}_m$, on either side of the multilayered system are considered. The expressions for *r* and *t* read:

$$r = \frac{-a_{21} + a_{11}\hat{N}_0 - a_{22}\hat{N}_m + a_{12}\hat{N}_0\hat{N}_m}{a_{21} + a_{11}\hat{N}_0 + a_{22}\hat{N}_m + a_{12}\hat{N}_0\hat{N}_m} \tag{3.6.4}$$

$$t = \frac{2\hat{N}_0}{a_{21} + a_{11}\hat{N}_0 + a_{22}\hat{N}_m + a_{12}\hat{N}_0\hat{N}_m} \tag{3.6.5}$$

Now, reflectivity *R* and transmission *T*, can be obtained from *r* and *t*, and correspond to:

$$R = |r|^2 \qquad T = \frac{\hat{N}_m}{\hat{N}_0}|t|^2 \tag{3.6.6}$$

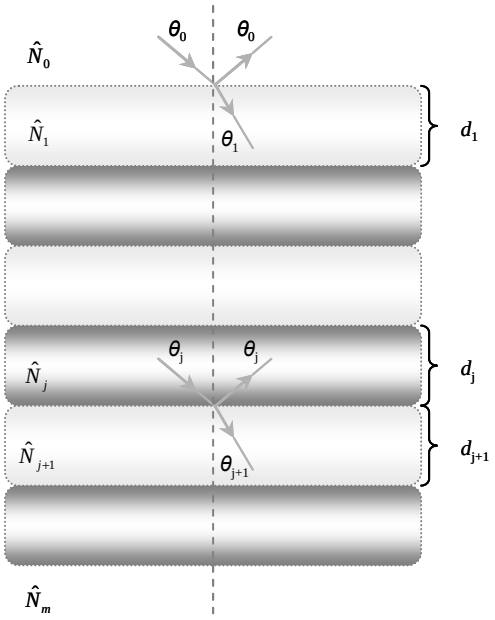

Figure 3.6.1 Schematic representation of a multilayer system with an arbitrary number of layers *j*, different complex optical parameters $\hat{N}_j$, and thicknesses d_j.

Chapter 4

Experimental Methods and Setup Description

The purpose of optical spectroscopy is to obtain the material's complex response as a function of frequency from about microwaves up to the UV, i.e. (10^{-1} ~ 10^{5} cm^{-1}). This is a very broad spectral range that requires the use of different spectroscopic techniques and hardware configurations in order to be covered. In the interval (10 ~ 10000 cm^{-1}), Fourier Transform (FT) spectrometers are widely employed. Various strategies of obtaining the dielectric function $\hat{\varepsilon}(\omega)$ and the optical conductivity $\hat{\sigma}(\omega)$ were discussed in (§1.2). Reflectance and spectroscopic ellipsometry are primary experimental tools utilized for this task. In the following, we introduce these two techniques along with the principle of FT spectroscopy. Further on, we describe the design of a new, home-built spectroscopy setup for near normal - incidence reflectance with high magnetic field and emphasize on several technical details and findings of critical importance to the normal operation of the apparatus.

4.1 Principle of Fourier Transform Spectroscopy

A Fourier Transform spectrometer is an adaption of the Michelson interferometer (Fig. 4.1.1). A collimated beam from a broadband light source is divided into two parts by a beamsplitter and sent to two mirrors, fixed and moving. These mirrors reflect the beams back to the beamsplitter where they recombine and interfere. The detected signal depends on the wavelength λ, of the light and the optical path difference between the two arms of the spectrometer $\delta = c\tau$ (c is the speed of light and τ is the time lag), introduced by the moving mirror. If δ is an integer multiple of the wavelengths $\delta = n\lambda$, $n = 1,2,3...$, a

constructive interference occurs and for $\delta = (2n+1)\lambda/2$, the beams interfere destructively.

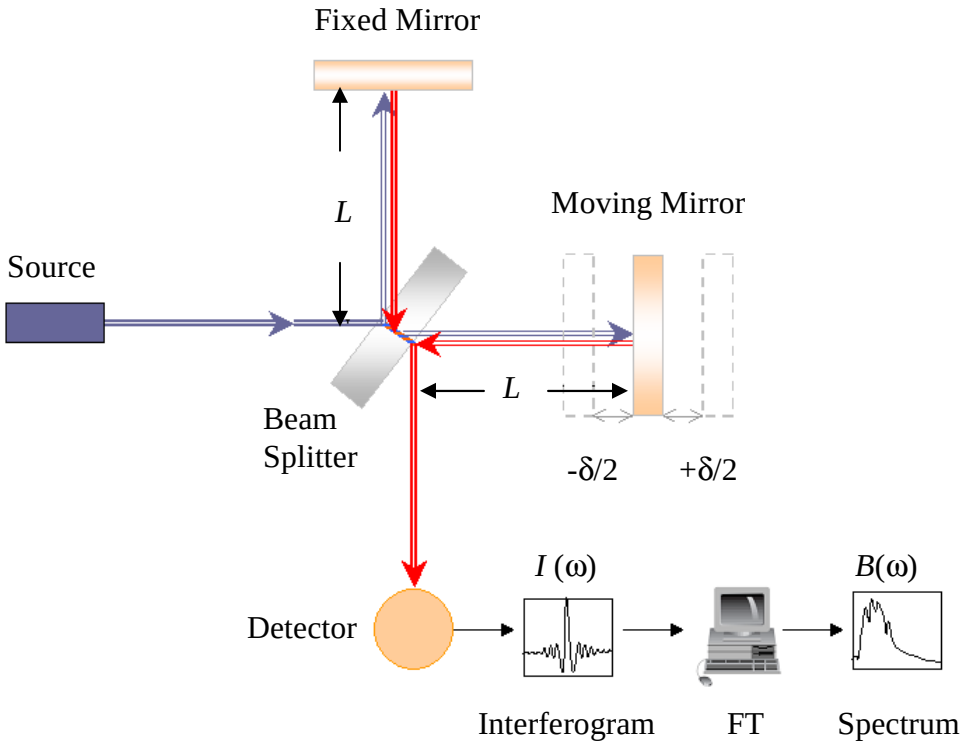

Figure 4.1.1 Sketch of a Fourier Transform (FT) spectrometer. The principle is based on the Michelson Interferometer.

Hence, the FT spectrometer measures an interferogram [4.1]:

$$I_Q(t) \propto [I_0 + I(\tau)] \tag{4.1.1}$$

Note that the integration time of the spectrometer is usually much bigger than the light's coherence time. The interferogram consists of a time averaged stationary part:

$$I_0 = \langle E^2(t-\tau) \rangle = \langle E^2(t) \rangle \tag{4.1.2}$$

and a part that depends on the time lag τ, (the autocorrelation function):

$$I(\tau) = \langle E(t)E(t-\tau) \rangle \tag{4.1.3}$$

Now, according to the Wiener-Khinchin theorem the autocorrelation function of a random stationary process can be expressed as a FT integral:

$$I(\tau) = \int_{-\infty}^{+\infty} B'(\omega) e^{i\omega\tau} d\omega \tag{4.1.4}$$

An inverse FT yields:

$$B'(\omega) = \frac{1}{2\pi}\int_{-\infty}^{+\infty} I(\tau)e^{-i\omega\tau}d\tau \qquad (4.1.5)$$

If $E(t)$ is a real function, and $I(\tau)$ and $B'(\omega)$ are even, equation (4.1.5) takes the form:

$$B(\omega) = 2B'(\omega) = \frac{1}{\pi}\int_{0}^{+\infty} I(\tau)\cos(\omega\tau)d\tau \qquad (4.1.6)$$

and the spectral density $B(\omega)$, i.e. the spectrum, is recovered.

The integral (4.1.6) is infinite, but for obvious reasons the interferogram is measured only over a finite mirror shift $\delta_{\max}$ (in FT spectrometers it is $\delta_{\max}$ that determines the maximal spectral resolution $\Delta\nu = 1/\delta_{\max}$). Special apodization functions are then applied so as the interferogram is properly truncated.

4.2 Reflectance Measurements

Near-normal incidence (small θ) reflectance measurements are straightforward and performed in a simple configuration as shown on (Fig. 4.2.1).

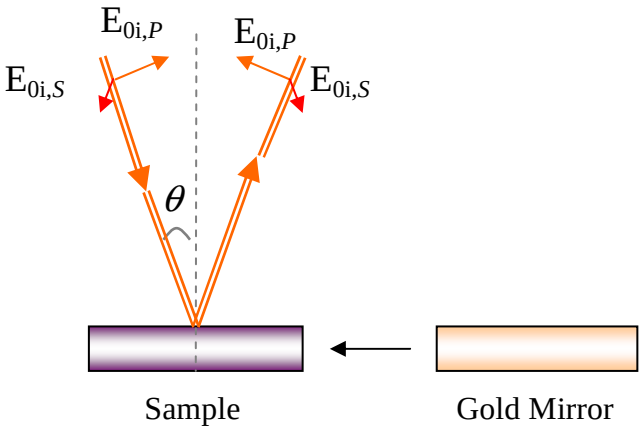

$$R^{Sample}(\omega) = \frac{|E_{0r}|^2}{|E_{0i}|^2} = |\hat{r}|^2 = \frac{I_r(\omega)}{I_i(\omega)} = \frac{I_r^{Sample}(\omega)}{I_r^{GoldMirror}(\omega)}$$

Figure 4.2.1 Typical near-normal reflectance measurement configuration. θ is the angle of incidence. As a reference, gold or aluminum mirrors are most commonly used. Depending on the spectral range, wire grid or prism polarizer can be used for selecting the polarization: *s*, *p*.

While the simplicity of this method is a strong advantage, there are however, some significant shortcomings: 1) on performing a reflectance measurement the reflected power is what is normally detected, hence the phase information is lost by taking the norm of the complex amplitude $\left|\hat{\tilde{E}}\right|^2 = E_0^2$. Subsequently only the norm (the reflectivity) is acquired and a Kramers-Kronig analysis or model fit of the reflectivity spectra is needed 2) the sample / mirror ratio could give a big contribution to experimental error in reflectance experiments. Selecting a proper reference and conditions for it, such that it imitates the sample characteristics (shape and roughness), can be a rather problematic task especially for small and irregular samples.

4.3 Reflectance with High Magnetic Field

Experimental setup for near-normal infrared reflectance measurements in high magnetic fields was assembled at Max Planck Institute for Solid State Research, by the author of this thesis. It currently operates in the far infrared (FIR) (30-700cm^{-1}) but can be easily configured to cover the entire infrared range. It consists of two major parts: a conventional Fourier Transform (FT) Bruker IFS 66v/S infrared spectrometer and a superconducting (SC) 8 Tesla split-coil magnet from Oxford Instruments. The reflectance optics unit and the support systems were designed by our group engineers and manufactured in the institute's workshop. An overview picture and a simplified scheme of the apparatus are given in (Figs 4.3.1, 2 & 3). A standard configuration in the FIR range (30-700 cm^{-1}) includes:

Sources: Hg-arc lamp (30-700 cm^{-1}), Globar (370-7500 cm^{-1})

Beamsplitter: 6 μm Mylar/Ge multilayer

Bolometer detector: Si, Liquid *He* (L*He*) cooled, at 4.2K, and pumped, at 1.8K from Infrared Laboratories, Arizona USA

Spectroscopic windows: 0.6 mm polyethylene for the magnet cryostat, 100 μm polypropylene or 1.3 mm, 5º - wedged, CVD diamond windows glued to titanium rings for the sample compartment - variable temperature insert (VTI) (Fig. 4.3.3).

Optics: A home-built optics system for near-normal ($\theta = 4°$) reflectance is utilized, (Fig. 4.3.3). Special care must be taken as it is situated in close proximity to the magnet. This requires the use of non-magnetic materials and parts like brass, aluminum and plastics, ceramic motor units if needed etc. Some types of stainless steel are also non-magnetic but must be carefully checked before use.

Sample compartment: Liquid *He* - bath, variable temperature insert (VTI), (1.6-300K).

Support systems: (Fig. 4.3.1): (1) Optical table with active high-pressure dampers (2) Hydraulic lifting system for the magnet maintenance (3) Rotating support for the magnet (allows in-plane and out-of-plane configuration measurements) (4) Silencer box with temperature controllers for the fore-vacuum pumps. In addition, all pumps are equipped with non-return valves (prevent the systems from air backflow in case of electricity shut down).

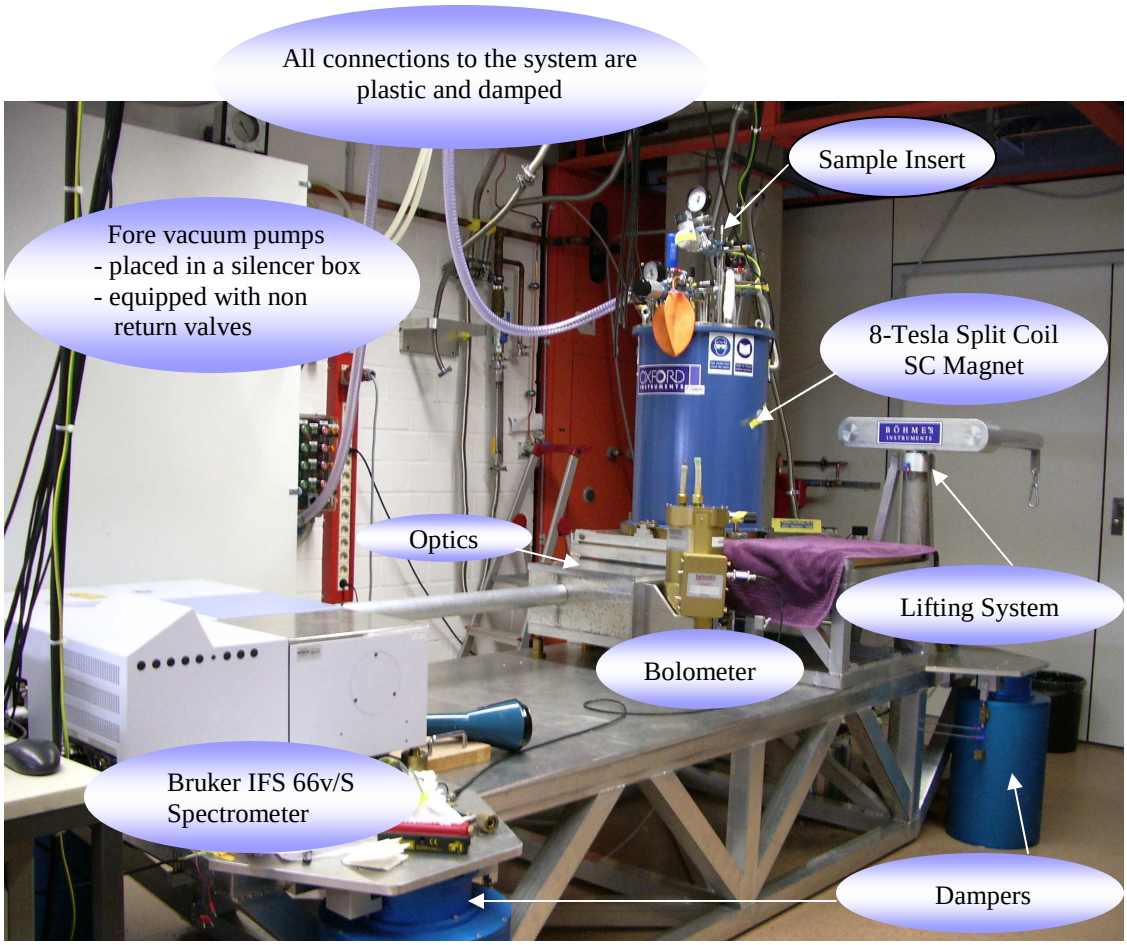

Figure 4.3.1 Reflectance with high magnetic field - an overview of the apparatus.

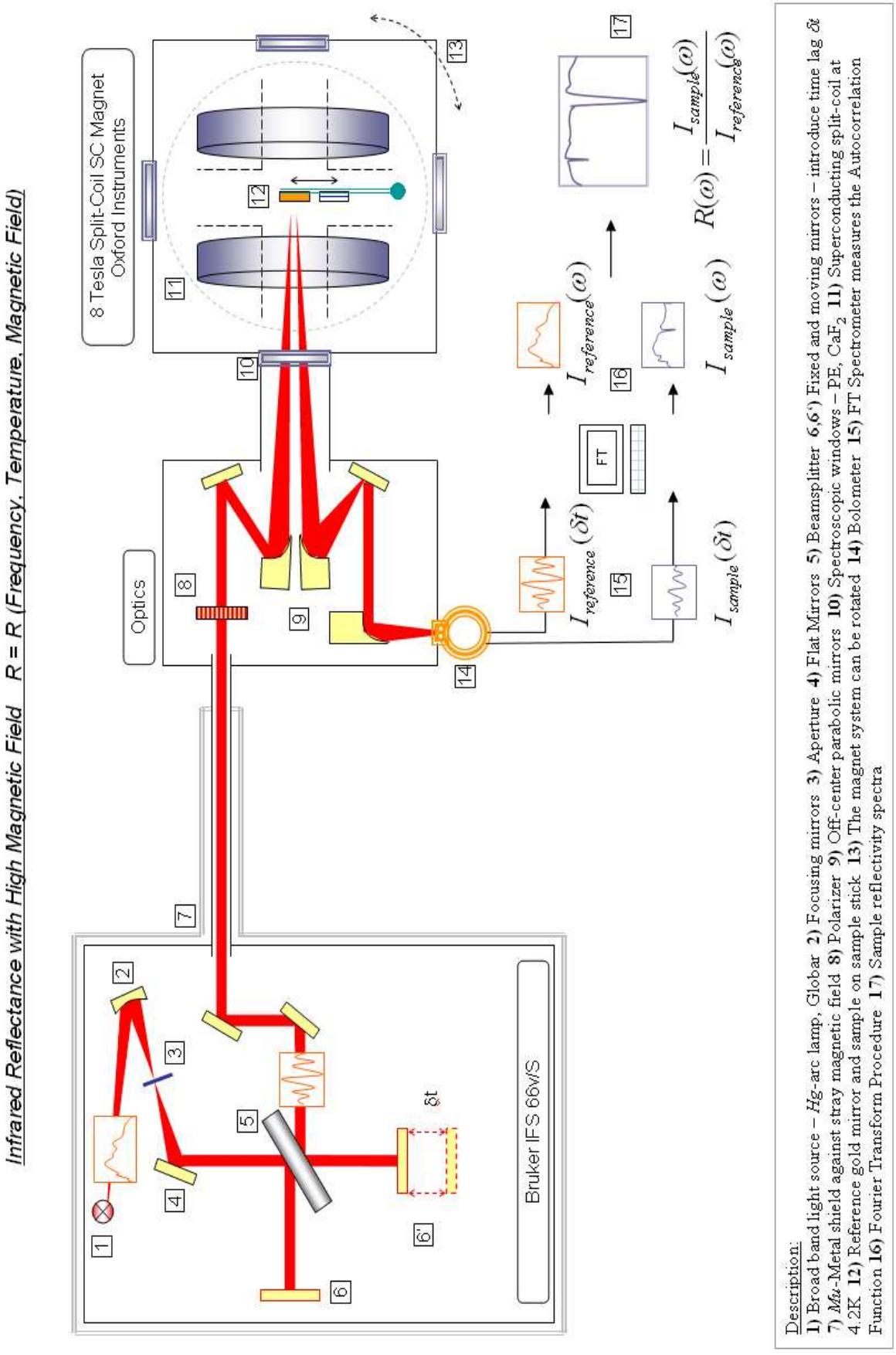

Figure 4.3.2 Reflectance with high magnetic field, a simplified scheme.

Reflectance optics unit

Figure 4.3.3 shows a top view and a detailed description of the optics.

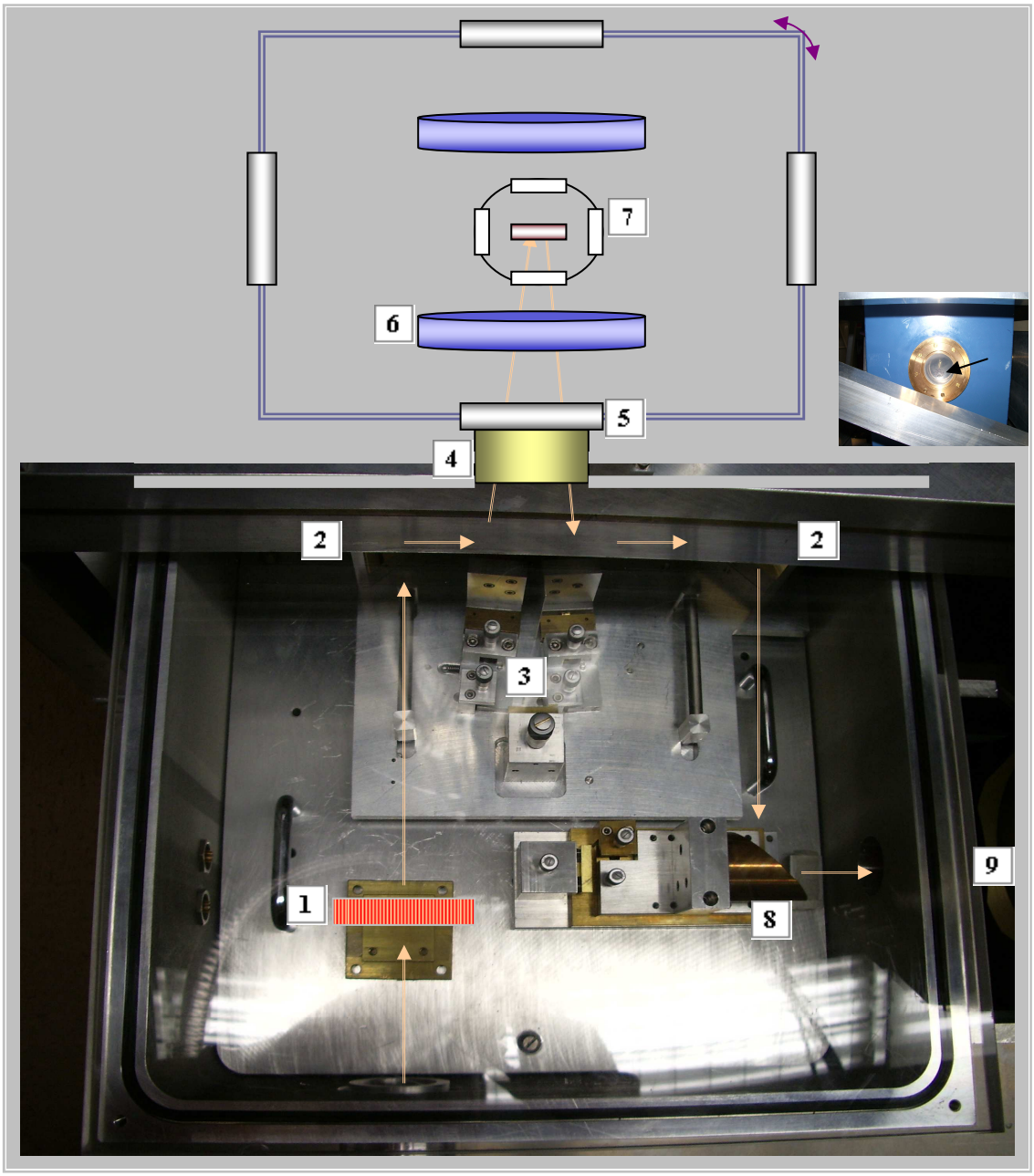

Figure 4.3.3 Optics system for near-normal (θ=4^{o}) incidence reflectance with magnetic field in the infrared range: 1) wire grid polarizer 2) flat mirrors 3) focusing mirrors 4) flange to the magnet compartment 5) polyethylene spectroscopic windows (highly hygroscopic materials are not appropriate as water tends to condense, see the inset) 6) SC coils at 4.2K 7) polypropylene or wedged diamond spectroscopic windows on the variable temperature insert (VTI) (with sample inside) 8) focusing mirror 9) bolometer detector

Sample stick and sample holder

The sample stick serves to insert the sample holder with the sample and the reference into the magnet sample compartment (the VTI) (Fig. 4.3.4 a & b). Furthermore, it functions as a sample positioning device and heater, and is indeed, a very important element. The accuracy of the reflectance measurements strongly depend on this part, therefore special attention has to be paid to its positioning system (including the adjusting screws) and the material the sample stick is made of. Few things can be critical here if high magnetic fields are to be applied and a wide temperature range studied:

1) First of all, measurements in high magnetic fields require no trace of magnetic materials, or whatsoever magnetic impurities, on any part of the sample stick, especially those entering the active magnet area. Magnetic inclusions in the stick's body lead to its bending on sweeping the magnetic field. Due to obvious reasons, this makes a comparative optical measurement impossible. We found out that this is the case with the sample stick provided by Oxford Instruments (Fig. 4.3.4 a), along with the 8-Tesla SC magnet. Currently, we use a home-built stick from fiberglass material.

2) The sample stick has to be properly positioned inside the VTI. If the sample stick is not properly attached (axial) to the positioning system and subsequently inserted into the magnet, a tilt angle may be present that would set different conditions for the sample and the reference with respect to the incident beam. Now if the beam is modulated, spurious interference fringes will appear in the spectra.

3) One should bear in mind that the sample stick length variation upon cooling/warming up is proportional to its absolute length. Therefore it requires regular position corrections on performing temperature dependence measurement. Along with the magnetic inclusions issue discussed above, this could be an obstacle if, for example, an ellipsometry measurement is intended where the angle of incidence must be kept fixed to a very high precision.

The sample holder is also a critical part. The important points concerning the sample holder are summarized in (Fig. 4.3.4 b).

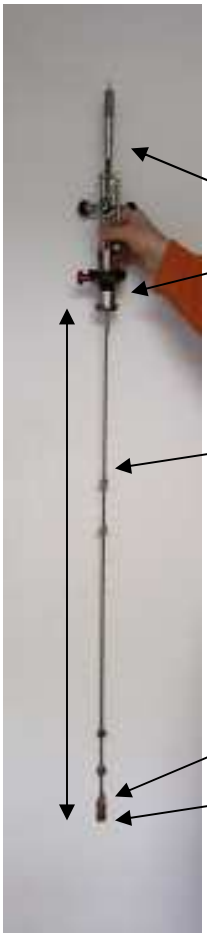

a)

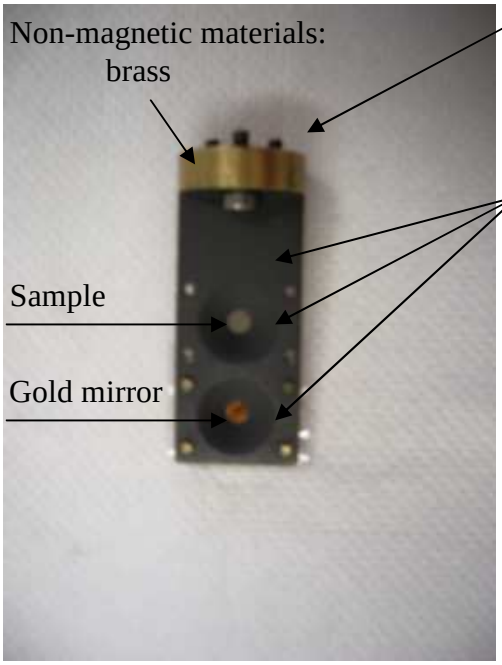

b)

Figure 4.3.4 a) sample stick **b)** sample holder with sample and mirror mounted.

Shielding from stray magnetic fields

Among the problems coming from the use of high magnetic fields is the stray magnetic field. Most magnet systems do not come shielded and if the stray field causes problems, measures must be taken. In case of a magnet system used for a wide range optical spectroscopy, where the light beam from an external source is required to enter the sample compartment, a complete shielding is even impossible. Normally, the stray field strength is not high (~80 Gauss at 8 Tesla and 2 meters away) and it decays rapidly, ($\propto r^{-3}$), with the distance. Even though weak, it can be quite enough to seriously interfere the normal operation of a large group of sensitive elements and devices whose work is based on electrical currents. Examples are: all charged gas light sources, detectors, sensors and gauges, and magnetic memory devices. If such a device is situated nearby the magnet and cannot be placed away, passive shielding could be an option. Introducing shielding materials around a magnet system is a nontrivial task. It is good to keep in mind that; 1) the better is the shielding material the more it attracts the magnetic field lines – that's why the design and the proper choice of a shielding material is crucial here 2) if the distance to the magnet is short and the amount of shielding material used is large, the magnetic field forces become significant. That, of course, will produce tension on both, the magnet and the object shielded, which is a potential danger (it may break the neck that carries the superconducting coils!). In addition, the magnetic field lines inside the sample area may bend and no longer be homogeneous which can be crucial in some cases. During the assembling of our reflectance setup we found that the normal operation of the Hg-arc lamp used as FIR source, even though placed at distance of 1,5 meters away from the magnet, is seriously impeded by the stray magnetic field. The effect induces a substantial change of the output signal on sweeping the magnetic field. The detected intensity increases or decreases depending on the magnetic field polarity. The spectra recorded showed that this effect is also frequency dependent. There are also some indications that the electronics inside the spectrometer is disturbed too. Possible solutions of this problem are to either place the spectrometer far away from the magnet system or to shield it. The former is not favorable as it reduces the beam intensity, which is highly undesirable. To ensure normal operation of the spectrometer we use a specially designed,

3.14 mm, *Mu*-metal (nickel-iron alloy: 75% nickel, 15% iron, plus copper and molybdenum, with very high magnetic permeability) shielding enclosure from Amuneal Manufacturing Corp. Philadelphia, USA, (Fig. 4.3.5). It is worth noting that the Si-bolometer was also carefully tested and did not show any deviation from its normal performance.

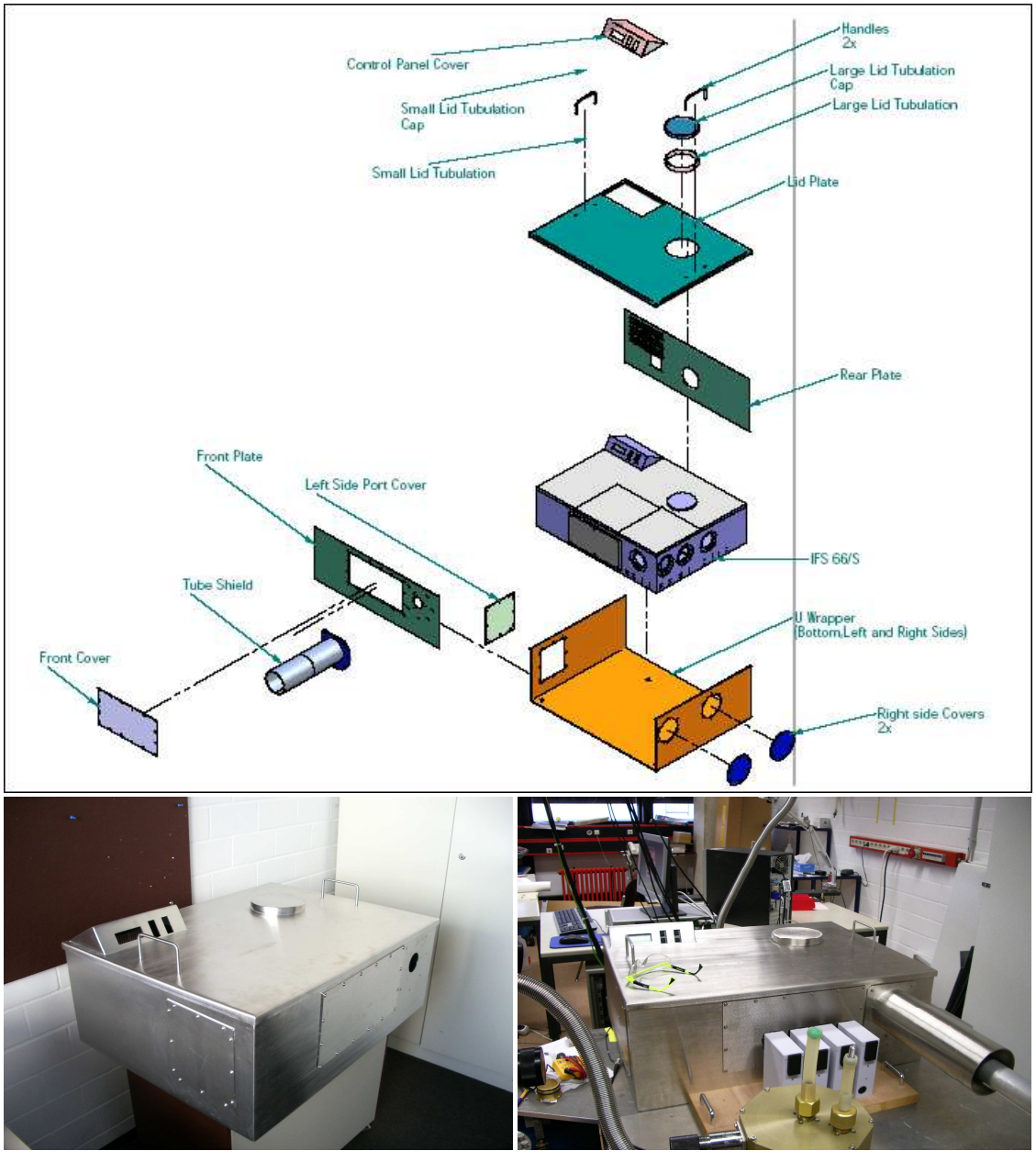

Figure 4.3.5 *Mu*-metal (3.14 mm) shielding enclosure for infrared Bruker spectrometer IFS 66v/S.

4.4 Spectroscopic Ellipsometry in the Infrared Range

The spectroscopic ellipsometry overcomes many of the disadvantages of reflectance measurements. The basis of ellipsometry is the measurement of the change of light polarization upon non-normal reflection. The Fresnel equations (3.3.1) imply that the two components of the electric field, *s* and *p*, experience different attenuation and phase shift upon reflection even for isotropic media. This difference becomes irrelevant on approaching normal incidence conditions. Ellipsometry measures the complex ratio of both reflection coefficients, $\hat{r}_p$ and $\hat{r}_s$, and that concludes the power of this technique (see also § 3.4):

$$\hat{\rho} = \frac{\hat{r}_p}{\hat{r}_s} = \frac{\left|\hat{r}_p\right|}{\left|\hat{r}_s\right|} e^{i\left(\phi_p - \phi_s\right)} = \tan\Psi e^{i\Delta} \qquad (4.4.1)$$

Figure 4.4.1 outlines the principle of spectroscopic ellipsometry.

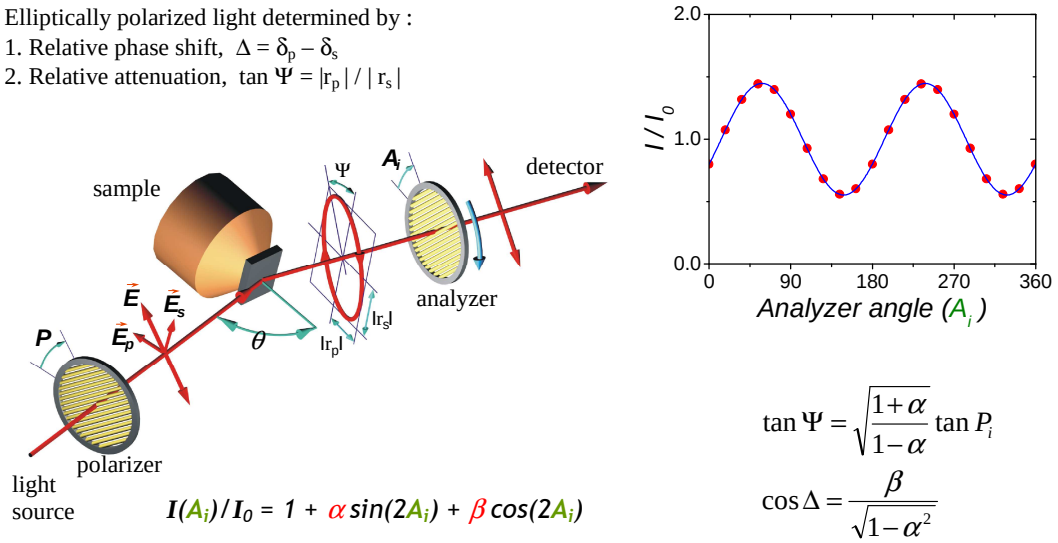

Figure 4.4.1 Sketch of spectroscopic ellipsometry setup in the infrared. *P* – polarizer angle (in this particular arrangement it is kept fixed), A_i – analyzer angle, θ - angle of incidence, α,β - sine and cosine Fourier coefficients.

The incident light is linearly polarized with a wire grid polarizer. In general, after being reflected, the light is elliptically polarized. The polarization ellipse is then probed with a second polarizer (analyzer). In practice, one measures the intensity of the reflected light at different analyzer angles, A_i, with respect to the plane of incidence (the harmonic function in the inset of Fig. 4.4.1):

$$I(A_i)/I_0 = 1 + \alpha \sin(2A_i) + \beta \cos(2A_i) \tag{4.4.2}$$

A linear least squares fit procedure is subsequently applied and the Fourier coefficients, α and β, determined for all frequencies. The ellipsometry angles, Ψ and Δ, are then calculated from [4.2]:

$$\tan\Psi = \tan P\sqrt{\frac{1+\alpha}{1-\alpha}} \qquad \cos\Delta = \sqrt{\frac{\beta}{1-\alpha^2}} \tag{4.4.3}$$

With the azimuthal angle of the ellipse, $0 \le \Psi \le 90$, and its ellipticity, $0 \le \Delta \le 180$, two independent quantities are experimentally determined. From those the complex dielectric function $\hat{\varepsilon}$ can be obtained. For a semi-infinite sample and a given angle of incidence, θ, the complex dielectric function is:

$$\hat{\varepsilon} = \sin^2(\theta) + \sin^2(\theta)\tan^2(\theta)\left(\frac{1+\hat{\rho}}{1-\hat{\rho}}\right)^2 \tag{4.4.4}$$

As the angle of incidence enters the equation (4.4.4) an accurate ellipsometric experiment requires its value be known with a high precision. Therefore the light beam has to be collimated in order to avoid any uncertainties in θ. This condition is a serious problem especially in the FIR range where intense light sources are not conventionally available. The use of synchrotron light source allows high accuracy measurements to be performed even on millimeter sized samples (Fig. 4.4.2), [4.3][4.4]. Typically the synchrotron light sources are about three orders of magnitude more brilliant (photons per solid angle per second) than conventional sources. Due to relativistic effects (v_{el}/c~0.99), the synchrotron radiation is emitted into a very narrow cone with small angular width of about: $\Delta\theta \approx (\pm 1^\circ)$. Furthermore, the dielectric function can be most accurately determined by ellipsometry if the angle of incidence θ is chosen such that $\Delta \approx \pi/2$. For a non-absorbing material ($k \to 0$), the condition $\Delta \approx \pi/2$ is fulfilled at the Brewster angle θ_B, $\tan\theta_B = n$. For an absorbing material ($k \neq 0$) it is fulfilled at the so-called pseudo

Brewster angle $\langle\theta_B\rangle$. For metallic samples, $\langle\theta_B\rangle$ is close to 90° in the FIR range. Grazing incidence conditions are therefore required, which lead to diffraction effects and enhanced surface sensitivity. Great care must be taken on performing experiments, and corrections for diffraction must be applied to the spectra in this case. An additional requirement that concerns the polarizer angle, P, is $|\tan P| \approx \tan\Psi$. This is easily met by tuning the polarizer angle. Another important point is that in case of anisotropic material only the so-called pseudo-dielectric function, $\langle\varepsilon\rangle$, is obtained by a single ellipsometry measurement. Depending on the crystal symmetry, all possible scattering geometries need to be measured and thus all components of $\langle\varepsilon\rangle$ obtained. The true dielectric function is then calculated by numerical procedures. Accurate ellipsometric measurements require also a high degree of polarization. Therefore the polarizers must be of very high quality. In the FIR range, (20cm^{-1} –700cm^{-1}), wire grid polarizers are in use and for the MIR range (400cm^{-1} – 4000cm^{-1}), wedged KRS-5. As for ellipsometry, the well-defined polarization state is crucial; all other optical elements like cryostat windows, bolometer windows, filters and etc. should alter the beam polarization as weakly as possible. Mylar foil (~3μm), CVD diamond, KBr and polyethylene are tested to give minimal effects.

Figure 4.4.2 Infrared spectroscopic ellipsometry setup installed at ANKA beamline, Forschungs Zentrum Karlsruhe. In the extreme FIR – FIR reagion synchrotron radiation is used. For the MIR range cnventional light sources are available. (LS) – the beam line, (IFS) – infrared FT spectrometer, (P) polarizer, (S) – sample cryostat, (A) – analyzer, (D) – LHe bolometer detector.

Chapter 5

$CaMnO_3$ / $CaRuO_3$ Superlattice System

In this chapter, a spectroscopic study of the perovskite superlattice (SL) system $CaMnO_3$/$CaRuO_3$ (CMO/CRO) is presented. It is a prototype system that combines an electron leakage from the paramagnetic metallic $CaRuO_3$ towards the adjacent layers of antiferromagnetic insulating $CaMnO_3$, to create new interface states and magnetoresistive properties intrinsically connected to ferromagnetic (FM) / antiferromagnetic (AFM) competing interactions.

5.1 Spectroscopic Study of $CaMnO_3$ / $CaRuO_3$ Superlattices

In the following study we make use of several spectroscopic probes of $CaMnO_3$ / $CaRuO_3$ superlattices including x-ray absorption spectroscopy (XAS), x-ray magnetic circular dichroism (XCMD), x-ray resonant magnetic scattering (XRMS) and far-infrared (FIR) spectral ellipsometry in order to develop a comprehensive experimental description of the charge transport properties as well as the valence state and magnetic polarization of Ru and Mn atoms near the interface [5.1]. FIR reflectance in high magnetic fields and complementary *dc*-transport probe were also applied to further elucidate spin-dependent charge transport peculiarities of the system below its magnetic transition temperature.

A problem of fundamental interest is the interface between a correlated metal and a Mott insulator, two of the most extensively investigated ground states of bulk transition metal oxides. The interface between the weakly correlated paramagnetic metal $CaRuO_3$ and the antiferromagnetic insulator $CaMnO_3$ is emerging as a model system where these issues can be explored experimentally without interference from interface polarity, incipient ferroelectricity, extensive disorder, misfit strain or orbital degeneracy.

5.1.1 Bulk Properties of $CaMnO_3$ and $CaRuO_3$

$CaMnO_3$ crystallizes in the perovskite structure (ABO_3), with small orthorhombic distortion, in the space group P_{nma} (Fig. 5.1.1.1). The compound is an insulator with nominal ionic picture $Ca^{2+}Mn^{4+}O_2^{2-}$, i.e. fully occupied t_{2g} states, ($t_{2g}{}^3{}_\uparrow\ e_g{}^0$), in high-spin configuration, S=3/2. An energy gap of ~0.4eV separates them from the empty e_g states. The Mn spins order antiferromagnetically, in all nearest-neighbour directions (G-type), below T_N~125K. The magnetic moment is slightly reduced from the spin-only value for Mn^{4+} ion, due to hybridization with O 2*p* states, and is ~ 2.65μ_B / Mn [5.2][5.3].

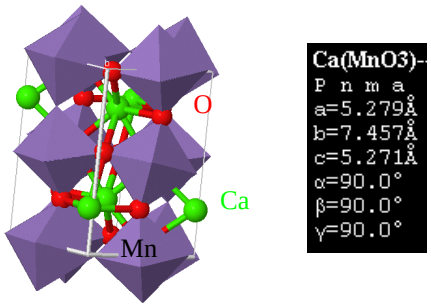

Figure 5.1.1.1 Crystal structure and lattice parameters of $CaMnO_3$. The pseudocubic cell parameter is a_c=3.73Å [5.4].

Theoretical studies of $CaMnO_3$ also find a G-type AF ground state and values for the magnetic moment in full agreement with the experiment [5.5][5.6]. X-ray photoemission and x-ray absorption spectroscopy studies on $CaMnO_x$ with $2.66 < x < 3.00$, showed that the main separations between the Mn 3*d*-bands closest to the Fermi level is of the order of 3eV and also that the band gaps are of the charge-transfer type ($U > \Delta$) [5.7][5.8].

The nature of the ground state of $CaRuO_3$ is on the other hand still elusive. Ruthenates have been a subject of extensive studies motivated mainly by the discovery of unconventional superconductivity in layered Sr_2RuO_4 [5.9]. $CaRuO_3$ and the isostructural $SrRuO_3$, are perovskites (ABO_3) with considerable $GdFeO_3$-type distortion resulting in an orthorhombic structure. The RuO_6 octahedra are connected via corner sharing as shown in figure 5.1.1.2. The conduction electrons move through this RuO_6 network and hence determine various electronic properties. The electronic configuration in the 4*d*-shell is

($t_{2g}^{3}\uparrow\, t_{2g}^{1}\downarrow$), in the low-spin state S=1. Optical spectroscopy and *dc*-transport studies report unusual temperature and frequency scaling in these ruthenates, $\rho(T) \sim T^{1/2}$ and $\sigma_1(\omega) \sim 1/\omega^{1/2}$, which have been interpreted as evidence of non-Fermi liquid behavior (NFL) [5.10].

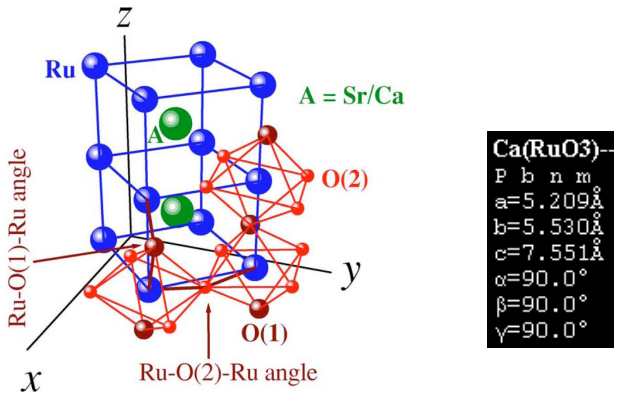

Figure 5.1.1.2 left: Schematic of the crystal structure of $SrRuO_3$ and $CaRuO_3$. **right:** Lattice parameters for $CaRuO_3$. The pseudocubic cell parameter, a_c=3.84Å [5.11][5.12].

While $SrRuO_3$ exhibits long-range ferromagnetic order below T_c~160K, $CaRuO_3$ remains paramagnetic at all temperatures. Some theoretical studies correctly find absence of long range magnetic order but suggest however, that the system is in the verge of ferromagnetic instability [5.13]. While the structure type is the same, the extent of distortion in these compounds differs resulting in a different Ru-O-Ru bond angle along *z*-axis and in the *xy*-plane. For $SrRuO_3$ the values are Ru-O(1)-Ru=167.6^o, Ru-O(2)-Ru=159.7^o and those in $CaRuO_3$: Ru-O(1)-Ru=149.6^o and Ru-O(2)-Ru=149.8^o, respectively. The larger deviation from 180^o, in the bond angle for $CaRuO_3$, should facilitate the ferromagnetic order and should also lead to enhancement of the effective electron correlation strength, $U/W \propto t$, which is not the case. This ratio turns out to be small (U/W ~ 0.2), as one may expect from systems with more extended 4*d*-orbitals, and is nearly the same for the both compounds, $CaRuO_3$ and $SrRuO_3$ [5.14]. Recent theoretical study emphasized on the role of the large A-O covalency in $CaRuO_3$, in contrast to $SrRuO_3$, for the destabilization of the magnetic state. The calculations indeed find a paramagnetic ground state for $CaRuO_3$. This most likely results from the smaller Ru-O-Ru angle appearing due to the significant Ca 3*d* – O 2*p* overlap [5.11].

5.1.2 Ferromagnetism in $CaMnO_3$ / $CaRuO_3$ Superlattices

$CaMnO_3$/$CaRuO_3$ superlattices have been shown to exhibit ferromagnetism and negative magnetoresistance at nearly identical onset temperatures, T_c~95K. The total magnetic moment of the superlattices was found not to depend on layer thickness, but on the number of interfaces suggesting that ferromagnetism occurs right at the interfaces between the adjacent layers (Fig. 5.1.2.1).

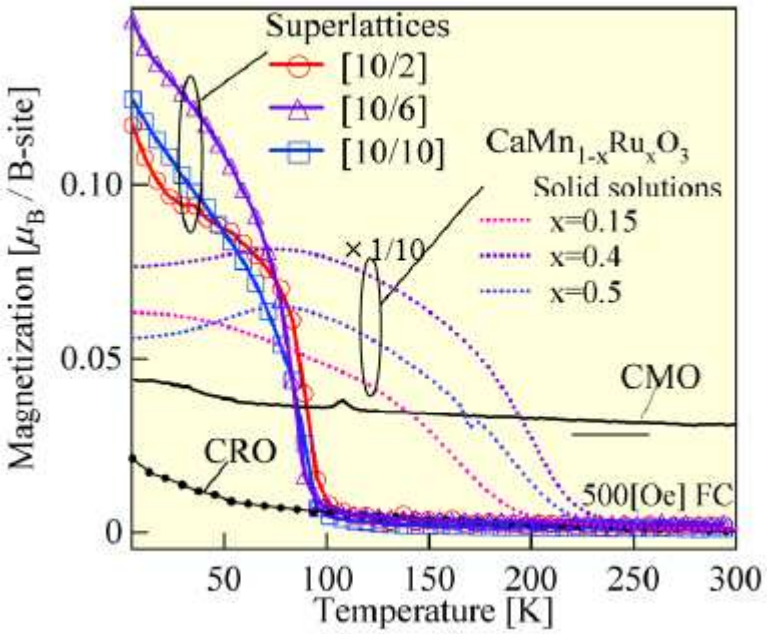

Figure 5.1.2.1 Temperature dependence of magnetization for three superlattice samples $CaMnO_3$/$CaRuO_3$. The digits in brackets denote thickness in unit cells for the respective compound. $CaMnO_3$ is being kept fixed to 10uc and for $CaRuO_3$, N=2,6 and 10, respectively. Control samples of $CaMnO_3$ (CMO), $CaRuO_3$ (CRO) and the solid solution $CaMn_{1-x}Ru_xO_3$, are also given for comparison [5.15].

A valence exchange between Mn^{4+} and Ru^{4+}, that is, Mn^{4+}+ Ru^{4+} <-> Mn^{3+}+ Ru^{5+}, was associated with the presence of ferromagnetism in this system prior to experimental study on solid solution $CaMn_{1-x}Ru_xO_3$ [5.15][5.16][5.17]. However, the origin of this double exchange-like ferromagnetism requires a charge transfer from the Ru to the Mn site. A recent density-functional electronic structure study of the $CaMnO_3$ / $CaRuO_3$ interface

revealed indeed a leakage of metallic electrons into the insulator side. This electron leakage is estimated to spread over several unit cells inside the antiferromagnetic $CaMnO_3$ and in turn to control the magnetism at the interface via competing double exchange <--> superexchange interactions. This competition is found to be effective within the first unit cell next to the interface and is also responsible for the canted magnetic moment, (Fig. 5.1.2.2) [5.18].

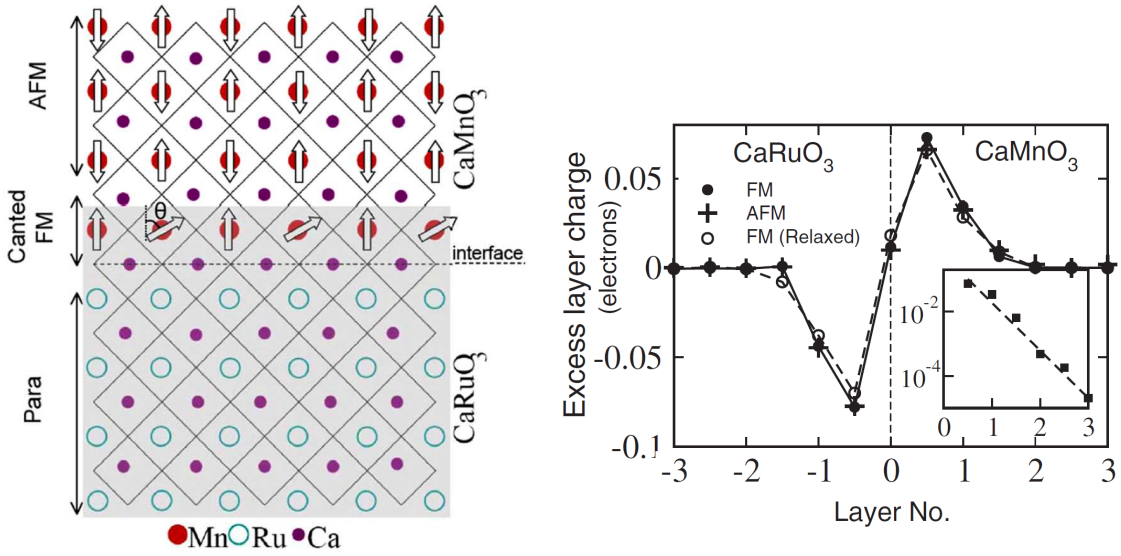

Figure 5.1.2.2 left: Schematic of interface $CaMnO_3$/$CaRuO_3$. A layer with canted magnetic moments forms due to electron leakage from $CaRuO_3$ towards the adjacent $CaMnO_3$ **right**: Charge profile near the interface [5.18].

5.1.3 Sample Preparation

A series of superlattices [$CaMnO_3$(10u.c.)/$CaRuO_3$(N u.c.)] × 6 (six times) // (001) $LaAlO_3$ (LAO) substrate, with N = 4 to 10 consecutive $CaRuO_3$ unit cells, were grown by pulsed laser deposition with a KrF excimer laser (λ = 248 nm, J=2 J/cm^2) at a substrate temperature of 720°C in 10 mTorr of pure oxygen using stoichiometric sintered targets. Upon deposition, all samples were *in-situ* annealed in 50-100 mTorr of oxygen for 5-10 minutes and then gradually cooled down to room temperature. Reflection high-energy electron diffraction (RHEED) oscillations observed *in-situ* as well as hard x-ray (XRD) data taken on the samples demonstrate flat, atomically sharp interfaces and lattice-matched epitaxial growth (Fig. 5.1.3.1).

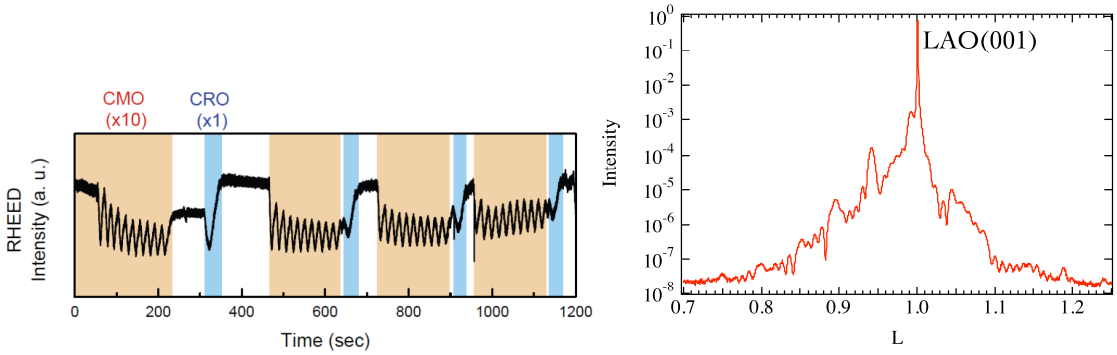

Figure 5.1.3.1 left: RHEED oscillations on growing $CaMnO_3$/$CaRuO_3$ superlattice sample with 10uc $CaMnO_3$ (CMO) and 1uc $CaRuO_3$ (CRO) **right:** XRD (8.4keV) pattern along [001] around the (001) $LaAlO_3$ fundamental peak. ($LaAlO_3$ a_c=3.828 Å).

In agreement with previous studies on this system (Fig. 5.1.2.1), magnetic susceptibility measurements on the samples indicate a net magnetization upon cooling below about 120 K, consistent with the Neel temperature of bulk antiferromagnetic $CaMnO_3$ [5.1].

5.1.4 Far-Infrared (FIR) Reflectance with High Magnetic Field and *dc*-Transport

Near-normal reflectance with high magnetic field in the FIR range and four-point contact *dc*-transport probe were applied in order to study the charge transport properties of the superlattice samples. A control sample with a 10nm thick $CaRuO_3$ single layer, deposited on a $LaAlO_3$ substrate, was also investigated. Utilizing the apparatus described in Chapter 4, reflectance measurements with unpolarized light were carried out in the FIR region (50 – 700 cm^{-1}), using *Hg*-arc source. The temperature was varied from room temperature down to 3K in magnetic fields up to 8 Tesla. The field was applied parallel and perpendicular to the superlattice samples. No difference in the optical response in the two field configurations, larger than the experimental error, was observed; hence we discuss the data taken in magnetic field directed along the *c*-axis, i.e., Kerr geometry (Fig. 5.1.4.1).

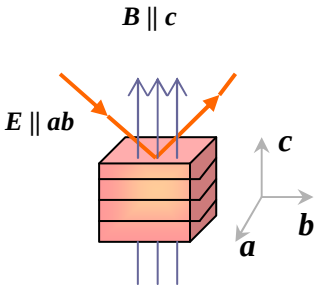

Figure 5.1.4.1 Schematics of the experimental setup. Superlattice sample in Kerr geometry.

Before we proceed to the evaluation of the temperature and magnetic field dependence, we discuss the implications of the substrate material in the FIR spectra. As the total thickness of the samples does not exceed several tens of nanometers; *d*~340Å, *d*~480Å for [CMO10uc/CRO4uc]×6 and [CMO10/CRO10]×6, respectively, and *d*~100Å for the reference sample CRO, the stronger contribution to the FIR spectra will be that of the substrate material LAO. Therefore, in order to obtain information from the reflectance spectra, we first needed temperature dependent measurements and an accurate model of a bare substrate. The (001) LAO spectra were afterwards modeled for all respective temperatures with a set of Lorentzians, equation (5.1.1), using the "RefFIT" program [5.19].

$$\hat{\varepsilon}(\omega) = \varepsilon_{\infty} - \frac{\omega_p^2}{\omega(\omega + i\gamma)} + \sum_j \frac{\omega_{pj}^2}{(\omega_{oj}^2 - \omega^2) - i\omega\gamma_j} \qquad (5.1.1)$$

Here, $\varepsilon(\omega \to \infty) = \varepsilon_{\infty}$ accounts for high-energy contributions to the dielectric constant, the second term describes the response from free carriers (Drude term), and the third one, is a sum over Lorentzians at ω_o, with plasma frequency ω_p and damping γ. The reflectivity is then calculated according to $R = \left|(1-\sqrt{\varepsilon})/(1+\sqrt{\varepsilon})\right|^2$. The experimental data and the corresponding fit curves for (001) LAO, at room temperature and at the lowest temperature of 3K, are compared in figure 5.1.4.2. Three strong phonon modes characterize the spectra of LAO in the FIR range. They were identified at: 182cm^{-1}, 427cm^{-1} and 648cm^{-1}, respectively. Several other weaker modes are also taken into account in the fit procedure.

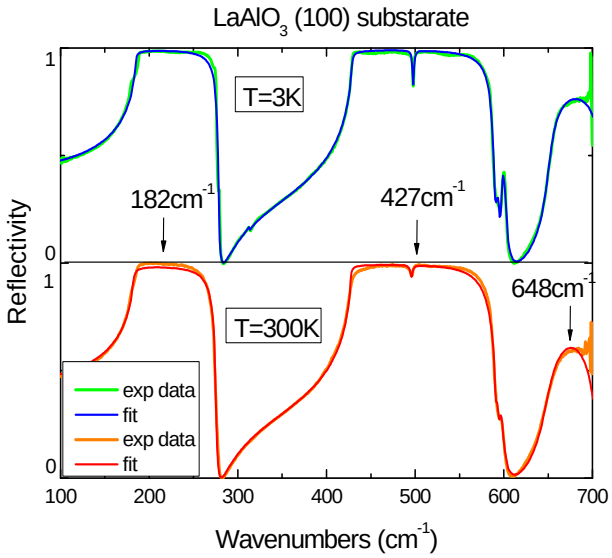

Figure 5.2.4.2 Reflectivity spectra of (001) $LaAlO_3$ substrate compared with the model fit curves at 3K (green/blue), and at 300K (orange/red). Tables with all fit parameters are given in Appendix 1.

Figures 5.1.4.3 (a), (b) and (c), represent the zero field reflectance $R(\omega, B=0)$ data for all samples at several different temperatures. As discussed above, the three strongest features due to LAO dominate the spectra. On the other hand, now for all samples the metallic contribution from CRO is superimposed which introduces a partial screening of the LAO phonon modes. This effect is clearly visible in the reflectance spectra and is more

pronounced in the case of the [CMO10/CRO10]×6//LAO sample, which effectively comprises the largest amount of CRO (~240 Å).

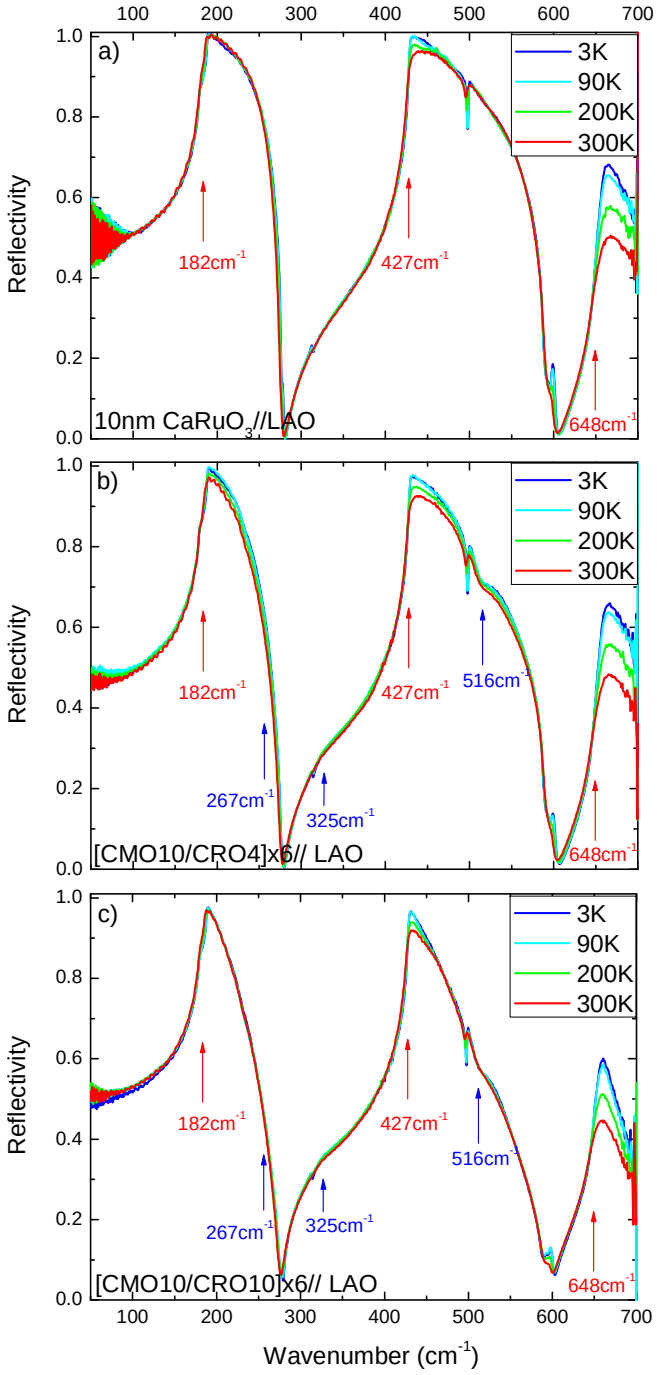

Figure 5.1.4.3 Zero field FIR reflectivity spectra at different temperatures for all samples **a)**10nmCRO//LAO **b)**[CMO10/CRO4]×6//LAO **c)**[CMO10/CRO10]×6//LAO. Red arrows mark the strongest LAO phonon modes and blue arrows indicate phonon frequencies of CMO.

The contribution from CMO is also noticeable in the reflectance spectra of the superlattice samples. The CMO phonon modes were identified from complementary measurements and fit procedure on single films of CMO. The positions of the strongest phonon modes are denoted by blue arrows in figures 5.1.4.3 (b) and (c). The main contribution in the reflectance spectra of the SL samples however, is that from CRO. This is also apparent from the spectra of single layer CRO, compared with the one of SL [CMO10/CRO4]×6//LAO, that both contain nearly equal portions of CRO, ~100Å and ~96Å, respectively. At first glance, the temperature dependence of the reflectivity spectra presented above is not very informative since it is essentially dominated by changes of the LAO phonon modes upon reducing the temperature. Subtraction of the substrate contribution to the spectra is therefore required but before describing this procedure, we first turn to the magnetic field induced effects on the reflectance spectra of the superlattice samples.

The proximity of metallic CRO to the antiferromagnetic CMO results in effective electron doping of Mn^{4+} sites across the interface, which in turn activates the FM double-exchange mechanism that competes with the AF superexchange. Anomalies in the transport properties and concomitant spin dependent effects are therefore to be anticipated with the onset around the magnetic transition temperature, T~100K (Fig. 5.1.2.1). As discussed above, in section 5.1.2, these were indeed observed in *dc*-transport measurements of CMO / CRO superlattices and $CaMn_{1-x}Ru_xO_3$ solid solutions. The optical measurements do have the advantage to be insensitive to the influence of substrate-induced steps or strain-induced dislocations on the current flow through the atomically thin layers in superlattice samples. The optical probe also avoids complications arising from the attachment of electrical contacts. Figures 5.1.4.4 (a) and (b), show experimental spectra taken at temperature of 3K and zero and 8 Tesla magnetic field for both superlattice samples, [CMO10/CRO4]×6 (upper panel) and [CMO10/CRO10]×6 (lower panel), respectively. The ratios between reflectance spectra taken at 8 Tesla and at zero field, R(8T) / R(0T), are given in red. Insets on the right hand side magnify the curves and they are plotted along with the corresponding fit results. The fit procedure is described below.

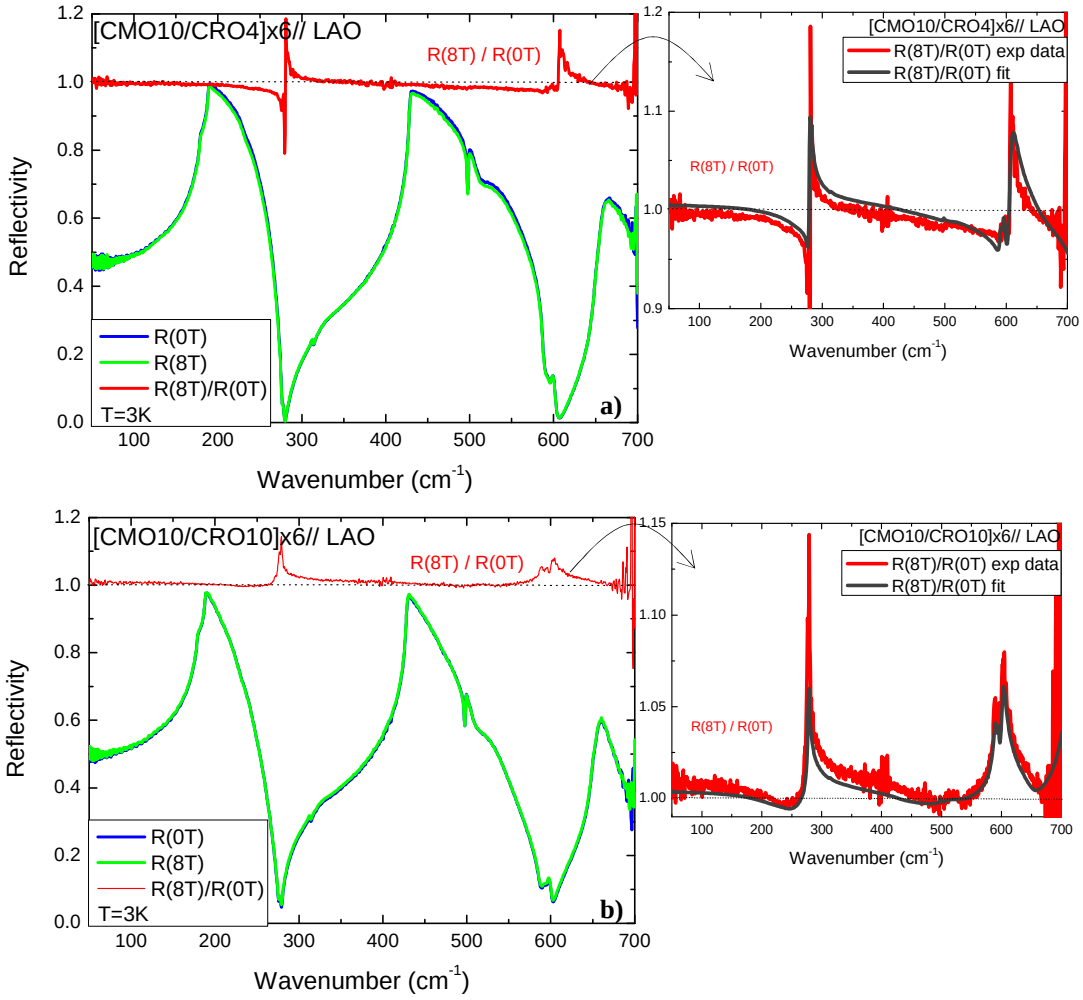

Figure 5.1.4.4 Reflectance spectra taken at zero field (blue) and 8Tesla (green) at fixed temperature, T=3K. The ratio R(8T)/R(0T), i.e. the 100% line, is given in red and zoomed in the small figures, along with the model curves **a)** SL [CMO10/CRO4]×6 and **b)** SL [CMO10/CRO10]×6.

A pronounced magnetic field induced effect on the reflectance spectra was observed for the two superlattice samples on decreasing the temperature below T~150K, which is in proximity to the magnetic transition. The ratio R(8)/R(0), is indicative of changes in spectra obtained under different conditions. While hardly visible in normal spectral plots (blue and green curves), the effects are clear when the ratio is taken. The model analysis of the superlattice reflectance spectra showed that the magnetic field dependence is a consequence of a reduction of scattering rate of the free charge carriers upon application of magnetic field, i.e. increase of "metallicity" due to negative magnetoresistance (MR).

This effect appears in the spectra as weak additional screening of the LAO phonon features that is effective at frequencies away from the ω_{TO}-ω_{LO} ranges, where the reflectance is anyway very high, hence giving the specific shape of the ratio R(8T) / R(0T).

Since the samples thickness is well below the wavelengths in the IR range, the superlattices can be treated as single layers according to the effective medium approach [5.20][5.21]:

$$\varepsilon_{eff}^{(ab)} = \frac{d_{CMO}\varepsilon_{CMO} + d_{CRO}\varepsilon_{CRO}}{d_{CMO} + d_{CMO}} \tag{5.1.2}$$

The magnetic field dependence for several temperatures was fitted utilizing a macro procedure based on "RefFIT - film on a substrate" model and Drude-Lorentz formula for the dielectric function, equation 5.1.1. Two parameters, ω_p and γ, were let free to fit the changes in the Drude response due to CRO. The parameters due to CMO phonon modes are irrelevant to the observed effects and were kept fixed. While the modeling of the temperature dependence may introduce uncertainties due to the substrate subtraction, very good quality fits were obtained for the magnetic field dependence at fixed temperature (Fig. 5.1.4.4 and 5).

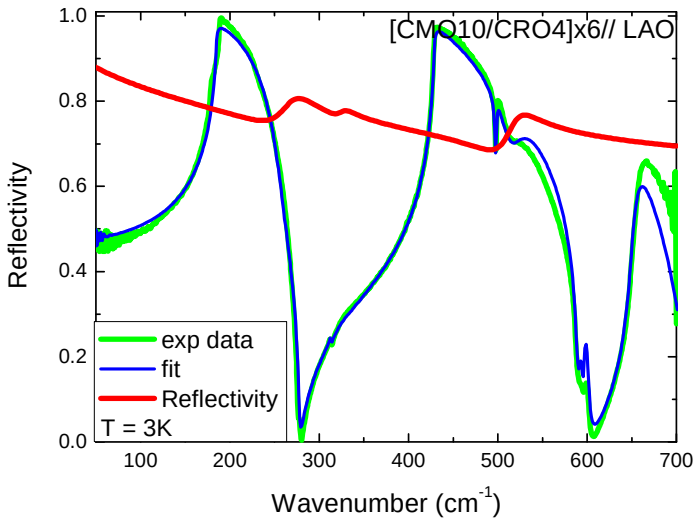

Figure 5.1.4.5 Comparative plot of experimental spectra (green) and fit (blue) at T=3K, for superlattice sample [CMO10/CRO4]×6. The red curve is the resulting reflectivity due to the superlattice only, i.e. without substrate.

Figures 5.1.4.6, 7 and 8 represent results from the fitting in terms of the *dc*-conductivity and resistivity according to:

$$\sigma_{dc}\left[\Omega^{-1}cm^{-1}\right] = \frac{\omega_p^2\left[cm^{-1}\right]/\gamma\left[cm^{-1}\right]}{60} \qquad (5.1.3)$$

All fit parameters are listed in Appendix 1.

Reflectivity spectra with magnetic field were also taken for the 10nm CRO//LAO single film. The corresponding zero field and 8 Tesla resistivity match well, within the error bar, all along the temperature scale (Fig. 5.1.4.6).

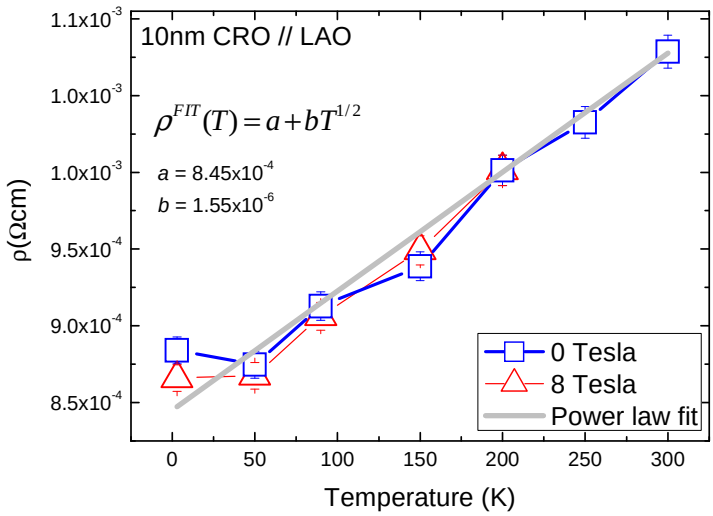

Figure 5.1.4.6 FIR reflectivity fit output in terms of resistivity for 10nm film CRO at several temperatures for zero (blue) and 8 Tesla (red) magnetic field. The two curves show small deviation at low temperatures. The grey line is a power law, $\rho(T) \sim T^{1/2}$, fit to the temperature dependence.

The resistivity ratio $\rho(300K)/\rho(3K)$, was found to be ~0.8 with a room temperature value of $\rho(300K) = 1.08\times10^{-3}(\Omega cm)$. The temperature dependence fits well with the power law $\rho(T) \sim T^{1/2}$, which is consistent with previous experimental studies on this material [5.10]. The superlattices, on the other hand, show very different behavior on reducing the temperature (Figure 5.1.4.7). Room temperature values for the resistivity for both SLs are higher then that of the CRO single layer: $\rho^{SL4}(300K) = 2.48\times10^{-3}$, for sample [CMO10/CRO4]×6 and $\rho^{SL10}(300K) = 1.8\times10^{-3}(\Omega cm)$, for [CMO10/CRO10]×6. Also, as can be expected, the SL sample with 4 unit cells CRO (~96Å CRO in total) has larger

resistivity compared to the SL with 10 unit cells CRO (~240Å CRO in total). Clear upturns in the temperature dependence of resistivity appear for the two SLs, around 150K and 100K, respectively. These temperatures are in proximity to the Neel temperature of $CaMnO_3$, T_N=125K, and also mark approximately the onset of negative magnetoresistance effect. On further cooling, the resistivity increases, down to the lowest measured temperature of 3K.

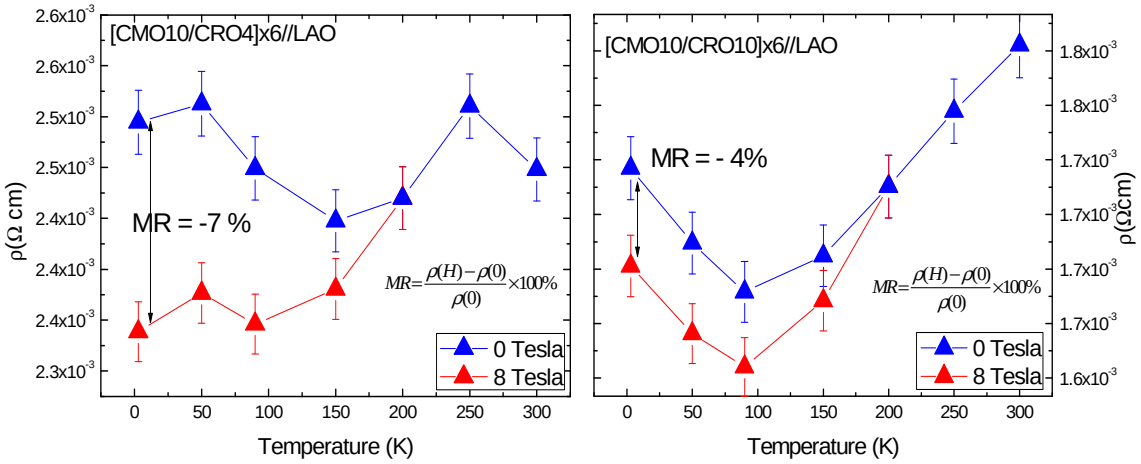

Figure 5.1.4.7 Temperature dependence of resistivity from fitted FIR reflectivity spectra at zero field (blue) and 8Tesla (red) for the SL samples **left:** [CMO10/CRO4]×6 and **right:** [CMO10/CRO10]×6. Both SLs show negative MR effect reaching its maximum values of ~7% and ~4%, respectively, at the lowest temperature of 3K.

The magnitude of the observed MR (equation 5.1.4), was estimated to be as large as (~7%) for SL samples with fewer CRO unit cells and higher resistivity, [CMO10/CRO4]×6, and about (~4%) for [CMO10/CRO10]×6.

$$MR(\%) = \frac{R(H) - R(0)}{R(0)} \times 100 \qquad (5.1.4)$$

Similar behavior in the temperature dependence of the resistivity has been observed in $CaMn_{1-x}Ru_xO_3$ solid solutions [5.17]. When the charge carriers are introduced by the Ru within the antiferromagnetic matrix of $CaMnO_3$, they become localized and the temperature dependence of resistivity resembles that of colossal magnetoresistance (CMR) manganites. However, in contrast to CMR manganites, in which the CMR effect has its maximum around the temperature of the metal-to-insulator transition, here the

observed MR increases with decreasing temperature from its onset down to the lowest point of 3K where it reaches maximum. This result is more reminiscent of the so-called giant magnetoresistance (GMR) effect and furthermore, it strongly suggests canted antiferromagnetic ground state.

Another possible signature of canted antiferromagnetism in these superlattices comes from the *dc*-conductivity, presented as a function of the applied magnetic field at fixed temperature of 3K (Fig. 5.1.4.8).

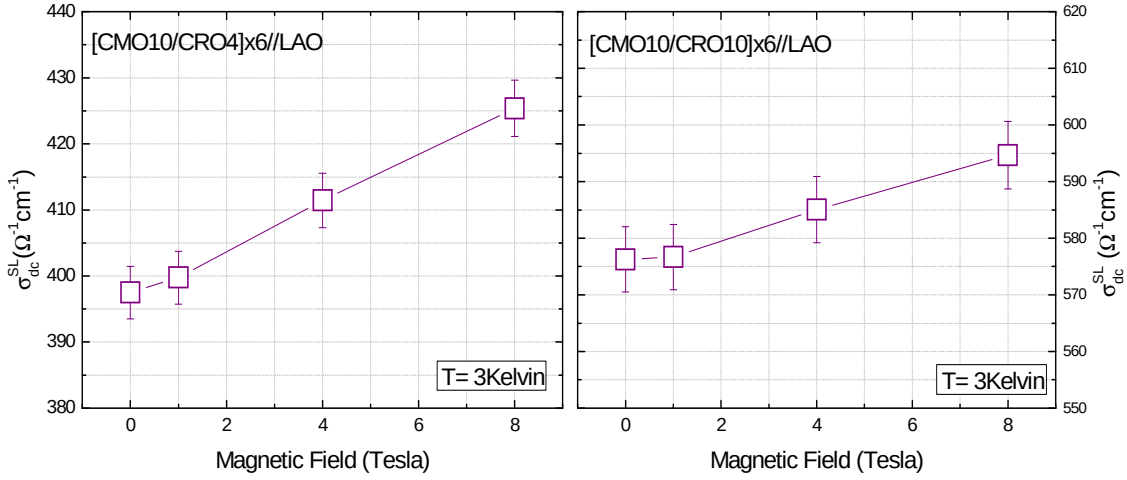

Figure 5.1.4.8 *dc*-conductivity extrapolated from fitting of FIR reflectivity as a function of magnetic field for SLs **left:** [CMO10/CRO4]×6 and **right:** [CMO10/CRO10]×6, at fixed temperature, 3K. Both superlattices show linear increase of the conductivity with no signature of saturation up to 8Tesla, the highest field experimentally available for our setup.

Interestingly, the *dc*-conductivity extrapolated from the fit to the FIR data increases linearly with the magnetic field and does not show signs of saturation up to 8 Tesla, which is the highest field accessible with our experimental setup. Independent four-point contact *dc*-transport measurement on the same superlattices, presented in figure 5.1.4.9 below, showed consistency in the temperature dependence of the resistivity obtained from the FIR reflectivity spectra.

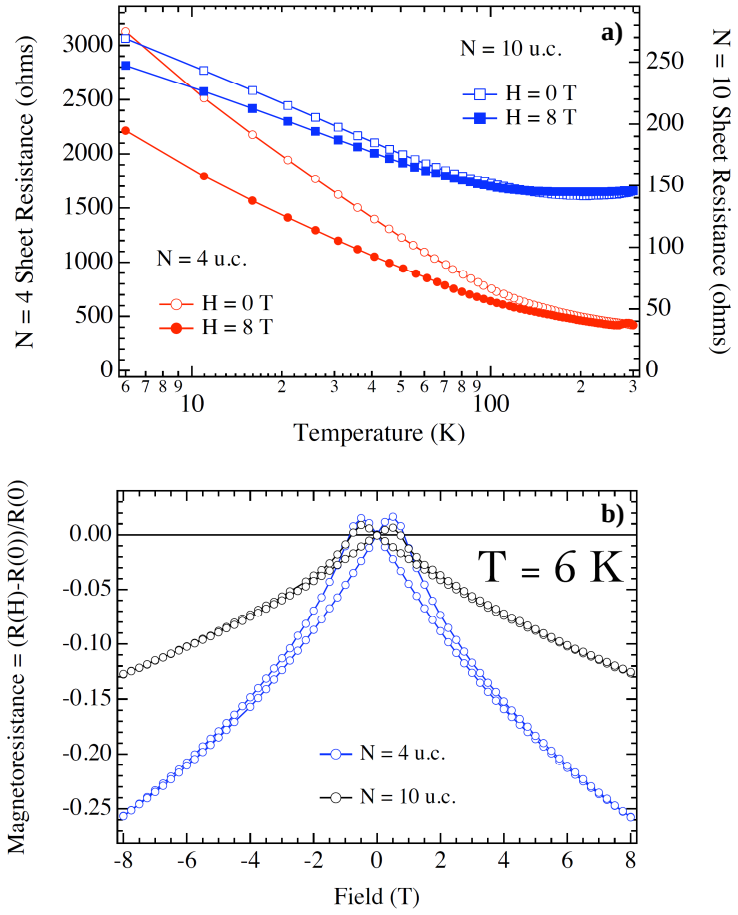

Figure 5.1.4.9 a) Resistance versus temperature at zero and 8 Tesla magnetic field, for superlattice sample [CMO10/CRO4]×6//LAO (red), and [CMO10/CRO10]×6//LAO(blue) **b)** Magneto-resistance as a function of the applied magnetic field at T=6K, for superlattice samples [CMO10/CRO4]×6//LAO (blue), and [CMO10/CRO10]×6//LAO (black) [5.22].

Similarly the *dc*-data reveal larger MR effect and larger resistance for SL sample with fewer unit cells CRO, i.e., [CMO10/CRO4]×6 compared to [CMO10/CRO10]×6. The temperature dependence also shows activated behaviour and onset of MR in the range 100-150K. The MR as a function of the applied magnetic field, (Fig. 5.1.4.9 (b)), shows nearly linear increase at T = 6K and agrees very well with the data presented in figure 5.1.4.8. The magnitude of the MR effect at T = 6K and 8 Tesla are however considerably larger here; ~25% for [CMO10/CRO4] and ~13% for [CMO10/CRO10] against ~7% and ~4% extracted from FIR reflectivity data.

5.1.5 Soft x-ray spectroscopy data

As discussed in section 2.3.1, x-ray techniques with synchrotron radiation constitute powerful experimental tool for element specific structural and spectroscopic studies of electronic and magnetic properties of solids and in particular, superlattice structures. In this section we present results from soft x-ray spectroscopy on the SL samples [$CaMnO_3$10uc/$CaRuO_3$ N=4 and 6uc]//LAO. Detailed information about the valence state and the magnetic polarization of Mn and Ru ions in our samples was obtained by x-ray absorption spectroscopy (XAS) and x-ray magnetic circular dichroism (XMCD) while the depth distribution of the net magnetization was inferred by x-ray resonant magnetic scattering (XRMS) [5.1]. The XAS and XMCD were carried out at beamline 4-ID-C of the Advanced Photon Source. Magnetic fields up to 7 Tesla generated by a cryomagnet were applied in the plane of the superlattices. The measurements were performed by monitoring the intensity, *I*, of left (−) and right (+) circularly polarized x-rays absorbed by the specimen using the surface/interface sensitive total-electron-yield (TEY), described in section 2.3.2 and in Ref. [5.23]. The sum, $I^+ + I^-$, yields the XAS signal, while the XMCD signal is derived from the difference, $I^+ - I^-$. Figures 5.1.5.1 & 2 show the results of the measurements.

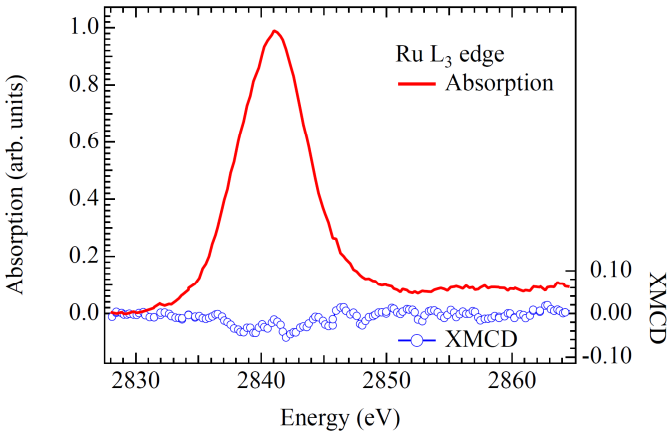

Figure 5.1.5.1 XAS (red) and XMCD (blue) measured at Ru L_3 edge for superlattice sample [CMO10/CRO4]×6 at T=10K.

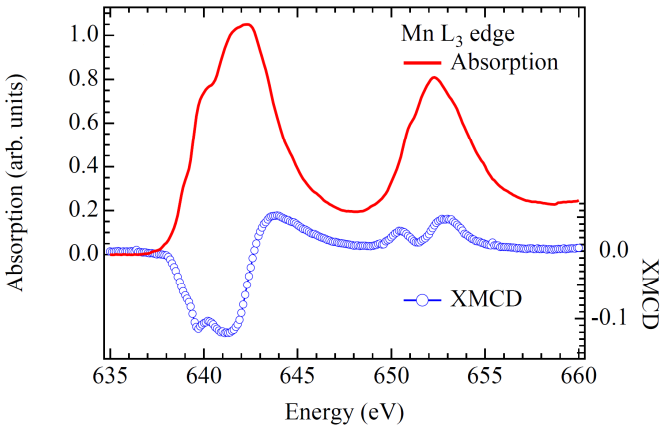

Figure 5.1.5.2 XAS (red) and XMCD (blue) measured at Mn L_3 edge for superlattice sample [CMO10/CRO6]×6 at T=10K

While the Ru XMCD signal does not exceed 3%, a clear XMCD signal of ~12% is observed at the Mn L-edge for both samples in a magnetic field of 7 Tesla. Using references the Ru XMCD places an upper bound of ~0.3μ_B on the net magnetic moment per Ru atom while the Mn XMCD corresponds to an average moment of 1 μ_B/Mn atom, which implies that the net magnetization is dominated by $CaMnO_3$, consistent with the theoretical work of Nanda *et al* [5.18]. The Mn XMCD data also provide two pieces of evidence supporting the theoretically predicted canted antiferromagnetic state localized near the interface. First, the XMCD signal is substantially lower than expected if the layers were fully ferromagnetic [5.24], and it wasn't found to exhibit significant hysteresis effects. Second, the XMCD for both superlattices vanishes upon heating above 100-120 K, the Neel temperature of bulk $CaMnO_3$, yet control measurements on an isolated $CaMnO_3$ film grown on $SrTiO_3$ (not shown here) revealed no XMCD signal above background, which implies that the Mn magnetism is due to the CRO/CMO interface and not due to the entire CMO layer. Comparison to reference samples also showed a valence state of both Ru and Mn ions close to 4+.

Now, in order to determine the length scale of the interface induced ferromagnetic polarization, we have performed XRMS measurements with circularly polarized x-rays at two photon energies in the vicinity of the Mn L_3 absorption edge. The XRMS experiments were carried out at the SIM beamline at the Swiss Light Source using the RESOXS chamber [5.25]. The reflected intensities I^+ and I^- were collected for two opposite directions of a magnetic field applied along the intersection of the superlattice and scattering planes. The amplitude of the magnetic field available in the chamber is

0.16 Tesla, which is sufficient to field cool the sample into a partially magnetized state. The resonant reflectivity in the charge channel ($I^+ + I^-$) exhibits a series of Bragg peaks characteristic of the superlattice periodicity, separated by interference (Kiessig) fringes due to the finite thickness of the sample (Fig. 5.1.5.3 (a)). The first photon energy (620 eV) was chosen off resonance allowing a structural analysis not relying on the knowledge of the resonant scattering factor (use of tabulated atomic scattering factor). The second one (639.2 eV, corresponding to the inflexion point of the Mn L_3 edge) was chosen to reduce the x-ray absorption while maximizing the real part of the magnetic scattering factor. The magnetic depth profile was obtained from an analysis of the dichroic difference, ($I^+ - I^-$), of the Bragg intensities. The analysis requires knowledge of the structural parameters of the superlattices (thickness, roughness, and density of the layers), which were derived from a refinement of off-resonant reflectivity data recorded at 620 eV and confirmed by the refinement of the resonant reflectivity using the resonant scattering factor derived from the XAS measurements. Although the fits exhibit some discrepancies with the data between the Bragg peaks, the relative intensities of the Bragg peaks and the widths of the intense ones are well described. The magnetic profile is probed by the charge-magnetic scattering in the ($I^+ - I^-$) signal. Figure 5.1.5.3 (b) displays the difference ($I^+ - I^-$) measured on top of the first four Bragg peaks normalized to the corresponding peak intensity (upper panel), as well as the results of simulations of this quantity for several models of the magnetic profile (Fig. 5.1.5.3 (c)). For the case of a superlattice, the key point is the q_z evolution due to the cross correlation of the charge and magnetic scattering in the XRMS signal. When the magnetic profile differs from the chemical profile, the sign varies depending on the thickness of the magnetic layer within the charge layer (Fig. 5.1.5.3 (c)).

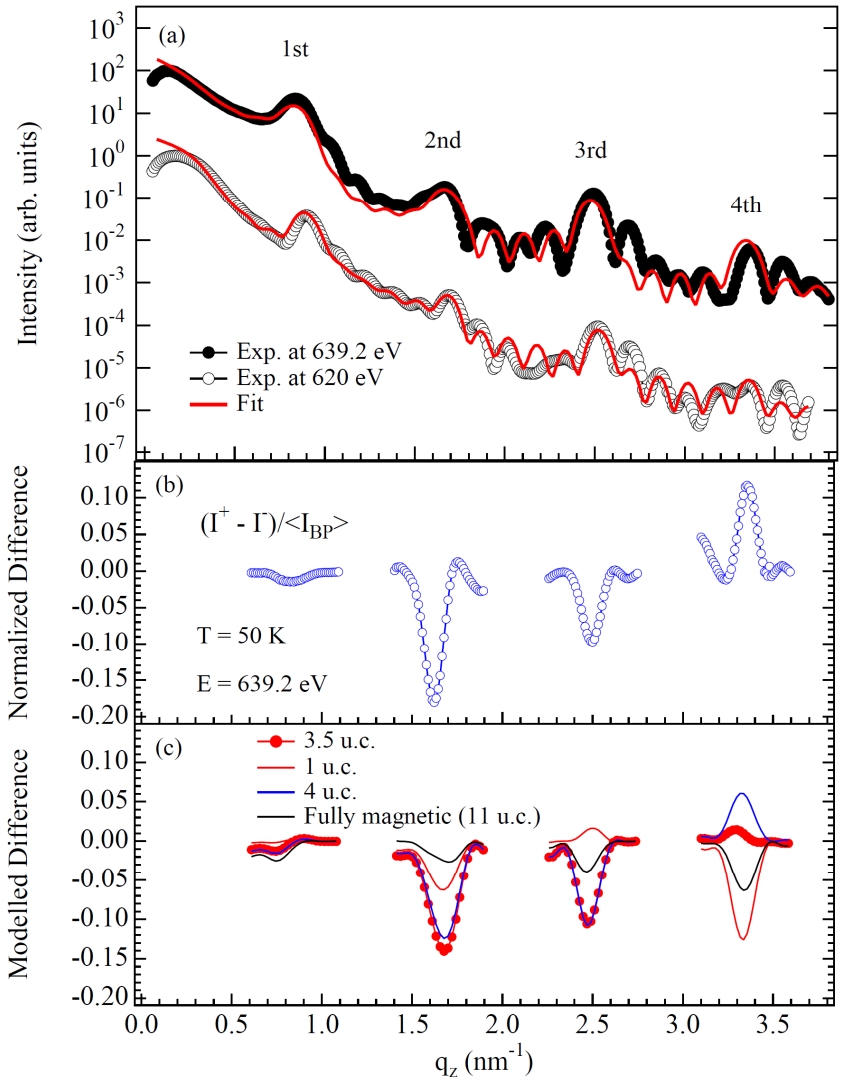

Figure 5.1.5.3 a) Specular reflectivity for two energies: E=639.2eV (Mn L_3) at T=50K (upper curve) and of resonance E=620eV at T=300K (lower curve) for superlattice sample [CMO10/CRO6]×6. Red lines represent structural fit **b)** dichroic difference (I^+ - I^-) measured at different Bragg peaks and normalized to the peak intensity and **c)** the corresponding calculated normalized differences for different layer thicknesses. Best fit is obtained for 3.5 unit cells [5.1].

By considering a simple symmetric step profile for the magnetization in $CaMnO_3$, composed of equally thick magnetic layers at the interfaces and a non-magnetic core layer, we can study the evolution of the sign and gain insight into the thickness of the magnetic layer near the interface. The simulated and observed intensities show very good agreement for an interfacial thickness of 1.38 nm (3.5 u.c.). This model reproduces both the experimentally observed sign sequence of (I^+ - I^-) at the Bragg peaks and its relative

amplitude. The absolute magnitude of the normalized difference was calculated with the constraint that its integral equals the XMCD signal discussed above (scaled for the lower applied magnetic field, see Fig. 5.1.5.2). As shown in figure 5.1.5.3 (c), the result also agrees closely with the experimental data. Despite its simplicity, the model therefore provides an excellent description of the salient features of the XRMS data. From this we conclude that the ferromagnetic polarization is not limited to the immediate vicinity of the interface, as theoretically predicted [5.18], but extends further into the CMO layer. Specifically, a model in which the net magnetization arises entirely from the first $CaMnO_3$ unit cell at the interface is ruled out by the behavior of (I^+ - I^-) at the third- and fourth-order Bragg peaks.

5.2 Conclusions

In Chapter 5 we have presented a comprehensive spectroscopy study on superlattice system [$CaMnO_3$ 10 / $CaRuO_3$ N = 4 and 6 unit cells] on (001) $LaAlO_3$ substrate. Control samples of single layers of $CaRuO_3$ and $CaMnO_3$ were also investigated. Utilizing various spectroscopy techniques we obtained a detailed picture of the charge transport properties at different temperatures and magnetic fields as well as complete magnetization profile of the superlattices. The valence state of Ru and Mn ions near the interface was also inferred.

FIR reflectance measurements at several temperatures, ranging from 3 to 300K, and magnetic fields up to 8 Tesla, were carried out. Using fit procedure based on effective medium approach and the Drude-Lorentz formula for the dielectric function, the reflectivity due to the superlattices was obtained. The results were presented in terms of *dc*-conductivity and resistivity. A magnetic field induced effect was observed in the two SL samples. The onset temperature was shown to be in proximity to the Neel temperature of $CaMnO_3$, T~125K, and found to result from a reduction of the scattering rate of the free carriers (due to $CaRuO_3$), upon application of magnetic field, i.e. negative magnetoresistance effect. Concomitant upturns in the temperature dependence of the resistivity also appear consistent with spin-dependent localization effects inherent to CMR manganites. It was further shown that the magnitude of this negative MR effect is

small and increases all the way from its onset point down to the lowest temperature of 3K, and hence is reminiscent to giant magnetoresistance (GMR) effect. The magnetic field dependence of the *dc*-conductivity, for the both samples at 3K, shows linear behavior with no indication of saturation up to the largest field of 8 Tesla. These findings strongly support canted antiferromagnetic ground state for CMO / CRO SL system. Independent four-point contact *dc*-transport probe have shown consistent results giving also confidence for the reliability of the measurements performed with the FIR magneto-reflectance setup, recently assembled and described in Chapter 4.

The XAS, XMCD, XRMS probes and the FIR spectroscopic ellipsometry study [5.1], led to conclusive results about the origin of the net magnetization in CMO / CRO superlattices and its spatial extent. XMCD revealed substantial polarization for Mn ions with values corresponding to canted magnetic moments, while negligible or absent for Ru nearby the interfaces. Applying XRMS and structural model calculations it was concluded that the ferromagnetic polarization is not limited to the immediate vicinity of the interface (~1 unit cell), as theoretically predicted in [5.18], but extends further into the CMO layer up to about 3.5 unit cells. XAS on the other hand, showed valence state for Mn and Ru close to 4+. FIR spectroscopic ellipsometry measurements also inferred largely unaltered effective number of charge carriers per Ru atom (~0.11) in these SLs, compared to bulk $CaRuO_3$ [5.10]. So, only a small number of electrons from metallic $CaRuO_3$ penetrate into antiferromagnetic insulating $CaMnO_3$ giving rise to canted state with a sizable net polarization that extends ~3.5 unit cells.

Our results therefore suggest that magnetic polarons (Fig. 5.2.1), which have been extensively investigated in bulk manganates [5.26][5.27], and other transition metal oxides, strongly influence the physical properties of oxide interfaces and should therefore be considered in the $CaMnO_3$ / $CaRuO_3$ SL system. Formation of magnetic polarons in the AF matrix of $CaMnO_3$ will induce activated behavior in the transport properties and subsequently, application of magnetic field would lead to their melting enhancing the electron mobility due to kinetic energy gain. This model picture is consistent also with our transport data.

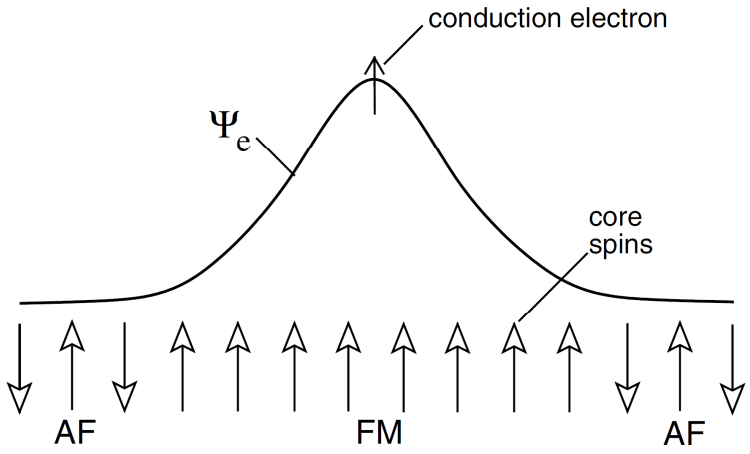

Figure 5.2.1 Sketch of a self-trapped magnetic polaron, showing ferromagnetic region of core spins, exchange-induced by the electron, and in which the electron becomes self-trapped [5.26]. Ideally, the ferromagnetic region is fully polarized but the realistic situation corresponds to a spin canted state, experimentally justified in our experiments.

Chapter 6

FIR Response of Ferromagnetic $YTiO_3$ in High Magnetic Field

In Chapter 2, the intriguing properties of $3d^1$ insulating titanates, $LaTiO_3$ and $YTiO_3$ were briefly reviewed. The strong experimental and theoretical interest in these compounds is focused on the link between the orbital and magnetic state, as they are less prone to severe Jahn-Teller distortions inherent of the e_g degenerate systems, hence, the large degeneracy is expected to be broken in a more subtle and interesting manner. An excellent example is $LaTiO_3$ compound, in which no evidence of orbital order has yet been reported. The $GdFeO_3$–type distortion on the other hand, always present in TMOs with perovskite structure, is also relatively weak in $LaTiO_3$, so that orbital fluctuations in the entire t_{2g} manifold maintain the G-type AF state. This situation resembles to some extent systems with occupied t_{2g} levels ($3d^3$), such as $CaMnO_3$ - another compound with a weak $GdFeO_3$ distortion and the same isotropic G-type AF magnetic state.

When the smaller Y ion substitutes La in $LaTiO_3$, the $GdFeO_3$ distortion is enhanced introducing larger bending of the Ti-O-Ti bond, which in turn facilitates the parallel FM spin ordered state. Now, whether and to which extent orbital fluctuations are present and play role in the more distorted $YTiO_3$, continues to be a subject of intense studies [6.1][6.2][6.3][6.4][6.5].

In the following chapter we present a FIR (100 – 700 cm^{-1}) polarized reflectivity study on single crystals of $YTiO_3$ at different temperatures in the interval 3K - 100K and subjected to high magnetic fields (MF), from 0 to 8 Tesla. The data collected in this experiment, in combination with FIR spectroscopic ellipsometry measurements, allowed us to identify all 25 infrared-active phonon modes in $YTiO_3$, see Ref. [6.6]. Furthermore, the optical response obtained along the three principal crystal axes, at several temperatures and magnetic fields, clearly showed a spin-phonon coupling below $T_M \sim 80K$, manifesting

itself as temperature and magnetic field-induced anomalous deviations in the oscillator parameters. Comparison between the temperature dependent phonon spectra taken at zero field, and the magnetic field dependence at fixed temperature, showed intriguing similarity. This observation directly reflects the interplay between the lattice vibrations and the spin order in $YTiO_3$. The phonons that were found to experience largest temperature and field-induced changes are associated with the group of Ti-O-Ti bond-bending modes, according to the assignment given in Ref. [6.9]. These effects are however weak, placing $YTiO_3$ in the group of systems with small spin-phonon coupling constants as expected from a t_{2g} system. The present spectroscopic measurements, initially intended at temperatures around the magnetic transition of $T_c \sim 30K$, revealed very large temperature range, up to T ~ 80-100K, for the field-induced effects, which is indicative of short range magnetic order. Similarly, a recent thermodynamic study on $YTiO_3$ single crystals finds extended (exceeding 100K) magnetic contribution in the specific heat that was related to the presence of spin-orbital fluctuations [6.7]. The origin of the characteristic temperature, $T_M \sim 80K$, is however not clear. Our study showed that this is also the onset temperature for deviations from the bare phonon-phonon anharmonic behavior, $\omega_{anh}(T)$, for many modes in $YTiO_3$. Other physical quantities, like the inverse magnetic susceptibility, lattice expansion coefficient α, and the dielectric constant, at energies of the optical bands, also show peculiarities at around 80 to 100K [6.6][6.7][6.8]. All these findings uncover a complex interplay between spin-orbit and lattice channels in $YTiO_3$, and while there is no direct evidence for a phase transition at $T_M \sim 80$ - 100K, a crossover, or some kind of weak exotic transition cannot be completely excluded. In the conclusion section, the observed phonon anomalies are discussed in the context of a mean field approach for spin-phonon coupling and modulation of the exchange interaction constant $J(r)$. Although a definitive model is so far not available, the experimental data indicate effects due to the degeneracy of the Ti t_{2g} orbitals in $YTiO_3$.

6.1 Bulk Properties of $YTiO_3$ and Sample Characterization

$YTiO_3$ crystallizes in the orthorhombic structure of $GdFeO_3$-type described by the P_{bnm} space group (Fig. 6.1.1), and the temperature dependent lattice expansion shows no structural phase transition on cooling below room temperature.

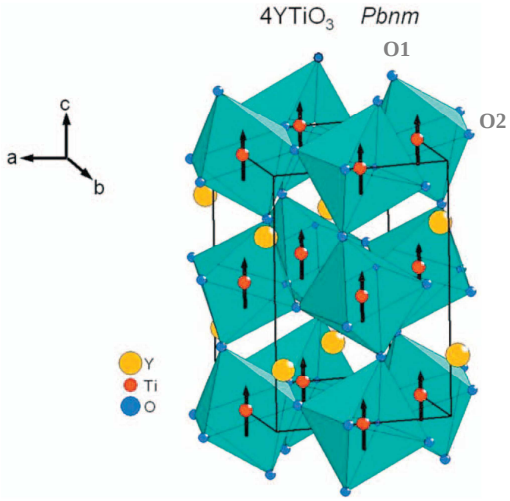

Figure 6.1.1 Orthorhombic structure of $YTiO_3$, space group P_{bnm}, with ferromagnetic alignment of Ti spins, from [6.9].

As already mentioned, $YTiO_3$ is a ferromagnetic Mott insulator with $T_c \sim 27$ - 30K, in electronic configuration t_{2g}^1 [6.10]. The Ti-O-Ti bond angle in $YTiO_3$ is 140° in the *ab* plane, and 144° along the *c*-axis. The large bond angle implies small overlap of the transition metal 3*d*, and the oxygen 2*p* orbitals, which leads to smaller electron transfer between nearest neighbor Ti sites than in $LaTiO_3$ [6.11]. Additional elongation along the *c*-axis in the FM state, by about 3%, of the TiO_6 octahedra is also observed. This distortion has been attributed to staggered ordering of the t_{2g} orbitals [6.12], (Fig. 6.1.2).

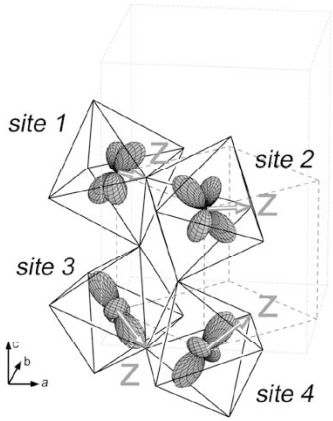

Figure 6.1.2 Orbital ordering pattern in $YTiO_3$. From [6.12].

An inelastic neutron scattering experiment revealed complex magnetic structure, comprising substantial *G*-type and *A*-type antiferromagnetic components in addition to the predominant ferromagnetic component. The magnon spectrum, on the other hand, is gapless and nearly isotropic, which is inconsistent with the orbitally ordered states thus far proposed for $YTiO_3$ [6.13].

High-quality single crystals of $YTiO_3$ were grown by the floating-zone method. X-ray diffraction shows that the $YTiO_3$ single crystals used for our experiments are untwinned, with mosaicity less than 0.03°. At room temperature, the lattice parameters are a=5.331(3) Å, b=5.672(4) Å, and c=7.602(6) Å, respectively. The samples were aligned along the principal axes and cut in the form of parallelepipeds with ~3 mm side each. The oxygen content was measured by heating small quantities of the as-grown crystals in O_2 flow using a differential thermal analysis gravimetric apparatus. Due to the $Ti^{3+} \rightarrow Ti^{4+}$ instability, single crystals of $YTiO_3$ always have an excess of oxygen above the exact stoichiometry formula. Based on the weight gain, the oxygen excess in the formula $YTiO_{3+\delta}$ is estimated at a level less than δ=0.013. The samples were further characterized by magnetometry using a superconducting quantum interference device. The inset of figure 6.1.3 (a) shows the temperature dependence of the magnetization for the $YTiO_3$ sample in the vicinity of T_c taken upon heating in a magnetic field of 1 kOe parallel to the *c*-axis direction after cooling in zero field. For the sample studied here, we estimate T_c ~ 30 K, which is amongst the highest values reported so far. Figure 6.1.3 (a), shows the temperature dependence of the inverse susceptibility $1/\chi_{mol}$, which exhibits nearly linear increase above 100K (χ_{mol} was corrected by temperature independent diamagnetic contribution $\chi_{dia} = -5.7\text{x}10^{-5}$ emu/mol). A fit to the Curie-Weiss law, $1/\chi_{mol} \approx \frac{8}{\mu_{eff}^2}(T - \vartheta)$ yielded a Curie-Weiss temperature of θ = 40K and effective magnetic moment μ_{eff} =1.66μ_B, that is slightly reduced with respect to the spin-only value of $\mu_s = 2\sqrt{S(S+1)} = 1.73\mu_B$ of Ti^{3+} ions with S = 1/2. The magnetization data in figure 6.1.3 (a) reveal significant deviations from Curie-Weiss mean-field behavior below about 100K. As a result, an inflection point in the temperature-dependent magnetization is observed at 27 K, a few degrees below T_c. Figure 6.1.3 (b) shows magnetization measurements for the three principal directions of $YTiO_3$ up to 7 Tesla at 5 K, well below

the magnetic transition temperature. The results reveal that the *c*-axis is the easy axis of magnetization, while the *b*-axis is hard. The saturated moment estimated in the easy direction, at the highest magnetic field of 7 T, is $\mu^c = 0.84\mu_B$, whereas $\mu^b = 0.82\mu_B$, in the hard direction - both reduced from $1\mu_B$.

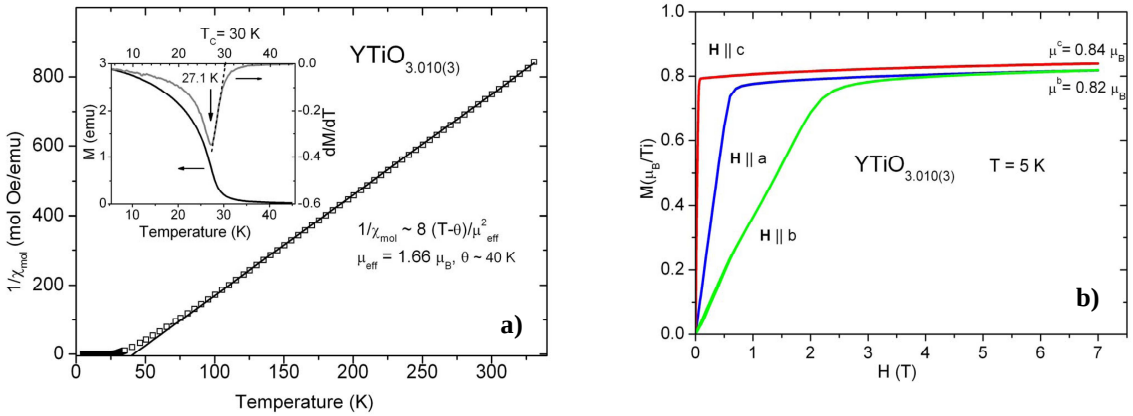

Figure 6.1.3 a) Temperature dependence of the inverse susceptibility (squares) of the $YTiO_3$ single crystal approximated by Curie-Weiss behavior at high temperatures (solid line). The inset shows the temperature dependence of the magnetization in the vicinity of T_C and its temperature derivative after zero-field cooling in a magnetic field of 1000Oe with **H**||*c*. The inflection point in the temperature-dependent magnetization is observed at T=27K. **b)** Magnetization of the $YTiO_3$ single crystal measured with magnetic field applied along *a*,*b*, and *c* axes, in *Pbnm* notation, at *T*=5 K [6.6].

6.2 Phonon Modes in $YTiO_3$: Experimental Data and Fit

The FIR response of $YTiO_3$ single crystal was obtained by a high-accuracy ellipsometry measurements using home-built ellipsometer, at beamline IR1 at the ANKA synchrotron in Karlsruhe, Germany, and near-normal incidence reflectance setup with high magnetic field, both described in Chapter 4. All 25 IR-active phonon modes were identified and assigned [6.6][6.9]. In the following section, FIR reflectivity data for all three principal crystal axes; *E*||*a*, *E*||*b* and *E*||*c* is presented. The spectra were taken at several temperatures in the interval from 3 to 100K and magnetic fields from 0 up to 8 Tesla, in steps of 1 Tesla. Good quality fits were obtained for all data using the "RefFit" code and set of Lorentzians [6.14]. All fit parameters are listed in Appendix 2.

6.2.1 Zero-Field Data

a-axis, *E||a(ac)*

Figure 6.2.1.1 shows zero field experimental reflectivity spectra and the fit curve for *a*-polarization at temperature of 3K. The identified phonon frequencies (in cm^{-1}) are indicated into the figure.

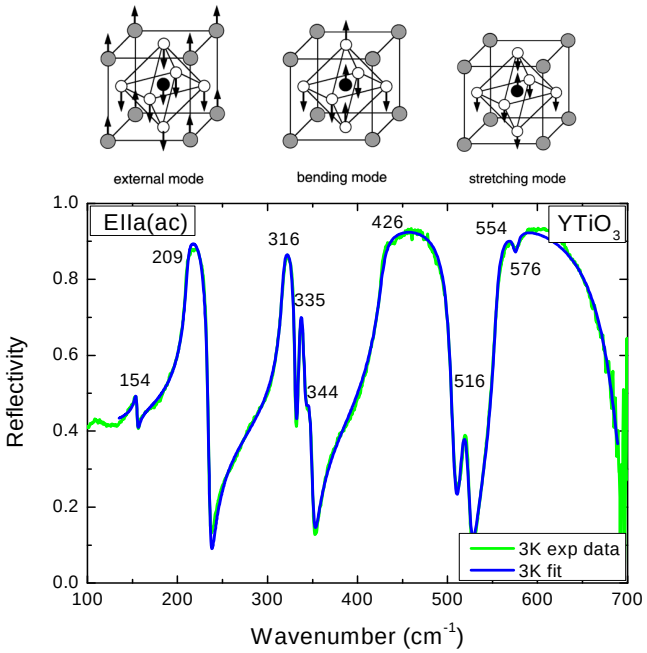

Figure 6.2.1.1 Experimental reflectivity spectra (green) and fit curve (dark blue) for *a*-polarization at T = 3K. Numbers indicate the phonon frequencies in (cm^{-1}). Schematics of the three basic phonon mode groups in cubic perovskites, from [6.15].

In *a*-direction, there are 9 modes out of 25 IR-active [$7B_{1u}(c)+9B_{2u}(b)+9B_{3u}(a)$], from all 60 Γ–point phonons calculated for orthorhombically distorted $YTiO_3$. The phonon modes are divided into three groups with characteristic frequencies: modes around ~ $170cm^{-1}$, or external modes, corresponding to TiO_6 octahedron vibration against the Y-atoms, around ~ $340cm^{-1}$ is the cluster of the bending modes (Ti-O-Ti bond angle modulation), and finally modes ~ $540cm^{-1}$ correspond to Ti-O stretching modes (bond length modulation). Lattice-dynamics calculations in the framework of the shell model were applied to determine and assign the eigenmodes in the orthorhombic $YTiO_3$ [6.9]. The eigenmodes and their assignment are given in the next section along with the results from the temperature and magnetic field dependence.

b-axis, *E||b(bc)*

In *b*-direction, there are also 9 IR-active phonon modes (Fig. 6.2.1.2).

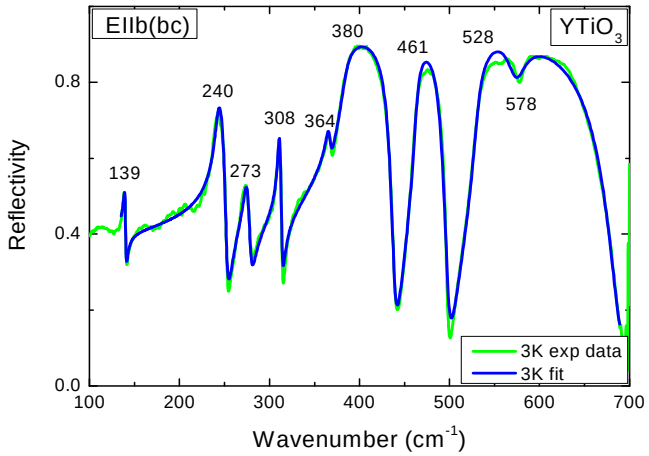

Figure 6.2.1.2 Experimental reflectivity (green) and fit curve (dark blue) for *b*-polarization at 3K. Numbers indicate the phonon frequencies in (cm^{-1}).

c-axis, *E||c(bc)*

Along *c*-axis there are 7 IR-active phonon modes (Fig. 6.2.1.3).

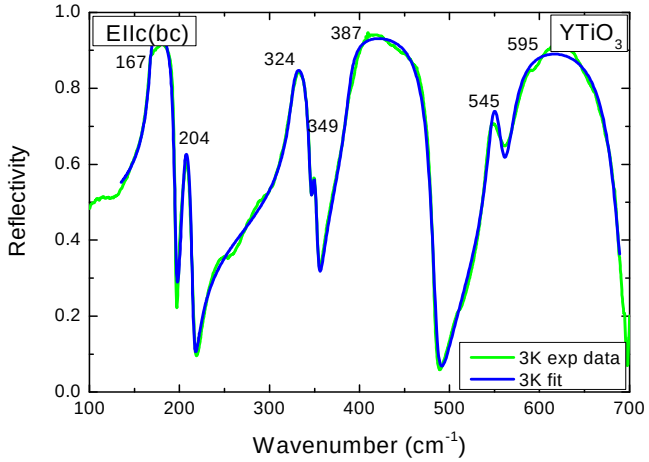

Figure 6.2.1.3 Experimental reflectivity (green) and fit curve (dark blue) for *c*-polarization at 3K. Numbers indicate the phonon frequencies in (cm^{-1}).

6.2.2 Magnetic Field and Temperature Dependence

a-axis, *E*||*a(ac)*, *B*||*b*

Figure 6.2.2.1 presents magnetic field dependence reflectivity spectra taken at temperature T = 30K, near of the magnetic transition. The magnetic field is applied perpendicular to the (*ac*) plane, i.e., along the *b*-axis. The spectrum ratio, R(8T) / R(0T), called also 100% line, is plotted and magnified into the figure on the right hand side along with the model fit curve. Here, and for the other two polarizations, we focus on the magnetic field dependence of the reflectivity spectra at this particular temperature point, as the observed magnetic field-induced effects are pronounced.

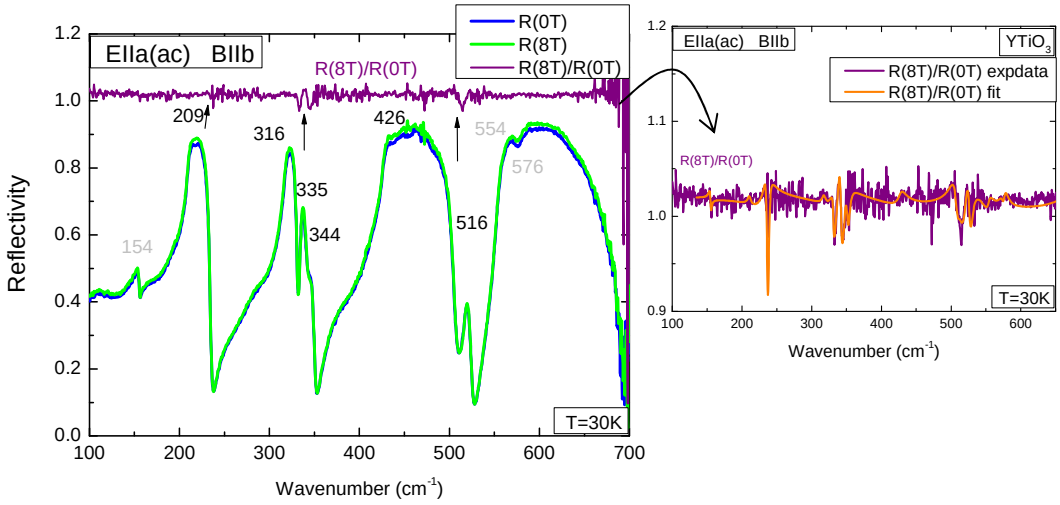

Figure 6.2.2.1 left: Reflectivity spectra E||*a* (*ac*-plane) and B||*b* configuration, at zero field R(0T) (blue) and at 8Tesla, R(8T) (green) taken near the magnetic transition temperature of T=30K. Numbers denote the phonon mode frequencies. The numbers given in black indicate phonon modes that respond noticeably to magnetic field. The ratio R(8T)/R(0T), plotted (in violet) represents the magnetic field-induced changes (black arrows point towards the features) **right:** R(8T)/R(0T) ratio, experimental data (violet), and the fit result (orange).

In order to clarify the observed effects upon application of magnetic field (the features in the R(8T) / R(0T) ratio, indicated by arrows in the figure), we have performed a model fit on the experimental data for all fields (0 to 8T) and temperature points (3 to 100K). The results yield changes in the oscillators characteristics; frequency, strength and damping.

Due to magnetostriction, all of the modes do experience some changes in magnetic field. However, in this particular polarization (E||*a* and direction of magnetic field B||*b*), the observed effects are very small, there are few modes close in frequency and it is therefore hard to estimate the contribution of each particular mode precisely. It is now instructive to compare the impact on the phonon modes due to application of magnetic field obtained at fixed T = 30K, to the temperature dependence when the system approaches and enters the magnetic state. Apart from the physical information one can get out of such study, the comparison can be a good point of reference as to whether the observed changes are real, or if they are artifacts from uncertainties in the measurement and/or the fitting procedure. Figure 6.2.2.2 shows experimental spectra taken at the lowest temperature of 3K and at the highest of 100K. Their R(3K) / R(100K) ratio, and the result from the fitting procedure are compared in the figure on the right hand side.

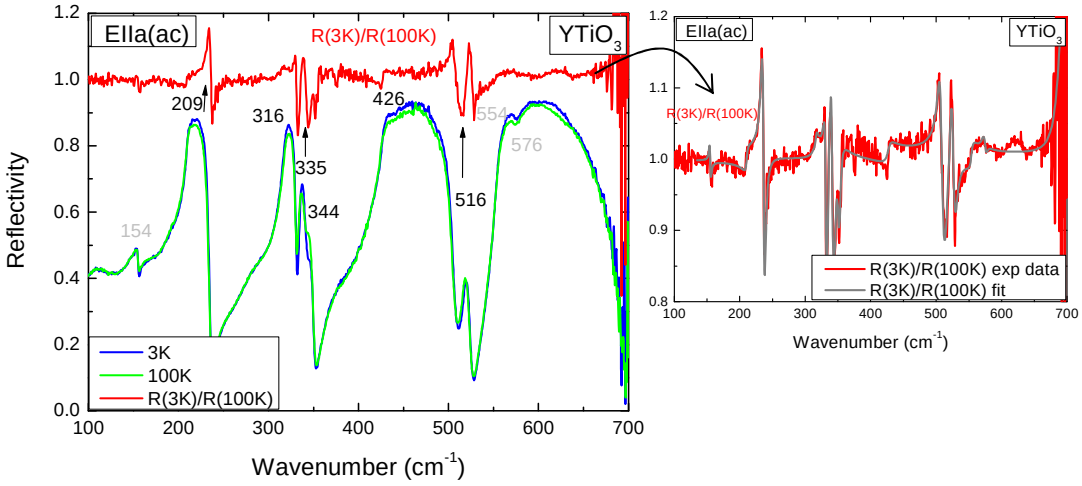

Figure 6.2.2.2 left: Zero field reflectivity spectra E||*a* (*ac*-plane), at T=3K (blue) and at T=100K (green). Numbers denote the phonon mode frequencies. The numbers given in black indicate phonon modes that undergo noticeable changes. The ratio R(3K)/R(100K), plotted (in red) represents the temperature induced changes **right:** R(3K)/R(100K) ratio, experimental data (red), and the fit result (grey).

Figures 6.2.2.3 below show the parameters, frequency ω_j and damping γ_j, obtained from fit of the phonon modes along the *a*-axis. Plots are given as a function of temperature at zero field (left), and as a function of the applied magnetic field at T = 30K (middle). The assignment and the calculated eigenvectors are shown for each particular mode (right).

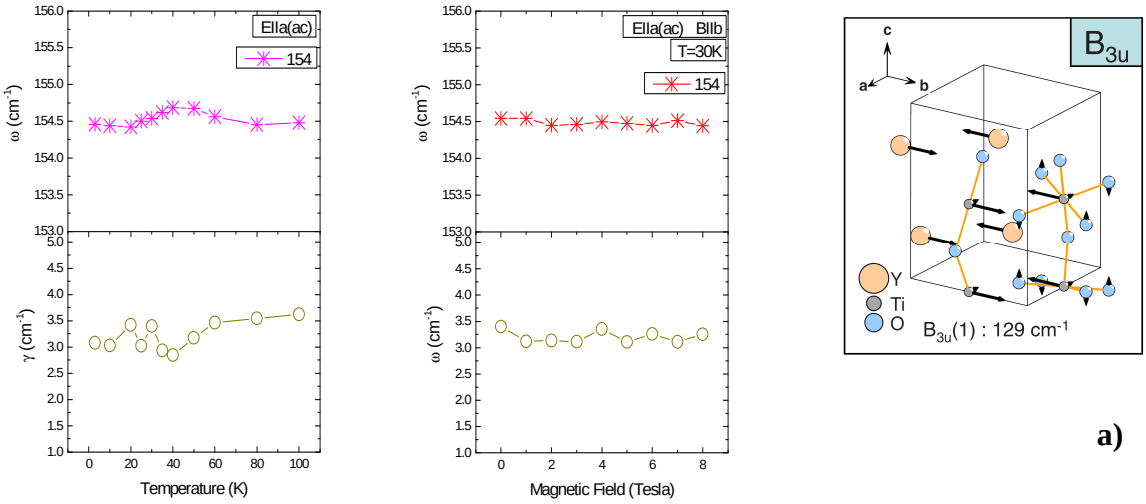
Ella(ac)
154
ω (cm-1)
γ (cm-1)
Temperature (K)
Ella(ac) Bllb
T=30K
154
Magnetic Field (Tesla)
B3u
c
a
b
Y
Ti
O
B3u(1) : 129 cm-1

a)

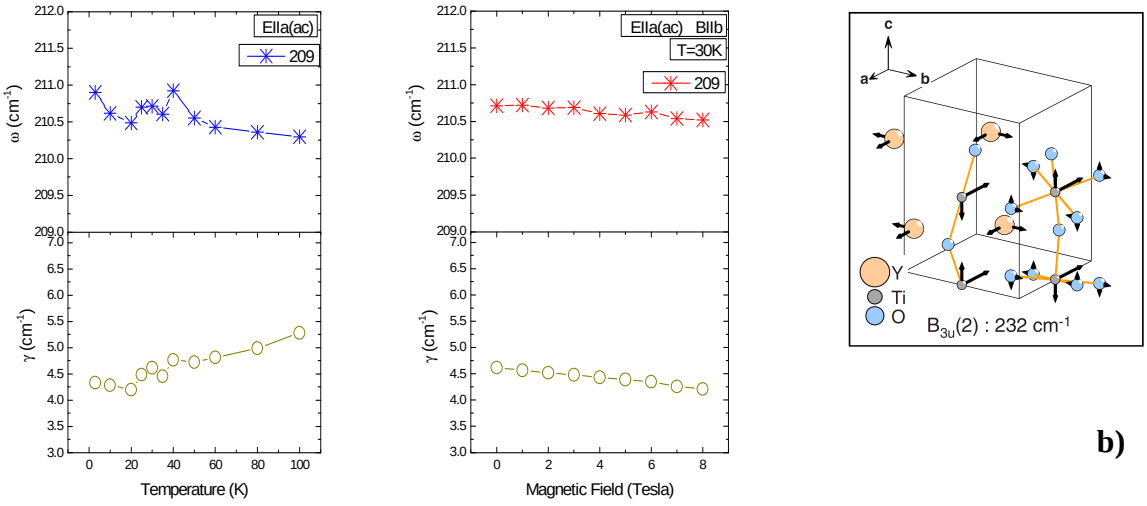
Ella(ac)
209
ω (cm-1)
γ (cm-1)
Temperature (K)
Ella(ac) Bllb
T=30K
209
Magnetic Field (Tesla)
c
a
b
Y
Ti
O
B3u(2) : 232 cm-1

b)

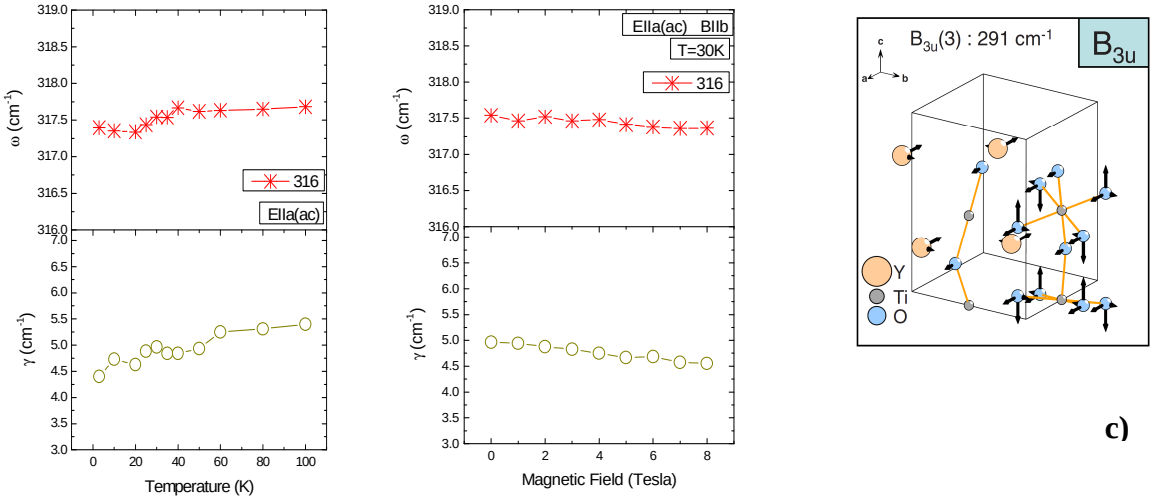
316
Ella(ac)
ω (cm-1)
γ (cm-1)
Temperature (K)
Ella(ac) Bllb
T=30K
316
Magnetic Field (Tesla)
B3u(3) : 291 cm-1
B3u
c
a
b
Y
Ti
O

c)

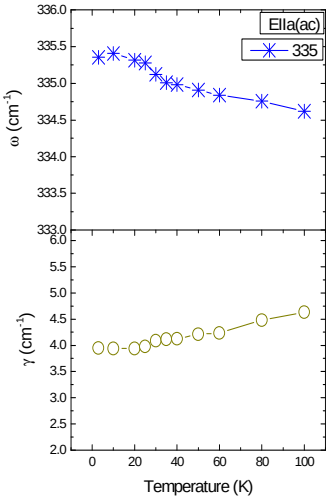
EIIa(ac)
335
ω (cm-1)
γ (cm-1)
Temperature (K)

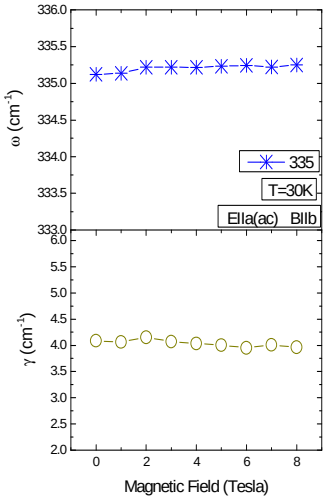
335
T=30K
EIIa(ac) BIIb
ω (cm-1)
γ (cm-1)
Magnetic Field (Tesla)

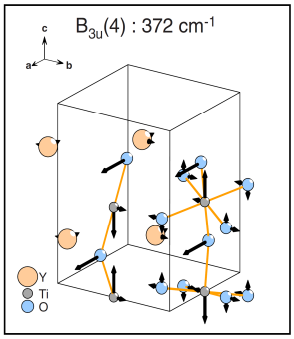
B3u(4) : 372 cm-1
Y
Ti
O

d)

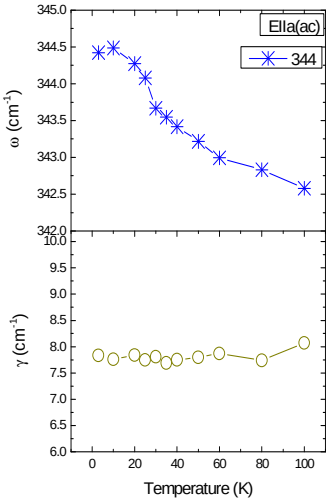
EIIa(ac)
344
ω (cm-1)
γ (cm-1)
Temperature (K)

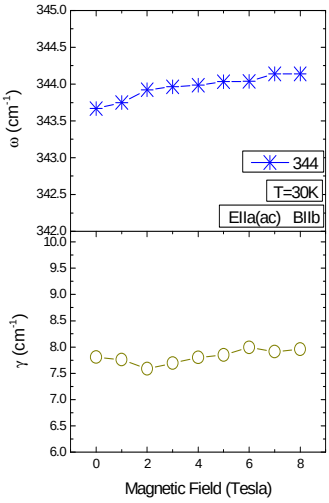
344
T=30K
EIIa(ac) BIIb
ω (cm-1)
γ (cm-1)
Magnetic Field (Tesla)

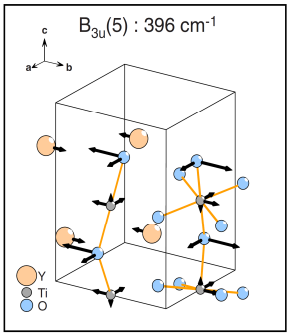
B3u(5) : 396 cm-1
Y
Ti
O

e)

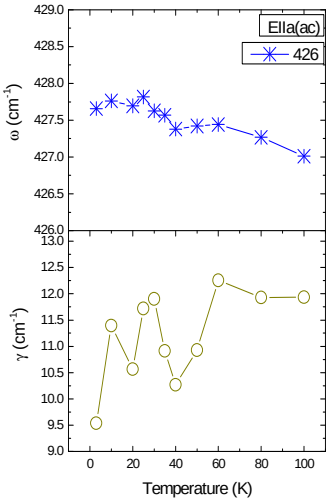
EIIa(ac)
426
ω (cm-1)
γ (cm-1)
Temperature (K)

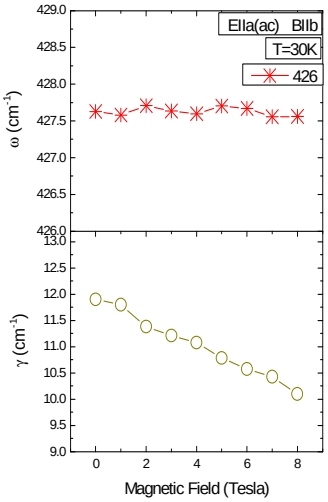
EIIa(ac) BIIb
T=30K
426
ω (cm-1)
γ (cm-1)
Magnetic Field (Tesla)

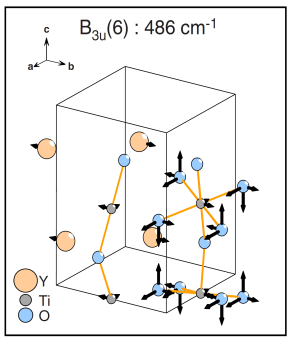
B3u(6) : 486 cm-1
Y
Ti
O

f)

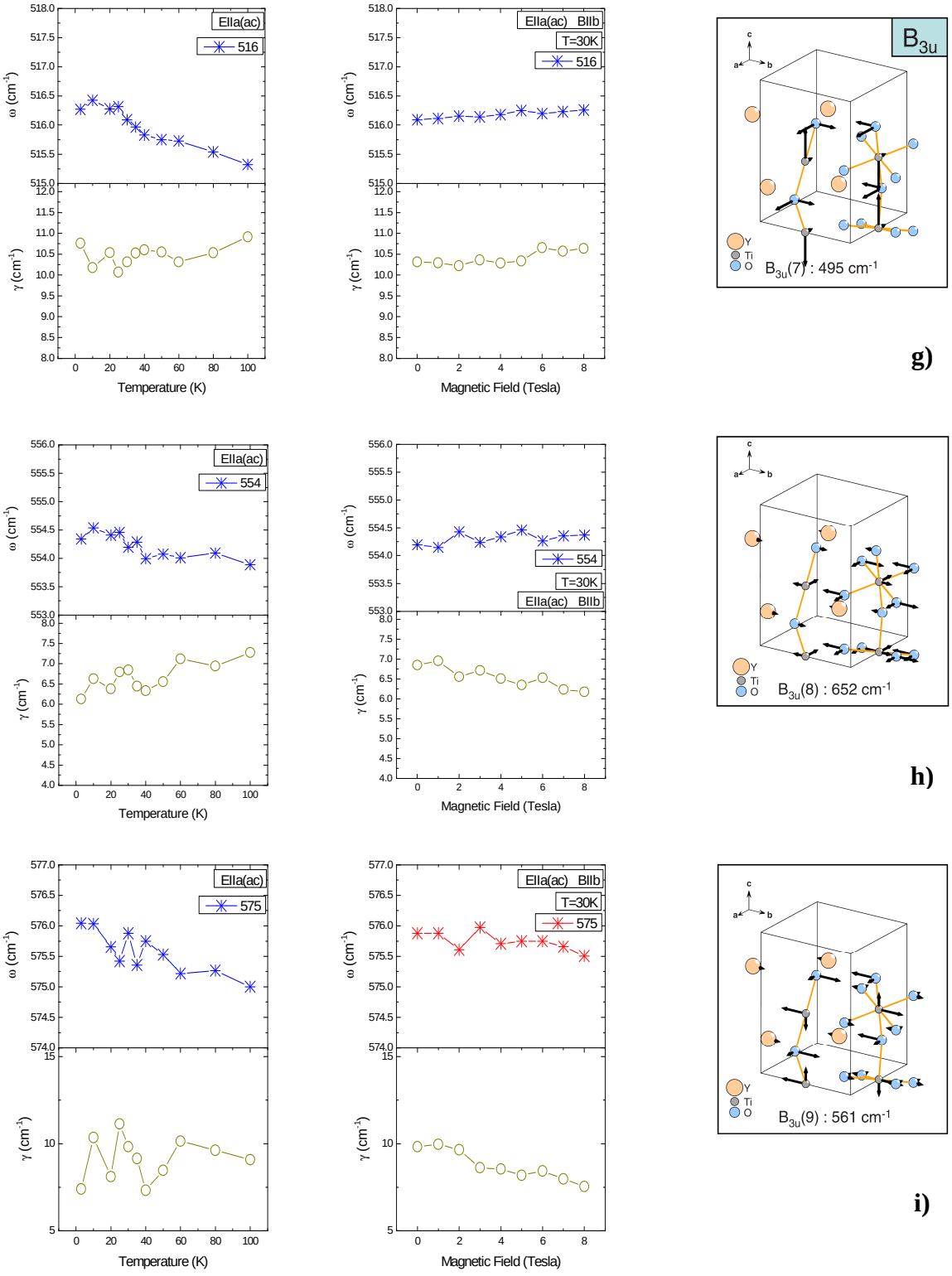

Figure 6.2.2.3 Zero field temperature (left columns), and magnetic field at T = 30K (mid columns), dependence of the oscillator parameters, frequency ω_0 (cm^{-1}) and damping γ (cm^{-1}), for the modes in E||*a* polarization and direction of magnetic field B||*b*,. The modes assignment is given in the boxes (right columns), from [6.9].

An interesting observation is that for some of the modes the increase of magnetic field at fixed temperature induces similar changes in their parameters on cooling at zero field. There are however some deviations from this behavior. The cases, in which the changes in the mode parameters are very small and oscillate, are referred to the experimental error bar (the connecting lines are only guide to the eye). For the rest of the data presented, we are confident, as the magnetic field and the temperature dependence are practically distinct measurements; we sweep the magnetic field from 0 to 8 Tesla at each temperature point. Furthermore one can compare the response from all three optical axes and search for consistency (we give such comparative plots in the conclusion section). The similarities in the magnetic field / temperature-induced changes can also be seen in the ratio spectra: R(8T) / R(0T) and R(3K) / R(100K), respectively. Such a qualitative similarity in the magnetic and temperature scales is indicative of spin-lattice coupling. The temperature dependence of the phonon parameters presented above, show also clear anomalies on approaching the magnetic transition. Some of the modes shift to higher frequencies, others soften. Deviations from the usual anharmonic behavior, i.e., without spin-phonon interaction, can be noticed even at temperatures, far above T_c. We will discuss these issues later in the conclusion section.

The mode at 154cm^{-1} (Fig. 6.2.2.3 (a)) belongs to the group of external modes and the eigenvectors indicate out-of-phase vibrations of Y and Ti atoms polarized along the *b*-axis. It has very small oscillator strength and shows small changes with temperature and field. The frequency however, exhibit anomaly around 40K and on further cooling it decreases. One can assume that magnetic field applied at T = 30K, induces small decrease of frequency too. The mode at 209cm^{-1} (Fig. 6.2.2.3 (b)), involve collective Y-Ti vibrations where Y and Ti move in opposite directions. Application of magnetic field and temperature decrease reduce its damping. The frequency experience a red shift according to the magnetic field dependence but the trend is not well defined in the temperature dependence. From the group of bending modes, 316 cm^{-1} and 426 cm^{-1} (Fig. 6.2.2.3 (c) and (f)), involve collective vibrations from O2 atoms and also some contribution due to in-phase vibrations of O1 and out-of-phase of Y atoms for the former. 316 cm^{-1} shows a definite red shift while 426 cm^{-1} increase its frequency. The modes at 335 cm^{-1} and 344 cm^{-1} (Fig. 6.2.2.3 (d) and (e)) also belong to this group and the one at

344 cm^{-1} is assigned as Ti-O1-Ti bond bending. The fit parameters for these modes show relatively large changes along B and T scales. The mode at 516 cm^{-1} (Fig. 6.2.2.3 (g)), is determined by O1 collective vibrations. On increasing the magnetic field, this particular mode increases its frequency as well as its damping. Finally, in the group of stretching modes, the one at 554 cm^{-1} (Fig. 6.2.2.3 (h)), is assigned to Ti - O2 collective out of phase vibration, and at 576 cm^{-1} (Fig. 6.2.2.3 (i)), *b*-polarized out-of-phase vibrations of Ti and O1 atoms. Both show blue shifts, except may be the 576 cm^{-1} upon application of field showing decrease of frequency.

The first three phonon modes along *a*-axis show tendency to soften on decreasing the temperature and upon application of field. Although for modes 154 cm-1 and 209 cm^{-1}, the changes are within the experimental error, the one at 316 cm^{-1} shows a definite red shift. The high frequency modes increase their frequency on cooling and upon application of magnetic field. Pronounced changes in the phonon parameters can be noticed at temperature around T ~ 40K.

b-axis, *E||b(bc), B||a*

In contrast to the magnetic field dependence along the *a*-axis, here, the field induced changes are much more clear (Fig. 6.2.2.4). The modes are well separated in frequency and it is easy to identify the contribution of each of them to the observed magnetic field effect with a good precision. As in the previous case, a fit procedure was applied for the magnetic field dependence at T = 30K as well as for the temperature dependence, from 3 to 100K, at zero field. Figures 6.2.2.4 and 6.2.2.5 below, compare the changes the phonon modes undergo in high fields to that on reducing the temperature. The total effect, i.e., the ratio spectra are given on separate figures (right) together with the results from the fit. In this case a simple look at the ratio lines is enough to conclude that the changes on sweeping the magnetic field resemble those induced from reducing the temperature.

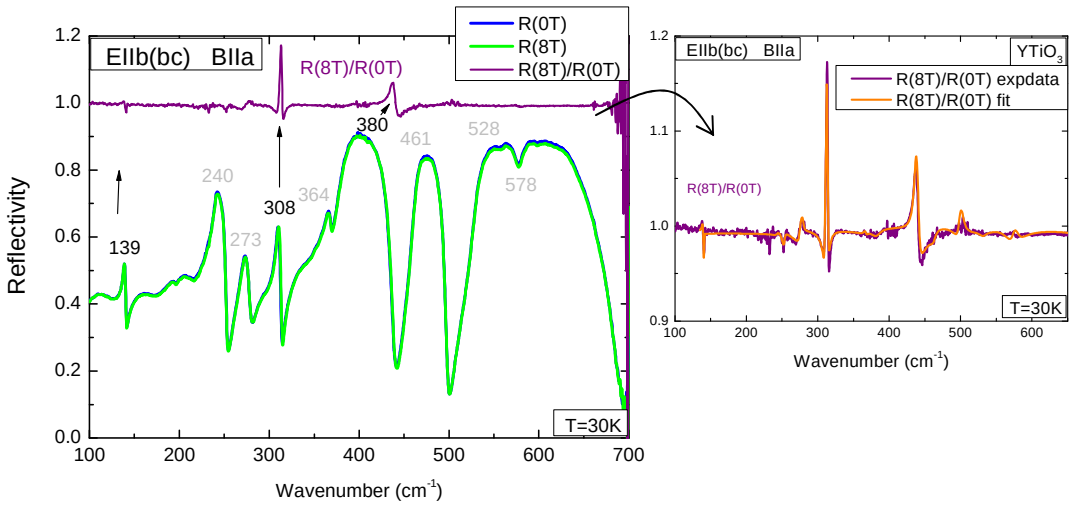

Figure 6.2.2.4 left: Reflectivity spectra E||*b* (*bc*-plane) and B||*a* configuration, at zero field R(0T) (blue) and at 8Tesla, R(8T) (green) taken near the magnetic transition temperature of T = 30K. Numbers denote the phonon mode frequencies. The numbers given in black indicate phonon modes that respond noticeably to magnetic field. The ratio R(8T)/R(0T), plotted (in violet) represents the magnetic field-induced changes (black arrows point towards the features) **right:** R(8T)/R(0T) ratio, experimental data (violet), and the fit result (orange).

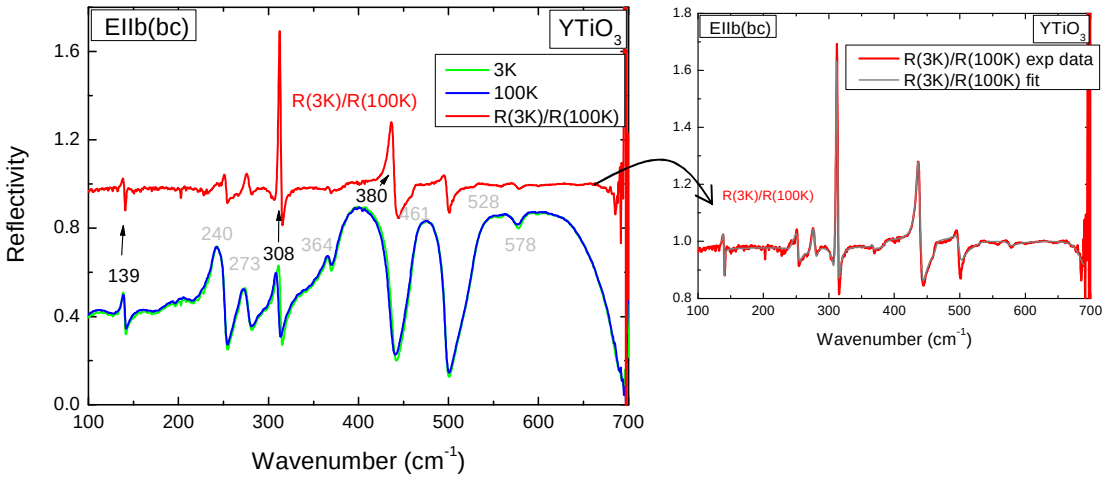

Figure 6.2.2.5 left: Zero field reflectivity spectra E||*b* (*bc*-plane), at T=3K (blue) and at T=100K (green). Numbers denote the phonon mode frequencies. The numbers given in black indicate phonon modes that change noticeably. The ratio R(3K)/R(100K), plotted (in red) represents the temperature induced changes **right:** R(3K)/R(100K) ratio, experimental data (red), and the model fit result (grey).

The following figures 6.2.2.6, represent results from fit of the modes in *b*-polarization.

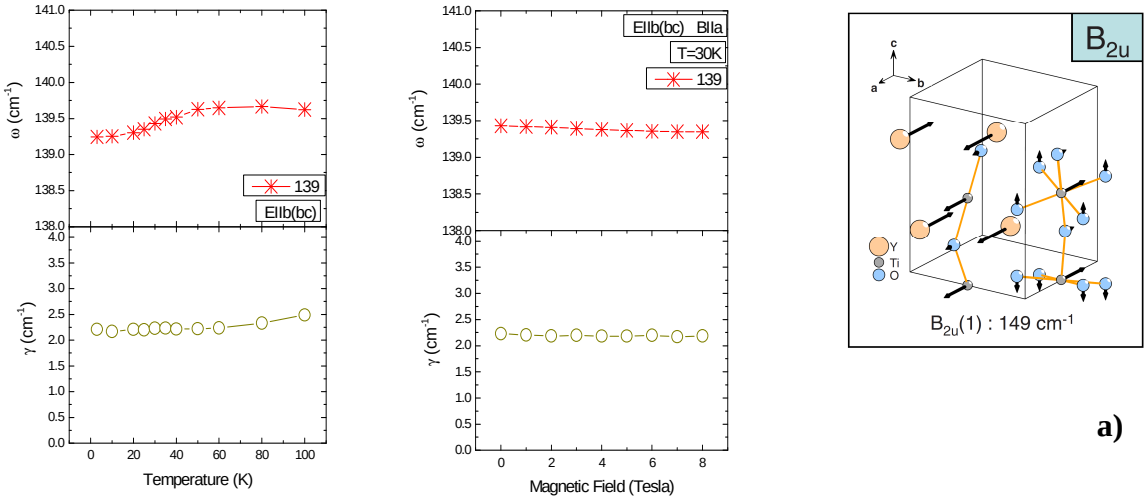

a)

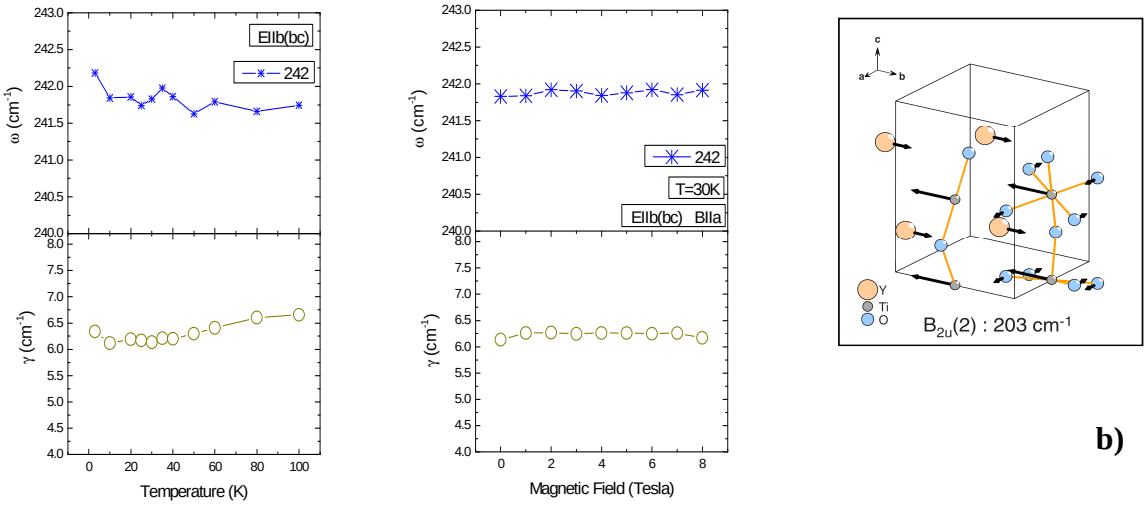

b)

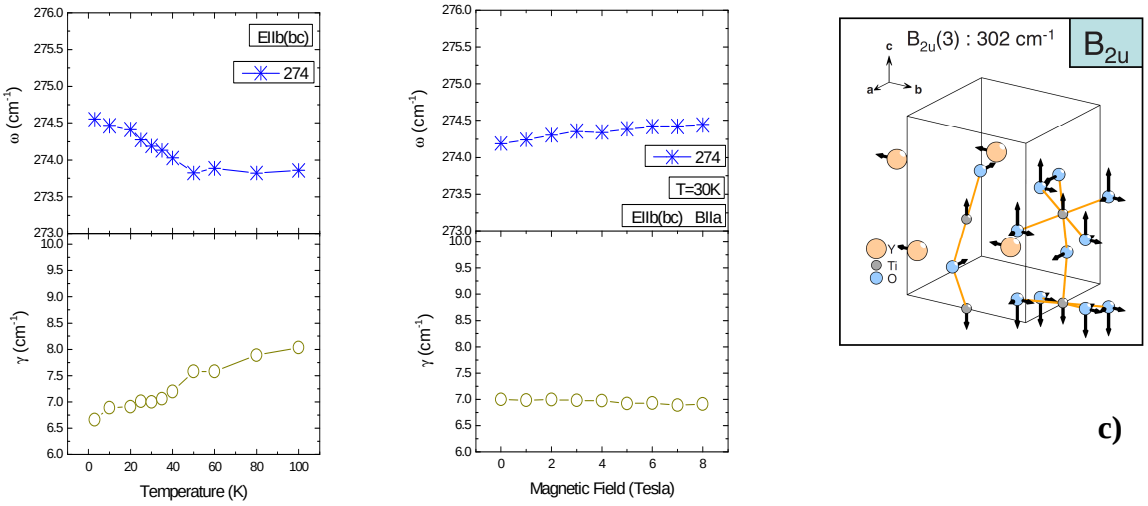

c)

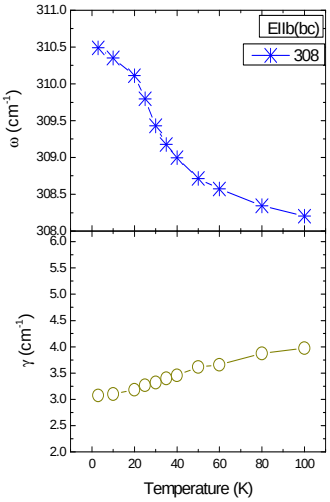
EIIb(bc)
308
ω (cm-1)
γ (cm-1)
Temperature (K)

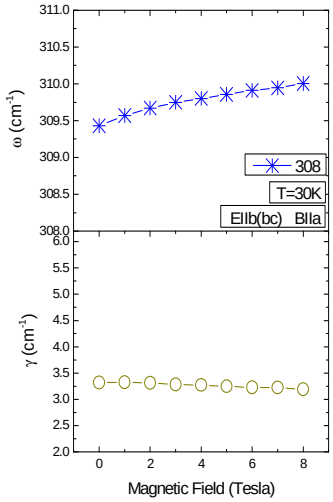
308
T=30K
EIIb(bc) BIIa
ω (cm-1)
γ (cm-1)
Magnetic Field (Tesla)

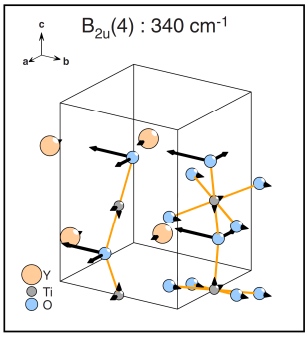
B2u(4) : 340 cm-1
Y
Ti
O

d)

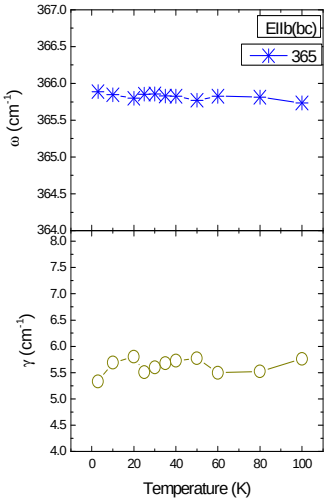
EIIb(bc)
365
ω (cm-1)
γ (cm-1)
Temperature (K)

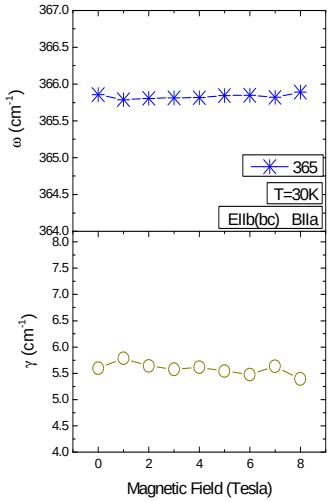
365
T=30K
EIIb(bc) BIIa
ω (cm-1)
γ (cm-1)
Magnetic Field (Tesla)

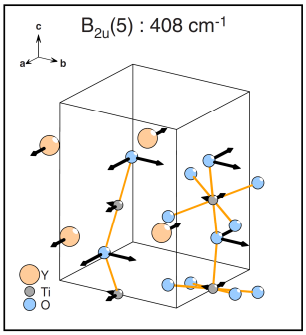
B2u(5) : 408 cm-1
Y
Ti
O

e)

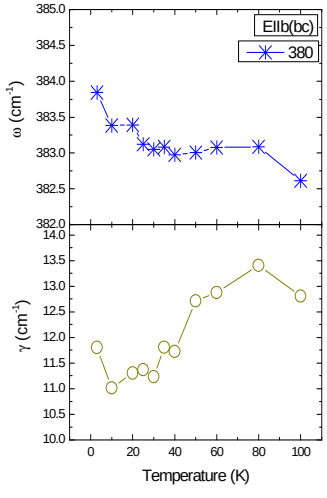
EIIb(bc)
380
ω (cm-1)
γ (cm-1)
Temperature (K)

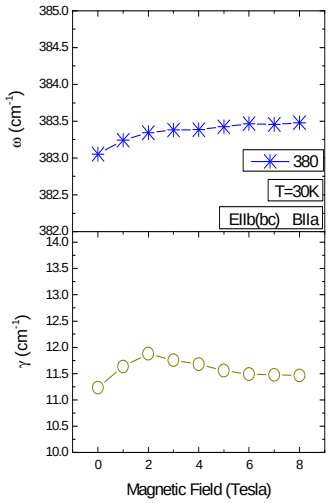
380
T=30K
EIIb(bc) BIIa
ω (cm-1)
γ (cm-1)
Magnetic Field (Tesla)

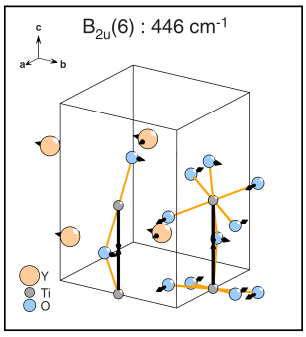
B2u(6) : 446 cm-1
Y
Ti
O

f)

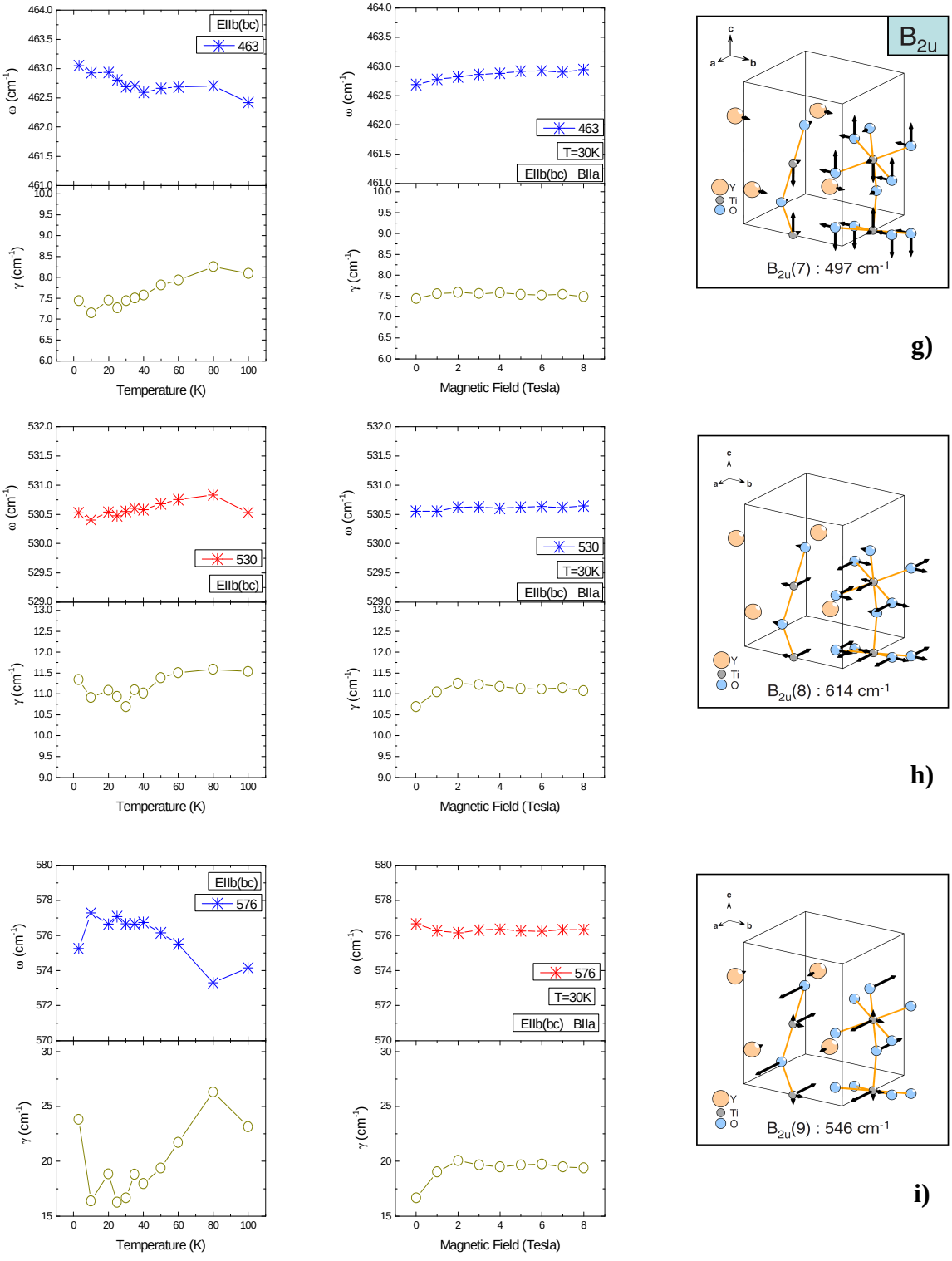

Figure 6.2.2.6 Zero field temperature (left columns), and magnetic field at T=30K (mid columns), dependence of the oscillator parameters, frequency ω_0 (cm^{-1}) and damping γ (cm^{-1}), for the modes in E||*b* polarization and direction of magnetic field B||*a*,. The modes assignment is given in the boxes (right columns).

The eigenvectors of the 139 cm^{-1} external mode (Fig. 6.2.2.6 (a)), indicate contribution primarily due to out-of-phase vibrations of Y and Ti atoms along *a*-axis. It shows a definite decrease of frequency with increasing the field and on cooling with an onset temperature of about 80K. The mode at 242 cm^{-1} (Fig. 6.2.2.6 (b)), is due to collective Y-Ti vibrations in opposite directions polarized in accordance with the mode symmetry. The induced changes are weak and oscillatory but one can assume an overall increase of frequency. 274 cm^{-1}, (Fig. 6.2.2.6 (c)), involve collective vibrations of O2 and Y atoms moving in opposite directions. It shows clear hardening below T ~ 40K and at high field.
The trends in the frequency change for the modes (Fig. 6.2.2.6 (d) to (g)) are similar. All show increase of frequency and decrease of damping. The one at 308 cm^{-1} is defined mainly by O1 vibrations, moving out-of-phase with the O2 atoms. At 365 cm^{-1}, is due to Ti-O1-Ti bending modulation. The 380 cm^{-1} mode is determined by O1 collective vibrations polarized according to the mode symmetry. However, the assignment of this particular mode is not unambiguous and can be exchanged with the eigenvectors for the $B_{2u}(5)$ mode (at 365 cm^{-1}), (Fig. 6.2.2.6 (e)). And the mode at 463 cm^{-1}, involves collective vibrations of O2 and Y atoms in opposite directions. Finally, the high frequency 530 cm^{-1} and 578 cm^{-1} are assigned to *b*-axis Ti-O2 bond stretching and symmetric *b*-polarized out-of-phase vibrations of Ti and O1 atoms, respectively. The former mode softens while the fit result for the latter shows a rather strong temperature dependence of frequency and damping. However, this could be an artifact coming from fitting of a limited spectral range.

c-axis, *E||c(bc), B||a*

Similarly, as for the previous two axes, the magnetic field dependence at T=30K is presented and compared with the zero field temperature data (Fig. 6.2.2.7 and 8).

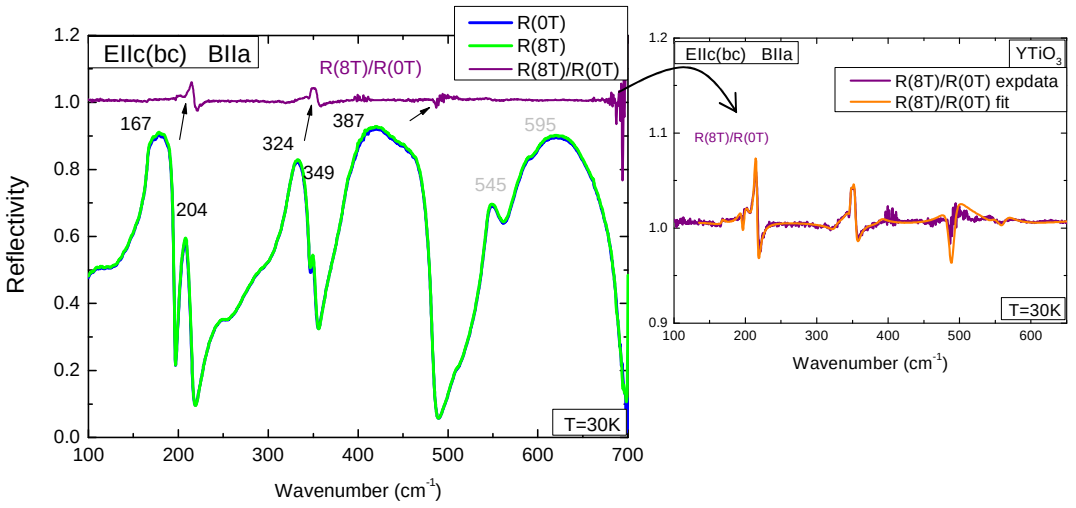

Figure 6.2.2.7 left: Reflectivity spectra E||*c* (*bc*-plane) and B||*a* configuration, at zero field R(0T) (blue) and at 8Tesla, R(8T) (green) taken near the magnetic transition temperature of T = 30K. Numbers denote the phonon mode frequencies. The numbers given in black indicate phonon modes that respond noticeably to magnetic field. The ratio R(8T)/R(0T), plotted (in violet) represents the magnetic field-induced changes (black arrows point towards the features) **right:** R(8T)/R(0T) ratio, experimental data (violet), and the fit result (orange).

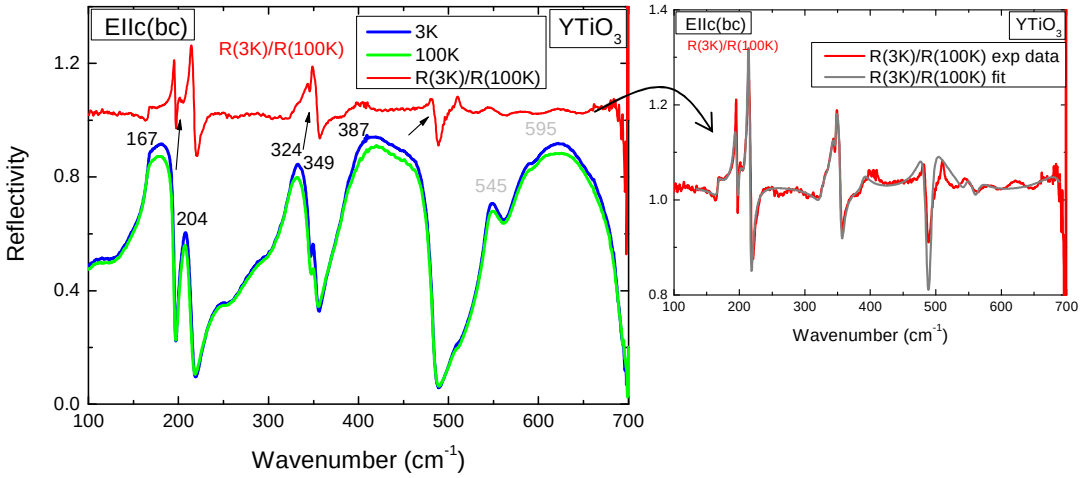

Figure 6.2.2.8 left: Zero field reflectivity spectra E||*c* (*bc*-plane), at T=3K (blue) and at T=100K (green). Numbers denote the phonon mode frequencies. The numbers given in black indicate phonon modes that change noticeably. The ratio R(3K)/R(100K), plotted (in red) represents the temperature induced changes **right:** R(3K)/R(100K) ratio, experimental data (red), and the fit result (grey).

In *c*-polarization, as in the E||*a* case, the magnetic field effects are somewhat weaker. On the following figures 6.2.2.9, the fit results for all seven modes along the *c*-axis are presented.

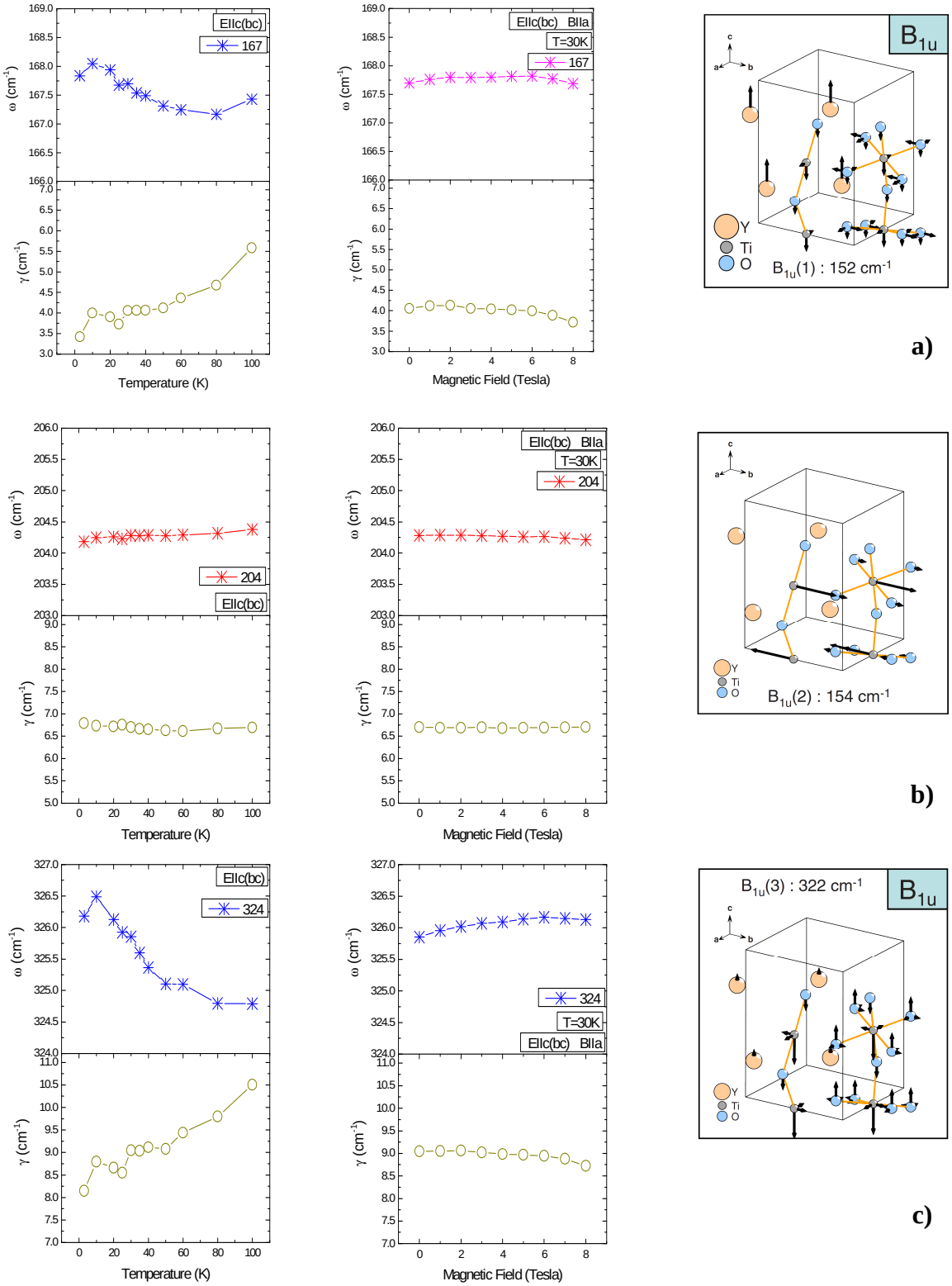

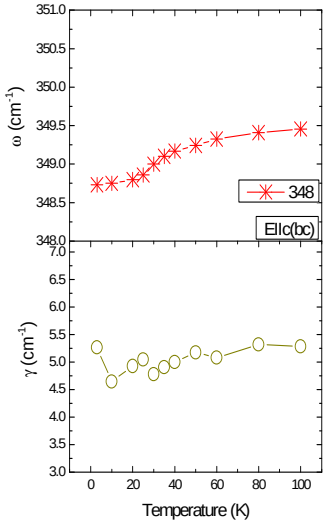
ω (cm⁻¹)
γ (cm⁻¹)
348
EIIc(bc)
Temperature (K)

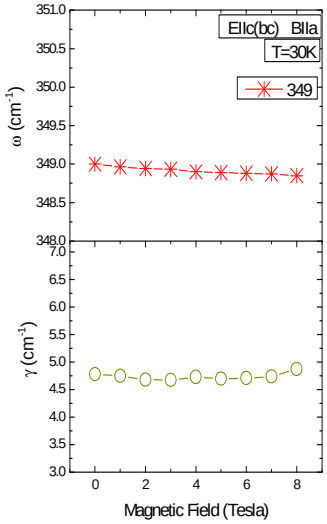
EIIc(bc) BIIa
T=30K
349
ω (cm⁻¹)
γ (cm⁻¹)
Magnetic Field (Tesla)

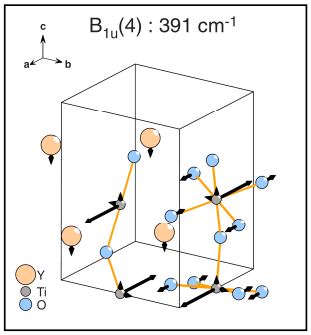
B1u(4) : 391 cm-1
c
a
b
Y
Ti
O

d)

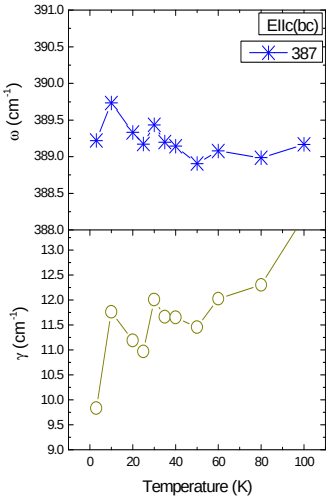
EIIc(bc)
387
ω (cm⁻¹)
γ (cm⁻¹)
Temperature (K)

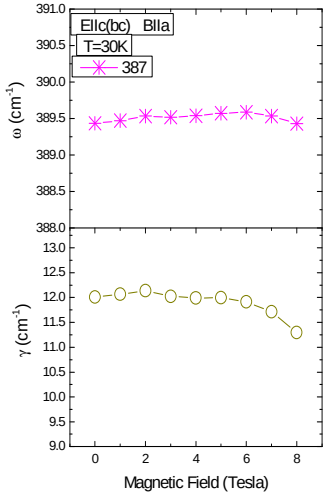
EIIc(bc) BIIa
T=30K
387
ω (cm⁻¹)
γ (cm⁻¹)
Magnetic Field (Tesla)

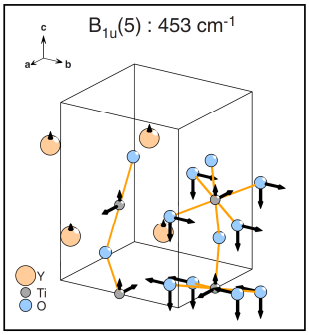
B1u(5) : 453 cm-1
c
a
b
Y
Ti
O

e)

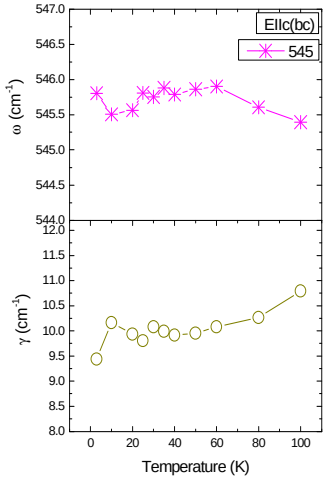
EIIc(bc)
545
ω (cm⁻¹)
γ (cm⁻¹)
Temperature (K)

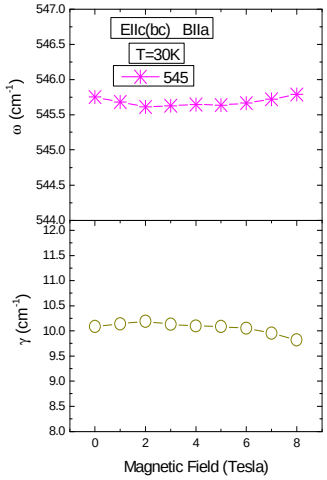
EIIc(bc) BIIa
T=30K
545
ω (cm⁻¹)
γ (cm⁻¹)
Magnetic Field (Tesla)

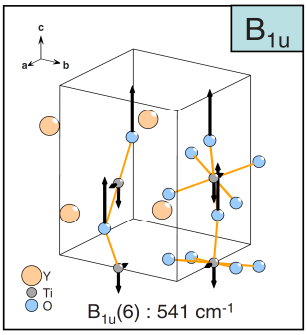
B1u
c
a
b
Y
Ti
O
B1u(6) : 541 cm-1

f)

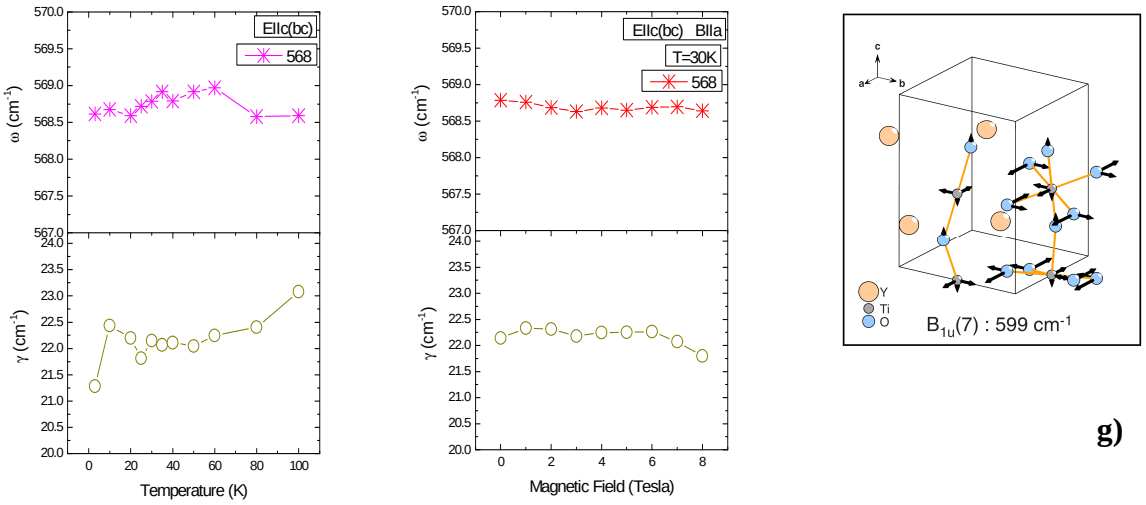

Figure 6.2.2.9 Zero field temperature (left columns) and magnetic field at T=30K (mid columns), dependence of the oscillator parameters, frequency ω_0 (cm^{-1}) and damping rate γ (cm^{-1}), for the modes in E||*c* polarization and direction of magnetic field B||*a*,. The modes assignment is given in the boxes (right columns).

The eigenvector of the 167cm^{-1} mode (Fig. 6.2.2.9 (a)), is determined by vibrations of TiO_6 octahedra against Y atoms along the *c*-axis, and the one of the 204cm^{-1} mode (Fig. 6.2.2.9 (b)), is mainly due to *b*-axis in-phase vibrations of Ti atoms in one plane and out-of-phase vibrations in different planes. With decreasing the temperature, the 167cm^{-1} mode shows an upturn in the frequency at 80K and starts to increase down to Tc~30K where a small anomaly is observed after which it keeps rising down to 10K where it starts to decrease. The observed changes are small and perhaps cannot be a taken as a basis for solid conclusions. The overall temperature dependence however shows increase of frequency and seems to show just the opposite behavior compared to the phonon in *b*-polarization, i.e., at 139cm^{-1}. The mode at 204cm^{-1} shows definitive softening. The next three phonons 324cm^{-1}, 349cm^{-1} and at 387cm^{-1}, belong to the group of bending modes (Fig. 6.2.2.9 (c), (d) and (e)). 324cm^{-1} as well as 387cm^{-1} are assigned to Ti-O2-Ti bending vibrations as the former has small admixture of O1 character due to movement of O1 atoms in-phase with Ti atoms. Both modes exhibit an overall increase of frequency and concomitant reduction of damping. The mode at 349cm^{-1} has very small oscillator strength and can be assigned to *a*-axis out-of-phase vibrations of Ti atoms. It shows a

smooth and well defined decrease of frequency. The higher frequency phonons, 545cm^{-1} and 568cm^{-1} (Fig. 6.2.2.9 (f) and (g)), are due to *c*-axis Ti-O1 bond length modulation and symmetric ab-polarized out-of-phase oscillations of Ti and O2 atoms. Both modes show very weak temperature and magnetic field dependence.

6.3 Discussion and Conclusions

Using a home-built near-normal incidence reflectance setup and spectroscopic ellipsometry, both described in Chapter 4, the temperature (3 to 100K) and magnetic field (0 to 8T) dependence of all 25 IR active phonon modes along the three principal crystal axes, E||*a*, E||*b* and E||*c*, in ferromagnetic $YTiO_3$ has been obtained. It was found that application of magnetic field influences the phonon mode characteristics and these are predominantly the Ti-O-Ti bond bending modulation modes. The experimental data was fitted by a sum of Lorentzians and the oscillator parameters, frequency ω_j and damping γ_j, were presented for all three directions, *a*, *b* and *c*, as a function of temperature at zero field, and as a function of the external magnetic field at fixed temperature of T = 30K, just above the T_c. The overall trend observed is that the mode parameters exhibit similar behavior in the induced changes with decreasing temperature and increasing magnetic field. This finding can be attributed to a spin-phonon coupling in $YTiO_3$. Interestingly, the onset of magnetic field induced effects on the phonon parameters was found to start far above the T_c, i.e., at T ~ 80-100K. We discuss this issue below. In *b*-polarization the observed magnetic field induced changes are large and clear, and they were accurately quantified. In contrast, along the *a*- and *c*-axes, the changes are weak, the phonons are close in frequency and it was difficult to extract precise quantitative information about the mode characteristics. The fit procedure in such cases may return ambiguous results. However, the comparative study between the magnetic field / temperature dependence give us confidence that the fit results are to a good extent reliable, moreover in the following, we will be interested mainly in trends, not in precise values.

Spin - Phonon Coupling in Other Compounds

Spin-phonon coupling and concomitant anomalies in the oscillator parameters in magnetic crystals close to temperature of magnetic transitions are relatively well studied [6.16][6.17]. In the manganites for example, the role of electron-lattice coupling in the emergence of magnetoresistive properties has been pointed by A. Millis [6.18][6.19]. The orbital state on the other hand, reflecting the electron-electron interaction is directly responsible for the variety of spin ordering configurations. Hence, a particular contribution to the electronic properties of neither of these degrees of freedom can be simply excluded. There are numerous experimental spectroscopic (infrared and Raman) studies that observe marked temperature and doping induced anomalies in the phonon mode parameters at the points where the magnetic and/or orbital state changes. For example, infrared reflectance experiments on $La_{1-x}Sr_xMnO_3$ crystals, at different doping levels i.e., x = 0.10 - 0.125 [6.20], showed pronounced effects predominantly on the (O-Mn-O) bond bending modes. For x = 0.11 and 0.125 (ferromagnetic metallic (FM)) phase, the modes were found to broaden and soften, while in the low-temperature orbitally ordered (ferromagnetic insulating (FI)) phase, they become sharper. These results revealed the strong correlation between electron magnetic and orbital state with the microscopic distortions of the Mn-O-Mn bond. The anomaly in the FM phase is assumed to originate from lattice instability due to competition between the double exchange (DE) interaction and the Jahn-Teller (JT) distortion. Similar conclusions have been made for the FM $La_{0.65}Sr_{0.35}MnO_3$ in Ref. [6.21]. The coupling between the DE interaction and the Mn–O–Mn angle is presumably based on the close relation between the bond angle and the bandwidth *W*. The observed effects in the orbitally ordered state are attributed to an enhancement of the effective charge of Mn in the Mn-O bond (in FI phase) and to the additional orbital polarization due to the orbital ordering.

A recent Raman study on series of orthorhombic $RMnO_3$, (R = Pr, Nd, Sm, Eu, Gd, Tb, Dy, Ho, Y), focused on the link between the magnetic structure and the emergence of deviations, $\Delta\omega(T) = \omega_{anh}(T) - \omega(T)$, from the usual anharmonic behavior ($\omega_{anh}(T) = \omega_o - C[1 + 2/(e^{\hbar\omega_o / k_B T} - 1)]$, where ω_o and C are adjustable parameters) in the

phonon spectrum [6.22][6.23]. It was established that the compounds with a large R^{3+} ionic radius r_R and A-type antiferromagnetic (AF) order, (R = Pr, Nd, Sm), exhibit significant softening and other anomalies around T_N involving mainly the B_{2g} stretching mode while for compounds with a small r_R and incommensurate magnetic structure, (R = Eu, Gd, Tb, Dy, Ho, Y), the effects are very weak or negligible. In the particular case of (R = Ho), E-type AF configuration, these effects were even absent. According to the model proposed by Granado *et al*. [6.24][6.22], the effect of phonon renormalization below T_N is proportional to the spin-spin correlation function $\langle S_i \cdot S_j \rangle$ for the nearest-neighbor (NN) spins at the *i*-th and *j*-th Mn sites. For example, in the A-type AF spin ordered $LaMnO_3$, in which a softening of 610 cm^{-1} Raman mode is observed, the *i*-th spin can be represented as:

$$S_i = \frac{M}{4\mu_B} + \Delta S_i \tag{6.3.1}$$

where M is the average sublattice magnetization per Mn^{3+} and ΔS_i is the spin fluctuation due to quantum and thermal effects. In case ΔS_i is neglected, the phonon renormalization scales with M^2. Thus, the renormalization in the phonon frequency due to spin-phonon coupling in $LaMnO_3$ (S = 2) can be approximated (mean-field) as:

$$\Delta\omega_{s-ph} \approx \omega(T) - \omega_{anh}(T) = \frac{1}{2m\omega}\frac{\partial^2 J(r)}{\partial u^2}\langle S_i \cdot S_j \rangle = \lambda_{s-ph}\left(\frac{M(T)}{4\mu_B}\right)^2 \tag{6.3.2}$$

where $\lambda_{s-ph} = \frac{1}{2m\omega}\frac{\partial^2 J(r)}{\partial u^2}$ is the coupling constant representing the phonon modulation of the NN exchange integral $J(r)$, ω is the corresponding mode frequency, and m and u are the mass and the displacement of the atom involved. This approach explains well the phonon behavior below T_N. However, in some cases the onset of the anomalous phonon shift is observed well above the actual magnetic transition temperature, see figure 6.3.1.

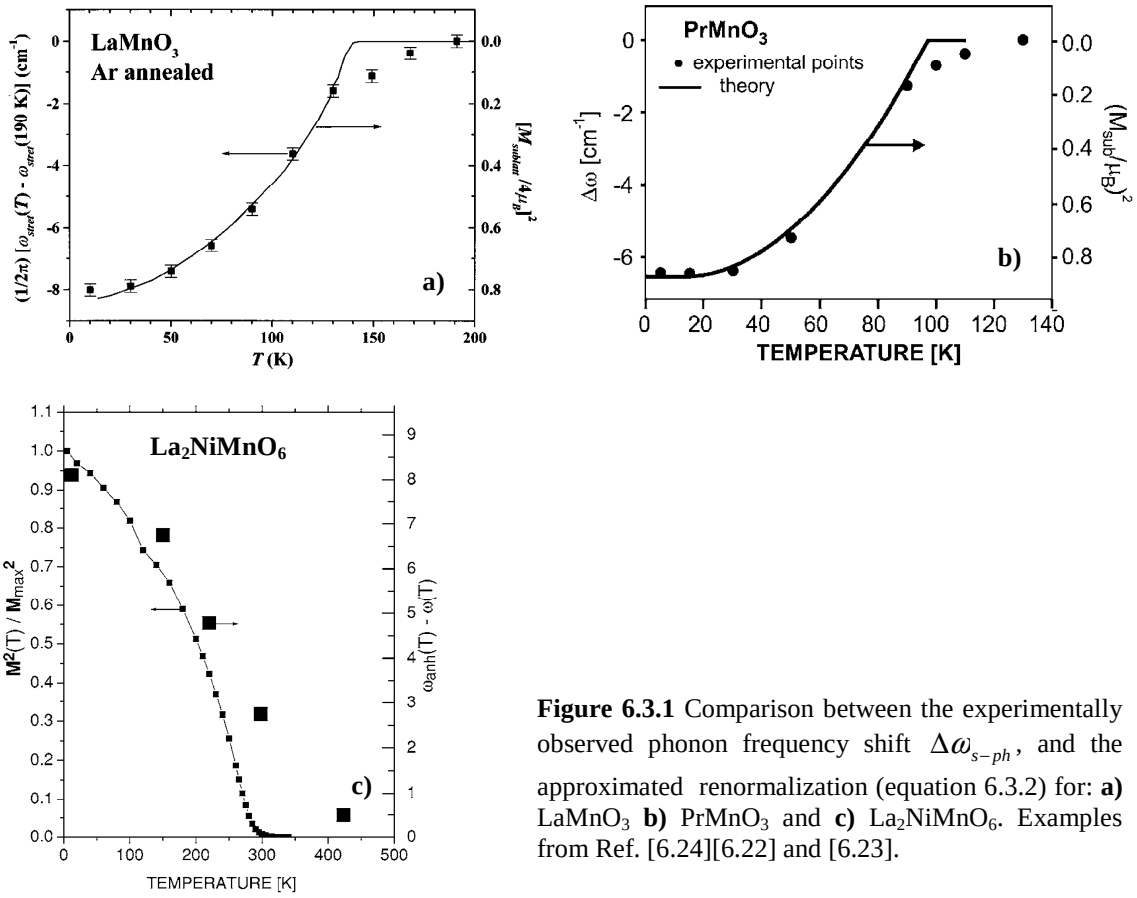

Figure 6.3.1 Comparison between the experimentally observed phonon frequency shift $\Delta\omega_{s-ph}$, and the approximated renormalization (equation 6.3.2) for: **a)** $LaMnO_3$ **b)** $PrMnO_3$ and **c)** La_2NiMnO_6. Examples from Ref. [6.24][6.22] and [6.23].

The renormalization of the phonon parameters above T_N can be explained by ferromagnetic correlations $\langle \Delta S_i \cdot \Delta S_j \rangle$ which exist even in the paramagnetic phase. In the more complex situations, in which the magnetic configurations result from competing FM nearest-neighbor and AFM next nearest-neighbor (NNN) interactions, like the incommensurate and E-type spin ordering, extensions that include all respective interactions in the model are necessary [6.22].

In a more recent and detailed study on $LaMnO_3$ two Raman bands, at 490 and 610 cm^{-1} respectively, were shown to exhibit softening behavior. The authors argued that a bare spin-phonon coupling mechanism is insufficient to describe the experimental data. A more sophisticated theoretical model that involves orbital-spin-phonon coupling is proposed to explain the results [6.25].

A comprehensive theoretical treatment of spin-phonon coupling in $RMnO_3$ manganites is given by JM. Wesselinova *et al*. in Ref. [6.26]. Expressions for the renormalized phonon energy and damping, renormalized spin-wave energy and spin exchange interaction constant J^{eff}, due to the spin-phonon interactions are derived. Numerical calculations, with parameters appropriate for orthorhombic $RMnO_3$ compounds and various spin-phonon interaction constants were presented, and found to be consistent with a large number of experimental results. Generally, the phonon frequency shifts below magnetic transition temperature are explained by the assumption for a spin-dependent force constant, given by the first and second derivatives of the nearest neighbor and next-nearest neighbor exchange interactions, $J_{1,2}(r_i\text{-}r_j)$, with respect to the phonon displacements. This may have negative or positive sign (for example due to FM / AFM interaction and competition), hence softening or hardening of the respective phonon mode. However, important here is that by monitoring the behavior of a specific lattice vibration it is, in principle, possible to obtain valuable information about the spatial dependence of the superexchange interaction. Further on we will try to discuss the data along this line too. Considering the above, a spectroscopic setup that allows for simultaneous probe of temperature and magnetic field dependence of the phonon spectrum can yield a great deal of physical information. As shown in the previous section, it offers a direct comparison of phenomena in temperature and magnetic field scales. For example, similar investigation has been carried out for the tri-layer ferromagnetic $Sr_4Ru_3O_{10}$ [6.27]. In this work, magnetic field and pressure-dependent Raman spectroscopy on the B_{1g} internal mode revealed information about structural modifications directly linked to the magnetism in the system. Furthermore, quantitative information about the magnetoelastic coupling between this particular mode, assigned to the internal vibrations of RuO_6 octahedra, and the Ru spins was obtained following the approximated expression for the contribution of the spin-spin correlation function to the phonon frequency (equation 6.3.2). In this study, $\lambda_{s\text{-}ph}$ was calculated from comparison of the derivative of the phonon frequency and the magnetization *M*, with respect to the magnetic field, $\partial\omega/\partial B = 2\pi\lambda_{s-ph}\left(M/\mu_B^2\right)\partial M/\partial B$, through the approximation $\left\langle S_i \cdot S_j \right\rangle \approx 2(M/2\mu_B)^2$, for (S = 1) system. Thus, a value for the spin-phonon coupling

constant, as high as $\lambda_{s\text{-}ph}$ = 5.2 cm^{-1}, was obtained for the B_{1g} internal mode in $Sr_4Ru_3O_{10}$. Other materials, in which the spin-phonon coupling is particularly strong and produces strong anomalies in the oscillator characteristics near and below the magnetic transition, are the spinel compounds [6.28][6.29]. Analysis on the spin-phonon coupling has also been made for $ZnCr_2O_4$, in Ref. [6.30], where the spin-spin correlation function is obtained from specific heat data. This procedure yields for the coupling constant in $ZnCr_2O_4$ a value of $\lambda_{s\text{-}ph}$ = 6.2 cm^{-1}.

Results for $YTiO_3$

In $YTiO_3$, the most pronounced magnetic field effects in the phonon spectra were found along the *b*-axis. Figure 6.3.2 shows experimental reflectivity data in terms of the difference: $R(T_i)$ - $R(T_{i+1})$ at zero field (Fig. 6.3.2 (a)), and R(8T) - R(0T) at various temperatures (T_i) (Fig. 6.3.2 (b)), along the *b*-axis. The two distinct features result from changes in the mode parameters at 308 cm^{-1} and 380 cm^{-1}, respectively. The curves at zero field are normalized by the temperature difference the two respective spectra were taken at. In order to compare the data measured at fixed temperature and nonzero magnetic field, similarly, the data is normalized by a factor according to k_B 1K = μ_B 1.489T.

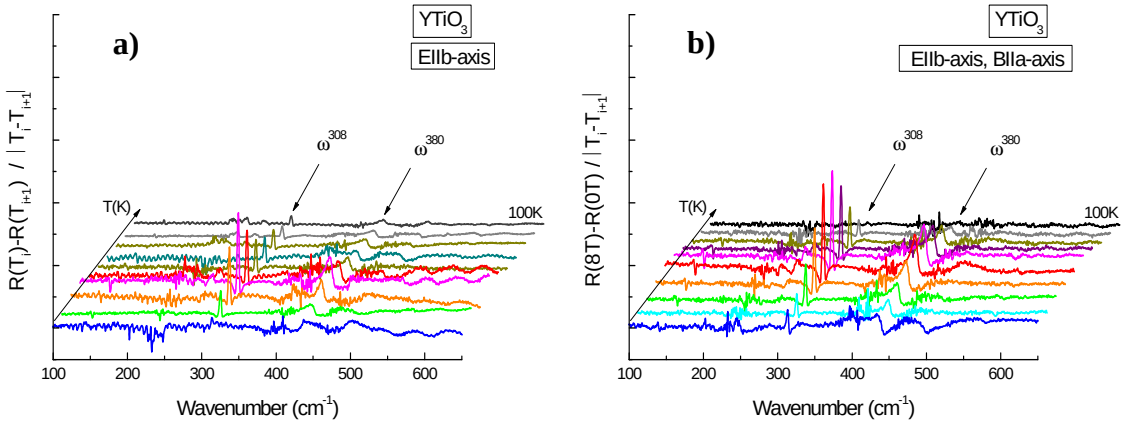

Figure 6.3.2 Experimental reflectivity spectra on $YTiO_3$ along *b*-axis. The data is presented in terms of difference: **a)** $R(T_i) - R(T_{i+1}) / |T_i - T_{i+1}|$ at zero field, and **b)** $R(8T) - R(0T) / |T_i - T_{i+1}|$.

The similarities in the temperature and magnetic field-induced changes are apparent. The effects in the zero field data peak at T ~ 30K (left), while the application of magnetic field broadens and pulls the transition to higher temperatures (right), (see also Fig. 6.3.3 (b), below). Noticeable magnetic field effects on the phonon modes start between T ~ 80 and 100K. As it was mentioned, the pronounced features on figures 6.3.2 correspond to changes in the parameters for modes at 308 cm^{-1} and 380 cm^{-1}. The fit procedure revealed that the phonon at 308 cm^{-1} increases its frequency on cooling from 100K to 3K with ~ 2 cm^{-1} at zero field (Fig. 6.3.3 (a)), while at field of 8 Tesla this change is a bit larger. The maximum for the field induced frequency shift occurs at T ~ 35K > T_c and it is around 0.6 cm^{-1}, as evident from figure 6.3.3 (c), where the difference $\omega^{308}(8T) - \omega^{308}(0T)$ is presented. This difference is free from the phonon-phonon anharmonic contribution $\omega_{anh}(T)$, since the magnetic field most likely does not alter that part. We therefore may safely assume that T_M ~ 80K marks the onset of deviations from the bare anharmonic behavior and that this anomalous behavior is unambiguously related to the spin degree of freedom.

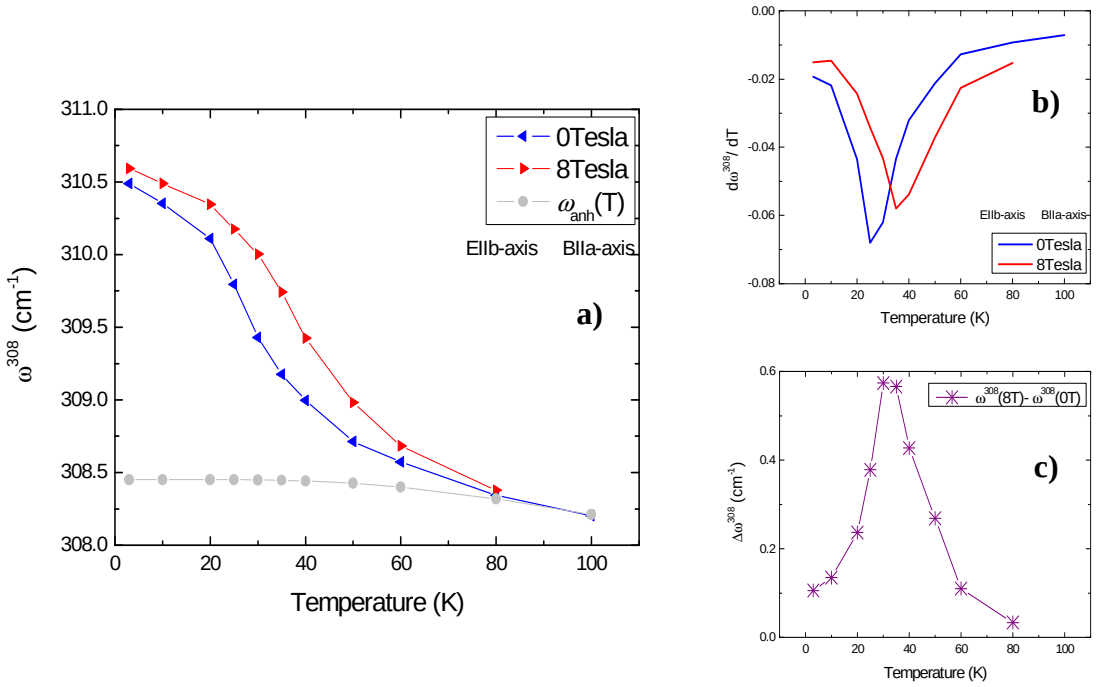

Figure 6.3.3 Fit results for the temperature dependence of: **a)** frequency for the 308cm^{-1}, *b*-axis mode at zero field (blue), at 8 Tesla (red) and the standard anharmonic (phonon-phonon interaction) dependence $\omega_{anh}(T)$ (grey) **b)** the respective temperature derivatives indicating the shift of magnetic transition temperature in 8 Tesla magnetic field **c)** the difference $\omega^{308}(8T)$-$\omega^{308}(0T)$, giving the magnetic field induced frequency shift with maximum of 0.6cm^{-1} at T~35K.

Figure 6.3.4 below, shows the estimate of the spin-phonon coupling constant applied to the *b*-axis 308 cm^{-1} mode.

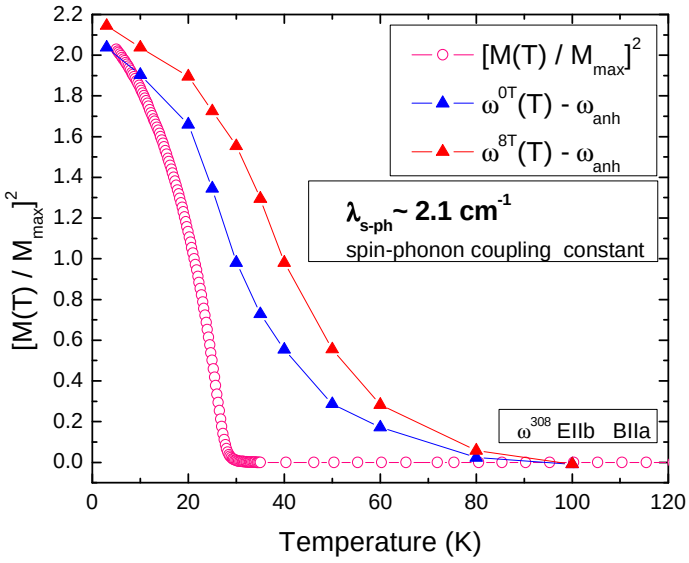

Figure 6.3.4 Comparative plot of $\Delta\omega = \omega(T) - \omega_{anh}(T)$ for the *b*-axis mode at 308 cm^{-1}, at zero field (blue triangles) and at 8Tesla (red triangles), with $(M(T)/M_{max})^2 \sim \langle S_i \cdot S_j \rangle$. The maximum magnetic moment per Ti site is M_{max} = 0.84 μ_B. The scaling coefficient $\lambda_{s\text{-}ph}$ is the spin-phonon coupling constant. For this particular phonon mode $\lambda_{s\text{-}ph} \sim 2.1 cm^{-1}$, estimated at T = 3K.

A value of $\lambda_{s\text{-}ph} \sim 2.1\ cm^{-1}$ for this particular phonon mode, showing the most pronounced effects, clearly places $YTiO_3$ to the compounds with a weak spin-phonon coupling compared to the examples given above. This result is expected since the hybridization between Ti t_{2g} and O *p*-orbitals, and in general for t_{2g} systems, is weaker than that of e_g systems. The more intriguing observation in figure 6.3.4 is that the spin related anomalous deviations in the phonon frequency extend far above the T_c, up to $T_M \sim$ 80-100K. This signals for the presence of short range magnetic order at temperatures of about three times the temperature of the actual long range FM transition at T_c = 30K. In accordance to this, a largely extended (up to five times the T_c) magnetic contribution has been found in the specific heat of $YTiO_3$ [6.7]. Such an anomalously high-temperature magnetic signal could in principle be explained by a spin fluctuation model with competing, and possibly low-dimensional, FM-AFM interactions. This however, would

contradict to the magnon spectrum measured in $YTiO_3$, which was found consistent with an isotropic 3D Heisenberg model with nearest-neighbor interactions, see Ref. [6.13]. These results could therefore be in support of a spin-orbital fluctuation model [6.1][6.2][6.3][6.7], where high-energy orbital fluctuations effectively suppress the long range spin order at temperatures far above the actual T_c.

In figures 6.3.5, 6 and 7 below, we summarize the fit results for the temperature dependence of the phonon mode frequencies along all three directions E||*a*, *b* and *c*, at zero field (curves in blue, red and magenta), and at 8 Tesla magnetic field (grey curves).

Because for some of the modes the temperature and magnetic field induced changes are rather weak, and with the footnote that the error bar in the frequency estimate is in order of the irregular oscillations seen in the curves, we choose to present each particular mode in a separate scale such that all features can be monitored.

From the temperature dependence of the phonon modes frequencies in figures 6.3.5, 6 and 7, three characteristic regions can be distinguished. The high-temperature behavior is apparently altered somewhere between 80 and 100K and is indicated by vertical red lines and T_M. At these temperatures, we define T_M = 80K, clear magnetic field-induced changes in the phonon frequencies start to appear. As discussed above, this point can be considered as an onset of deviations from the bare phonon-phonon anharmonic part - $\omega_{anh}(T)$. This is surely true, at least for the modes showing the largest magnetic field-induced effects, like the *b*-axis 308 cm^{-1} mode shown also in figures 6.3.2 and 3. The phonons experiencing largest field-induced shifts in their frequencies are given in red frames in figures 6.3.5, 6 and 7. For some of the modes T_M is an onset of abrupt changes, although small, followed by a turning point centered at around T ~ 40K. Examples are the modes in figures 6.3.5 (a), and may be (b) and (c), along the *a*-axis, as well as for the *c*-axis modes in figures 6.3.7 (f) and (g). The temperature of T_M ~ 80K can probably be also related to the temperature dependence of the thermal expansion coefficient α, obtained for $YTiO_3$ [6.7], as it shows modest slope changes for all three axes around T ~ 100K. In the temperature interval T = 20 ~ 80K, the application of high magnetic field (the grey curves in figures 6.3.5, 6 and 7), simply increase / decrease (for blue / red shifted modes) further the frequency change rate, pulling and broadening the maximum, and the magnetic transition respectively, to higher temperatures i.e. T ~ 35K, regardless

of the direction of the magnetic field. This behavior was also demonstrated above with the temperature dependence of the derivatives $(\partial\omega/\partial T)$ for *b*-axis 308cm^{-1} mode (see figures 6.3.3 (b) and 6.3.2). Application of magnetic field at fixed temperature in this temperature range (Figs. 6.2.2.3, 6 and 9), shows consistency with the temperature dependence at zero field.

The third region, below T ~ 20K, well into the FM state, indicated by vertical blue lines in figures 6.3.5, 6 and 7, is characterized by a change in the slope in the phonon frequencies for some modes, like for example, the *b*-axis 308 cm^{-1} mode, (Fig. 6.3.6 (d)), which corresponds to the saturation of the field-induced shift, see also figures 6.3.2, 6.3.3 (b) and (c). For other modes, like the first three along the *a*-axis, (Fig. 6.3.5 (a), (b) and (c)), or those along the *c*-axis, (Fig. 6.3.7 (a), (b) and (f)), T ~ 20K could be considered to introduce a turning point. This could be connected to the long range spin order and specifically to TiO_6 octahedra elongation along the *c*-axis which is the direction of the spin moments in $YTiO_3$. The application of magnetic field B||*a*, at temperatures below T ~ 20K may then lead to spin flip and elongation of octahedra along *a*-axis [6.8], explaining the low temperature T < 20K, 8 Tesla, data. Obviously, due to the long range FM spin order, the temperature of T ~ 20K, is the onset of anisotropy in the magnetic field and temperature scales in contrast to the range T ~ 20 - 100K, where the field and temperature sweep do have qualitatively the same impact on the oscillator parameters regardless of the magnetic field direction. By comparing figures 6.3.5, 6 and 7, the phonon frequencies along the *b*-axis, end up somewhat smoother at low temperatures than *a*- and *c*-axes modes. The weak anomalies, appearing at T ~ 20K in the phonon modes frequencies are also consistent with the anomalies in the lattice expansion data at T ~ T_c, reported in [6.7] and [6.8].

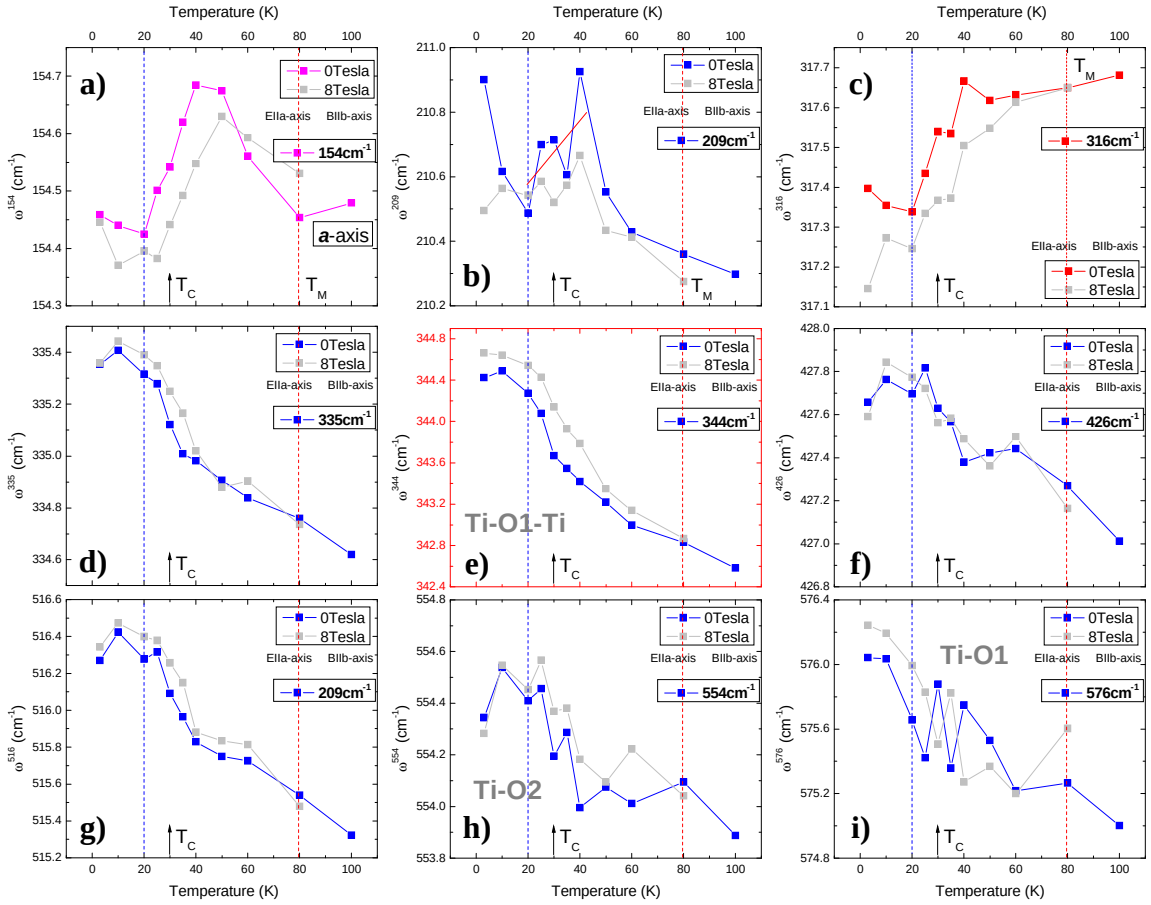

Figure 6.3.5 Results from fit of the temperature dependence of the modes frequency along the *a*-axis, at zero field (curves in blue denote hardening, in red-softening and magenta-turning point) and at 8 Tesla B||*b*, magnetic field (grey curves). The phonon modes that show the largest effects in magnetic field are given in red frames. The vertical red lines indicate the onset of magnetic field-induced changes in the phonon modes (T_M ~ 80K), the Curie temperature T_c ~ 30K is indicated by an arrow, and the vertical blue lines indicate the T ~ 20K anomalies very likely related to the long range FM order.

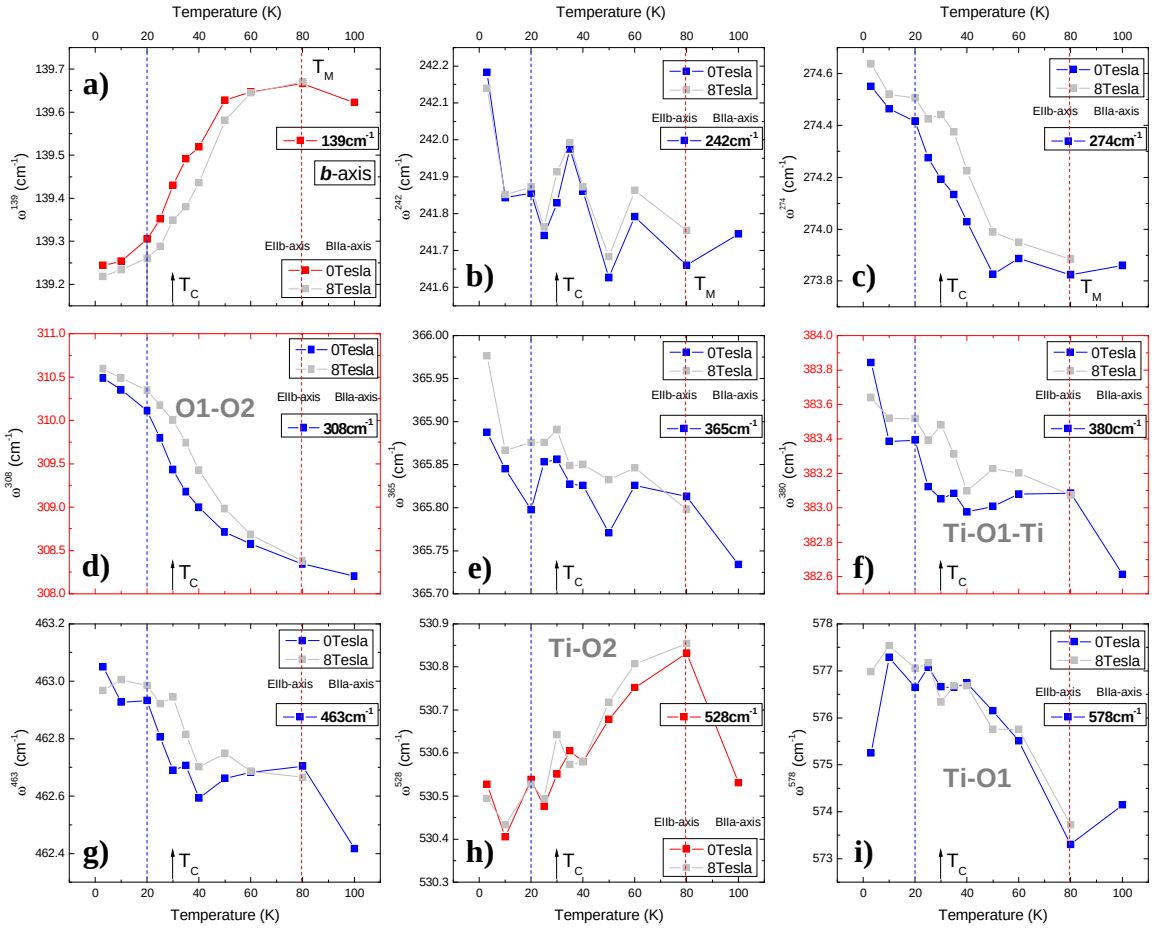

Figure 6.3.6 Results from fit of the temperature dependence of the modes frequency along the *b*-axis, at zero field (curves in blue denote hardening, in red-softening and magenta-turning point) and at 8 Tesla B||*a*, magnetic field (grey curves). The phonon modes that show the largest effects in magnetic field are given in red frames. The vertical red lines indicate the onset of magnetic field-induced changes in the phonon modes (T_M ~ 80K), the Curie temperature T_c ~ 30K is indicated by an arrow, and the vertical blue lines indicate the T ~ 20K anomalies very likely related to the long range FM order.

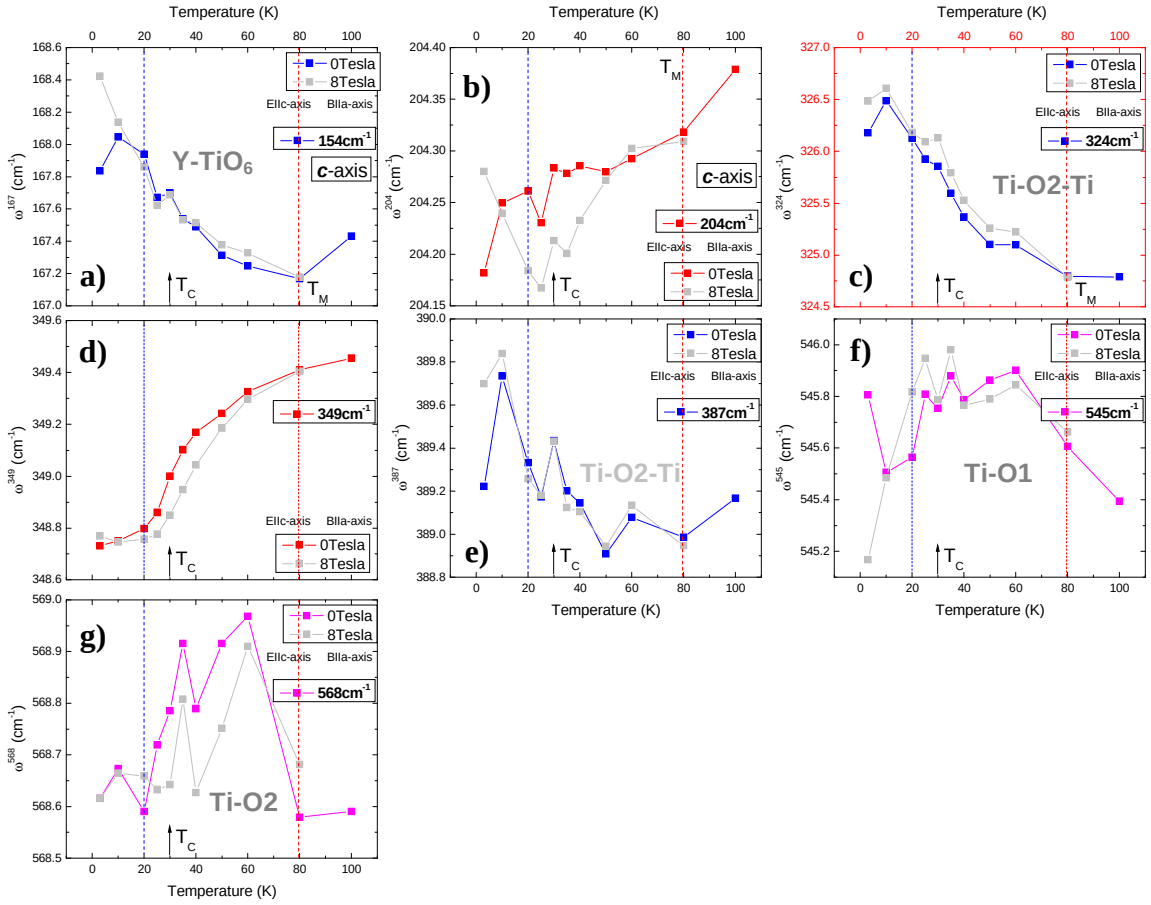

Figure 6.3.7 Results from fit of the temperature dependence of the modes frequency along the *c*-axis, at zero field (curves in blue denote hardening, in red-softening and magenta-turning point) and at 8 Tesla B||*a*, magnetic field (grey curves). The phonon modes that show the largest effects in magnetic field are given in red frames. The vertical red lines indicate the onset of magnetic field-induced changes in the phonon modes (T_M ~ 80K), the Curie temperature T_c ~ 30K is indicated by an arrow, and the vertical blue lines indicate the T ~ 20K anomalies very likely related to the long range FM order.

Let's now consider the modes along *a*,*b* and *c*-axes, that show the largest effects in magnetic field, given in the red frames in figures 6.3.5, 6 and 7. These are predominantly vibrations associated with the Ti-O-Ti bong angle modulations, i.e., bond-bending modes: the *a*-axis at 344 cm^{-1} (Ti-O1-Ti) (Fig. 6.3.5 (e)), the *b*-axis at 308 cm^{-1} (O1-O2) and 380 cm^{-1} (Ti-O1-Ti) (Fig. 6.3.6 (d) and 6.3.6 (f), respectively), and along the *c*-axis the mode at 324 cm^{-1} (Ti-O2-Ti) (Fig. 6.3.7 (c)). Note that the eigenvectors for the *b*-axis mode at 308 cm^{-1} show that it is determined mostly by out-of-phase O1–O2 vibrations (the eigenvectors for the respective modes are given in figures 6.2.2.3, 6 and 9). This result is however puzzling since all of them show hardening and the induced frequency shifts, involving different O1 and O2 atoms along the polarizations considered, span practically all directions. According to Wesselinowa *et al*. [6.26], the shift of the phonon spectra is determined not only by the sign of the spin-phonon interaction constant (softening / hardening), but also on its magnitude. This magnitude is connected to the first and second derivative of the exchange interaction constant $J(r_i\text{-}r_j)$, which depends on the distance between neighboring spins. So it can be smaller if the distance is bigger and vice versa. It is also shown that at a given positive value of the spin-phonon interaction constant, the phonon frequency generally decreases with increasing the exchange interaction constant *J*, i.e., a red shift. Whatever happens with the magnitude of the exchange constant inferred from Ti-O-Ti bond-bending modes, (Fig. 6.3.5 (e), 6.3.6 (f), (d), and 6.3.7 (c)), it is still unusual that along all polarizations, E||*a*, *b* and *c*, we encounter the same blue shift having in mind the anisotropic lattice distortions in $YTiO_3$ ($GdFeO_3$-type, see for example [6.7][6.8]), and the symmetry of the 3*d* t_{2g} orbitals. If the bond angle modulation favors or disfavors the exchange interaction along a particular direction, this should happen at the expense of some of the other directions, which is not the case. This observation is consistent with the nearly isotropic spin Hamiltonian inferred from inelastic neutron scattering study on $YTiO_3$ single crystals, Ref. [6.13].

On the other hand, again from figures 6.3.5, 6 and 7, one may assume that along the *a*- and *b*-axes, the phonons from the bending and stretching groups show predominantly blue shifts on cooling while those along the *c*-axis tend to soften at low temperatures. This, in principle, could signal for anisotropy in the orbital overlap and hence in the exchange coupling $J(r)$. More specifically, due to the increase of orbital overlap along the

c-axis and the out-of-plane exchange coupling J_c when the system enters the low-temperature regime. Scenarios with e_g - t_{2g} orbital hybridization, resulting from the larger $GdFeO_3$-distortion in $YTiO_3$, have already been proposed by Mochizuki and Imada [6.11] to explain the AFM – FM state switch from $LaTiO_3$ towards $YTiO_3$. Such hybridization would introduce anisotropy and corresponding changes into the bandwidth *W*. Indeed, the dielectric function at energies of the optical bands has been found to exhibit crossover points in the temperature dependence at T ~ 100K [6.6]. A relevant experiment would be then to probe the range of optical bands in $YTiO_3$ in the presence of high magnetic fields.
In conclusion, since the FIR experimental data and the fit results presented above yielded relatively weak effects and small changes, for some of the modes they are even on the verge of the experimental error, we therefore cannot draw solid conclusions out of it. Nevertheless there are clear correlations between the temperature and magnetic field scales in the phonon mode parameters, as well as between the three polarizations, which comes in support of the experimental data and the fit procedure. Note that the three data sets (along the different directions) were collected from three separate experimental runs, and modeled by an automated macro procedure with three different Lorentz oscillators sums. This spectroscopy study allowed us to identify accurately all 25 infrared-active phonon modes in $YTiO_3$. The detailed temperature and magnetic field dependence showed unambiguously that spin-phonon coupling is present in this compound and by using a simple mean-field model we estimated weak spin-phonon coupling constant. This is however not surprising since $YTiO_3$ is a t_{2g} system. We also showed largely extended (up to T_M ~ 80 - 100K) temperature range for the magnetic field-induced effects on the phonon modes. We attribute this later finding to the presence of short range magnetic order in $YTiO_3$ that persist at temperatures far above the actual magnetic transition of T_c ~ 30 K. The precise interpretation of the temperature and field dependences of the mode parameters presented here would be very difficult task. A suitable model very likely will have to include a complex spin-orbit-phonon interplay in $YTiO_3$, which is not in the scope of this thesis.

Chapter 7

Summary

The complex properties of transition metal oxides (TMO) are ultimately due to the strong correlations between the electrons. It is the specificity of the *d*-orbital states in a given TMO compound that determines the interaction strength and the spatial anisotropy in the electronic system. The spin degree of freedom then naturally emerges to form a particular magnetic configuration, for example in Mott insulators, the parent state of unconventional superconductivity and colossal magnetoresistance effect. It is also nowadays well recognized that all of the above factors, including the lattice, contribute to the variety of ground states found in TMOs. Serious efforts are being made by many experimental and theoretical groups in the development of spectroscopic methods that allow for high-resolution studies of charge, orbital, magnetic and phonon states. Examples are optical spectroscopy, neutron scattering, and synchrotron-based soft x-ray absorption and scattering techniques, which are also particularly suitable for investigations of artificial TMO superlattices (SL). A basic introduction to these subjects is given in the first part of the thesis, **Chapters 1** to **3**.

Together with a short introduction of the main experimental techniques in optical spectroscopy, reflectance and spectroscopic ellipsometry, **Chapter 4** describes the design and construction of a new experimental apparatus for near-normal infrared reflectance with high magnetic fields. The setup is situated at Max Planck Institute for Solid State Research. It is based on the commercially available Fourier-transform infrared spectrometer and a superconducting 8 Tesla split-coil magnet. We stress on several critical technical details and findings during the assembly and commissioning process of this instrument. In particular, magnetic elements and alloys (even in small amounts) have to be kept out of the magnet's active area and areas that are influenced by stray fields. This includes light sources and detectors, especially devices based on charged vapors such as the *Hg*-arc lamp, which had to be shielded by a specially designed *Mu*-metal

enclosure. The setup allows high-precision measurements on different samples (bulk and superlattices) in the infrared range, at temperatures from 1.6 to 300 Kelvin, variable angle of linear polarization, and magnetic fields up to 8 Tesla in parallel or transverse configuration. It is currently operational in the far infrared (30 – 700 cm^{-1}), but can be easily configured to cover the entire infrared range.

Chapter 5 presents a comprehensive spectroscopic study of a prototypical superlattice system comprised of the antiferromagnetic insulator $CaMnO_3$ and the paramagnetic metal $CaRuO_3$. This SL system recently attracted interest due to the observation of interface ferromagnetism at temperatures below T~125 K, the Néel temperature of pure $CaMnO_3$.
Furthermore, $CaMnO_3$ / $CaRuO_3$ is suitable as a model system where the issues of interface electronic and magnetic reconstruction can be explored experimentally without interference from interface polarity, incipient ferroelectricity, extensive disorder, misfit strain or orbital degeneracy. The theoretical work of Nanda *et al*. (*Phys. Rev. Lett*. **98**, 216804 (2007)) showed that an electron leakage from the paramagnetic metallic $CaRuO_3$ into the adjacent layers of the antiferromagnetically ordered insulating $CaMnO_3$ can create a canted magnetic state at the interface, as a result of competing ferromagnetic double-exchange and antiferromagnetic superexchange interactions. The motivation of our spectroscopic study was to test this theoretical model and to obtain a detailed understanding of the new interface state.
Superlattices of $CaMnO_3$ / $CaRuO_3$ were therefore investigated by means of x-ray absorption spectroscopy (XAS), x-ray magnetic circular dichroism (XCMD), x-ray resonant magnetic scattering (XRMS) and far-infrared (FIR) spectral ellipsometry. The results allowed us to develop a comprehensive experimental description of the charge transport properties as well as the valence state and magnetic polarization of Ru and Mn atoms near the interface. FIR reflectance with high magnetic fields and complementary *dc*-transport probes were also applied to further elucidate the spin-dependent charge transport properties of the system near and below its magnetic transition temperature. Specifically, we have investigated SL samples with variable thickness of one of the constituents, $CaRuO_3$, while the thickness of $CaMnO_3$ was kept constant. The SLs were grown on (001) $LaAlO_3$ substrates. Control experiments on single layers of $CaRuO_3$ and

$CaMnO_3$ were also performed. The XMCD and XRMS studies established the origin of the net magnetization in $CaRuO_3$ / $CaMnO_3$ superlattices and its spatial extent, while the XAS and FIR data are sensitive to the valence state and charge carrier concentration. XMCD revealed substantial magnetic polarization for Mn ions with an amplitude consistent with the predicted canted antiferromagnetic state, while the polarization is negligible or absent for Ru nearby the interfaces. Applying XRMS and structural model calculations it was concluded that the ferromagnetic polarization is not limited to the immediate vicinity of the interface, as theoretically predicted (~1 unit cell), but extends further into the $CaMnO_3$ layer to about 3.5 unit cells. The enhanced magnetic penetration depth may be a consequence of the formation of magnetic polarons. The XAS data showed that the valence state of both ions, Mn and Ru, is close to 4^+. FIR spectroscopic ellipsometry measurements also inferred an effective number of charge carriers per Ru atom (~ 0.11) that is identical (within the experimental error) to that of bulk $CaRuO_3$. This implies that only a small number of electrons from metallic $CaRuO_3$ penetrate into antiferromagnetic insulating $CaMnO_3$ giving rise to canted state with a sizable net polarization that extends to about 3.5 unit cells.

FIR reflectance measurements at several temperatures ranging from 3 to 300 K and magnetic fields up to 8 Tesla were also carried out. Using a fit procedure based on an effective medium approach and the Drude-Lorentz formula for the dielectric function, the reflectivity of the superlattices was deduced. A magnetic field induced enhancement of the optical conductivity (negative magnetoresistance) was observed in the SL samples. The onset temperature was shown to be close to the Néel temperature of $CaMnO_3$, T_N ~ 125 K, and found to result from a reduction of the scattering rate of the free carriers upon application of the magnetic field. It was further shown that the magnitude of this negative magneoresistance effect is small and increases all the way from its onset point down to the lowest temperature of 3 K and hence, is reminiscent of the “giant magnetoresistance” effect in metallic heterostructures. The magnetic field dependence of the conductivity showed linear behavior with no indication of saturation up to the largest field of 8 Tesla, strongly supporting the canted antiferromagnetic ground state in this SL system. Finally, a four-point contact *dc*-transport probe showed results consistent with those of the FIR

study providing confidence in the reliability of the measurements performed with the magneto-reflectance setup described in Chapter 4.

In **Chapter 6** we present a FIR (100 – 700 cm^{-1}) polarized reflectivity study of single crystals of the Mott-insulating ferromagnet $YTiO_3$ at different temperatures, in the interval 3 to 100 K, and subjected to magnetic fields from 0 to 8 T. We have identified all 25 infrared-active phonon modes. Furthermore, the optical response obtained along the three principal crystal axes showed evidence of spin-phonon coupling manifesting itself as temperature and magnetic field-induced anomalies in the oscillator parameters. Due to magnetoelasticity, nearly all phonons in $YTiO_3$ respond to magnetic field. The phonons that were found to experience the largest field- and temperature-induced changes are associated with the group of Ti-O-Ti bond-bending modes. A quantitative analysis of these anomalies in terms of a mean-field model places $YTiO_3$ in the group of compounds with small spin-phonon coupling constants. This is expected for this system since the single Ti valence electron occupies the transition metal t_{2g} orbitals, which hybridize only weakly with the surrounding oxygen *p*-orbitals. A surprising aspect in the FIR data of $YTiO_3$, is the persistence of the magnetic field induced phonon anomalies up to ~ 80 - 100K, far above the Curie temperature T_C ~ 30K. This contrasts strongly with similar results on other metal oxides and indicates the presence of ferromagnetic short-range order over an unusually large temperature range. The FIR data are, however, consistent with thermodynamic experiments that recently uncovered a magnetic contribution to the thermal expansion persisting up to ~ 100 K, and with spectral ellipsometry experiments that revealed spectral weight rearrangements between different optical bands around the same temperature. While a quantitative theoretical description of these data is thus far not available, they point to a complex interplay between spin, orbital, and lattice degrees of freedom due to the near-degeneracy of the Ti t_{2g} orbitals.

Zusammenfassung

Die komplexen Eigenschaften von Übergangsmetalloxiden (transition metal oxide, TMO) beruhen letztendlich auf den starken Elektronenkorrelationen. Die genaue Besetzung der d-Orbitale in einer gegebenen TMO Verbindung bestimmen die Stärke der Wechselwirkungen und die räumliche Anisotropie des Elektronensystems. Die Spinfreiheitsgrade führen dann natürlicherweise zu einer bestimmten, magnetischen Konfiguration, wie sie z. B. in Mott-Isolatoren, den Ausgangsverbindungen der Hochtemperatursupraleiter und den Verbindungen, die den kolossalen Magnetowiderstandseffekt zeigen, beobachtet wird. Heutzutage ist es auch wohlbekannt, dass alle obengenannten Faktoren, einschließlich des Kristallgitters, zur Vielfalt der Grundzustände beitragen, die in TMOs gefunden werden können. Viele experimentelle und theoretische Gruppen unternehmen große Bemühungen, spektroskopische Methoden zu entwickeln, die die hochaufgelöste Untersuchung der Ladungs-, Orbital-, Phonon- und magnetischen Zustände erlauben. Es handelt sich hierbei z.B. um optische Spektroskopie, Neutronenstreuung, sowie Absorptions- und Streutechniken, die auf am Synchrotron erzeugter weicher Röntgenstrahlung basieren. Eine elementare Einführung in diese Gebiete wird in den **Kapiteln 1 bis 3** im ersten Teil dieser Dissertation gegeben.

Zusammen mit einer kurzen Einführung der wichtigsten experimentellen Methoden der optischen Spektroskopie, der Reflexion und der spektroskopischen Ellipsometrie, beschreibt **Kapitel 4** einen neuen experimentellen Aufbau zur Messung der Infrarotreflexion in hohen Magnetfeldern. Der Aufbau befindet sich im Max-Planck-Institut für Festkörperforschung. Er basiert auf einem kommerziell erhältlichen Infrarot-Fourierspektrometer und einem supraleitenden 8-Tesla Magneten. Wir behandeln mehrere kritische technische Details und Erkenntnisse, die während des Aufbaus und der Inbetriebnahme gesammelt wurden. Insbesondere müssen magnetische Elemente und Legierungen (selbst in kleinen Mengen) aus dem aktiven Bereich und den Streufeldern des Magneten herausgehalten werden. Das schließt Lichtquellen und Detektoren ein, insbesondere solche, die auf geladenen Dämpfen basieren, wie z.B.

Quecksilberdampflampen, die durch eine speziell entworfene *Mu*-Metall-Abdeckung abgeschirmt werden mussten. Der Aufbau erlaubt hochpräzise Messungen an verschiedenen Bulk- und Übergitterproben im Infrarotbereich, bei Temperaturen zwischen 1.6 und 300 Kelvin, mit variablem Polarisationswinkel und in magnetischen Feldern von bis zu 8 Tesla in paralleler oder transversaler Konfiguration. Zurzeit wird es im fernen Infrarotbereich (30 – 700 cm^{-1}) betrieben, man kann es aber leicht so konfigurieren, dass es den gesamten Infrarotbereich abdeckt.

Kapitel 5 beschreibt eine umfassende spektroskopische Untersuchung eines prototypischen Übergittersystems, bestehend aus dem antiferromagnetischen Isolator $CaMnO_3$ und dem paramagnetischen Metall $CaRuO_3$. Dieses Übergittersystem rückte in den Mittelpunkt des Interesses, da in ihm Grenzflächen-Ferromagnetismus unterhalb von ~125 K, der Néel-Temperatur von reinem $CaMnO_3$, beobachtet wurde. Darüber hinaus ist $CaMnO_3/CaRuO_3$ als Modellsystem geeignet, um elektronische und orbitale Rekonstruktionen an den Grenzflächen zu untersuchen, ohne den Einfluss von Grenzflächenpolarität, einsetzender Ferroelektrizität, starker Unordnung, Verspannungen durch Gitterfehlanpassung oder orbitaler Entartung. Die theoretische Arbeit von Nanda *et al.* (*Phys. Rev. Lett*. **98**, 216804 (2007)) hat gezeigt, dass ein Entweichen von Ladungsträgern aus dem paramagnetischen, metallischen $CaRuO_3$ in die benachbarten Schichten aus antiferromagnetisch geordnetem, isolierendem $CaMnO_3$ zu einem magnetischen Zustand aus verkanteten Momenten an der Grenzfläche führen kann. Dies ist das Ergebnis der Konkurrenz zwischen der ferromagnetischen Doppelaustausch- und der antiferromagnetischen Superaustauschwechselwirkung. Die Motivation unserer spektroskopischen Untersuchung bestand darin, dieses theoretische Modell zu prüfen und den neuartigen Grenzflächenzustand zu verstehen.

Das aus $CaMnO_3/CaRuO_3$ bestehende Übergitter wurde mittels Röntgenabsorptionsspektroskope (XAS), Röntgenzirkluardichroismus (XMCD), resonanter magnetischer Röntgenstreuung (XRMS) und spektraler Ferninfrarot (FIR)-Ellipsometrie untersucht. Die Ergebnisse erlaubten es uns, eine umfassende experimentelle Beschreibung der Ladungstransporteigenschaften sowie des Valenzzustandes und der magnetischen Polarisation der Ru- und Mn-Atome an der

Grenzschicht zu entwickeln. FIR-Reflexionsmessungen in hohen Magnetfeldern sowie komplementäre dc-Ladungstransportmessungen wurden ebenfalls durchgeführt, um die spinabhängigen Ladungstransporteigenschaften des Systems nahe bei und unterhalb seiner magnetischen Übergangstemperatur genauer zu bestimmen. Insbesondere untersuchten wir Übergitter, in denen die Dicke eines der Konstituenten, nämlich $CaRuO_3$, variiert wurde, während die Dicke von $CaMnO_3$ konstant gehalten wurde. Die Übergitter wurden auf (001)-$LaAlO_3$ abgeschieden. Kontrollexperimente an $CaRuO_3$- und $CaMnO_3$-Einzelschichten wurden ebenfalls durchgeführt. Die XMCD- und XRMS-Untersuchungen haben den Ursprung der Magnetisierung der $CaRuO_3$/$CaMnO_3$ Übergitter und ihre räumliche Ausdehnung ermittelt, während die XAS und FIR Messungen auf die Valenzzustände und Ladungsträgerdichte empfindlich ist. Durch die XMCD Messungen konnte eine wesentliche magnetische Polarisation der Mn-Ionen ermittelt werden, mit einer Amplitude die mit dem vorhergesagten, verkanteten antiferromagnetischen Zustand übereinstimmt. Dagegen ist die Polarisation der Ru-Ionen nahe den Grenzschichten verschwindend gering. Die Anwendung von XRMS und strukturelle Modellrechnungen zeigten, dass die ferromagnetische Polarisation sich nicht, wie theoretisch vorhergesagt, auf die direkte Nachbarschaft der Grenzschichten beschränkt (~1 Einheitszelle), sondern sich etwa 3.5 Einheitszellen weit in die $CaMnO_3$-Schichten erstreckt. Die erhöhte magnetische Eindringtiefe könnte die Konsequenz der Bildung eines magnetischen Polarons sein. Die XAS-Daten zeigten, dass die Valenzzustände sowohl der Mn- als auch der Ru-Ionen nahe bei 4+ sind. Die spektroskopischen FIR-Ellipsometriemessungen lieferten auch eine effektive Dichte von ~0.11 Ladungsträger pro Ru-Atom, was innerhalb des experimentellen Fehlers mit der Dichte in massivem $CaRuO_3$ übereinstimmt. Daraus kann man folgern, dass nur eine kleine Anzahl an Elektronen aus dem metallischen $CaRuO_3$ in das isolierende, antiferromagnetische $CaMnO_3$ eindringen und den verkanteten Zustand mit einer beträchtlichen Polarisation verursachen, welche sich etwa 3.5 Einheitszellen weit in $CaMnO_3$ erstreckt.

Es wurden ebenfalls FIR-Reflexionsmessungen bei mehreren Temperaturen zwischen 3 und 300 K und Feldern bis zu 8 Tesla durchgeführt. Es wurde eine Fittingroutine benutzt, die auf einer “Effektives Medium“- Näherung und der Drude-Lorentz Formel für die

dielektrische Funktion basiert, um die Reflektivität der Übergitter zu bestimmen. Das Anlegen des Magnetfeldes verursachte eine Erhöhung der optischen Leitfähigkeit (negativer Magnetowiderstand) in zwei der Übergitter. Die Temperatur, bei der dies einsetzte, lag nahe bei der Néel-Temperatur von $CaMnO_3$ (T_N~125 K), und es wurde festgestellt, dass diese Erhöhung auf Grund der Reduktion der Streurate der freien Ladungsträger bei Anlegen des Magnetfeldes zustande kam. Es konnte weiterhin gezeigt werden, dass die Größenordnung dieses Magnetowiderstandseffekts klein ist und kontinuierlich mit Absenken der Temperatur auf 3 K zunimmt, und somit an den Riesenmagnetowiderstandseffekt in metallischen Heterostrukturen erinnert. Die Magnetfeldabhängigkeit der Leitfähigkeit zeigte ein lineares Verhalten und selbst bei dem höchsten Feld von 8 Tesla keine Anzeichen einer Sättigung, was ebenfalls stark für einen verkanteten, antiferromagnetischen Grundzustand im Übergittersystem spricht. Schließlich zeigte die Vierpunktmessung des *dc*-Widerstandes Ergebnisse, die mit den FIR-Ergebnissen konsistent waren und somit das Vertrauen in die Verlässlichkeit der mit dem Magneto-Reflexionsaufbau (Kap. 4) gemachten Messungen stärkten.

In Kapitel 6 präsentieren wir eine polarisierte FIR (100 – 700 cm^{-1}) Reflexionsuntersuchung an Einkristallen des ferromagnetischen Mottisolators $YTiO_3$ bei verschiedenen Temperaturen zwischen 3 und 100 K und Feldern zwischen 0 und 8 Tesla. Wir konnten alle 25 infrarot-aktiven Phononenmoden identifizieren. Darüber hinaus zeigte die optische Antwort entlang den drei kristallographischen Hauptachsen Hinweise auf eine Spin-Phonon-Kopplung, die sich in temperatur- und magnetfeldinduzierten Anomalien der Oszillatorparameter manifestierte. Wegen der Magnetoelastizität reagieren nahezu alle Phononen in $YTiO_3$ auf das Magnetfeld. Die Phononen mit den stärksten feld- und temperaturinduzierten Änderungen gehören zu der Gruppe der Ti-O-Ti Beuge Schwingung Moden. Nach einer quantitative Analyse dieser Anomalien im Rahmen eines Meanfield-Modells gehört $YTiO_3$ zur Gruppe der Verbindungen mit kleinen Spin-Phonon-Kopplungskonstanten. Dies ist auch zu erwarten, da das einzelne Ti-Valenzelektron die t_{2g} Übergangsmetallorbitale besetzt, die nur schwach mit den umgebenden Sauerstoff *p*-Orbitalen hybridisieren. Ein überraschender Aspekt der $YTiO_3$ FIR-Daten ist die Tatsache, dass die magnetfeldinduzierten Phononanomalien bis etwa 80

K zu beobachten sind, weit oberhalb der Curietemperatur von T_C ~ 30 K. Dies bildet einen starken Gegensatz zu ähnlichen Ergebnissen bei anderen Metalloxiden und deutet auf eine kurzreichweitige ferromagnetische Ordnung über einen ungewöhnlich großen Temperaturbereich hin. Die FIR-Daten sind allerdings konsistent mit thermodynamischen Messungen, die vor kurzem einen magnetischen Beitrag zur thermischen Ausdehnung bei Temperaturen bis zu 80 – 100 K zeigten. Sie sind ebenfalls konsistent mit Ellipsometriemessungen, die eine Umverteilung des spektralen Gewichts zwischen verschiedenen optischen Banden bei ähnlichen Temperaturen zeigten. Obwohl eine quantitative theoretische Beschreibung dieser Daten zurzeit nicht möglich ist, deuten die Ergebnisse auf eine komplexe Wechselwirkung zwischen Spin-, Orbital- und Gitterfreiheitsgraden, auf Grund der fast-Entartung der Ti-t_{2g} Orbitale hin.

Appendix

(1) to Chapter 5

Fit parameters of the FIR spectrum of (001) $LaAlO_3$ substrate at T = 3 Kelvin

oscillator # ($\varepsilon_\infty = 4.5$) T = 3K	ω_0 [cm^{-1}]	ω_p [cm^{-1}]	γ[cm^{-1}]
1	184.85	710.77	1.68
2	313.07	19.77	1.96
3	428.57	857.9	1.69
4	498.04	51.63	1.99
5	591.8	32.97	5.24
6	596.86	33.99	3.59
7	650.96	299.72	11.57

Fit parameters of the FIR spectrum of (001) $LaAlO_3$ substrate at T = 100 Kelvin

oscillator # ($\varepsilon_\infty = 4.5$) T = 100K	ω_0 [cm^{-1}]	ω_p [cm^{-1}]	γ[cm^{-1}]
1	184.39	713.52	1.76
2	313.13	19.07	2.05
3	428.44	862.55	1.10
4	497.86	48.83	2.06
5	591.78	30.56	5.04
6	596.72	33.25	3.86
7	650.69	300.40	12.58

Fit parameters of the FIR spectrum of (001) $LaAlO_3$ substrate at T = 200 Kelvin

oscillator # (ε_∞ = 4.5) T = 200K	ω_o [cm^{-1}]	ω_p [cm^{-1}]	γ[cm^{-1}]
1	183.45	711.54	2.15
2	313.13	11.49	2.62
3	427.99	862.75	0.92
4	497.07	43.13	2.71
5	591.78	22.21	4.12
6	596.14	28.35	4.19
7	649.5	297.66	16.38

Fit parameters of the FIR spectrum of (001) $LaAlO_3$ substrate at T = 300 Kelvin

oscillator # (ε_∞ = 4.5) T = 300K	ω_o [cm^{-1}]	ω_p [cm^{-1}]	γ[cm^{-1}]
1	182.22	712.41	2.61
2	427.37	863.93	1.25
3	495.89	37.23	3.21
4	591.75	14.92	3.12
5	595.38	20.88	3.91
6	647.93	291.62	20.19

Fit parameters of the FIR spectrum of 10 nm thick single layer control sample of $CaRuO_3$ at T = 3 – 300 Kelvin and B = 0 Tesla

T [K] ($\varepsilon_\infty = 3$) B = 0T	ω_0 [cm^{-1}]	ω_p [cm^{-1}]	γ[cm^{-1}]
3	0	8033.71227	950.90377
50	0	8153.07424	969.03952
90	0	8272.13078	1041.07811
150	0	8480.15168	1125.15619
200	0	8577.93027	1227.92387
250	0	8613.67601	1276.89762
300	0	8525.22755	1306.62762

Fit parameters of the FIR spectrum of 10 nm thick single layer control sample of $CaRuO_3$ at T = 3 – 150 Kelvin and B = 8 Tesla

T [K] ($\varepsilon_\infty = 3$) B = 8T	ω_0 [cm^{-1}]	ω_p [cm^{-1}]	γ[cm^{-1}]
3	0	8185.4743	967.01909
50	0	8317.12551	1000.1608
90	0	8369.69781	1058.09598
150	0	8470.3678	1135.03072

Fit parameters of the FIR spectrum of SL samples [CaMnO3 10 unit cells / $CaRuO_3$ 4 unit cells] × 6 (33.6 nm) at T = 3 – 300 Kelvin and B = 0 Tesla

T [K] ($\varepsilon_\infty = 3$) B = 0T	ω_0 [cm^{-1}]	ω_p [cm^{-1}]	γ[cm^{-1}]
3	0	5555.411	1294.0037
50	0	5545.0213	1296.57565
90	0	5643.35092	1316.04601
150	0	5964.14309	1445.43705
200	0	5910.53184	1429.9346
250	0	6238.78143	1640.20271
300	0	6199.58872	1587.69582

Fit parameters of the FIR spectrum of SL samples [CaMnO3 10 unit cells / $CaRuO_3$ 4 unit cells] × 6 (33.6 nm) at T = 3 – 150 Kelvin and B = 8 Tesla

T [K] ($\varepsilon_\infty = 3$) B = 8T	ω_0 [cm^{-1}]	ω_p [cm^{-1}]	γ[cm^{-1}]
3	0	5806.35069	1320.92173
50	0	5735.1063	1305.36917
90	0	5875.40339	1356.08899
150	0	6041.57923	1450.57971

Fit parameters of the FIR spectrum of SL samples [CaMnO3 10 unit cells / $CaRuO_3$ 10 unit cells] × 6 (48 nm) at T = 3 – 300 Kelvin and B = 0 Tesla

T [K] ($\varepsilon_\infty = 3$) B = 0T	ω_0 [cm^{-1}]	ω_p [cm^{-1}]	γ[cm^{-1}]
3	0	9244.25298	2471.63411
50	0	9200.94482	2390.4856
90	0	9276.75669	2391.60525
150	0	9432.61459	2502.01284
200	0	9613.20202	2657.47492
250	0	9387.8705	2595.12476
300	0	9818.87493	2897.54803

Fit parameters of the FIR spectrum of SL samples [CaMnO3 10 unit cells / $CaRuO_3$ 10 unit cells] × 6 (48 nm) at T = 3 – 150 Kelvin and B = 8 Tesla

T [K] ($\varepsilon_\infty = 3$) B = 8T	ω_0 [cm^{-1}]	ω_p [cm^{-1}]	γ[cm^{-1}]
3	0	9048.77297	2294.89102
50	0	9291.97257	2366.32717
90	0	9164.54694	2276.24604
150	0	9423.63223	2460.74058

(2) to Chapter 6

Fit parameters of the FIR spectrum of $YTiO_3$ single crystal at T = 3 – 100 Kelvin, B = 0 Tesla and linear polarization E||***a***-axis (*ac*). The fit procedure was found to be more stable after an additional oscillator (the parameters are given in red in the following tables) was introduced.

ω_o[cm^{-1}]	ω_p[cm^{-1}]	γ[cm^{-1}]	ω_o[cm^{-1}]	ω_p[cm^{-1}]	γ[cm^{-1}]	ω_o[cm^{-1}]	ω_p[cm^{-1}]	γ[cm^{-1}]
516.26962	154.88818	10.76454	576.04229	76.08082	7.40586	62117.26945	74451.40166	800349.93913
516.42344	150.86465	10.1776	576.03395	91.87228	10.3525	79168.19894	96395.95875	1.15196E6
516.27759	154.47198	10.53439	575.65517	81.62189	8.10982	83849.26788	104521.96564	1.18286E6
516.31521	149.01983	10.06719	575.42221	99.85591	11.1362	91138.02783	106340.05798	1.76418E6
516.0904	150.36659	10.31434	575.87815	89.82226	9.82682	93456.5812	109815.04842	1.50336E6
515.96388	153.94711	10.52692	575.35768	90.13164	9.15518	116764.98293	139784.93268	2.68239E6
515.82886	153.74421	10.60563	575.7485	78.34522	7.32477	96082.5725	109591.70196	2.05301E6
515.74947	153.26821	10.55148	575.52941	85.66642	8.47069	111124.24366	131132.04216	2.38752E6
515.72599	151.58387	10.31326	575.21799	91.16422	10.14695	113835.25252	134571.36593	1.95977E6
515.53953	153.06499	10.53369	575.26598	92.405	9.62694	133020.39562	158887.01634	3.41571E6
515.32316	153.15148	10.91611	575.00085	86.48076	9.08764	150556.143	180411.37588	3.65714E6

ω_o[cm^{-1}]	ω_p[cm^{-1}]	γ [cm^{-1}]	ω_o[cm^{-1}]	ω_p[cm^{-1}]	γ [cm^{-1}]	ω_o[cm^{-1}]	ω_p[cm^{-1}]	γ[cm^{-1}]	ω_o[cm^{-1}]	ω_p[cm^{-1}]	γ[cm^{-1}]
335.3548 1	174.6570 5	3.9489	344.4228 4	117.3490 6	7.8352	427.6574	878.0241 4	9.53881	554.3438 2	496.2953 8	6.12899
335.4079 3	173.6546 8	3.93883	344.4872 1	116.3894 6	7.7605	427.7620 9	877.1603 2	11.39353	554.5377 5	496.1811 6	6.63194
335.3151 8	173.8495 5	3.93859	344.2720 7	118.6903	7.84223	427.6959 2	882.3726 8	10.56485	554.4090 4	498.5188 4	6.3807
335.2781 9	170.4181 9	3.97765	344.0784 4	117.4686 5	7.74817	427.8162 7	868.6163	11.71763	554.4566 4	491.4853	6.79589
335.1207 6	169.1450 1	4.08633	343.6680 2	119.8894 8	7.80671	427.6282 2	866.4908 2	11.90075	554.1950 5	486.6126	6.84579
335.0084	170.5684	4.11768	343.5455 9	120.7334 4	7.69247	427.5670 3	872.3368	10.9135	554.2865 1	491.9300 1	6.44811
334.9812 2	169.0689	4.12421	343.4181 5	120.9807 5	7.75157	427.3795 5	865.8107 9	10.26916	553.9956 6	486.6241 4	6.33649
334.9064 9	169.8532 5	4.21153	343.2174 7	122.4983 9	7.79913	427.4221 3	869.1348 7	10.92669	554.0752 3	488.6386 5	6.55566
334.8388 7	168.0515 5	4.23228	342.9949 8	124.1198 4	7.87111	427.4414 7	865.4684 8	12.25517	554.0112 5	484.9343	7.12134
334.7586 7	172.7626 7	4.48102	342.8313 9	125.0664 9	7.73947	427.2688 8	871.8511 9	11.92833	554.0945 6	490.8305 8	6.94234
334.6196	174.3389 5	4.63507	342.5804 6	129.6396 1	8.07201	427.0124	871.3422 8	11.93341	553.8880 8	488.1230 7	7.27877

T [K] ($\varepsilon_\infty = 4$)	ω_o[cm^{-1}]	ω_p[cm^{-1}]	γ [cm^{-1}]	ω_o[cm^{-1}]	ω_p[cm^{-1}]	γ[cm^{-1}]	ω_o[cm^{-1}]	ω_p[cm^{-1}]	γ[cm^{-1}]
3	154.45885	75.72767	3.08083	210.90025	458.95289	4.33085	317.39712	499.27328	4.40117
10	154.44008	79.07987	3.02643	210.61561	461.30496	4.28489	317.35449	498.73095	4.72894
20	154.42483	82.759	3.42077	210.48707	465.25176	4.19809	317.33837	503.32393	4.62899
25	154.50116	75.69481	3.02333	210.69897	456.34604	4.48369	317.43436	493.92102	4.88226
30	154.54188	76.93046	3.39936	210.71339	456.00024	4.6161	317.5394	494.62656	4.96645
35	154.61964	73.5871	2.93494	210.60547	460.03068	4.45531	317.53452	499.54485	4.84136
40	154.68471	67.86393	2.84669	210.92489	453.64534	4.76619	317.66614	495.20427	4.84505
50	154.67466	72.65135	3.17501	210.55227	459.11597	4.72369	317.61744	498.85948	4.93441
60	154.5604	76.44938	3.46369	210.42839	458.472	4.814	317.63177	497.30075	5.25162
80	154.45334	75.62855	3.54487	210.36042	461.979	4.98855	317.64966	501.26194	5.31189
100	154.47895	74.11221	3.62326	210.29807	461.70481	5.28185	317.68117	500.70068	5.40127

Fit parameters of the FIR spectrum of $YTiO_3$ single crystal at T = 3 – 80 Kelvin, B = 8 Tesla (B||***b***-axis) and linear polarization E||***a***-axis (*ac*)

ω_p[cm^{-1}]	γ [cm^{-1}]	ω_o[cm^{-1}]	ω_p[cm^{-1}]	γ[cm^{-1}]	ω_o[cm^{-1}]	ω_p[cm^{-1}]	γ[cm^{-1}]	ω_o[cm^{-1}]	ω_p[cm^{-1}]	γ [cm^{-1}]
507.0248	5.46863	516.34341	163.5876	11.49057	576.24252	64.40686	5.59299	59224.6471	79293.44099	491942.21144
499.31388	6.45808	516.47298	152.1421	10.28798	576.19286	91.2903	9.36016	74717.90401	92192.49239	1.09335E6
503.23885	6.17751	516.39871	156.11694	10.62752	575.99384	78.03884	7.56254	145001.3482	183717.40404	3.65102E6
501.23569	6.17954	516.37831	152.308	10.16574	575.82934	88.88065	8.37124	167725.2717	202591.76025	6.62274E6
500.59758	6.17317	516.25703	156.30968	10.63673	575.50581	78.4577	7.54417	184789.74185	231808.76837	5.90074E6
499.12834	6.09932	516.14859	155.57037	10.65905	575.82357	83.02398	7.71008	252386.16945	309439.87858	1.31444E7
501.77346	5.56557	515.88154	161.20081	11.34672	575.27062	69.08016	5.97921	249982.33369	313559.97184	1.23123E7
498.50815	5.97419	515.83383	160.45446	11.1846	575.36772	71.83417	6.24299	248035.64394	313721.10767	9.88011E6
493.0722	6.75113	515.81354	152.44247	10.3345	575.19933	89.32868	8.82923	265398.20389	313492.68127	1.46498E7
494.33251	6.75538	515.47826	156.47038	10.98303	575.603	82.03814	8.12423	271604.37714	335493.38416	1.21242E7

ω_p[cm^{-1}]	γ [cm^{-1}]	ω_o[cm^{-1}]	ω_p[cm^{-1}]	γ [cm^{-1}]	ω_o[cm^{-1}]	ω_p[cm^{-1}]	γ [cm^{-1}]	ω_o[cm^{-1}]	ω_p[cm^{-1}]	γ [cm^{-1}]	ω_o[cm^{-1}]
515.67323	3.98629	335.35854	180.19497	3.92757	344.66261	120.60175	8.02407	427.58948	900.63574	7.88759	554.28264
501.61127	4.64308	335.44307	174.71791	3.94475	344.64151	115.53045	7.70351	427.84337	881.55514	10.87839	554.54746
506.17992	4.48354	335.39029	176.29243	3.93314	344.54271	117.52132	7.7968	427.77339	887.94112	10.04709	554.45319
501.29177	4.56529	335.34812	174.88644	4.03012	344.42736	115.94945	7.71401	427.72072	881.21536	10.73503	554.56675
505.36145	4.55393	335.2493	174.20157	3.96295	344.13762	120.01144	7.95718	427.56144	884.41609	10.09821	554.36822
504.42649	4.65211	335.16474	173.15516	4.02646	343.9276	119.69711	7.83866	427.58235	881.29106	10.09715	554.38062
508.52391	4.28521	335.01978	175.87003	4.12746	343.78645	123.41562	7.98181	427.48678	888.62649	8.32144	554.18306
508.88081	4.50205	334.87974	173.78356	4.19704	343.34714	125.89159	8.07576	427.36151	885.48479	9.03231	554.0945
499.41699	5.09645	334.90301	170.34438	4.29248	343.13792	122.88121	7.80745	427.4973	870.96646	11.67824	554.22248
505.49426	5.0637	334.73587	175.008	4.53927	342.86603	127.3457	7.89168	427.16293	879.29307	11.06701	554.04062

T [K] ($\varepsilon_\infty = 4$)	ω_o[cm^{-1}]	ω_p[cm^{-1}]	γ[cm^{-1}]	ω_o[cm^{-1}]	ω_p[cm^{-1}]	γ[cm^{-1}]	ω_o[cm^{-1}]
3	154.44543	79.51177	2.91218	210.49523	474.82384	3.87224	317.14568
10	154.37028	80.85537	3.10413	210.56302	463.30657	4.19548	317.273
20	154.39532	82.21949	3.27711	210.5422	467.11506	4.09794	317.24581
25	154.3822	80.19647	3.32585	210.58553	462.59254	4.24762	317.33432
30	154.44108	81.16311	3.25304	210.52047	466.33127	4.2095	317.36709
35	154.49194	76.60485	3.05132	210.57338	464.0461	4.28684	317.37273
40	154.54758	73.86135	2.90224	210.66534	467.05531	4.30821	317.5044
50	154.62992	76.30154	3.33443	210.43378	468.67809	4.40527	317.54765
60	154.59267	76.85354	3.51561	210.4129	460.50989	4.76876	317.61321
80	154.5303	76.55297	3.55761	210.27516	466.31147	4.83261	317.64907

Fit parameters of the FIR spectrum of $YTiO_3$ single crystal at T = 3 – 100 Kelvin, B = 0 Tesla and linear polarization E||***b***-axis (*bc*)

ω_p[cm^{-1}]	γ [cm^{-1}]	ω_o[cm^{-1}]	ω_p[cm^{-1}]	γ[cm^{-1}]	ω_o[cm^{-1}]	ω_p[cm^{-1}]	γ[cm^{-1}]	ω_o[cm^{-1}]	ω_p[cm^{-1}]	γ [cm^{-1}]
480.80501	7.44173	530.52715	585.91535	11.34541	575.24806	149.38074	23.81326	45774.0611	67666.32691	281381.34806
488.71524	7.14888	530.40506	598.56343	10.91222	577.28633	122.45856	16.38365	52072.95233	80452.50285	345931.28232
488.46305	7.45095	530.53786	596.46676	11.08376	576.64592	132.03544	18.8396	70759.53919	108463.0872	670107.08302
491.15523	7.26935	530.47559	599.18587	10.93754	577.07221	122.43344	16.27034	72343.83833	112120.35982	643378.72302
495.80119	7.43899	530.55088	602.41509	10.69567	576.65741	124.29042	16.66591	72788.71204	113897.1787	676442.36844
492.9155	7.50628	530.60473	597.71504	11.09876	576.64677	132.64084	18.80857	76793.71998	118022.60059	755245.90627
494.62034	7.57415	530.58018	598.9324	11.01792	576.737	129.32268	17.95008	78580.48452	121284.95082	791878.54078
491.75137	7.81598	530.67767	595.91004	11.38667	576.14581	134.33418	19.38129	80777.01022	122608.13555	840165.18428
493.20812	7.93242	530.75179	595.90797	11.50925	575.50981	143.64055	21.71202	85898.36293	130261.25084	958935.94709
494.456	8.25499	530.83172	594.19466	11.58966	573.30123	162.53289	26.31152	96346.049	146200.74473	1.21609E6
501.71729	8.09365	530.5306	601.56018	11.53499	574.14665	148.33509	23.14432	99828.90743	155419.14599	1.29666E6

ω_p[cm^{-1}]	γ [cm^{-1}]	ω_o[cm^{-1}]	ω_p[cm^{-1}]	γ [cm^{-1}]	ω_o[cm^{-1}]	ω_p[cm^{-1}]	γ [cm^{-1}]	ω_o[cm^{-1}]	ω_p[cm^{-1}]	γ [cm^{-1}]	ω_o[cm^{-1}]
206.05164	6.66304	310.48834	223.7735	3.07342	365.88747	287.04095	5.3324	383.84254	892.56025	11.8042	463.05016
215.48765	6.8893	310.35316	231.49492	3.10158	365.84507	307.62238	5.69133	383.38438	904.60256	11.01334	462.92723
214.94011	6.9108	310.10978	229.89806	3.18109	365.79754	306.43531	5.80166	383.3918	899.08219	11.30546	462.93269
219.15242	7.01185	309.79614	231.68171	3.26577	365.85315	302.07238	5.50957	383.12208	904.12576	11.36708	462.80564
219.43648	6.99877	309.42983	231.48567	3.32081	365.85597	309.88218	5.59715	383.0516	904.59561	11.23445	462.68997
216.81559	7.06004	309.17613	228.2552	3.39678	365.82718	299.67922	5.67818	383.08341	898.85002	11.809	462.70664
219.26447	7.19661	308.99692	228.88767	3.45415	365.82577	303.69173	5.72748	382.97546	899.081	11.72323	462.59226
221.72221	7.57962	308.71358	226.7194	3.61577	365.77062	293.76137	5.77084	383.00798	892.74553	12.71238	462.66182
218.65336	7.58184	308.57305	223.88177	3.65749	365.82601	287.01096	5.49562	383.07829	893.27284	12.87562	462.68274
219.24344	7.88876	308.34339	221.60014	3.87513	365.8129	285.80493	5.52484	383.08533	890.60984	13.40707	462.70454
220.31044	8.03538	308.20217	223.13964	3.97392	365.73402	301.58032	5.76102	382.61273	901.40923	12.80561	462.41665

T [K] ($\varepsilon_\infty = 4$)	ω_o[cm^{-1}]	ω_p[cm^{-1}]	γ[cm^{-1}]	ω_o[cm^{-1}]	ω_p[cm^{-1}]	γ[cm^{-1}]	ω_o[cm^{-1}]
3	139.24413	79.73195	2.21244	242.18237	360.96817	6.33693	274.55111
10	139.25343	82.43455	2.16605	241.84289	376.43602	6.11793	274.46472
20	139.30471	81.76862	2.20936	241.85497	375.07572	6.19256	274.4166
25	139.35217	81.93287	2.1998	241.74044	380.21959	6.16638	274.2757
30	139.43013	81.95031	2.23	241.82861	380.67902	6.13295	274.19257
35	139.49193	80.32616	2.23451	241.9751	374.66814	6.20951	274.1336
40	139.51887	80.35003	2.2161	241.86006	378.37496	6.19885	274.02877
50	139.62788	78.24434	2.22163	241.62663	380.5755	6.29471	273.82555
60	139.64719	77.84498	2.23928	241.79169	375.32979	6.41099	273.88681
80	139.666	77.29977	2.33224	241.65993	374.80338	6.60376	273.82413
100	139.62205	78.11823	2.48915	241.74441	374.58247	6.65541	273.85986

Fit parameters of the FIR spectrum of $YTiO_3$ single crystal at T = 3 – 80 Kelvin, B = 8 Tesla (B||***a***-axis) and linear polarization E||***b***-axis (*bc*)

ω_p[cm^{-1}]	γ [cm^{-1}]	ω_o[cm^{-1}]	ω_p[cm^{-1}]	γ [cm^{-1}]	ω_o[cm^{-1}]	ω_p[cm^{-1}]	γ [cm^{-1}]	ω_o[cm^{-1}]	ω_p[cm^{-1}]	γ [cm^{-1}]
491.2573	7.1125	530.4941 4	602.0254 7	10.87949	576.9788 4	129.7573 4	17.82359	70891.88 005	110863.7 952	648270.7 5808
489.8197 3	7.05447	530.4331 7	601.2404 8	10.89847	577.5332 9	121.5696 2	15.8826	72412.13 924	112751.1 0446	676228.5 561
490.5929 9	7.28275	530.5270 7	600.9386 5	10.94134	577.0574	127.4462 3	17.45413	76098.78 872	118388.3 081	764359.3 004
490.1774 3	7.18461	530.4939 1	600.0854	11.01661	577.1685 1	124.4525 7	16.70135	78305.14 31	121760.9 2788	747030.1 1486
490.9336 4	7.48777	530.6421 7	599.2095 2	11.07373	576.3323 7	135.2163 9	19.38994	85388.16 168	132023.6 5716	946946.2 5775
491.5731	7.40214	530.5733 7	598.5224 2	11.14308	576.6798 4	133.3159 2	18.92135	88676.76 552	136898.0 4951	1.01198E 6
494.0571 6	7.44975	530.5792 3	600.7076 2	10.97143	576.6812 1	129.3783 1	17.79205	90160.81 013	139970.7 8423	1.06002E 6
489.1666 1	7.76194	530.7174 6	593.6850 5	11.56571	575.7552 3	140.2340 5	21.05055	95768.20 106	144504.4 493	1.14971E 6
493.2565 9	7.87455	530.8068 4	597.1627	11.64373	575.7522 4	144.3006 4	21.6016	98709.80 675	150100.5 4739	1.28347E 6
494.6247	8.20181	530.8542	595.1993 5	11.71849	573.7137 6	161.5627 7	26.00221	108717.0 9353	165616.3 2733	1.52302E 6

ω_p[cm^{-1}]	γ [cm^{-1}]	ω_o[cm^{-1}]	ω_p[cm^{-1}]	γ [cm^{-1}]	ω_o[cm^{-1}]	ω_p[cm^{-1}]	γ [cm^{-1}]	ω_o[cm^{-1}]	ω_p[cm^{-1}]	γ [cm^{-1}]	ω_o[cm^{-1}]
208.37175	6.51026	310.59429	230.01737	2.97178	365.9762	300.28849	5.23326	383.63904	914.0552	10.70231	462.96745
214.39365	6.83228	310.48849	231.5417	3.04469	365.86668	308.48296	5.63068	383.5198	908.48859	10.81675	463.00462
214.1862	6.85193	310.34647	230.9936	3.08444	365.87587	310.64169	5.75806	383.51697	905.71702	10.88459	462.98561
216.64241	6.95531	310.17461	230.91958	3.15415	365.87589	303.23221	5.48898	383.39098	906.56615	11.18414	462.92169
214.70115	6.91158	310.00375	228.5043	3.19103	365.89048	298.86975	5.39241	383.48066	904.08502	11.46366	462.94527
214.65668	6.8939	309.74192	228.94473	3.27389	365.84879	300.72492	5.61768	383.31187	903.05019	11.45827	462.81415
217.88509	7.05977	309.42428	229.80837	3.36204	365.85005	304.86625	5.62953	383.09777	903.5831	11.47574	462.7014
218.19078	7.43014	308.98227	224.91243	3.5573	365.83233	283.71091	5.47031	383.2267	893.95878	12.97467	462.74939
217.62994	7.54949	308.68342	223.69006	3.63808	365.84628	284.3025	5.45384	383.20141	895.76352	12.85736	462.68608
218.61603	7.85979	308.37721	221.45981	3.84663	365.79824	282.99744	5.51984	383.07324	893.7012	13.45038	462.66528

T [K] ($\varepsilon_\infty = 4$)	ω_o[cm^{-1}]	ω_p[cm^{-1}]	γ[cm^{-1}]	ω_o[cm^{-1}]	ω_p[cm^{-1}]	γ[cm^{-1}]	ω_o[cm^{-1}]
3	139.21825	82.58658	2.17576	242.13926	369.84629	6.12412	274.63786
10	139.2338	83.07125	2.19445	241.85136	376.57336	6.08955	274.52047
20	139.2606	82.84599	2.18415	241.87191	376.06608	6.11591	274.50599
25	139.28809	82.47571	2.17852	241.76413	378.48517	6.1688	274.42519
30	139.34856	81.57121	2.18594	241.91306	374.22517	6.17113	274.442
35	139.37961	81.14179	2.20569	241.99232	373.62175	6.19965	274.37526
40	139.43604	81.1215	2.20219	241.87229	377.88087	6.16318	274.22517
50	139.58073	77.94828	2.21322	241.68346	376.83679	6.38985	273.98867
60	139.64469	77.01942	2.21475	241.86234	373.99006	6.38462	273.94939
80	139.67041	76.9248	2.34986	241.7542	373.35307	6.56717	273.88473

Fit parameters of the FIR spectrum of $YTiO_3$ single crystal at T = 3 – 100 Kelvin, B = 0 Tesla and linear polarization E||***c***-axis (*bc*)

ω_p[cm^{-1}]	γ [cm^{-1}]	ω_o[cm^{-1}]	ω_p[cm^{-1}]	γ [cm^{-1}]	ω_o[cm^{-1}]	ω_p[cm^{-1}]	γ [cm^{-1}]	ω_o[cm^{-1}]	ω_p[cm^{-1}]	γ [cm^{-1}]
804.12214	9.83267	545.80524	549.0108	9.44139	568.61542	531.55153	21.28374	750.74512	519.05625	28.55413
789.71312	11.76052	545.50574	527.68385	10.16367	568.67333	494.85691	22.43534	789.89937	629.57797	23.00821
786.93422	11.18783	545.56397	530.89899	9.93771	568.59002	503.8044	22.20029	763.47566	533.70348	27.50801
792.23568	10.96848	545.80822	538.55683	9.80659	568.7189	510.72984	21.81336	756.83531	519.1689	29.26076
789.35326	12.00782	545.75298	530.26095	10.08165	568.78572	496.93822	22.14812	775.03541	574.04856	27.7639
790.734	11.66133	545.87866	534.13418	9.99052	568.91557	503.99449	22.07001	763.48262	536.54197	29.27875
791.48737	11.64875	545.78744	531.73099	9.91485	568.78943	509.61518	22.10924	761.9222	531.14467	29.62182
793.12117	11.45448	545.86311	535.90725	9.95576	568.91571	510.42258	22.0479	759.71654	527.12247	30.29099
791.2838	12.02256	545.90083	533.4923	10.08162	568.96842	507.08931	22.24867	757.5177	512.18992	30.68179
790.80897	12.29956	545.60635	528.41546	10.26601	568.57903	501.20259	22.40321	770.39973	558.29403	26.82684
781.89867	13.66971	545.39383	521.16996	10.79204	568.5903	485.88442	23.07983	766.19539	515.86919	28.73181

ω_p[cm^{-1}]	γ [cm^{-1}]	ω_o[cm^{-1}]	ω_p[cm^{-1}]	γ [cm^{-1}]	ω_o[cm^{-1}]	ω_p[cm^{-1}]	γ [cm^{-1}]	ω_o[cm^{-1}]	ω_p[cm^{-1}]	γ [cm^{-1}]	ω_o[cm^{-1}]
530.01085	3.4192	204.18179	160.25043	6.78965	326.17953	673.70486	8.14874	348.73118	129.38124	5.26609	389.22109
517.8373	3.99616	204.24939	156.14244	6.73189	326.48805	653.30598	8.79585	348.75071	117.73119	4.64608	389.73401
517.39468	3.90502	204.26104	155.67198	6.71979	326.12571	657.07418	8.6604	348.79777	118.4733	4.92903	389.33177
522.25521	3.72823	204.23026	156.05047	6.75797	325.92378	662.65798	8.54986	348.85983	118.21543	5.04631	389.17232
517.66475	4.05589	204.28325	153.43229	6.70255	325.85413	654.54876	9.04825	348.99991	109.33286	4.78189	389.43457
519.81827	4.06377	204.27796	152.98375	6.66317	325.59671	658.64214	9.03766	349.10202	109.29388	4.90677	389.19966
520.54558	4.06523	204.28544	152.71543	6.6516	325.365	660.23591	9.1152	349.16893	109.19727	5.00305	389.14379
523.11413	4.11998	204.27971	152.57472	6.62998	325.10253	664.29896	9.07951	349.24245	110.2983	5.17618	388.90738
519.89944	4.36292	204.29236	150.96819	6.61304	325.09789	658.27841	9.44011	349.32574	106.87631	5.07933	389.07735
519.37317	4.67228	204.31792	150.84382	6.67258	324.79479	657.5456	9.79979	349.41006	108.33765	5.31937	388.98523
507.3268	5.58695	204.37879	148.09213	6.69532	324.78949	642.93701	10.50629	349.45543	103.77366	5.28441	389.16678

T [K] ($\varepsilon_\infty = 4$)	ω_o[cm^{-1}]
3	167.83594
10	168.04614
20	167.93962
25	167.67176
30	167.69817
35	167.53819
40	167.48895
50	167.31327
60	167.24744
80	167.16668
100	167.4311

Fit parameters of the FIR spectrum of $YTiO_3$ single crystal at T = 3 – 80 Kelvin, B = 8 Tesla (B||***a***-axis) and linear polarization E||***c***-axis (*bc*)

ω_p[cm^{-1}]	γ [cm^{-1}]	ω_o[cm^{-1}]	ω_p[cm^{-1}]	γ [cm^{-1}]	ω_o[cm^{-1}]	ω_p[cm^{-1}]	γ [cm^{-1}]
523.86901	10.2004	568.61567	493.67049	22.8351	788.01288	614.78307	22.83642
526.91026	10.14864	568.66441	495.26094	22.54095	791.22469	635.10314	22.91598
543.43647	9.52817	568.65892	527.10456	21.63274	744.44404	479.74343	31.97802
547.75105	9.47765	568.63274	525.95791	21.31358	749.85768	509.54698	30.11847
536.96791	9.82193	568.64239	507.93582	21.79426	766.71039	559.33888	28.61117
543.26024	9.64572	568.80783	523.07083	21.67515	745.76566	482.68283	32.86374
535.9765	9.75382	568.62706	517.7943	21.89044	757.75676	525.40864	30.34189
537.33056	9.9999	568.75134	503.45965	21.85382	768.38525	563.72401	26.40936
533.02174	10.15179	568.91016	501.30862	22.23777	765.26986	540.76976	28.65281
530.70189	10.2453	568.68146	504.61195	22.43016	764.07326	534.77173	29.66578

ω_p[cm^{-1}]	γ [cm^{-1}]	ω_o[cm^{-1}]	ω_p[cm^{-1}]	γ [cm^{-1}]	ω_o[cm^{-1}]	ω_p[cm^{-1}]	γ [cm^{-1}]	ω_o[cm^{-1}]	ω_p[cm^{-1}]	γ [cm^{-1}]	ω_o[cm^{-1}]
155.9776	6.53136	326.48719	651.36492	8.73012	348.76897	120.27832	4.70059	389.69863	786.59644	11.69908	545.16741
156.33517	6.61319	326.60756	651.95214	8.76735	348.74659	119.17588	4.62177	389.83884	790.43971	11.90422	545.48465
158.66141	6.69977	326.18235	667.67377	8.35268	348.75699	125.71724	5.08952	389.25684	797.08074	10.36413	545.81704
159.06135	6.74605	326.09233	671.37972	8.2413	348.77578	125.70322	5.16523	389.1797	800.78474	10.30681	545.94684
156.38928	6.70725	326.12901	660.87613	8.72534	348.84986	117.70165	4.87429	389.4309	794.18982	11.2954	545.7867
156.23558	6.68982	325.7928	666.96859	8.63567	348.94832	118.11458	5.06021	389.12349	797.15296	10.92585	545.97981
155.13292	6.6845	325.52645	665.68191	8.84972	349.04297	115.29772	5.06272	389.10367	794.92392	11.10271	545.76571
153.411	6.62364	325.25948	664.66824	8.98126	349.18624	111.94043	5.1227	388.94427	793.88516	11.39007	545.78946
151.18496	6.59824	325.22258	657.1911	9.40883	349.2964	107.04191	5.00919	389.13365	791.28302	12.07312	545.84399
151.04838	6.68128	324.7861	658.55322	9.75539	349.40425	109.27077	5.39772	388.94567	791.4152	12.30681	545.66179

T [K] ($\varepsilon_\infty = 4$)	ω_0[cm^{-1}]	ω_p[cm^{-1}]	γ [cm^{-1}]	ω_0[cm^{-1}]
3	168.42185	513.96971	4.34725	204.27994
10	168.13704	517.44269	4.05571	204.23945
20	167.85872	525.00253	3.55237	204.18405
25	167.62251	529.1534	3.38236	204.16712
30	167.68707	522.76938	3.71644	204.21288
35	167.53136	525.53689	3.67116	204.20059
40	167.51393	524.47752	3.80773	204.23255
50	167.37775	523.88705	4.08925	204.27139
60	167.32657	519.43283	4.43157	204.30213
80	167.17755	519.66341	4.68815	204.30923

References

Chapter 1

[1.1] N. Mott "The Basis of the Electron Theory of Metals, with Special Reference to the Transition Metals" *Proc. Phys. Soc. A* **62** 416 (1949)

[1.2] G. Jonker and J. Van Santen "Ferromagnetic compounds of manganese with perovskite structure" *Physica* **16**, 337 (1950)

[1.3] J. Bednorz and K. Müller "Possible high-Tc superconductivity in the Ba-La-Cu-O system" *Z. Phys. B* **64**, 189 (1986)

[1.4] Y. Tokura and N. Nagaosa "Orbital Physics in Transition-Metal Oxides" *Science* **288**, 462 (2000)

[1.5] B. Keimer *et al*. "Spin Dynamics and Orbital State in $LaTiO_3$" *Phys.Rev.Lett.* **85**, 3946 (2000)

[1.6] G. Khalliulin and S. Maekawa "Orbital Liquid in Three-Dimensional Mott Insulator: $LaTiO_3$" *Phys.Rev.Lett.* **85**, 3951 (2000)

[1.7] M.K. Wu *et al*. "Superconductivity at 93K in a new mixed-phase Y-Ba-Cu-O compound system at ambient pressure" *Phys.Rev.Lett.* **58**, 908 (1987)

[1.8] Y. Maeno *et al*. "Superconductivity in a layered perovskite without cooper" *Nature* **372**, 532 (1994)

[1.9] K. Takada *et al*. "Superconductivity in two-dimensional CoO_2 layers" *Nature* **422**, 53 (2003)

[1.10] Y. Kamihara *et al*. "Iron-Based Layered Superconductor $La[O_{1-x}F_x]FeAs$ with Tc=26 K" *J.Am.Chem.Soc.* **130**, 3296 (2008)

[1.11] Y. Tokura (*COMOP today, presentation*)

[1.12] J. Chakhalian *et al.* "Magnetism at the interface between ferromagnetic and superconducting oxides" *Nature* **2**, 244 (2006)

[1.13] J. Chakhalian *et al*. "Orbital Reconstruction and Covalent Bonding at an Oxide Interface" *Science* **318**, 1114 (2007)

[1.14] A. Ohtomo *et al*. "Artificial charge-modulation in atomic-scale perovskite titanate superlattices" *Nature* **419**, 378 (2002)

[1.15] S. Okamoto and A. Millis "Electronic reconstruction at an interface between a Mott insulator and a band insulator" *Nature* **428**, 630 (2004)

[1.16] K.Takahashi *et al*. "Interface ferromagnetism in oxide superlattices of $CaMnO_3$ / $CaRuO_3$" *ApplPhysLett.* **79**, 1324 (2001)

[1.17] A. Ohtomo and H.Y. Hwang "A high-mobility electron gas at the $LaAlO_3/SrTiO_3$ heterointerface" *Nature* **427**, 423 (2004)

[1.18] N. Nakagawa *et al*. "Why some interfaces cannot be sharp" *Nature Materials* **5**, 204 (2006)

[1.19] Source: http://hoffman.physics.harvard.edu/research/SCmaterials.php (From Hudson's Group at Massachusetts Institute of Technology USA)

[1.20] M. Coey "Thin Skins for magnetic sensitivity" *Nature Materials* **4**, 9 (2005)

[1.21] Source: http://www.thespectroscopynet.com

[1.22] H. Kuzmany in "Solid-State Spectroscopy" *Springer-Verlag Berlin Heidelberg* (1998)

[1.23] M. Dressel and G. Grüner in "Electrodynamics of Solids" *Cambridge University Press* (2002)

[1.24] S. Dordevic and D. Basov "Electrodynamics of correlated electron matter" *Ann. Phys. (Leipzig)* **15**, 545 (2006)

[1.25] V. Hinkov in "In-Plane Anisotropy of the Spin-Excitation Spectrum in Twin-Free $YBa_2Cu_3O_{6+x}$" *PhD Thesis* Max-Planck Inst. Stuttgart, Germany (2007)

[1.26] S. Ishihara and S. Maekawa "Resonant x-ray scattering in manganites: study of the orbital degree of freedom" *Rep. Prog. Phys.* **65**, 561(2002)

[1.27] M. Haverkort in "Spin and orbital degrees of freedom in transition metal oxides and oxide thin films studied by x-ray absorption spectroscopy" *PhD Thesis Universitaet zu Koln* Koln (2005)

[1.28] C. Ulrich *et al*. "Orbital excitations in $YTiO_3$ and $LaTiO_3$ probed by resonant inelastic soft x-ray scattering" *Phys. Rev. B* **77**, 113102 (2008)

Chapter 2

[2.1] Y. Tokura and N. Nagaosa "Orbital physics in transition-metal oxides" *Science* **288**, 462 (2000)

[2.2] G. Khaliullin "Orbital Order and Fluctuations in Mott Insulators" *Prog.Theor.Phys. Suppl.* **160**, 155 (2005)

[2.3] B. Keimer *et al*. "Spin Dynamics and Orbital State in $LaTiO_3$" *Phys.Rev.Lett.* **85**, 3946 (2000)

[2.4] G. Khaliullin and S. Maekawa "Orbital Liquid in Three-Dimensional Mott Insulator: $LaTiO_3$" *Phys.Rev.Lett.* **85**, 3951 (2000)

[2.5] S. Csiszar "X-ray diffraction and X-ray absorption of strained CoO and MnO thin films" *PhD Thesis University of Groningen* (2005)

[2.6] Y. Tokura "Colossal Magnetoresistive Oxides" *Gordon and Breach*, London (1999)

[2.7] G. Jonker & J. Van Santen "Ferromagnetic compounds of manganese with perovskite structure" *Physica* **16**, 337 (1950)

[2.8] S. Jin *et al*. "Thousandfold change in resistivity in magnetoresistive La-Ca-Mn-O films" *Science* **264,** 413 (1994)

[2.9] Y. Tokura, Presentation "COMOP today"

[2.10] Y. Tokura "Critical features of colossal magnetoresistive manganites" *Rep.Prog.Phys*. **69**, 797 (2006)

[2.11] I. Zegkinoglou "Resonant and High-Energy X-Ray Scattering Studies on Strongly Correlated Electron Systems in Transition Metal Oxides" *PhD Thesis* Max-Planck Inst. Stuttgart, Germany (2007)

[2.12] J. Hubbard "Electron correlations in narrow energy bands" *Proc. Roy. Soc. London Ser. A* **276**, 238 (1963)

[2.13] S. Maekawa *et al*. "Physics of transition metal oxides" *Springer-Verlag* (2004)

[2.14] M. Imada *et al*. "Metal-insulator transitions" *Rev.Mod.Phys*. **70**, 1039 (1998)

[2.15] J.B. Goodenough "Magnetism and the Chemical Bond" *Robert E. Krieger Publishing Company, Huntington*, New York (1976)

[2.16] Peter Horsch, Max Planck Inst. Stuttgart, lecture notes

[2.17] N. Kovaleva *et al*. "Spin-controlled Mott-Hubbard bands in $LaMnO_3$ probed by optical ellipsometry" *Phys.Rev.Lett.* **93**, 147204 (2004)

[2.18] E. Saitoh *et al*. "Observation of orbital waves as elementary excitations in a solid" *Nature* **410**, 180 (2001)

[2.19] W-G. Yin *et al*. "Orbital ordering in $LaMnO_3$: electron-electron versus electron-lattice interactions" *Phys.Rev.Lett*. **96,** 116405 (2006)

[2.20] C. Zener "Interaction between the *d*-shells in transition metals" *Phys. Rev.* **81**, 440 (1951)

[2.21] C. Zener "Interaction between the *d*-shells in the transition metals I", "Ferromagnetic compounds of manganese with perovskite structure II" *Phys. Rev.* **82**, 403 (1951)

[2.22] P.W. Anderson and H. Hasegawa "Considerations on double exchange" *Phys. Rev.* **100** 675 (1955)

[2.23] P.G. de Gennes "Effects of double exchange in magnetic crystals" *Phys. Rev.* **118** 141 (1960)

[2.24] D. Khomskii in "Electronic structure, exchange and magnetism in oxides", *Lecture Notes*

[2.25] A. Millis *et al*. "Double exchange alone does not explain the resistivity in $La_{1-x}Sr_xMnO_3$ " *Phys. Rev. Lett.* **74,** 5144 (1995)

[2.26] T. Chatterji "Colossal Magnetoresistance Manganites" *Kluwer Academic* (2004)

[2.27] M. Hennion and F. Moussa "The precursor phase of the CMR metallic state probed by spin and lattice dynamics" *New Journ.Phys.* **7**, 84 (2005)

[2.28] M. Coey "Charge ordering in oxides" *Nature* **430**, 155 (2004)

[2.29] S. Mori *et al*. "Paired and unpaired charge stripes in the ferromagnetic phase of $La_{0.5}Ca_{0.5}MnO_3$" *Phys.Rev.Lett*. **81**, 3972 (1998)

[2.30] P. Radaelli *et al*. "Wigner crystal and bi-stripe models for the magnetic and crystallographic superstructures of $La_{0.333}Ca_{0.667}MnO_3$" *Phys.Rev. B* **59**, 14440 (1999)

[2.31] M. Pissas and G. Kallias "Phase diagram of the compound $La_{1-x}Ca_xMnO_3$ ($0.5<x<0.9$)" *Phys.Rev. B* **68**, 134414 (2003)

[2.32] M. Salamon "The physics of manganites: Structure and transport" *Rev.Modern Phys.* **73**, 583 (2001)

[2.33] A. Millis "Lattice effects in magnetoresistive manganese perovskites" *Nature* **392**, 147 (1998)

[2.34] E. Dagotto "Complexity in strongly correlated electron systems" *Science* **309**, 257 (2005)

[2.35] E. Dagotto "Open questions in CMR manganites, relevance of clustered states and analogies with other compounds including the cuprates" *New Journ. Phys*. **7**, 67 (2005)

[2.36] H. Meskine and S. Satpathy "Self-trapped magnetic polaron in electron doped $CaMnO_3$" *J.Phys.Condens.Matter* **17**, 1889 (2005)

[2.37] R. Kilian and G. Khaliullin "Orbital polarons in the metal-insulator transitions of manganites" *Phys.Rev. B* **60**, 13458 (1999)

[2.38] V. Kiryukhin "Nanoscale structural correlations in magnetoresistive manganites" *New Journ. Phys*. **6**,155 (2004)

[2.39] M. Mochizuki and M. Imada "Orbital physics in the perovskite Ti oxides" *New J. Phys*. **6**, 154 (2004)

[2.40] T. Katsufudji *et al.* "Transport and magnetic properties of Mott-Hubbard system whose bandwidth and band filling are both controllable $R_{1-x}Ca_xTiO_{3+y/2}$" *Phys.Rev.B* **56**, 10145 (1997)

[2.41] N. Kovaleva *et al*. "Optical response of ferromagnetic $YTiO_3$ studied by spectral ellipsometry " *Phys.Rev. B* **76**, 155125 (2007)

[2.42] C. Ulrich *et al*. "Raman scattering in the Mott-insulators $LaTiO_3$ and $YTiO_3$: Evidence for orbital excitations" *Phys.Rev.Lett*. **97**, 157401 (2006)

[2.43] C. Ulrich *et al*. "Orbital excitations in $YTiO_3$ and $LaTiO_3$ probed by resonant inelastic soft x-ray scattering" *Phys.Rev.B* **77**, 113102 (2008)

[2.44] E. Pavarini E. *et al*. "Mott transition and suppression of orbital fluctuations in orthorhombic $3d^1$ perovskites" *Phys.Rev.Lett*. **92**, 176403 (2004)

[2.45] I. Schuller "New class of layered materials" *Phys. Rev. Lett.* **44**, 1597 (1980)

[2.46] K. von Klitzing *et al*. "A new method for high-accuracy determination of the fine structure constant based on quantized Hall resistance" *Phys. Rev. Lett*. **45**, 494 (1980)

[2.47] D. C. Tsui *et al*. "Two-dimensional magnetotransport in the extreme quantum limit" *Phys. Rev. Lett*. **48**, 1559 (1982)

[2.48] F. Wilczek "Fractional statistics and anyon superconductivity" *World Scientific* (1990)

[2.49] P. Bonderson "Detecting non-abelian Statistics in the ν=5/2 fractional quantum Hall state" *Phys.Rev.Lett*. **96**,16803 (2006)

[2.50] J. Schlappa "Investigation of electronic order using resonant soft x-ray diffraction" *PhD Thesis Universitaet zu Koln* Koln (2006)

[2.51] Joachim Stöhr, Stanford Synchrotron Radiation Laboratory, Presentation

[2.52] M. Haverkort "Spin and orbital degrees of freedom in transition metal oxides and oxide thin films studied by x-ray absorption spectroscopy" *PhD Thesis Universitaet zu Koln* Koln (2005)

[2.53] M. Hossain *et al*. "Crystal-field level inversion in lightly Mn-doped $Sr_3Ru_2O_7$" *Phys.Rev.Lett*. **101**, 016404 (2008)

[2.54] C. Chen *et al*. "Out-of-plane orbital characters of intrinsic doped holes in $La_{2-x}Sr_xCuO_4$" *Phys.Rev.Lett*. **68**, 2543 (1992)

[2.55] R. Nakajima "X-ray magnetic circular dichroism spectroscopy in transition metal thin films" *PhD Thesis at Stanford University* (1998)

[2.56] E. Schierle "Antiferromagnetism in thin films studied by resonant magnetic soft x-ray scattering" *PhD Thesis Freien Universität Berlin* (2006)

[2.57] J.P. Hannon and G.T. Trammell "X-ray Resonance Exchange Scattering" *Phys.Rev.Lett*. **61**, 1245 (1988)

[2.58] J.M. Tonnerre *et al*. "Depth Magnetization Profile of a Perpendicular Exchange Coupled System by Soft-X-Ray Resonant Magnetic Reflectivity" *Phys.Rev.Lett.* 100, 157202 (2008)

[2.59] N. Jaouen *et al*. "An apparatus for temperature-dependent soft X-ray resonant magnetic scattering" *J.Synchriotron Rad*. 11, 353 (2004)

[2.60] S. M. Valvidares *et al*. "Resolving antiferromagnetic states in magnetically coupled amorphous Co-Si-Si multilayers by soft x-ray resonant magnetic scattering" *Phys. Rev. B* **78**, 064406 (2008)

[2.61] T. Holden *et al*. "Proximity induced metal insulator transition in $YBa_2Cu_3O_7/La_{2/3}Ca_{1/3}MnO_3$ superlattices " *Phys.Rev.B* **69**, 64505 (2004)

[2.62] J. Stahn "Magnetic proximity effect in perovskite superconductor/ferromagnet multilayers" *Phys. Rev. B* **71**, 140509 (2005)

[2.63] J. Chakhalian *et al.* "Magnetism at the interface between ferromagnetic and superconducting oxides" *Nature* **2**, 244 (2006)

[2.64] J. Chakhalian *et al*. "Orbital Reconstruction and Covalent Bonding at an Oxide Interface" *Science* **318**, 1114 (2007)

[2.65] A. Ohtomo and H.Y. Hwang "A high-mobility electron gas at the $LaAlO_3/SrTiO_3$ heterointerface" *Nature* **427**, 423 (2004)

[2.66] N. Nakagawa *et al*. "Why some interfaces cannot be sharp" *Nature Materials* **5**, 204 (2006)

[2.67] J. Eckstein "Oxide interfaces, whach out for lack of oxygen" *Nature Materials* **6**, 473 (2007)

[2.68] A. Ohtomo *et al*. "Artificial charge-modulation in atomic-scale perovskite titanate superlattices" *Nature* **419**, 378 (2002)

[2.69] S. Okamoto and A. Millis "Electronic reconstruction at an interface between a Mott insulator and a band insulator" Nature 428, 630 (2004)

[2.70] S. Seo *et al*. "Optical study of free-carrier response of $LaTiO_3$ / $SrTiO_3$ superlattices" *Phys.Rev.Lett*. **59**, 266801 (2007)

[2.71] H. Yamada *et al*. "$LaMnO_3/SrMnO_3$ interfaces with coupled charge-spin-orbital modulation" *Appl.Phys.Lett*. **89**, 052506 (2006)

[2.72] S. Smadici *et al*. "Electronic reconstruction at $SrMnO_3$-$LaMnO_3$ superlattice interfaces" *Phys.Rev.Lett*. **99**, 196404 (2007)

[2.73] S. Okamoto and A. Millis "Spatial inhomogeneity and strong correlation physics: A dynamical mean-field study of a model Mott-insulator–band-insulator heterostructure" *Phys.Rev. B* **70**, 241104 (2004)

Chapter 3

[3.1] M. Dressel and G. Grüner in "Electrodynamics of Solids" *Cambridge University Press* (2002)

[3.2] F. Mena in "Optics and Magnetism: From Itinerant to Localized Electrons" *PhD Thesis at University of Groningen*, ISBN 90-367-2128-8 (2004)

[3.3] H. Kuzmany in "Solid-State Spectroscopy" *Springer-Verlag Berlin Heidelberg* (1998)

[3.4] D. Ginsberg in "Physical Properties of High-Temperature Superconductors" *World Scientific Publishing Company* (1990)

[3.5] "RefFit-Program to fit optical spectra" by Alexey Kuzmenko, *University of Geneva* http://optics.unige.ch/alexey/reffit.html

[3.6] S. Dordevic and D. Basov "Electrodynamics of correlated electron matter" *Ann. Phys. (Leipzig)* **15**, 545 (2006)

[3.7] O.S. Heavens in "Thin Film Physics" *Methuen, London* (1970)

[3.8] M. Mazilu *et al*. "Modular method for calculation of transmission and reflection in multilayered structures" *Appl.Optics* **40**, 6670 (2001)

Chapter 4

[4.1] В.Вагин "Светосильные спектральные приборы" "*Наука*" (*Физика и Техника Спектроскопии*) (1988)

[4.2] J. Humlicek in "Infrared electrodynamics from ellipsometric measurements" *Ferroelectrics*, ***176:1***, 221, *Taylor and Francis, London* (1996)

[4.3] R. Henn "Far infrared ellipsometry using synchrotron radiation: the out-of-plane response of $La_{2-x}Sr_xCuO4$" *Thin Solid Films* **313-314**, 642 (1998)

[4.4] C. Bernhard in "Investigation of the Far-Infrared Dielectric Response of High-Tc Cuprate Superconductors with the Technique of Spectroscopic Ellipsometry"

Chapter 5

[5.1] J. Freeland *et al*. "Charge transport and magnetization profile at the interface between a correlated metal and an antiferromagnetic insulator" *Submitted for Publication* (2009)

[5.2] A. Filippetti and W. Pickett "Magnetic reconstruction at the (001) $CaMnO_3$ surface" *Phys.Rev.Lett*. **83**, 4184 (1999)

[5.3] E. Wollan and W. Koehler "Neutron diffraction study of the magnetic properties of the series of perovskite-type compounds [(1-x)La, xCa]MnO_3" *Phys.Rev.* **100**, 545 (1955)

[5.4] D. Sousa *et al*. "Ca-site substitution induced a metal–insulator transition in manganite $CaMnO_3$" *Mater. Chem. and Phys*. **109**, 311 (2008)

[5.5] W. Pickett and D. Singh "Electronic structure and half-metallic transport in the $La_{1-x}Ca_xMnO_3$ system" *Phys.Rev. B* **53**, 1146 (1996)

[5.6] C. Cardoso "*Ab-initio* calculations of the Ruddlesden–Popper phases $CaMnO_3$, $CaO(CaMnO_3)$ and $CaO(CaMnO_3)_2$" *J.Phys.Condens. Matter* **20**, 035202 (2008)

[5.7] G. Zampieri *et al*. "Electronic structure of $CaMnO_x$ with $2.66<x<3.00$ studied with photoemission and x-ray-absorption spectroscopy" *Phys.Rev. B* **58**, 3755 (1998)

[5.8] G. Zampieri *et al*. "XPS and XAS spectra of $CaMnO_3$ and $LaMnO_3$" *Physica B* **320**, 51 (2002)

[5.9] Y. Maeno *et al*. "Superconductivity in a layered perovskite without cooper" *Nature* **372**, 532 (1994)

[5.10] Y. Lee *et al*. "Non-Fermi liquid behavior and scaling of the low-frequency suppression in the optical conductivity spectra of $CaRuO_3$" *Phys.Rev. B* **66**, 041104 (2002)

[5.11] K. Maiti "Role of covalency in the ground-state properties of perovskite ruthenates: A first-principles study using local spin density approximations" *Phys.Rev. B* **73**, 235110 (2006)

[5.12] A. Zayak *et al*. "Structural, electronic, and magnetic properties of $SrRuO_3$ under epitaxial strain" *Phys. Rev. B* **74**, 094104 (2006)

[5.13] I. Mazin and D. Singh "Electronic structure and magnetism in Ru-based perovskites" *Phys.Rev. B* **56**, 2556 (1997)

[5.14] K. Maiti and R. Singh "Evidence against strong correlations in 4*d* transition-metal oxides $CaRuO_3$ and $SrRuO_3$" *Phys.Rev. B* **71**, 161102 (2005)

[5.15] K. Takahashi *et al*. "Interface ferromagnetism in oxide superlattices of $CaMnO_3$ / $CaRuO_3$" *Appl.Phys.Lett.* **79**, 1324 (2001)

[5.16] H. Yamada *et al*. "Optical magnetoelectric effect at $CaRuO_3$–$CaMnO_3$ interfaces as a polar ferromagnet" *Appl.Phys.Lett.* **92**, 062508 (2008)

[5.17] A. Maignan *et al*. "Ferromagnetism and metallicity in the $CaMn_{1-x}Ru_xO_3$ perovskites: a highly inhomogeneous system" *Solid State Comm.* **117**, 377 (2001)

[5.18] B. Nanda *et al*. "Electron leakage and double-exchange ferromagnetism at the interface between a metal and an antiferromagnetic insulator: $CaRuO_3$/$CaMnO_3$" *Phys.Rev.Lett.* **98**, 216804 (2007)

[5.19] "RefFit-Program to fit optical spectra" by Alexey Kuzmenko, University of Geneva

[5.20] A. Duborka *et al*. "Infrared study of YBCO/LCMO superlattices" *Thin Solid Films* **455-6**, 172 (2004)

[5.21] S. Seo *et al*. "Optical study of free-carrier response of $LaTiO_3$ / $SrTiO_3$ superlattices" *Phys.Rev.Lett*. **59**, 266801 (2007)

[5.22] Plots from private communication; J. Freeland University of Illinois, Chicago USA

[5.23] J. Chakhalian *et al*. "Orbital Reconstruction and Covalent Bonding at an Oxide Interface" *Science* **318**, 1114 (2007)

[5.24] K. Terai *et al*. "X-ray magnetic circular dichroism and photoemission studies of ferromagnetism in $CaMn_{1-x}Ru_xO_3$ thin films" *Phys.Rev. B* **77**, 115128 (2008)

[5.25] N. Jaouen *et al.* "An apparatus for temperature-dependent soft X-ray resonant magnetic scattering" *J. Synchrotron Rad*. **11**, 353 (2004)

[5.26] H. Meskine and S. Satpathy "Self-trapped magnetic polaron in electron-doped $CaMnO_3$" *J. Phys. Condens. Matter* **17**, 1889 (2005)

[5.27] C. Chiorescu *et al*. "Impurity conduction and magnetic polarons in antiferromagnetic oxides" *Phys.Rev. B* **76**, 020404 (2007)

Chapter 6

[6.1] G. Khaliullin "Orbital Order and Fluctuations in Mott Insulators" *Prog.Theor.Phys. Suppl.* **160**, 155 (2005)

[6.2] C. Ulrich *et al*. "Raman scattering in the Mott-insulators $LaTiO_3$ and $YTiO_3$: Evidence for orbital excitations" *Phys.Rev.Lett*. **97**, 157401 (2006)

[6.3] C. Ulrich *et al*. "Orbital excitations in $YTiO_3$ and $LaTiO_3$ probed by resonant inelastic soft x-ray scattering" *Phys.Rev.B* **77**, 113102 (2008)

[6.4] E. Pavarini *et al*. "Mott transition and suppression of orbital fluctuations in orthorhombic $3d^1$ perovskites" *Phys.Rev.Lett*. **92**, 176403 (2004)

[6.5] J-G. Cheng *et al*. "Transition from Orbital Liquid to Jahn-Teller Insulator in Orthorhombic Perovskites RTiO$_3$" *Phys.Rev.Lett*. **101**, 087205 (2008)

[6.6] N. Kovaleva *et al*. "Optical response of ferromagnetic $YTiO_3$ studied by spectral ellipsometry" *Phys.Rev. B* **76**, 155125 (2007)

[6.7] W. Knafo *et al*. "Ferromagnetism and lattice distortions in the perovskite$YTiO_3$" *Phys.Rev. B* **79**, 054431 (2009)

[6.8] A. Komarek *et al*. "Magnetoelastic coupling in RTiO$_3$ (R=La,Nd,Sm,Gd,Y) investigated with diffraction techniques and thermal expansion measurements" *Phys.Rev. B* **75**, 224402 (2007)

[6.9] N. Kovaleva *et al*. "Dipole-active optical phonons in $YTiO_3$: Ellipsometry study and lattice-dynamics calculations" *Phys.Rev. B* **79**, 045114 (2009)

[6.10] A. Bocquet *et al*. "Electronic structure of early 3d-transition-metal oxides by analysis of the 2p core-level photoemission spectra" *Phys.Rev. B* **53**, 1161 (1996)

[6.11] M. Mochizuki and M. Imada "Orbital physics in the perovskite Ti oxides" *New J. Phys*. **6**, 154 (2004)

[6.12] F. Iga *et al*. "Determination of the orbital polarization in $YTiO_3$ by using soft x-ray linear dichroism" *Phys.Rev.Lett*. **93**, 257207 (2004)

[6.13] C. Ulrich *et al*. "Magnetic Order and Dynamics in an Orbitally Degenerate Ferromagnetic Insulator" *Phys. Rev. Lett*. **89**, 167202 (2002)

[6.14] "RefFit-Program to fit optical spectra" by Alexey Kuzmenko, University of Geneva

[6.15] A. Takazawa *et al*. "Investigation of phonon anomaly in the orbital order state of $La_{1-x}Sr_xMnO_3$ (x~1/8)" *J. Phys. Soc. Japan* **70**, 902 (2001)

[6.16] JM. Wesselinowa "Self-consistent theory of spin-phonon interactions in Heisenberg ferromagnets" *Z. Phys. B. Cond. Matter* **68**, 57 (1987)

[6.17] JM. Wesselinowa "Effect of magnetic ordering on the phonon damping in ferromagnetic semiconductors" *J. Phys. Condens. Matter* **3**, 5231 (1991)

[6.18] A. Millis *et al*. "Double exchange alone does not explain the resistivity in $La_{1-x}Sr_xMnO_3$" *Phys. Rev. Lett.* **74,** 5144 (1995)

[6.19] A. Millis "Lattice effects in magnetoresistive manganese perovskites" *Nature* **392**, 147 (1998)

[6.20] A. Takazawa *et al*. "Investigation of phonon anomaly in the orbital order state of $La_{1-x}Sr_xMnO_3$ (x~1/8)" *J. Phys. Soc. Japan* **70**, 902 (2001)

[6.21] J. Irwin *et al*. "Oxygen isotope effect on the vibrational modes of $La_{1-x}Ca_xMnO_3$" *Phys. Rev. B* **59**, 9362 (1999)

[6.22] J. Laverdiere *et al*. "Spin-phonon coupling in orthorhombic $RMnO_3$ (R=Pr, Nd, Sm, Eu, Gd, Tb, Dy, Ho, Y): A Raman study" *Phys. Rev. B* **73**, 214301 (2006)

[6.23] Iliev *et al*. "Raman spectroscopy evidence of strong spin-phonon coupling in epitaxial thin films of the double perovskite La_2NiMnO_6" *Appl. Phys. Lett*. **90**, 151914 (2007)

[6.24] E. Granado *et al*. "Magnetic ordering effects in Raman spectra of $La_{1-x}Mn_{1-x}O_3$" *Phys.Rev. B* **60**, 11879 (1999)

[6.25] Xu Jiasi *et al*. "Orbital-spin-phonon coupling in Jahn-Teller-distorted $LaMnO_3$: Softening of the 490 and 610 cm^{-1} Raman-active modes" *Phys. Rev. B* **75**, 012409 (2007)

[6.26] JM. Wesselinowa and St. Kovachev "Magnetic ordering effects in the phonon spectra of orthorhombic $RMnO_3$ compounds" *J. Phys. Condens. Matter* **19**, 176211 (2007)

[6.27] R. Gupta *et al*. "Field – and pressure-induced phases in $Sr_4Ru_3O_{10}$: A spectroscopic investigation" *Phys. Rev. Lett*. **96**, 067004 (2006)

[6.28] J. Hemberger *et al*. "Spin-driven phonon splitting in bond-frustrated $ZnCr_2S_4$" *Phys. Rev. Lett.* **97**, 087204 (2006)

[6.29] T. Rudolf *et al*. "Spin-phonon coupling in antiferromagnetic chromium spinels" *New J. Phys.* **9**, 76 (2007)

[6.30] A. Sushkov *et al*. "Probing spin correlations with phonons in the strongly frustrated magnet $ZnCr_2O_4$" *Phys. Rev. Lett*. **94**, 137202 (2005)

Acknowledgements

First of all, I would like to express my gratitude to Professor Bernhard Keimer for accepting me as a PhD student in his group at Max Planck Institute for Solid State Research, Stuttgart, for giving me the opportunity to work and learn in one of the most exciting fields in solid state physics, that of transition metal oxide materials, for his supervision and constant support through these years.

Special thanks to Claudia Hagemann for being always kind and patient, especially with the numerous administrative issues during my first weeks in Germany.

I also express my very special thanks to:

--- in order of appearance --- ☺ :

…all people that connected me and invited me in the group: Christian Bernhard, Biliana Gasharova and my sister Svetla

…to my supervisors: Christian Bernhard and Alexander Boris, and the entire ellipsometry group: Natalia Kovaleva, Li Yu, Taryl Kirk and later on: Yulia Matiks and Paul Popovich

…to Denitsa Shopova, my first and best bulgarian friend in Stuttgart
- *Thanks a Lot Denitsa, for Being Always Around!*

…to the group engineers, for their precise work and original solutions in building up the optical spectroscopy apparatus: Dietrich Böhme - *Herzlichen Dank Herr Böhme*, Benjamin Bruha and Heiko Uhlig

…to all group members, for the wonderful working atmosphere and the nice time we had together ☺☺☺: Dr. Raichle, Dr. Hinkov, Dr. Zegkinoglou, Dr. Bohnenbuck, Dr. Suchaneck, Mohamed Bakr, Dr. Aynajian, Dr. Damljanovic, Dr. Sung Seok A. Seo, Dr. Eva Benckiser, Daniel Haug, Ji-Tae Park, Martin Rahlenbeck ☺ Thank You Guys ☺ Philippe Leininger, Mathieu Le Tacon, Sibel Bayrakci, Monika Rawolle, Nadir Driza, George Jackeli, Jiri Chaloupka, Giniyat Khaliullin, Heinrich Klann, Manfred Ohl and Michael Schulz… Peter Lemmens, Clemens Ulrich, Maël Guennou, Jörg Strempfer, Lucia Capogna, Jacques Chakhalian, Heon Jung Kim, Myung-Whun Kim

My Very Special Thanks once again to Dr. Sung Seok A. Seo for the nice and fruitful discussions on oxide superlattices, also to Dr. Ho Nyung Lee, Dr. Vladimir Hinkov, Dr. Eva Benckiser, Dr. Maurits Haverkort, Dr. Jean-Mark Tonnerre, Dr. Stephane Grenier and Thomas Tietze, to the members of the Technology Group at MPI: Professor Hanns-Ulrich Habermeier, Georg Cristiani, Dr. Yoshiharu Krockenberger, Benjamin Stuhlhofer and Stefan Heinze

…to the wonderful people in the institute, from the administration, the post office, from the workshop, Forschungsbedarf Laden, Tieftemperatur and to Dimi and Thomas ☺

…to my football mates: Ilya, Misha, Vitaliy, Sergey, Thomas, Slavko, Matias…and all others

…to my best friends in Germany and in Sofia: Denitsa, Dimitar, Andrea, Petia, Vladi Anton (Thanks for joining at Barcode☺)
Cveti, Stefan, Iveta, Angel, Irena, Ceco i Mitko ☺
Andrei, Ivo and Cveti, Chacho and Alex, Krasi, Gogo, Lenko and especially Valentina ☺

…to all my family, for their love, support and encouragement: Reni, Lucy, Dancho, Svetla, to my beloved niece Yoana ☺… *now it is only smiles kid, you will always be with us!*, Pavel, Rumi, Momchi, Marta and Mario……Обичам Ви.....also to Joro and Herr V. Kölle for the insights on various essential topics ☺

List of Publications

1) M. Baleva, E. Goranova, V. Darakchieva, S. Kossionides, M. Kokkosis, P. Jordanov "Influence of grain size on the optical conductivity of β-$FeSi_2$ layers" *Vacuum* **69**, 425–429 (2003)

2) E. Goranova, B. Amov, M. Baleva, E. Trifonova, P. Yordanov "Ion beam synthesis of Mg_2Si" *J. Materials Science* **39**, 1857–1859 (2004)

3) N.N. Kovaleva, A.V. Boris, P. Yordanov, A. Maljuk, E. Brücher, J. Strempfer, M. Konuma, I. Zegkinoglou, C. Bernhard, A.M. Stoneham and B. Keimer "Optical response of ferromagnetic $YTiO_3$ studied by spectral ellipsometry " *Phys.Rev.B* **76**, 155125 (2007)

4) Li Yu, D. Munzar, A.V. Boris, P. Yordanov, J. Chaloupka, Th. Wolf, C.T. Lin, B. Keimer and C. Bernhard "Evidence for Two Separate Energy Gaps in Underdoped High Temperature Cuprate Superconductors from Broadband Infrared Ellipsometry" *Phys.Rev.Lett.* **100**, 177004 (2008)

5) N.N. Kovaleva, A.V. Boris, L. Capogna, J.L. Gavartin, P. Popovich, P. Yordanov, A. Maljuk, A.M. Stoneham and B. Keimer "Dipole-active optical phonons in $YTiO_3$: Ellipsometry study and lattice-dynamics calculations" *Phys.Rev. B* **79**, 045114 (2009)

6) W. Knafo, C. Meingast, A.V. Boris, P. Popovich, N.N. Kovaleva, P. Yordanov, A. Maljuk, R.K. Kremer, H. v. Löhneysen and B. Keimer "Ferromagnetism and lattice distortions in the perovskite$YTiO_3$" *Phys.Rev.B* **79**, 054431 (2009)

7) J.W. Freeland, J. Chakhalian, A.V. Boris, J.-M. Tonnerre, J.J. Kavich, P. Yordanov, S. Grenier, P. Popovich, H.N. Lee and B. Keimer "Charge transport and magnetization profile at the interface between a correlated metal and an antiferromagnetic insulator" *Submitted for Publication* (2009)